MASTER

PROCEEDINGS OF THE

2nd International Topical Conference on HIGH POWER ELECTRON and ION BEAM Research and Technology

October 3-5, 1977

Volume II of II

LABORATORY OF PLASMA STUDIES

CORNELL UNIVERSITY

ITHACA, NEW YORK

Sponsored by:

ERDA
AFOSR
L.P.S., CORNELL

Conf-771035--12

PROCEEDINGS OF THE

2nd International Topical Conference on HIGH POWER ELECTRON and ION BEAM Research and Technology

October 3-5, 1977

Volume II of II

J.A. Nation and R.N. Sudan
Editors

LABORATORY OF PLASMA STUDIES

CORNELL UNIVERSITY

ITHACA, NEW YORK

Sponsored by:

ERDA
AFOSR
L.P.S., CORNELL

ACKNOWLEDGMENTS

Conference Organizing Committee

R. C. Davidson, ERDA
R. L. Gullickson, AFOSR
L. S. Levine, ERDA
J. A. Nation, Cornell
E. Ott, Cornell
R. N. Sudan, Cornell (Chairman)

Conference Staff

P. C. Ackley
J. M. Discenza
E. M. Jeddry (Conference Coordinator)
R. A. Rosenbluth
R. A. Saltsman

CONTENTS

VOLUME I

Energy Deposition in Targets

Beam Plasma Interactions

Charged Particle Rings

CONTENTS

VOLUME II

Collective Accelerators

Technology

Laser Applications

COLLECTIVE ACCELERATORS

COLLECTIVE ION ACCELERATION IN A VACUUM DIODE

J. L. Adamski, P. S. P. Wei, J. R. Beymer, R. L. Guay and
R. L. Copeland — Boeing Aerospace Co., Seattle, Washington 98124

Abstract

Recent experiments in a "Luce-Type[1]" vacuum diode have been made utilizing time-resolved spectroscopic measurements of anode plasma expansion velocity by line broadening and Doppler shift techniques, electrostatic and magnetic probe measurements of space charge potential well movement, time of flight Faraday cup measurements, and nuclear activation ion energy measurements. Preliminary results using a 3 MeV, 90 KA, 40 nsec electron beam from the FX-75 accelerator show mean proton energies between 5-10 MeV with an energetic tail in excess of 30 MeV with corresponding 10-20 KA peak ion current and 5-10 nsec pulse width. Ion beam current modulation has been observed as a result of the typical diode current modulation due to accelerator waveguide reflections. A brief discussion of a modified one-dimensional ion emission law[2] is given and the results will be compared to the Olson model[3] for gas ionization neutralization.

I. Introduction

Figure 1 shows a schematic of the experimental vacuum diode.

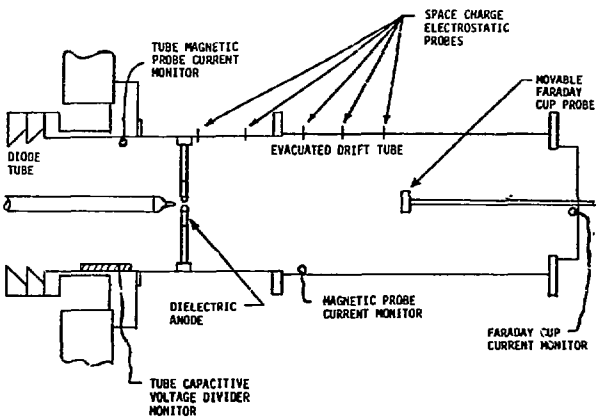

Figure 1. A Schematic of the Experimental Vacuum Diode

Initially, the unpinched hollow electron beam causes an avalanche breakdown of the dielectric anode material on the diode side, causing the surface of the dielectric anode to be covered with highly-conducting

anode plasma. This assumption is verified experimentally in that (1) the diode can not deliver a relativistic electron beam unless the anode is about at ground potential and (2) photographs and damage due to streamer "tracks" show streamers exist on the diode side of the dielectric anode. Anode material vaporized by the intense electron beam and streamers is subsequently ionized and forms the dense anode plasma. This anode plasma is essential in establishing bipolar diode flow to initiate electron beam pinching and also acts as an ion source from which space charge limited ion emission into the virtual cathode can occur. The ion source in the vacuum case involves space charge limited emission in contrast to the collisional and avalanche induced ionization for the gas injection case. The initial accelerating electric field is formed by space charge stopping of the injected beam electrons in the same manner as the Olson model.[3] As ions are accelerated toward the beam front, they partially neutralize the beam electrons allowing it to propagate in excess of the original space charge limiting current. This allows the beam front to "breakaway" from the anode region. The electric field of the un-neutralized beam front continues to accelerate the ions.

II. Theory

For the one-dimensional case of space charge limited ion emission from the anode plasma, one may draw an analogy to the bipolar diode where opposing electron and ion currents are space charge limited. Here, the virtual cathode behaves as a real cathode in the sense that the electric field is zero there and the injected electrons from the diode all slow to zero velocity and are accelerated back toward the anode (for 1-D flow). Actually, the radial electric field in the vicinity of the virtual cathode causes these slowed down electrons to flow radially to the wall. The solution of Poisson's equation for bipolar diode flow may be found in Reference 2. The boundary conditions at the anode are satisfied in

view of the high conductivity of the anode plasma. With anode plasma densities about 10^{18} (electrons/cc), the collisionless skin depth is about 5.3×10^{-4} cm, implying that the electric field drops off very rapidly inside the plasma layer. The emitted ion density is

$$n_i(0) \doteq \frac{4}{9}\frac{\varepsilon_0}{e}\left(\frac{j_e}{j_c}\right)\frac{V}{d^2}(1+\alpha)^{1/2} \qquad (1)$$

where $\left(\frac{j_e}{j_c}\right)$ is the ratio of electron current density at the anode to the non-relativistic current density, $\underline{V}$ is the virtual cathode potential, $\underline{d}$ is the gap between the virtual cathode position and the anode plasma, and $\alpha = \frac{eV_0}{2mc^2}$, where V_0 is the diode voltage.

For typical experimental parameters V_0 = 3.0 MV, (j_e/j_c) = 1.4, V = 6.0 MV, d = 6.1 cm, assuming an injected beam risetime of 5.0 nsec, $n_i(o) \doteq 1.1 \times 10^{13}$ ions/cc.

This is sufficient to cause complete space charge neutralization which is necessary for well "breakaway" or beam propagation. Of course, the emitted ion density should fall off very rapidly as the well leaves the anode and the ion pulse should be very narrow.

For a zero risetime electron beam, a one-dimensional analysis similar to that of Reference 5 predicts the axial electric field at the anode plasma boundary at the time of the first electron reflection to be

$$E_z(o) = \frac{2\gamma_0^{1/2} J_0}{\varepsilon_0 \omega_b} \qquad (2)$$

where J_0 is the injected beam current density and ω_b is the beam plasma frequency. This equation is in agreement with one-dimensional particle in cell calculations at the time of the first electron reflection.

For a finite risetime beam, the electric field at anode plasma boundary at the time of the first electron reflection was found to be

$$E_z(o) = \frac{3}{2^{1/3}}\frac{(\tau_r \omega_b \gamma_0)^{1/3}}{(\varepsilon_0 \omega_b)} J_0, \qquad (3)$$

where τ_r is the beam risetime, ω_b is the beam plasma frequency, and J_o is the beam current density. Equation (3) implies that the time of first electron reflection is

$$t_{ref.} = \frac{3}{2^{1/3}} \frac{(\omega_b \tau_r \gamma_o)^{1/3}}{\omega_b} \qquad (4)$$

which agrees with the constant coefficient in the result obtained by Olson in Reference 3, pg. 587.

The ion current risetime should depend upon the rate at which this accelerating electric field reaches its peak value. This ion current risetime was observed to be about 2 to 3 nsec. The ion current fall time should depend upon how fast the V and d terms in Eq. (1) change with time. This is observed to be somewhat slower than the risetime and is typically 5 nsec. The peak ion current is estimated to be about 10 to 20 KA peak.

III. Experimental Results

(1) The FX-75 R.E.B. Accelerator

The FX-75 electron beam accelerator was used in these experiments. Figure 2 shows typical simulation results from the FXPULSE code[4] with the experimental waveforms (dashed) for an 8 mm gap superimposed. The accelerator was divided into 245 one-dimensional cells with a corresponding one-way transit time of 0.1 nsec for the T.E.M. waves. An R, L, C lumped equivalent circuit with generalized time-varying parameters was used to represent the beam in the gap. For the ion acceleration run shown here constant values for these beam parameters were used in view of the experiment, although the code has been used for time-dependent diode parameters.[4] Note the strong modulation of the waveform due to discontinuities in the accelerator waveguide network. The simulation waveforms are normalized to the charged line voltage.

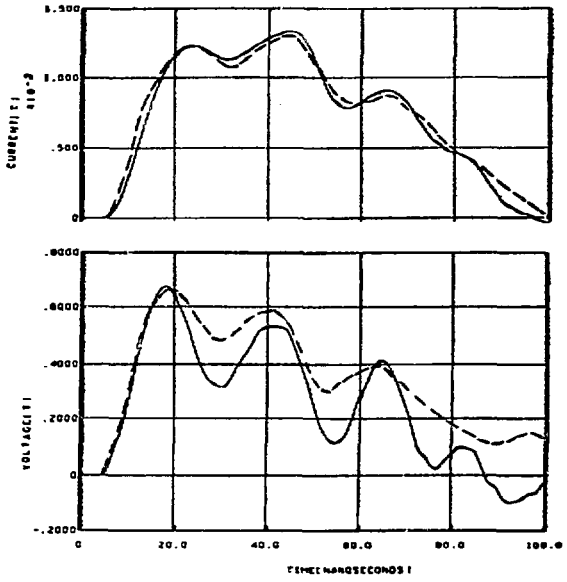

Figure 2. Experimental Typical Current (Top) and Voltage (Bottom) For an 8 mm Gap (Dashed) Superimposed on the FXPULSE Results.

(2) Spectroscopic Measurements

Optical spectroscopy was used as a diagnostic technique for investigation of the plasma properties of the ion source plasma in the anode aperture. The Hilger-Watts E 498 visible-near u.v. spectrograph has a reciprocal linear dispersion of 5-50 Å/mm over the range 2000-5000 Å and is used with Kodak 1F and SWR emulsion plates. A photomultiplier may be fitted to the output for time resolved spectral line measurements.

The spectroscopic study identified spectral line radiation of ionized states of carbon through C^{+4}. Analysis of the carbon line emission intensities yields an estimate of the plasma temperature at 50-100 eV and density at $5 \times 10^{17}/cm^3$. The velocity of the plasma was estimated to be $\sim 2 \times 10^7$ cm/sec from a measurement of the Doppler shift in the C^{++} 2297 Å

line. A more complete description of the spectroscopic studies will be given in a future paper.[6]

(3) Faraday Cup Measurements

Figure 3 shows a graph of both wavefront velocity and displacement vs. time obtained by moving the Faraday cup from 5.0 cm to 80.0 cm from the anode. Although the wavefront displacement is non-linear, two linear regression curves are drawn. Curve (1), a least squares fit taking all of the displacement data into account, represents protons with 4.6 MeV energy. Curve (2), a least squares fit taking only the displacement data for t < 10.0 nsec which is about the beam risetime, represents protons with 18.2 MeV energy.

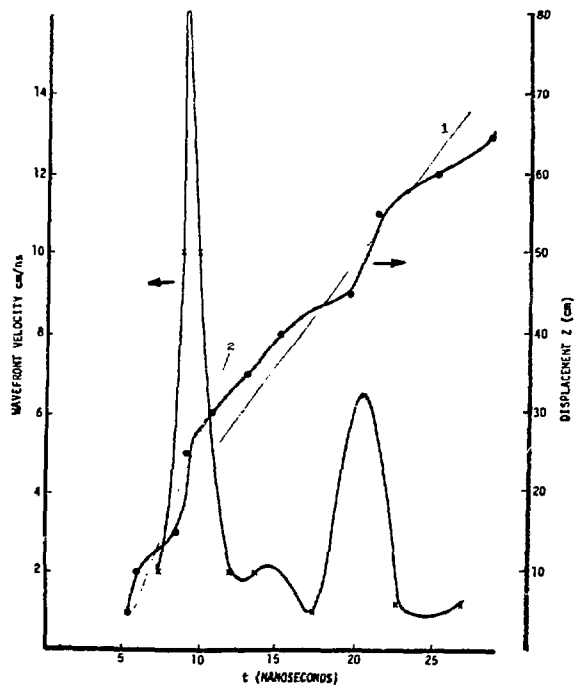

Figure 3. Electron Wavefront Displacement and Velocity, (Dielectric Anode)

Figure 4 shows a typical ion beam current waveform with a transverse magnetic field applied to eliminate beam electrons. The peak measured current is about 4 KA. The fraction of the ion current sampled in the Faraday cup experiments can be compared with the full current by comparing Faraday cup radioactivity levels with targets exposed to the direct beam. From this comparison the full ion current is estimated to be 3 to 5 times the Faraday cup reading, in rough agreement with simple analytic calculations. Note the striking similarity between the ion current waveform in Figure 4 and the wavefront velocity shown in Figure 3.

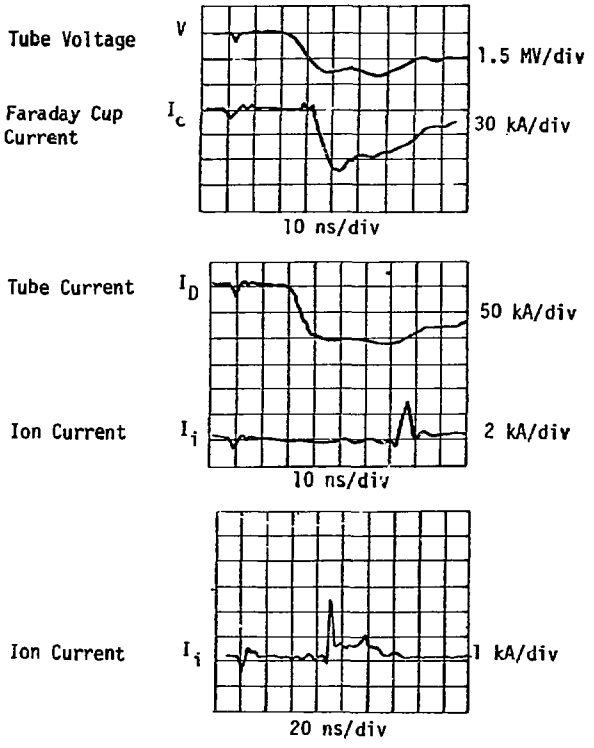

Figure 4. Ion Beam Current Waveform

(4) Electrostatic Space Charge Probe Data

Figure 5 shows a typical set of space charge probe data. The electrostatic probes are highly directional capacitively coupled charge sensitive devices. Figure 5 shows the position of the un-neutralized propagating wavefront with time at four probe positions shown in Figure 1. This data seems to be consistent with the time-of-flight data discussed above.

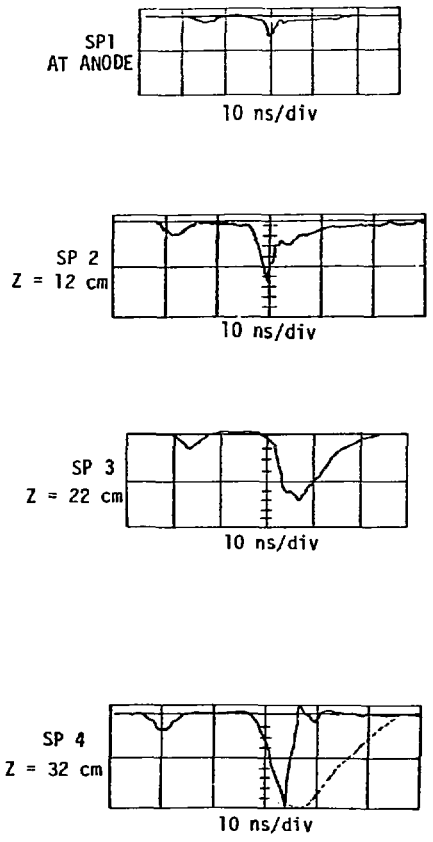

Figure 5. Typical Set of Space Charge Probe Data

(5) Magnetic Current Probe Data

The magnetic current probe, shown in Figure 1, located downstream from the dielectric anode showed current pulses which were very similar to the diode tube current pulse except that the risetime was considerably less (5.0 nsec) due to time-dependent electron beam pinching in the diode.

(6) Nuclear Activation Measurements

A simple method for determination of the proton energy in the ion beam involves use of a target comprised of stacked thin foils with a high nuclear cross section for activation by the incident particle beam. The maximum depth of penetration in the stack indicates the peak beam energy through well-known range-energy relationships and the fall off of activation through the stack provides a general indication of energy spectrum. A stack of thin (0.125 mm) copper foils was exposed to the accelerated ion beam. The reaction $^{63}Cu(p,n)^{63}$ Zn was used to monitor induced sample activity. The reaction has a threshold of 4.2 MeV and ^{63}Zn has a half life of 38.5 min. The foils were counted with a calibrated Ge(Li) detector system and the foil activity data is plotted in Figure 6. The figure also indicates proton range on the lower scale and shows measureable activity at a range of 30 MeV protons. The distribution of activity however, indicates the bulk of the ion beam had an energy much lower than the 30 MeV peak.

IV. Conclusion

We have attempted to explain in simple theory and experiment an ion acceleration system in which an unneutralized beamfront accelerates a high current, short duration ion pulse out of the anode plasma. Acceleration continues downstream as the unneutralized space charge region propagates ahead of the ion beam neutralized electron beam. Experimental measurement of the ion energy indicates a large fraction of the

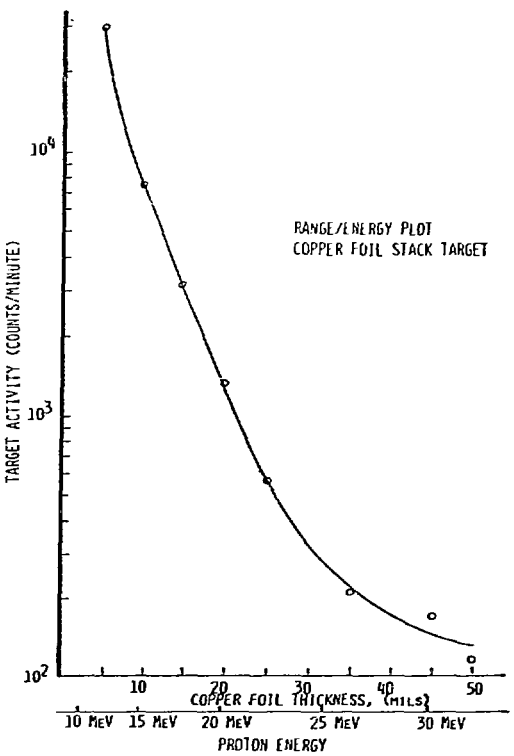

Figure 6. Target Activity vs. Copper Foil Thickness

current has an energy between 5-10 MeV in agreement with the virtual cathode model of Olson but the higher energy ions are unexplained by this model.

From the experimental results presented the peak energies are found at a downstream distance of 30 cm corresponding to the period of more rapid wavefront motion shown in Figure 3, Curve 2. Possibly, a few of the emitted protons can follow the high initial wavefront velocity shown in Figure 3 (curve 2) which occurs just after virtual cathode formation, while the bulk of the accelerated ions are between 5.0 to

10.0 MeV. The actual ion source in the vacuum diode is space charge limited ion emission from the anode plasma in contrast to the gas ionization processes discussed by Olson.[3] The one-dimensional ion emission law predicts kiloampere currents as experimentally observed. We conclude that even though the average ion energy is close to the energies predicted by Olson, there is no real "stationary well" stage and the ions are continually being accelerated by the electric field of the un-neutralized beam front.

It is interesting to note that the modulated electron beam from FX-75 also produces a similarly modulated ion beam. This may be a simple way to generate a long pulse train of ion pulses by designing the appropriate accelerator components.

References

1. J. S. Luce, H. L. Sahlin, and T. B. Crites, I.E.E.E. Trans. Nucl. Sci. NS-20 (3), 336 (1973); and J. S. Luce, Ann. N.Y. Acad. Sci. 251, 217 (1975).
2. J. W. Poukey, Appl. Phys. Lett., Vol. 26, No. 4 (1975).
3. C. L. Olson, Phys. of Fluids, Vol. 18, No. 5 (1975).
4. R. L. Copeland, doctoral dissertation, Dept. of Electrical Engineering, Univ. of Tennessee, Knoxville, Tenn., June, 1977.
5. J. W. Poukey and N. Rostoker, Plasma Phys. 13, 897 (1971).
6. P.S.P. Wei, A.P.S. Division of Plasma Physics Meeting, Oct. 1977, Atlanta, Ga.

A WAVE ACCELERATOR FOR COLLECTIVE ION ACCELERATION

R. Adler, G. Gammel, J. A. Nation, M. E. Read* and R. Williams

Cornell University, Ithaca, New York 14853

and

P. Sprangle and A. Drobot

Naval Research Laboratory, Washington, D.C. 20375

Abstract

Aspects of the experimental program at Cornell for the generation of a large amplitude space charge wave, suitable for the demonstration of a wave particle accelerator, are presented.

An account is given of the wave growth in a slow wave structure, and of the measured values of the electric field and phase velocities of the wave, after extraction into a uniform tube. The electric field measured is in excess of 30 kV/cm and the phase velocities consistent or slightly lower than the expected values.

Progress towards the development of a suitable ion source for use as an injector is also summarized and experiments designed to elucidate the collective processes involved are described.

Introduction

The application of relativistic electron beams to collective ion acceleration has been studied in many laboratories. Most of these schemes use the acceleration occurring in the potential well at the head of the electron beam. Sloan and Drummond [1] first proposed the use of negative energy waves on a relativistic electron beam as a technique for

* Present address: Naval Research Laboratory, Washington, D.C. 20375.

coupling from electron beams to protons in an accelerator. Since that time, Nation [2], Sprangle [3], and other workers [4] have proposed configurations in which the slow space charge wave may be used for the proton acceleration.

As shown in this paper, techniques exist for the growth of large amplitude space charge waves and diagnostics have been developed to measure both the wave amplitude and phase velocity. The limits achievable on these parameters remain to be determined.

Theoretical analysis shows that the space charge wave will only have a zero phase velocity at the space charge limiting current. Present experimental studies and computer simulations are attempting to resolve how low a phase velocity is realizable in practice in the presence of a large amplitude wave.

Concurrent with the presently reported studies on wave growth and extraction we are also studying approaches to providing a suitable ion injector for the wave accelerator. In the first of these we plan to use a Luce diode configuration to provide a proton beam with a sufficiently high energy to inject into the wave. The aspects of that activity reported in the present work indicate briefly recent diagnostic developments which help elucidate the collective acceleration mechanism involved. In an alternate approach, the initial low energy acceleration is accomplished in a modified wave growth section where the first spatial harmonic is used to couple to the protons. Numerical solutions to the linear dispersion relation in this type of structure have also been obtained.

Experimental Observations of Space Charge Waves

The experimental configuration used in the wave generation is shown in Fig. 1. The electron beam is provided from a pulse line which has

been typically operated in the range 250 kV to 950 kV with extracted beam currents of up to 1 kA. The pulse duration is 100 nsec. The beam is generated in and propagated along a strong axial magnetic field ($B_z \geq 10$ kGauss).

The slow wave structure is a disk loaded waveguide with cavities having a period of 5.0 cm and a diameter of 12.7 cm. It supports TM modes in the central section and standing TEM modes in the radial cavities. The electrical length of the radial cavities is increased through the use of the lucite filler. This permits lower frequency operation of the system, which, with the parameters used, behaves as a series of weakly coupled TM 010 mode cavities. Higher frequency oscillation is also present corresponding to an interaction between the beam and the TM 020 cavity mode. In comparison with the slow wave structure described later in this paper, the ratio of the amplitudes of the first space harmonic to the amplitude of the fundamental is small. The experimental device also does not support a TEM mode contribution to the dispersion relation.

The measured output wavetrain is always close to 1.25 GHz, a frequency about 10% higher than that obtained in the unloaded transmission structure. At the lower voltage range used, the wave energy propagation is against the electron beam motion and signal delays in the envelope corresponding to group velocities as low as -0.05 c have been observed. In the higher voltage mode of operation the instability appears to be convective and growth exponential throughout the full 115 cm of the slow wave system. The measured growth rate, observed from magnetic probes located close to the ends of the radial arms, was as high as 0.3 db/cm. Instability corresponding to an interaction between the beam and the TM 020 mode of the cavity at a frequency of 3.0 GHz has also been observed.

The signal level in this mode is not yet well established, but is a significant fraction of that found for the fundamental mode. It seems possible to suppress the higher frequency mode through the use of appropriately designed coupling between the adjacent cavities. Figure 2 shows a plot of the signal strength versus position in the slow wave structure. The beam had an energy of about 700 keV.

At present we have only grown waves on beams with ratios of current to limiting current of less than about 0.5. The electric field of the wave, in these cases, varies between 20 and 30 kV/cm. The wave field condition determining the onset of self trapping of the electrons is given by

$$E_z \approx \frac{k}{\gamma_{ph}} (\gamma_{ew} - 1) \frac{m_o c^2}{e}$$

where

$$\gamma_{ew} = \gamma_e \gamma_{ph} [1 - \beta_o \beta_{ph}]$$

is the value of the relativistic factor measuring the difference in the electron velocity and the wave phase velocity. γ_{ph} is the relativistic factor for the wave phase velocity measured in the laboratory frame. This field has a value estimated in the range E ~ 10 - 60 kV/cm. This field is in the range of the fields measured experimentally. It should be noted that at higher values of the ratio I/I_L the trapping field increases to a value an order of magnitude greater than that quoted above and that fields of a few hundred kilovolts/cm should be attainable with a moderate energy beam before self trapping develops.

Following the wave growth section the beam is extracted into a uniform pipe with a diameter of 2.9 cm. Extensive development of diagnostic techniques to measure the wave electric field and phase velocity in this section, where the slow electromagnetic wave is cut off, has been

completed and first measurements of these parameters have been obtained. The measurement technique, which is described elsewhere [5], uses a double loop mounted in a side tube, just outside the waveguide wall, oriented to pick up the wave magnetic field. The loop feeds a subtractor to reduce common mode pick-up of the electrostatic field. The loop is calibrated at the wave frequency in a coaxial system using the pipe as the outer conductor of the coaxial cable. The calibration permits measurement of the wave magnetic field as a function of time and with the aid of the known dispersion relation for the wave, permits calculation of the electric field on axis. To complete this evaluation it is necessary to know the wave phase velocity. This has been determined using two similar calibrated probes separated from each other by a known distance, in an interferometer arrangement. The interference signal from the two detectors gives a direct measurement of the wavelength of the space charge wave and hence the phase velocity.

The results obtained in the experiments performed so far are summarized in Table 1.

V_D(kV)	I (A)	I/I_L	β_{ph}(calc.)	β_{ph}(expt.)	E_z(r=0)kV/cm
700	700	0.2	0.75	0.70±0.07	20
270	800	0.50	0.50	0.30±0.10	32

Table 1.

The experimental results are consistent with or less than those expected based on calculations of the wave phase velocity as a function of the ratio of the beam to limiting current. The low voltage result may indicate that non-linear effects result in a reduction of the slow wave phase

velocity. Further experiments are in progress to confirm this result. The modulation of the beam is substantial with potential well depth to beam injection voltage ratios of 0.13 and 0.34, respectively. The corresponding ratios for the ratio of the r.f. current to the beam current are 0.25 and 0.33 , respectively. With lower phase velocities the wave potential well is smaller for comparable electric fields. The permissible electric field to remain in the linear regime also increases rapidly with decreasing phase velocity.

Particle Injector Studies

In view of the problems associated with the generation of very low phase velocity waves, we plan to develop an injector which will produce protons with energies of order 20 - 30 MeV. A device suitable for this ion generation in a wave acceleration test concept experiment is the Luce [6] diode. This device has been shown to generate protons with energies of up to 22 times the diode injection energy. It relies on a three stage acceleration process which is not well understood. In our present experiments we have concentrated on developing a single stage device and on devising new diagnostics techniques to elucidate the acceleration mechanism involved. Previous experiments [7] have strongly suggested that the acceleration is associated with ions being trapped in the moving space charge well at the head of the electron beam. The virtual cathode formed propagates in this case as a result of the neutralization of the beam by the fast protons. A new probe system has been devised which may be mounted in either the side wall of the tube or in the end of the tube. The probe consists of a Faraday cup covered with multiple layers of absorber and measures the relative electron current to each layer of the absorber. The probe therefore gives a measurement of the relative distribution of electron energies and is capable of resolving electrons

with energies greater than the injection energy. Such electrons have been predicted in beam head acceleration analysis where well depths of up to three times the beam energy are expected. The side wall cups also record the motion of the well. Preliminary experiments suggest the presence of some electrons with energies greater than the beam injection energy. The single stage device used produces [7] protons with energies up to eight times the diode voltage.

An alternate acceleration mechanism capable of accelerating low energy ions in a space charge wave uses the space harmonic properties of a periodic structure. This mechanism, which was originally proposed by Sprangle, is described with reference to Fig. 3. An annular beam is propagated close to the boundary of a ridged waveguide. The gap length is one-half of the period of the structure. To satisfy the boundary conditions at the ridged surface requires that the wave be composed of a number of space harmonics, with appropriate ratios of amplitudes to satisfy the requirement that the electric field drop to zero on the conducting surfaces and be finite in the gaps. At any operating frequency having any frequency ω and wave number k there will also exist a spectrum of space harmonics with wavenumbers

$$k_n = k_o + \frac{2\pi n}{L}$$

where L is the period of the structure and n an integer. For the structure shown, the amplitude of the first space harmonic varies from $2/\pi$ of the amplitude of the fundamental at the ridged surface to zero at the smooth wall. In this form of accelerator, we propose to grow a large amplitude wave by means of the unstable interaction between the slow space charge wave and the fundamental (ω, $k = k_o$) of the structure and to trap the ions in the first space harmonic. The ion energy may be

increased by adiabatically increasing the period of the structure. The lowest unstable portions of the dispersion relation for a uniform structure of the type illustrated in Fig. 3 is shown in Fig. 4. In this figure we show the real and imaginary parts of the frequency as a function of the wavenumber k. Only that portion of the curve appropriate to the interaction in the fundamental mode is shown. The wave is unstable over a broad range of values of k_o and has a peak corresponding to a phase velocity of about 0.6 c. The ratio of the beam to limiting current in this case was about 0.2 and corresponds to conditions easily achievable. The growth rate of the instability is very large and is comparable to the wave frequency, as was observed in the experiments reported earlier, albeit in a somewhat different configuration. The second peak in the growth rate of the instability corresponds to the interaction between the space charge wave and a higher frequency mode of the structure. The growth rate of this instability is comparable to that found for the fundamental interaction. This result is consistent with observations in the experiment.

In addition to this interaction between the beam and the waveguide mode we must also examine the interactions occurring with the space harmonics. These interactions must exist simultaneously with the wave number $k = k_o$ interaction and also must have appropriate ratios of amplitudes to satisfy the boundary conditions. The amplitude of the first space harmonic has a peak value for the configuration used and its amplitude is greater than 60% of the fundamental. In this example, which has not been optimized, the wave has a phase velocity of about 0.6 c. The first space harmonic has a phase velocity of about 0.15 c. This corresponds to a proton energy of less than 10 MeV. This proton energy is much more readily achieved than the higher energy ions needed for acceleration in a

uniform tube, and it seems likely that even this energy requirement can be relaxed if necessary.

Conclusions

Present experiments have shown that it is possible to generate slow space charge waves on pencil beams in slow wave structures and to extract the beams into a uniform tube. Wave phase velocities have been measured, with modest ratios of beam to limiting current, of order 0.3 c and are expected to become lower as the beam current is enhanced. The wave electric field is about 30 kV/cm in these experiments and is also expected to scale with increased beam current. Numerical calculations of the growth rate in a similar class of structure, but with an external annular beam, have shown that high instability growth rates are readily achievable. The results bear a strong similarity to those found in the experiment.

Future work will concentrate on the development of simulation codes, and experimentally on the control of the instability growth. Future experiments will also use structures with high space harmonic content so as to be able to exploit the acceleration capability of the first space harmonic of the wave electric field.

Acknowledgment

The Cornell work was supported by the National Science Foundation. The collective acceleration studies in the Luce diode configuration were also supported, in part, by B.M.D.A.T.C.

References

1. M. Sloan and W. Drummond, Phys. Rev. Lett. 31, 1234 (1973).
2. G. Gammel, J. A. Nation, and M. E. Read, Bull. Am. Phys. Soc. 21, 1184 (1976). Also based on a research proposal submitted in 1974.

3. P. Sprangle, A. Drobot, and W. Mannheimer, Phys. Rev. Lett. 36, 1180 (1976).

4. S. Yadavalli, Appl. Phys. Lett. 29, 272 (1976).

5. G. Gammel, J. A. Nation, and M. E. Read, to be published in Rev. Sci. Instruments.

6. J. S. Luce, Ann. N.Y. Acad. Sci. 217 (1975).

7. R. Williams, J. A. Nation, and M. E. Read, Bull. Am. Phys. Soc. 21, 1059 (1976).

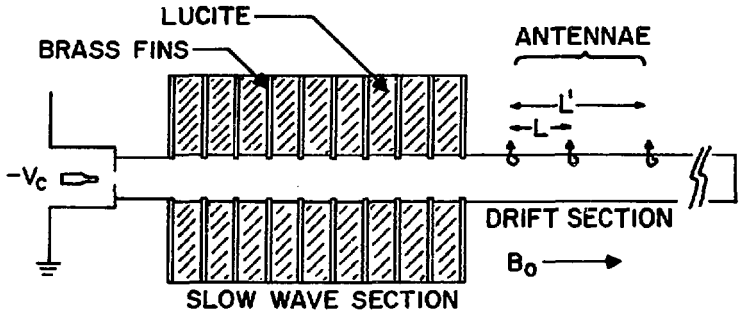

Fig. 1. Experimental configuration showing wave-growth section. Beam phase velocity and electric field measurements are made in the uniform section.

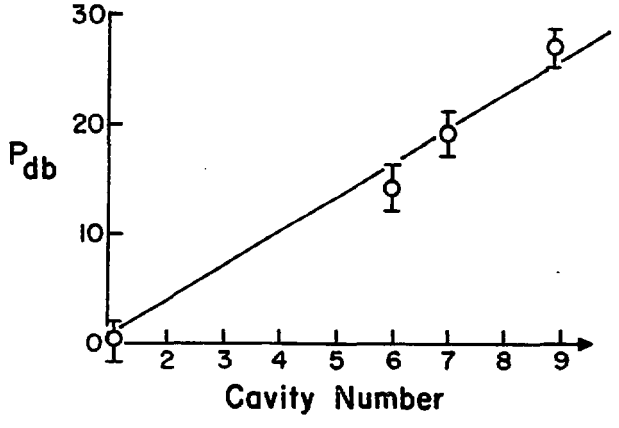

Fig. 2. Relative signal strength versus cavity number, for a 700 keV beam.

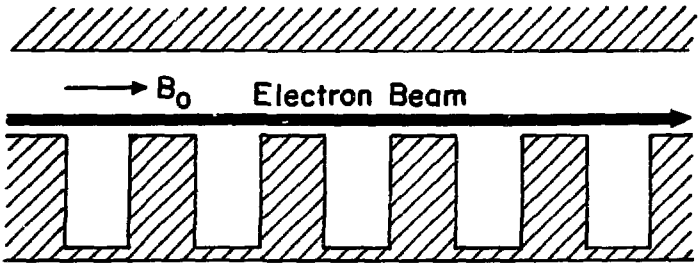

Fig. 3. Slow wave structure, and beam geometry used in determining the dispersion relation in Fig. 4. The beam is located about 2 mm from the wall and carries a current of about 2 kA/cm.

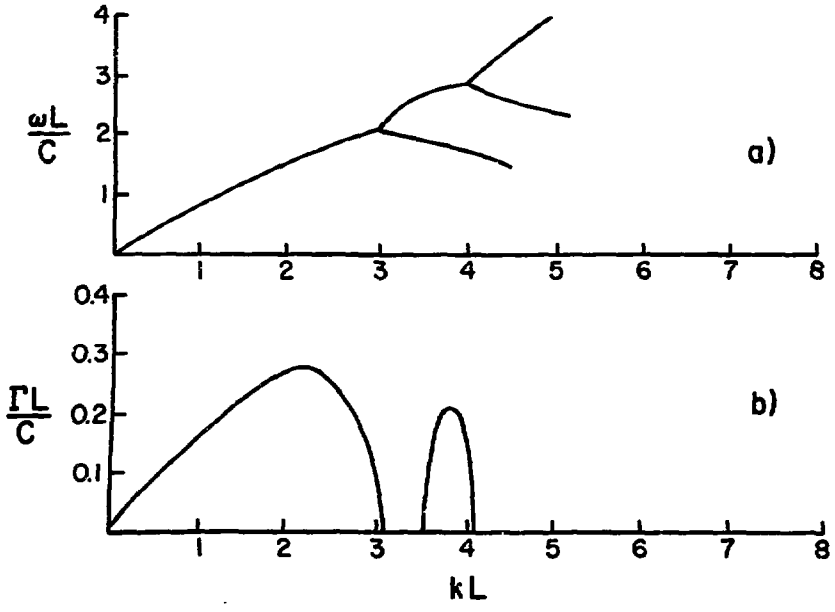

Fig. 4. The real (ω) and imaginary (Γ) parts of the wave frequency. The periodic structure length is of order 2 cm and the beam energy 650 keV.

LINEAR BEAM COLLECTIVE ION ACCELERATION FOR FUSION APPLICATIONS

W. W. Destler and H. Kim

University of Maryland, College Park, Maryland 20742

Summary

At the University of Maryland, studies of the collective acceleration of protons and heavy ions using a Luce diode configuration have been underway for several years. Systems of floating electrodes and/or slow-wave structures downstream of the diode have been investigated in an attempt to increase the accelerated ion energy. Using a 1.5 MeV, 30 kA, 30 ns electron beam pulse, proton energies in excess of 16 MeV and heavy ion (carbon, nitrogen) energies greater than 50 MeV have been achieved. Typical ion current is estimated to be 1 kA or greater, and the collective accelerating field in the post diode region has been measured to be greater than 100 MV/m. The possibility of achieving heavy ion pellet fusion by using collective ion accelerators of this type as injectors for higher energy accelerators will be discussed in the context of observed ion beam properties.

I. Introduction

Studies of the collective acceleration of ions by linear (nonrotating) electron beams have been underway at several laboratories in recent years. Acceleration of ions by the interaction of a linear electron beam with a neutral gas background was first reported by Graybill, et al.[1] The acceleration of ions in vacuum, where the positive ions are

provided by an insulating anode material, was first reported by Luce.[2] Using this type of diode configuration, protons and heavier ions have been accelerated to energies in excess of 20 times the electron beam energy, with peak proton energies reported up to 45 MeV. Investigations of this acceleration process are currently underway at Cornell,[3] Kirtland Air Force Base,[4] and Maryland.[5]

Much of the interest in this type of collective ion accelerator has resulted from possible applications of such systems to heavy ion pellet fusion experiments. In particular, intense ion beams of the required current and energy might be produced by using linear beam collective ion accelerators as injectors for higher energy accelerators. Such applications will require significantly higher quality ion beam pulses (in terms of beam current, energy, admittance, purity, and reproducibility) than have been generated thus far. In this paper, recent results of experiments designed to investigate the acceleration process in Luce-type diodes will be reported and discussed in the context of possible applications of such accelerators to heavy ion fusion schemes.

II. Experimental Studies

The general experimental configuration is shown in Fig. 1. An intense relativistic electron beam pulse (1-2 MeV, 20-40 kA, 30 ns FWHM) is produced by the electron injector used for the Maryland ERA experiments, described in another paper at this conference. An adjustable gap, gas-filled prepulse switch is located in series with the injector output.

The electron beam is emitted from a tungsten needle cathode located 6-7 mm in front of the anode plane. The insulating anode, which contains the material to be accelerated, has an 11 mm hole bored in it to allow most of the electron beam to pass through the anode plane into the acceleration region. A system of floating electrodes, described previously,[5] is located in the post diode region, and a pulsed magnetic field coil may be installed in the region downstream of the anode plane to provide an axial guide field of up to 10 kilogauss.

Accelerated ions are detected by foil activation techniques, and stacked copper or aluminum foils are used to determine the ion energy spectra. Neutron producing reactions are detected using silver activation techniques by two Geiger Mueller tubes located at 0° and 90° from the system axis. Faraday cups and fast magnetic probes are available to monitor the properties of the ion loaded electron beam.

(a) Heavy Ion Acceleration. The acceleration of heavy ions (C,N,O,F) has been achieved by using anode insulators made of teflon (containing C and F) and a carbon rich epoxy casting (containing C,H,O,N, and other materials). The acceleration of these heavy ions onto aluminum targets has led to the production of Al^{28}, Cl^{34m}, N^{13}, and C^{11}. In addition, the presence of Al^{28} and Al^{29} has been detected from activated carbon targets and Ne^{19} from gold foils. From the various cross sections for the production of these products using these targets, and from stacked aluminum foil measurements, the heavy ion energy is estimated to be greater than 50 MeV. In order to obtain a more definitive

measurement of the heavy ion energy, the alpha activity of the gold foils was measured with no activity detected. This places an upper limit on the accelerated carbon ion energy of 60 MeV, a limit on the nitrogen energy of 70 MeV, and on fluorine of 90 MeV. The production of Ne^{19} from a gold target by F^{19} ions is therefore attributed to a nucleon exchange reaction requiring an incident ion energy somewhat less than the Coulomb barrier.

The acceleration of heavy ions is always accompanied by proton acceleration (even when a teflon anode is used) with observed proton energies measured to be greater than 10 MeV. Since the presence of large amounts of Zn^{63} and Zn^{65} has been detected in the first copper floating electrode located only 3 cm downstream of the anode plane, the collective accelerating field must be greater than 150 MV/m in the acceleration region. The proton component of the heavy ion beam is attributed to inadequate vacuum in the system and to impurities on the surface of the anode and cathode.

(b) Effect of Preionization in the Anode Region. Enhanced acceleration of heavy ions has been achieved by using the electron injector prepulse to provide a small amount of preionization in the anode region before the arrival of the main electron beam pulse. Typical diode voltage and current waveforms are shown in Fig. 2. By carefully adjusting the prepulse switch gap, the time at which the injector prepulse breaks over the prepulse switch gap may be varied, thus providing a preionizing pulse of about 100 kV and 1 kA at the diode in advance of the main beam pulse. The

duration of this preionizing pulse has been plotted as a function of the prepulse switch gap and is shown in Fig. 2. It is evident that the reproducibility of the preionizing pulse duration for a given switch gap is not very good. If the gap is closed too far, the prepulse arrives at the diode so far in advance of the main pulse that the anode-cathode gap is closed by the resulting plasma and the diode is shorted.

Figure 3 shows a plot of neutron production as a function of this preionizing pulse duration for two different anode materials and several different target foils. The highest ion beam energies and currents as measured by foil activation techniques are always accompanied by high neutron fluxes, and the plots show clearly that the most consistently effective ion acceleration is achieved when a preionizing pulse of about 100 ns duration is applied to the diode region. The points beyond 150 ns in both plots correspond to diode shorts. Effective acceleration using the carbon plastic anode is achievable using little or no preionization probably because the protons contained in this material can migrate into the accelerating region much more rapidly than heavier ions. This judgment is confirmed by the fact that it was not possible to introduce any preionization in a diode with a hydrogen-rich anode (high density polyethylene) without shorting the diode.

Improved reproducibility and protection against diode shorting may be achievable by providing the preionization using a different technique such as striking a surface

discharge across the anode insulator with an external pulser. Preliminary experiments to investigate this possibility are currently underway. Such a technique would provide substantially more control over the species and number of ions to be accelerated than do the present systems.

(c) Effect of an Applied Magnetic Field. In order to determine the effect of a magnetic guide field on the acceleration process, a pulsed magnetic field system capable of applying up to 10 kilogauss in the post-diode region was constructed. The field was designed to facilitate experiments using a downstream slow-wave structure to increase the ion energy as discussed in a previous paper.[6] In these experiments, no preionization was provided in the anode region and the system of two floating electrodes was present in the acceleration region. Plots of relative neutron flux and foil activation for heavy ions accelerated onto aluminum targets is shown as a function of applied magnetic field in Fig. 4. It is clearly evident that substantial ion acceleration is achieved only when the applied magnetic field is below 4 kilogauss. Further studies of this phenomenon are currently in progress.

III. Problems in Applying Collective Ion Acceleration to Pellet Fusion.

The characteristics of collectively accelerated ion beams, in particular the high peak currents and low duty cycles of such beams, makes them very attractive for applications to pellet fusion schemes. The observed pulse lengths of a few nanoseconds and peak currents of a few kiloamperes

are well within the calculated requirements for pellet fusion. The ion energy, however, is less than 100 MeV typically, and it may be a difficult task to raise the energy to the required multi-GeV level by collective acceleration techniques alone. In light of the apparent difficulty in reaching the required beam energies, the use of a collective ion accelerator as an injector for an induction accelerator has been suggested by Reiser.[7] Meanwhile, attempts to further increase the ion beam energy in collective accelerators are continuing. The introduction of a helical slow-wave structure in the acceleration region has been proposed[6] in an attempt to increase the ion beam energy, and experiments in this area will be performed as a joint effort of the Kirtland Air Force Base Group and the University of Maryland. Using the FX-100 and PR 1590 electron accelerators at Kirtland, heavy ion energies of a few hundred MeV are possible. A numerical simulation of beam propagation in a helix is being performed at the Los Alamos Scientific Laboratory.[8]

Heavy ion pellet fusion will require the acceleration of very heavy materials, such as uranium, in order to maximize the energy delivered to the pellet. Using Luce-type diodes, efficient acceleration of protons and carbon, nitrogen, oxygen, and fluorine ions has been achieved thus far. A brief attempt to accelerate heavier metallic ions, such as aluminum, has been made at the University of Maryland with inconclusive results. The acceleration of metallic ions may require an external means of plasma formation as discussed in section IIb of this paper. In addition, an

external means of plasma formation should improve the overall accelerated beam quality and reproducibility. In particular, it should provide better control over the number and species of ions to be accelerated, and might even be used to improve the admittance of the accelerated ion beam. Studies of the feasibility of this approach are currently underway at the University of Maryland.

In conclusion, before a final determination of the feasibility of using collective ion accelerators in a heavy ion pellet fusion scheme can be made, much additional experimental and theoretical work is required.

Acknowledgments

It is a pleasure to acknowledge the assistance of T. Dao in the preparation of the experiments reported here. Assistance in identifying nuclear reaction products was provided by V. Viola and W. Walters of the Nuclear Chemistry Department at the University of Maryland. Useful discussions with M. Reiser, G. Zorn, C. Striffler, M. Rhee, D. Hudgings, and R. Meger are also acknowledged. This work was supported by the National Science Foundation.

References

1. S. E. Graybill and J. R. Ublum, J. Appl. Phys. 41, 236 (1970).
2. J. S. Luce, Annals of N.Y. Acad. of Science 25, 2171 (1975).
3. R. Williams et al., Bull. APS II, 21 (Oct. 1976).
4. R. B. Miller and R. J. Faehl, IEEE Trans. NS-24 (June 1977).

5. C. N. Boyer, H. Kim, and G. T. Zorn, Proc. Int. Topical Conf. of Electron Beam Res. & Tech. Vol. II (Albuquerque, N.M., 1975).

6. C. N. Boyer, W. W. Destler, and H. Kim, IEEE Trans. NS-24 (June 1977).

7. M. P. Reiser, IEEE Trans. NS-24 (June 1977).

8. B. B. Godfrey, R. J. Faehl, B. S. Newberger, W. R. Shanahan, and L. E. Thode, Proc. 2nd Int. Topical Conf. on High Power Electron and Ion Beam Res. & Tech. (Ithaca, N.Y., Oct. 1977).

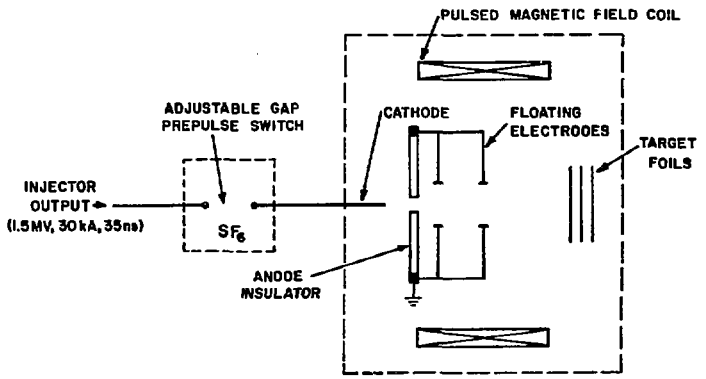

Fig. 1. General experimental configuration.

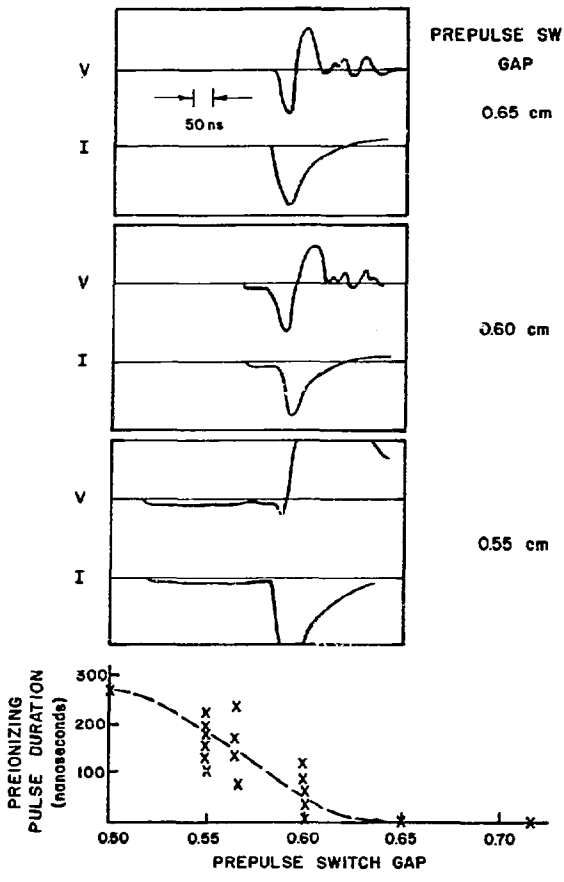

Fig. 2. Typical voltage and current waveforms for three different prepulse switch gap settings, used to construct the plot of preionizing pulse duration versus prepulse switch gap.

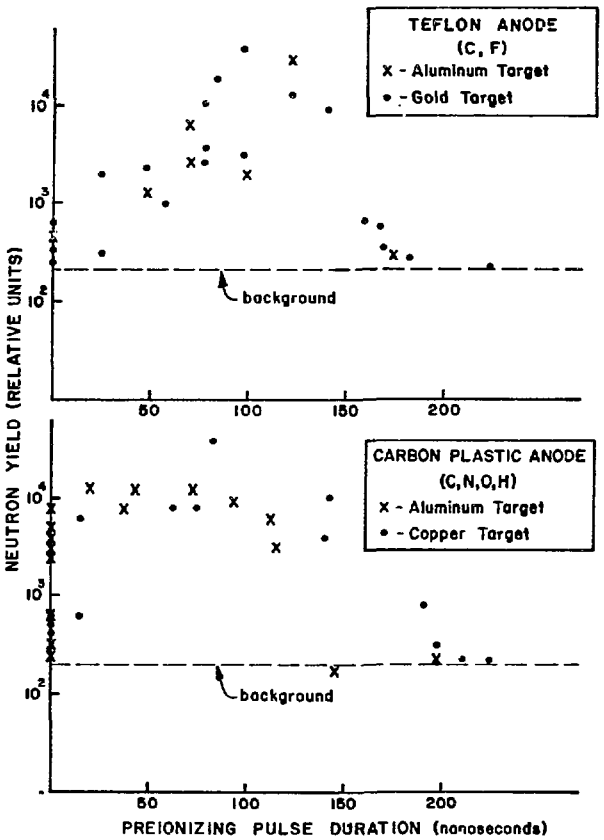

Fig. 3. Relative neutron flux as a function of preionizing pulse duration.

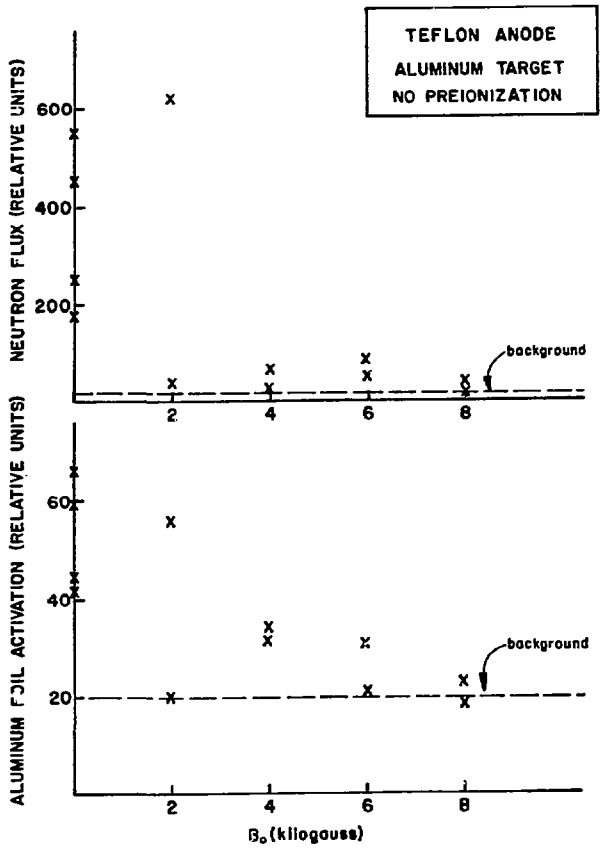

Fig. 4. Relative neutron flux and foil activation as a function of applied magnetic field in the acceleration region.

A NEW COLLECTIVE PARTICLE ACCELERATOR

Moshe Friedman

Plasma Physics Division
Naval Research Laboratory
Washington, D.C. 20375

A simple and novel mechanism for a collective particle accelerator is proposed. It is suggested that a density modulated intense relativistic electron beam propagating in a spatially modulated magnetic field can drag particles (electrons or ions) and accelerate them to high energies. This new mechanism can generate high particle current. A strong radial electric field exists in the mechanism ensuring radial confinement of the accelerated ions.

In the last few years there was interest in using an intense relativistic electron beam (IREB) for ion acceleration. (1-6) It has been suggested that waves "riding" on an IREB can, under certain conditions, accelerate ions. These waves can take the form of cyclotron waves, (4) slow beam waves (5) or large amplitude electrostatic "well" associated with the front of an IREB. (6) By manipulating beam parameters (e.g. current, magnetic field, geometry etc.) the phase velocity of these waves can be controlled. When the phase velocity is small enough ions can be trapped by the wave. By "accelerating" the wave (i.e. increasing its phase velocity) the trapped ions will be dragged and gain energy from the wave. If during the acceleration process an ion escapes from the wave the acceleration phase will end and the ion will be lost. The generation of these waves and the control of their phase velocity may require beam parameters which are not attainable (e.g. monochromatism of particle energy).

In this letter a new mechanism for a collective accelerator is proposed. This mechanism can accelerate ions as well as electrons and it is free of some of the problems of current collective accelerators.

The axial electric field, on axis, produced by an annular unneutralized magnetically focused IREB propagating through a drift tube of radius R is

$$E_z \approx -\left[\frac{1}{2\pi\epsilon_0}\frac{\partial Q}{\partial z}\right] \ell n \frac{R}{r_b} - \left[\frac{\mu}{2\pi}\frac{\partial I}{\partial t}\right] \ell n \frac{R}{r_b} + \frac{Q}{2\pi\epsilon_0}\frac{1}{r_b}\frac{\partial r_b}{\partial z}\,, \tag{1}$$

where Q is the charge/length. $Q = I/v$, I is the beam current, r_b is the beam radius and v is the electron velocity. Equation (1) was obtained from Maxwell equations under the assumption that the axial characteristic length is greater than the radius of the drift tube. By covering the drift tube walls with a thin dielectric layer of thickness δR and permeability ϵ one gets from Eq. (1) (after some rearranging)

$$E_z \approx -\frac{\mu}{2\pi}\frac{1}{\beta^2\gamma^2}\frac{\partial I}{\partial t} \ell n \frac{R}{r_b} + \frac{\mu}{2\pi\beta^2}\frac{\epsilon}{\epsilon - 1}\frac{\delta R}{R}\frac{\partial I}{\partial t} + \frac{Q}{2\pi\epsilon_0}\frac{1}{r_b}\frac{\partial r_b}{\partial z} \tag{2}$$

by choosing

$$\frac{\delta R}{R} \approx \frac{\epsilon}{\epsilon - 1}\frac{1}{\gamma^2} \ell n \frac{R}{r_b} \tag{3}$$

one gets

$$E_z \approx \frac{Q}{2\pi\epsilon_0}\frac{1}{r_b}\frac{\partial r_b}{\partial z}\,. \tag{4}$$

In a case where a modulated IREB (7) is propagating through a rippled magnetic field one inserts in Eq. (4) the following:

$$Q \approx \frac{Q_0}{2}\left(\sin\left(\frac{2\pi}{\lambda}z - 2\pi f t\right) + 1\right), \tag{5}$$

and

$$r_b \approx r_0 + r_1 \cos\frac{2\pi z}{L}\,; \quad r_1 < r_0, \tag{6}$$

where f and λ are the frequency and wavelength of the modulation $\lambda f = v$, r_0 is the equilibrium radius of the IREB, r_1 is the amplitude of the oscillations of the IREB due to

the influence of the rippled magnetic field and L is the wavelength of the rippled magnetic field. Here we assume that the parallel velocity of the electrons is $v \approx c$.

$$E_z \approx -\frac{Q_0}{4\pi\epsilon_0}\left(\frac{r_1}{r_0}\right)\frac{2\pi}{L}\sin\frac{2\pi z}{L}\left[\sin\left(\frac{2\pi z}{\lambda}-2\pi ft\right)+1\right], \tag{7}$$

rearranging Eq. (7) one gets

$$E_z \approx -\frac{1}{4}\frac{Q_0}{\epsilon_0}\left(\frac{r_1}{r_0 L}\right)\left\{\cos\left[2\pi z\left(\frac{1}{\lambda}+\frac{1}{L}\right)-2\pi ft\right]-\cos\left[2\pi z\left(\frac{1}{L}-\frac{1}{\lambda}\right)+2\pi ft\right]+2\sin\frac{2\pi z}{L}\right\}. \tag{8}$$

Equation (8) describes two "waves" with phase velocities

$$\begin{aligned} &(1)\quad v_{\phi 1} = v\,\frac{L}{L+\lambda} \qquad \text{forward wave,} \\ &(2)\quad v_{\phi 2} = -v\,\frac{L}{\lambda - L} \qquad \text{backward wave.} \end{aligned} \tag{9}$$

Figure 1 shows the phase velocity of these waves as a function of L. The amplitude of these waves is

$$E_{z0} \approx \frac{Q}{4\epsilon_0}\left(\frac{r_1}{r_0 L}\right). \tag{10}$$

Both waves can accelerate ions but only the backward wave can accelerate electrons since it can have phase velocity approaching c.

The acceleration force acting on particles with velocity v', by this collective mechanism, is impulsive in nature. During a period $T = [(\lambda \pm L)/2]/v = (L/2)/v'$ a favorably phased particle will be under the influence of a time-average electric field $2E_{z0}$. For a subsequent period no force will act on the particle. Formally, this mechanism resembles a nonlinear Landua damping process in which a fictitious wave (the rippled magnetic field) with wavelength L and zero frequency combine with a beam wave of wavelength λ and frequency f to exert a force on a particle and accelerate it.

If electrons are to be accelerated by this mechanism the backward wave has to be used. By choosing $\lambda \approx 2L$ the phase velocity of the backward wave is c. An IREB of

80 kA current and particle energy of 3 MeV can easily be modulated with a 1 GHz frequency. The automodulation (7) technique which is used to modulate the IREB can also increase the particle energy within the beam to $V \approx 5$ MeV. Passing this beam through a rippled magnetic field with $L = 15$ cm and $r_1/r_0 \approx 0.30$ one gets $E_{z0} \approx 15$ MV/meter. Figure 2 shows schematically the proposed accelerator.

The electron accelerator can work in two modes. In the first mode the duration of the accelerated electrons is about the duration of the IREB. In that case the accelerated current I_1 and the final energy of the accelerated electrons E_f has to satisfy the relation

$$I_1 E_f \leq IV. \tag{11}$$

Here, each bunch loses energy continuously along the acceleration length.

In the second mode of operation the duration of I_1 is smaller than $(L/2)/c$. Only during this duration each bunch loses energy. In that case

$$I_1 E_f \leq IV \frac{S}{L}, \tag{12}$$

where S is the total length of the accelerator, $S >> L$ and $S \lesssim c\tau/2$ and τ is the duration of the IREB. From Eqs. (10) and (12) one gets

$$I_1 \lesssim 4\epsilon_0 V_c (r_0/r_1). \tag{13}$$

In practice I_1 may have to be smaller so as to reduce effects of two stream instability. It seems (8) that if $I_1 \approx 0.1\ I$ the growth rate of the instability will be small especially for high γ.

The final energy of the accelerated electrons will be

$$E_f = (E_z L)\frac{S}{L}\ ; \quad S = c\tau/2 \tag{14}$$

for $\tau = 100$ ns and for the same IREB parameters mentioned earlier one gets $E_f \approx 200$ MeV, $S = 15$ meters and $I_1 = 8$ kA.

The same mechanism that accelerates electrons can accelerate ions. Here, too, we use the backward wave for acceleration. (One can also use the forward wave for ion

acceleration.) In addition to the acceleration force there is a radial force, generated by the IREB, focusing the ions. A simple way for looking at the focusing force is to consider the case of solid ion beam flowing within an annular IREB. Here two forces will act on an ion. The first force results from the self electric field of the ion beam. This electric field will accelerate an ion to a outward radial velocity at the radius of the IREB.

$$V_{ri} \approx \sqrt{\frac{1}{2}\frac{ZeQ_i}{2\pi\epsilon_0 M}} \tag{15}$$

where Q_i is the charge/length of the ion beam Z is the effective charge of the ion and M its mass. A second force acts on the ions when they enter the trajectories of the electrons. This force will give an ion an inward radial velocity of

$$v_{ri} \approx \sqrt{\frac{ZeQ}{2\pi\epsilon_0 M}\frac{\delta a}{a}} \tag{16}$$

where δa is the thickness of the IREB. From Eq. (15) and (16) we can see that the ion current that can be radially confined inside an IREB is

$$I_{\text{ion}} \approx 2\,\frac{\delta a}{a}\,\frac{v_i}{v}\,I. \tag{17}$$

If we take I = 80 kA, $v_i/v \simeq 0.06$, Z = 1, $\delta a/a \approx 0.1$ we get that $I_{\text{ion}} \approx 10^3$ amps can be focused. Similar calculation shows that 100 amps of U^{+10} can be focused when the initial velocity of the ions is v_i = 0.006 c.

The mechanism for ion acceleration is similar to the electron acceleration discussed earlier. At the axial position where the ions start the acceleration we choose L and λ such that

$$V_{\phi 2} = -v\,\frac{L}{\lambda - L} = v_i (\ll c).$$

For the case of Z = 1 v_i = 0.06 c one choses L = 10 cm, and λ = 170 cm. For I = 80 kA and $r_1/r_0 \approx 0.067$ the accelerating electric field $E_z \approx 5$ MV/m. In order to maintain the force and the ion in phase, L has to be changed. While the ion is accelerating L is changing such that $V_{\phi 2} = v_i$. At the same time $(r_1/r_0)\,L$ is being kept constant such that

$E_z \approx 5$ MV/m. This easily can be done for any L up to $L = 45$ cm. When $L = 45$ cm, one gets $r_1/r_0 \approx 0.3$ and $v_{\phi 2} \approx 0.36\ c$ corresponding to energy of 67 MeV. Since values of r_1/r_0 greater than 0.3 may not be technically possible one has to increase L without increasing (r_1/r_0). In that case E_z will drop when L increases beyond 45 cm and the acceleration length will become very long. In order to avoid long accelerator and be able to get energies greater than 67 MeV the ion beam has to be injected into a second generator. At the injection point $L = 10$ cm, $\lambda = 38$ cm and $r_1/r_0 \approx 0.15$ such that $E_z \approx 11.2$ MV/m, and $v_{\phi 2} = 0.36\ c$. Changing L from 10 cm to 19 cm, $v_{\phi 2}$ increases to c. Simultaneously r_1/r_0 is being changed to 0.3 so that E_z stays constant and is equal to 11.2 MV/m. Only 100 meters of acceleration length are needed to obtain particle energy of 1 GeV.

A similar considerations can show that for a beam of U^{+10} ions to reach energy of 1 GeV it is necessary to have acceleration length of 44 meters.

For the acceleration mechanisms to work, ions with the right velocity have to be injected into the IREB. The injection mechanism is part of the acceleration mechanism. This is shown in Fig. 2. The modulated IREB is being terminated on a metal plate or foil. The place of termination is the equator of one of the mirror magnetic field. Ions will accelerate between the metal plate and the apex of the mirror magnetic field and reach a velocity

$$v_i \approx \frac{Ze}{M} \frac{Q}{\epsilon_0} \left(\frac{r_1}{r_0 L}\right) \frac{\lambda}{c} . \tag{18}$$

It is easy to show that with the IREB parameters discussed earlier one can get $v_i \approx 0.06\ c$ for $Z = 1$.

One of the important parameters in the above mechanism is the strength of the external magnetic field. It was found (9,10) that an IREB propagating through a rippled magnetic field produces microwave radiation and its characteristics were drastically modified. It was likewise found that a critical magnetic field existed above which very little microwave power was produced and the beam characteristics did not change.

$$B_c \simeq \frac{2\pi}{L} \frac{mc}{e} \gamma. \tag{19}$$

For L = 15 cm, γ = 10, one gets $B_c \approx 7$ kG.

In summary a new collective particle accelerator is being proposed. This new type of accelerator can accelerate ions as well as electrons.

A similar idea was suggested in 1975 by A.N. Lebedev and K.N. Pazin (11). They suggested that a bunched electron beam propagating through a corrugated metal tube can support beam waves. These beam waves can be used to accelerate particles to high energies. However, there are experimental and theoretical evidence that an electron beam propagating through a corrugated drift tube is unstable. It interacts with slow rf waves (which are being supported by the structure) generating high power microwave radiation (12).

In the mechanism discussed in this paper the electron beam is propagating in a smooth metallic drift tube. The beam can interact only with fast rf waves. The interaction is very weak and under certain conditions very little microwave radiation is produced and no beam determination is being observed (10).

The author would like to thank Drs. J. G. Siambis and T. Lockner for helpful discussions.

REFERENCES

1. S. Graybill and J. Uglum, *J. Appl. Phys.* 41, 236 (1970).
2. S. E. Rosmskii, A. A. Rukhadze and V. G. Rukhlin, *JETP Lett.* 14, 34 (1971).
3. S. Putnam, *Phys. Rev. Lett.* 25, 1129 (1970).
4. M. L. Sloan and W. E. Drummond, *Phys. Rev. Lett.* 31, 1234 (1973).
5. P. Sprangle, A. T. Drobot and W. M. Manheimer, *Phys. Rev. Lett.* 36, 1180 (1976).
6. C. L. Olson, *Phys. of Fluids* 18, 585 (1975) and *Phys. of Fluids* 18, 598 (1975).
7. M. Friedman, *Phys. Rev. Lett.* 24, 303 (1974).

8. M. Friedman, J. G. Siambis and D. P. Bacon, *Appl. Phys. Lett.* 28, 308 (1976).

9. M. Friedman and M. Herndon, *Phys. Rev. Lett.* 29, 55 (1972).

10. M. Friedman and M. Herndon, *Phys. Fluids* 16, 1982 (1973).

11. A. N. Lebedev and K. N. Pazin, *Atomnaya Energiya* 41, 244 (1976).

12. N. F. Kovalev, M. I. Petelin, M. D. Raizer, A. V. Smozgonskii and L. E. Tsoff, *Zh. Eksp. Teor. Fiz. Pisina Red* 18, 232 (1973).

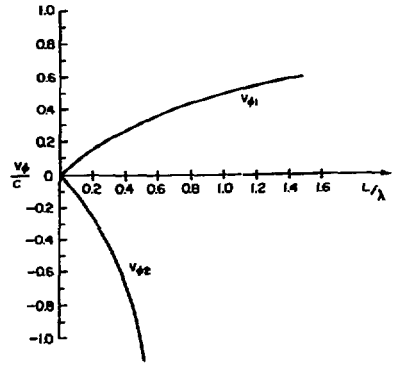

Fig. 1 — Phase velocities of forward and backward waves as a function of L/λ.

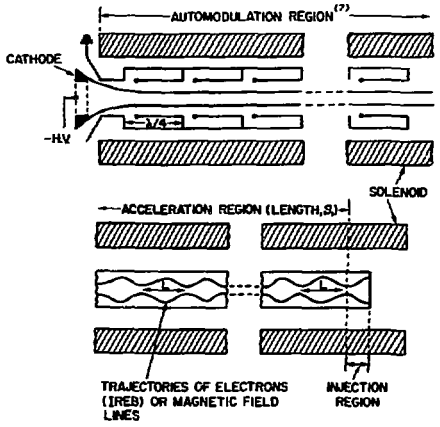

Fig. 2 — Schematics of the proposed acceleration scheme. (Top) The automodulation region. (Bottom) The acceleration region and the injection region.

D-4

RELATIVISTIC ELECTRON BEAM CYCLOTRON WAVE GROWTH IN HELICAL SLOW WAVE STRUCTURES*

B. B. Godfrey, R. J. Faehl, B. S. Newberger,
W. R. Shanahan, and L. E. Thode
Theoretical Division, Los Alamos Scientific Laboratory
Los Alamos, New Mexico 87545

One of the more promising and thoroughly studied proposals for high energy collective ion acceleration is Autoresonant Acceleration: Ions trapped in the electrostatic wells of large amplitude slow cyclotron waves in an unneutralized intense relativistic electron beam are accelerated by the increase of wave phase velocity as the beam propagates along a magnetic guide field of decreasing strength. A critical component of this scheme is growth of coherent, large amplitude waves. Here, we consider wave growth by interaction of the beam with a helical slow wave structure. Specific topics include (1) equilibrium charge and current distributions on the helix, (2) linear wave growth spectra including the effects of radial inhomogeneity, (3) wave growth and saturation, and (4) extraction of cyclotron waves from the amplifier cavity. Movies of two-dimensional computer simulations are presented. We find that waves of amplitude adequate for planned feasibility experiments can indeed be obtained.

I. INTRODUCTION

Collective ion acceleration is a highly speculative, yet potentially very significant, application for intense relativistic electron beams. Eventually, it may permit the compact and economical acceleration of substantial currents of light or heavy ions to hundreds of MeV per nucleon. All collective

acceleration schemes presently envisioned involve three key stages. Slowly moving large amplitude electrostatic potential wells are established in an intense relativistic electron beam, an adequate number of ions are trapped in those wells, and the wells with trapped ions are smoothly accelerated to velocities approaching that of the beam. Obvious sources for such potential wells are the large charge gradient at the head of an electron beam and large amplitude Langmuir or cyclotron waves in the body of the beam.[1]

One of the more promising and thoroughly studied high energy collective ion acceleration schemes is the Autoresonant Acceleration proposal by Sloan and Drummond.[2] It employs the slow cyclotron wave in an unneutralized intense relativistic electron beam propagating in vacuum along a strong axial magnetic field. Control of the wave phase velocity is achieved through spatial variation of the guide magnetic field. Austin Research Associates, Inc. is soon to begin an experimental investigation of this concept.[3] A 30 kA, 3 MeV, 200 ns electron beam will be used. Present plans call for the cyclotron waves to be grown in a slow wave structure at 3.4 kg. The beam is then adiabatically compressed in a field increasing to 25 kg, and ions loaded. Subsequent decrease of the axial field to 2.5 kg in the acceleration section should yield 30 MeV ions.

For a successful experiment, the wave growth section must produce reasonably monochromatic, large amplitude, axially symmetric slow cyclotron waves while avoiding competing, disruptive instabilities. We at Los Alamos Scientific Laboratory are studying both analytically and computationally wave

amplification in a sheath helix slow wave structure, one of two active candidates for the planned experiment. Our results, although not yet complete, are encouraging.

Section II describes the problem of establishing equilibrium between the beam and the helix. This is important, because the helix, being both capacitive and inductive, can support large transients lasting throughout the beam pulse. We show, however, that a proper combination of resistive termination of the helix and shaping of the beam pulse reduces transients to an innocuous level. Return currents in the helix, which disrupt the externally applied magnetic guide field, probably can be treated in the same way.

Because the slow cyclotron wave is of negative energy, while the helix-supported wave is of positive energy, they interact to produce a moderately rapidly growing convective instability which is to be responsible for cyclotron wave amplification. Section III gives the linear theory of this instability, obtained numerically from GRADR, a dispersion relation solver for radially inhomogeneous, cylindrically symmetric, cold fluid beam equilibria.[4] Analytic approximations are also provided.

Based on the linear theory, two-dimension computer simulations in cylindrical geometry have been performed with CCUBE.[5] Simulations show that, for a 2.65 cm radius beam in a 15° pitch helix at 3.8 cm both enclosed in a metal waveguide at 5.7 cm, cyclotron waves grow from a fractional modulation of 1/2% to about 40% is just more than a meter distance. Growth stops only when the waves leave the helix or electrons actually strike the helix. Wave growth obeys linear theory well,

with little sign of nonlinear effects even at large amplitude. All this appears in Section IV.

Section V discusses extraction of the large amplitude cyclotron waves from the helical amplifier. To date, our investigation has been limited to comparison of the linearized eigenmodes in the helix and in a waveguide of equal radius. Although frequency and wavenumber are essentially unchanged, the radial profiles of the wave components are significantly modified. The impact of this mismatch remains to be seen.

II. BEAM-HELIX EQUILIBRIUM

Fig. 1 shows the relativistic electron beam just entering the helix. The small plus signs at the helix and outer conducting waveguide represent image charges induced by the beam. Placement of these plus signs is meant to illustrate a key feature of the early time beam-helix interaction. Image charges on the helix move at a velocity

$$v_H = \frac{c \sin \psi}{[1 - (1 + \frac{1-\alpha}{\ell n\, \alpha})\cos^2 \psi]^{1/2}} \quad , \qquad \alpha \equiv (R_H/R_W)^2 < 1 \quad , \tag{1}$$

which for our purposes is somewhat less than the beam velocity, $v_B \approx c$. For example, with the parameters cited in the Introduction, $v_H \approx 0.3\ c$. Therefore, even though both ends of the helix may be grounded, the head of the beam soon outruns image charges on the helix and sees the outer conductor as the ground plane. For the experimental beam parameters, space charge effects limit R_W to no greater than 2.4 R_B for a fast beam risetime. The 80 ns risetime contemplated in the Austin Research Associates, Inc. experiment will, of course, substantially weaken this constraint.

Of greater importance is the fact that, because the beam reaches the far end of the helix before helix image charges do, additional images charges begin flowing onto the helix. The two streams of image charge from each end do not interact when they meet near the center but simply flow on to the helix ends, where they reflect, and so continue to stream back and forth indefinitely. Our simulations have shown this behavior to disrupt seriously the electron beam, as might be expected.

Image charge flow can be described reasonably well by the wave equation

$$\frac{\partial^2 \rho}{\partial t^2} - v_H^2 \frac{\partial^2 \rho}{\partial z^2} = 0 \quad , \tag{2}$$

with the boundary conditions $\rho + \rho_o = 0$ at either end, $Z = 0$ and L. Here, ρ and ρ_o are the charge per unit length on the helix and in the beam. Eq. (2) can be solved to give a recurrence relation for, e.g., charge flowing to the right at the right boundary.

$$\rho_+(t,L) = \rho_+(t-2L/v_H,L) - \rho_o(t-L/v_H) - \rho_o(t-2L/v_H-L/v_B). \tag{3}$$

Beam charge is parameterized by the time it entered the helix at the left.

The asymptotic solution to Eq. (3) is

$$\begin{aligned} \rho_+(\omega = 0) &= -\rho_o\,(1 + v_H/v_B)/2 \quad , \\ \rho_+(\omega = \pi v_H/nL) &= -\rho_o\,(2/n\pi)\,\omega\tau/(1 + \omega^2\tau^2) \quad , \end{aligned} \tag{4}$$

for $\omega\tau >> 1$, where τ is the characteristic rise time of the beam. Our goal, clearly, is to minimize the oscillatory part of ρ_+. For the example cited above, a helix length of one meter, and τ = 80 ns, the oscillatory part is of order 5%. Additional reduction of transients can be achieved by placing

resistive materials at various points in the system. With a graded resistance between the helix and the outer conductor near the downstream end of the helix, we have reduced transients in simulations to about 1% with $\omega_1\tau \sim 6$.

Even with oscillations in the helix image charges eliminated, a return current

$$I_H/I_B = -(v_H/v_B)^2 \qquad (5)$$

persists. This current perturbs the magnetic guide field by

$$\Delta B_z = 2I_H(1 - \alpha)/(R_H\, c \tan \psi) \quad , \qquad (6)$$

or about 300 g for our example. The return current can be eliminated from the helix by terminating it to ground through a resistive load. Alternatively, ΔB_z can be externally compensated.

III. LINEAR THEORY

The helix supports a wave, $\omega = kc \sin \psi$, which interacts with the slow cyclotron wave of the beam, $\omega = kv_B - \omega_c/\gamma$ to produce a convective instability with group velocity approximately c/2. The point of intersection of the two waves in ω - k space is

$$k = \omega_c/\gamma(v_B - c \sin \psi) \quad . \qquad (7)$$

Austin Research Associates, Inc. has obtained an approximate analytic growth rate for a radially homogeneous beam, $\gamma >> 1$, $kR_B >> 1$, $R_H = R_B$, and $R_W = \infty$.[6] The latter two constraints can be relaxed to give

$$\Gamma = \frac{\omega_p}{2\gamma}\left(\frac{\Omega_c R_B}{c} \sin 2\psi\right)^{1/2}\left(e^{-2k(R_H-R_B)} - e^{-2k(R_W-R_B)}\right) \quad . \qquad (8)$$

To improve upon these estimates, we employ GRADR, a computer code which solves Maxwell's equations together with the

relativistic cold fluid equations linearized about any given cylindrical beam equilibrium.[4] In particular, it can treat the effects of beam energy radial inhomogeniety, $\gamma(r)$, caused by the self-fields of the beam. Fig. 2 presents results from this code for the parameters used throughout this article. The growth rate peaks at $\Gamma = 6.8 \cdot 10^8$ sec^{-1}, corresponding to $k = 0.46$ cm^{-1} and $\omega = 3.7 \cdot 10^9$ sec^{-1}. With a computed group velocity of 0.6 c, the instability growth length is 27 cm, or about two wavelengths. Incidentally, Eq. (7) predicts the numerically determined wavenumber precisely, if we use for γ its value at the beam edge, 5.75. With the same choice, Eq. (8) gives a growth rate too large by nearly a factor of two. In view of the many approximations required in obtaining Eq. (8), agreement is good.

IV. WAVE GROWTH AND SATURATION

In order to corroborate linear theory and, more importantly, to determine the saturation level and mechanism for the beam-helix cyclotron instability, we carried out a series of two-dimensional, relativistic, electromagnetic computer simulations with CCUBE[5] configured for cylindrical coordinates. Simulations employed the beam and guide field parameters previously described but varies lengths and radii for the helix and outer conductor. Numerically well matched end conditions were used for the helix, rather than the physical terminations shown in Fig. 1, because we were interested primarily in wave growth and saturation under ideal conditions. Cyclotron waves were injected at an amplitude of 1/2% of the beam radius at the upstream end of the simulation grid and allowed to grow as they propagated downstream.

For values of R_H in the range 3.2 cm to 4.4 cm, cyclotron waves grew spatially (as measured by modulation of the beam radius and by field strengths at the helix) with a growth length approximating that predicted by GRADR until either beam particles struck the helix or waves left the downstream end of the grid. Well depth increased approximately logarithmically with modulation amplitude.[7] We expect that saturation by particle trapping would occur for sufficiently large helix radius; however, cost and time constraints prevent pursuing this issue.

These simulations suggest that helix and conductor radii of 3.8 cm and 5.7 cm will prove suitable for the planned experiment, and so we have used those values throughout the report in numerical examples. With these radii the beam wave strikes the helix after about 4.5 e-foldings, or 120 cm. The helix should, therefore, be terminated at 100 cm, giving a potential well depth of 0.5 MeV. Maximum acceleration field strength on axis is 120 keV/cm, which is more than adequate. Corresponding electric field strength at the helix is about 1/3 that amount and should not cause breakdown problems. Fig. 3 shows wave growth and saturation in a 160 cm system.

V. WAVE EXTRACTION

Fig. 4 contrasts the radial structure of characteristic components of the linearized cyclotron eigenmode, determined by GRADR, in the helix and in a metal cylinder of equal radius. Frequency and wavenumber correspond to the maximum growth rate from Fig. 2, and, with frequency fixed, wavenumber is essentially identical for the two geometries. If the disparity in radial structure persists in the nonlinear regime,

as is likely, a real danger exists that wave coherence may be lost when the cyclotron waves exit the helix amplifier. In a few months, we hope to begin simulation studies of adiabatic transitions designed to minimize any such ill effects.

VI. ACKNOWLEDGMENT

We are endebted to E. P. Cornet for his valuable comments at various stages of this research.

REFERENCES

*Research supported jointly by the Air Force Office of Scientific Research and the Energy Research and Development Administration.

1. See, e.g., papers from the 1977 Particle Accelerator Conference (Chicago, 16-18 Mar. 77), IEEE Nuc. Sci. 24, 1625-1667 (1977).
2. M. L. Sloan and W. E. Drummond, Phys. Rev. Lett. 31, 1234 (1973).
3. W. E. Drummond, et al., unpublished.
4. B. B. Godfrey, in preparation.
5. B. B. Godfrey and W. R. Shanahan, in N. G. Cooper (ed.), "Theoretical Division Annual Report, July 1975-Sept. 1976," LA-6816-PR (Los Alamos Scientific Laboratory, 1977), p. 147.
6. W. E. Drummond, et al., AFWL-TR-75-296 (Air Force Weapons Laboratory, Albuquerque, 1976), App. O.
7. B. B. Godfrey, IEEE Plas. Sci., to be published.

CAPTIONS

Figure 1. Conceptualized transition from cylindrical waveguide to helical amplifier cavity. Radial dimensions are scaled to R_B = 2.65 cm, R_H = 3.8 cm, and R_W = 5.7 cm. Small plus signs represent image charges.

Figure 2. Frequency and growth rate of the beam-helix cyclotron instability for a 15° helix pitch as a function of wavenumber. Units are ω_p and ω_p/c, respectively.

Figure 3. Growth of cyclotron wave in helical cavity. Plots, top to bottom, are electron positions in cavity cross section, contours of the electrostatic potential, and electron axial momenta. Helix is at r = 3.8 c/ω_p.

Figure 4. Plots of perturbed radial momentum and axial electric field of a slow cyclotron wave in a 15° helix or in a waveguide each of radius 3.8 c/ω_p.

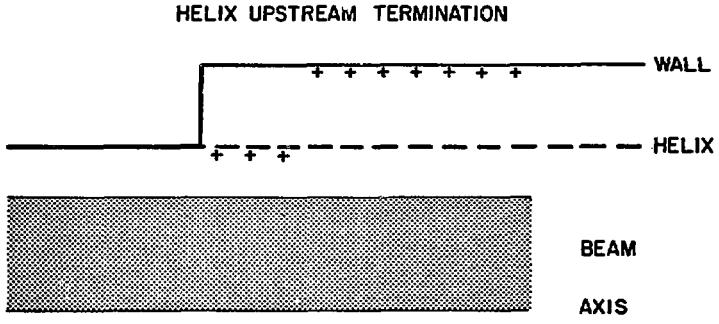
HELIX UPSTREAM TERMINATION
WALL
HELIX
BEAM
AXIS

Fig. 1

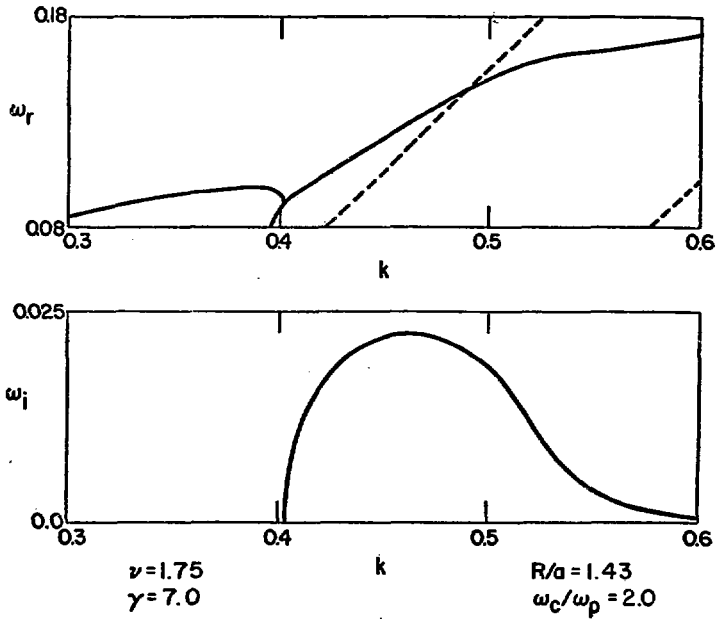
0.18
ω_r
0.08
0.3
0.4
0.5
0.6
k
0.025
ω_i
0.0
0.3
0.4
0.5
0.6
k
$\nu = 1.75$
$\gamma = 7.0$
R/a = 1.43
$\omega_c/\omega_p = 2.0$

Fig. 2

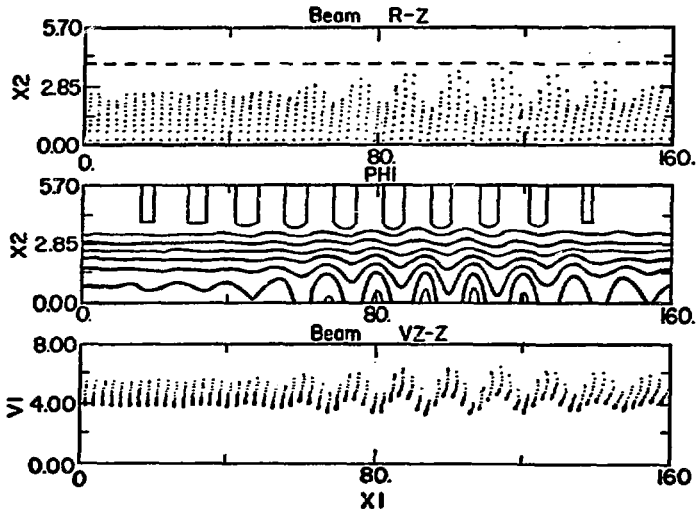
Beam R-Z
5.70
X2 2.85
0.00
0.
80.
160.
PHI
5.70
X2 2.85
0.00
0.
80.
160.
Beam VZ-Z
8.00
VI 4.00
0.00
0
80.
160
XI

Fig. 3

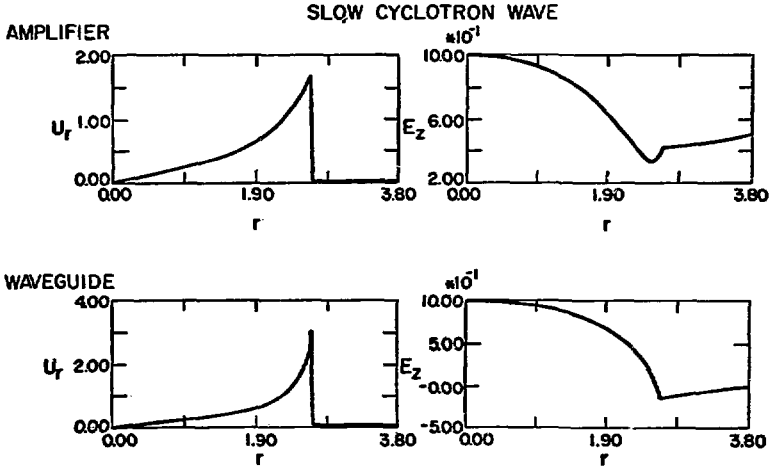
SLOW CYCLOTRON WAVE
AMPLIFIER
U_r
2.00
1.00
0.00
0.00
1.90
3.80
r
E_z
*10⁻¹
10.00
6.00
2.00
0.00
1.90
3.80
r
WAVEGUIDE
U_r
4.00
2.00
0.00
0.00
1.90
3.80
r
E_z
*10⁻¹
10.00
5.00
-0.00
-5.00
0.00
1.90
3.80
r
ν = 1.75
R/a = 1.43
k = 0.46
γ = 7.0
ω_c/ω_p = 2.0
m = 0

Fig. 4

DIELECTRIC GUIDE CONTROLLED COLLECTIVE ION ACCELERATION*

A. Greenwald and R. Little

Spire Corporation, Patriots Park, Bedford, MA 01730

Relativistic electron beams with $v/\gamma \simeq 1$ have been propagated in a hard vacuum without external magnetic fields through cavities lined with dielectric materials[1]. Charge neutralization was provided by ions removed from the surface of the dielectric liner by intense radiation bombardment. Protons were accelerated to energies 2 to 10 times the peak electron energy (70-100 keV). Ion energy increased with the cavity length. Ion velocity scaled directly as the injected current density. A model of the acceleration mechanism, correlating ion velocity with that of the electron beam front, will be presented. Subsequently, this work was scaled to higher energies[2].

I. INTRODUCTION

Collective ion acceleration by pulsed electron beams has been investigated by a number of research groups[3]. In general, the approach has been to inject an electron beam into a low pressure neutral gas, producing ions by collision, and accelerating these ions in the electrostatic potential well, behind the beam front.

* Supported by AFOSR under Contract FY3592-77-10122

Ions were produced in this experiment by electron bombardment of dielectric material surrounding the electron beam. Some ions were trapped and accelerated by the potential well associated with the beam front. The velocity of the beam front was controlled by the current pulse shape and geometry of the beam guide.

The experiments and results are described in Section II. The theory is discussed in Section III.

II. EXPERIMENTS

The dielectric guides used in this experiment (Figure 1) were thick walled cylindrical plastic tubes placed inside a vacuum chamber with conducting walls. The inner diameter varied between 5.7 cm to 30 cm and the guide length was 10 to 30 cm. An electron beam was injected into the guide through a mesh anode (65-77% transparency). The field emission cathode was made of carbon, scored to improve beam uniformity. A Faraday cup placed at the exit of the guide was used to measure the electron beam current. Ions were detected using a magnet and apertures to prevent electrons from reaching the Faraday cup.

The pulsed power supply for the field emission diode was a d.c. charged one ohm coaxial transmission line[4]. The line was charged between 150 kV and 200 kV; the stored energy was 200-300 joules. The typical electron beam injected

into the guide had a peak current between 7.3 and 9.4 kA in a 100 ns pulse. Maximum electron energy was between 65 and 83 keV.

The electron beam was space charge limited and also exceeded the Alfvén-Lawson[5] criteria for propagation of an electron beam in a charge neutralizing background. Without the dielectric guide the electron beam would propagate no more than 1 cm away from the anode. With the dielectric guide, electron current loss could be reduced below 25% (Figure 2)[6,7].

Experiments on electron beam transmission used dielectric liners pressed against the vacuum chamber walls. The insulator thickness exceeded the maximum range of electrons in the material. Initial electron current from the guide (Figure 2) closely followed the vacuum results without a dielectric liner. Approximately 50 ns into the electron beam pulse the transmitted current rose sharply to within 25% of the injected total. The 10% - 90% risetime of this transmitted current was a factor of three sharper than the injected current for all dielectric materials tested. The transmission experiment was repeated with a conductive screen (50% transparency) placed on the inside surface of the dielectric. As shown in Figure 3, the transmission for Teflon fell 75% while for the other plastics peak current transmission efficiency fell only 40%, but showed greater delays and slower rising currents.

Measurements of the transmitted ion current (Figure 4) were made with the smaller dielectric cylinder shown in

Figure 1. The ion beam was separated from the electron beam by a 480 gauss magnet placed between the dielectric cylinder and the Faraday cup. Two apertures, 1.25 cm diameter, were placed on either side of the magnet to reduce electrical noise. These apertures reduced the beam current reaching the detector to 5% of the value in the dielectric guide. The maximum detected high energy ion current at the Faraday cup was 0.6 amperes in a pulse 4ns FWHM. Assuming a uniform spatial distribution, the total number of accelerated ions in a single pulse was approximately 3×10^{11}.

A time of flight measurement, Figure 5, determined the velocity of the accelerated ions in a 15 cm long polymethylmethacrylate (Lucite) guide to be 6.25×10^{8} cm/sec. For protons, ions released by a hydrogen loaded dielectric, this velocity represented an energy of 207 keV per ion ($\beta = 0.021$). This was approximately three times greater than the maximum electron energy observed, 67 keV. This result was consistant with collective ion acceleration observed when an electron beam was propagated through a low pressure neutral gas[8] where typical maximum ion energies were three times the maximum electron energy.

The experiment was repeated with longer dielectric guides (20-30 cm). The ion current at peak velocity was reduced by 50% but the proton energy increased to 422 keV ($\beta = 0.030$). The energy of the ions increases with the length of the dielectric guide in these two experiments. This result was opposite to earlier observations of collective ion acceleration

in a neutral gas[8]. Timing information also showed that the ions arrived at the guide exit at the back of the electron beam front.

Two experiments were performed to determine the variation of ion energy with electron beam current density, $\vec{J}$. In one case the anode mesh was changed to vary the current injected into the guide for the same diode parameters. In the second case, the diameter of the cathode and guide and the A-K gap were increased 50% maintaining, approximately, the same total current. Results are given in Figure 6. The ion energy increased with current density. Also, there appeared to be a threshold value of $\vec{J}$ below which ions would not be accelerated although the electron beam still propagated to the end of the guide.

III. DISCUSSION OF RESULTS

The space charge limited current for an electron beam propagating in an infinite cylindrical conducting pipe is given by[8]:

$$I_c = 17{,}000\beta\gamma \frac{(\gamma^{2/3} - 1)^{3/2}}{1 + 2 \ln (R/a)} \text{ amperes}$$

where R is the radius of the wall, a the radius of the beam, βc the electron velocity, and $\gamma = (1 - \beta^2)^{-1/2}$. For the dimensions of the experiment shown in Figure 1, and assuming 67 keV electrons, the limiting current is only $\simeq$ 130 amperes. This implies that the multikiloampere electron beam injected into the guide will blow up radially with most of the current impinging

upon the dielectric walls. Many electrons will be reflected back into the diode by the high electric fields and a small current will propagate with $I < I_c$. As shown in Figure 2, this small forward electron current is equal to the transmitted current in vacuum without a dielectric guide.

Because the dielectric walls are thicker than the maximum range of the electrons, those electrons which bombard the dielectric guide walls stop in depth. On a short time scale ($<<$ 1 μsec) electric charge and thermal energy accumulate on the plastic surface until flashover[6] and/or partial melting occur. These processes release gas from the dielectric surface[9] that is ionizied by the intense electron beam. The ions created are drawn into the beam. A threshold value of charge and energy per unit area of material irradiated exists for the release of ions. Typical values for Lucite (from the measured transmitted current delay time in these experiments) are approximately 0.5 μcoul/cm^2 and 0.01 cal/cm^2 respectively.

The rate at which charge and energy are delivered to the guide walls thus determines the rate of ion production. Since the electron beam will not propagate until the space charge fields are partially neutralized by these ions, the velocity of the beam front into the region where the guide walls are being irradiated is also proportional to the rate at which charge and energy are delivered (per unit area) to the dielectric surface. This implies that the velocity of the beam front is directly proportional to the electron current at the front and inversely proportional to the radius of the guide at the position of the beam front.

Thus, the beam front will advance at a constant rate of acceleration (neglecting relativistic effects) in a cylindrical dielectric guide when the electron energy is approximately constant and the current increases linearly in time with small transmission losses. This model can explain the data reported here that shows collectively accelerated ion energy increasing with the length of the dielectric guide.

Collective ion acceleration is limited by the potential well depth of the beam, power balance at the beam front, and for this method, material properties. The axial electrical field in a space charge limited electron beam is proportional to the current density. This explains the ion acceleration cutoff in Figure 6. As R increased for constant I, the force on the ions fell as $1/R^2$ whereas the acceleration of the beam front fell as $1/R$; below a threshold value of $\vec{J}$ the ions fell behind the beam front and were not accelerated.

To compute a possible limit to maximum ion energy due to power balance we can assume that the energy density in the electron beam, in the electromagnetic fields, and in the ion beam is constant[10]. Equating the power at the beam front to that in the diode implies a maximum ion velocity of $v/c \leq 0.42\ V/I$ where V/I is the diode impedence in ohms. This limit was not important because the diode had high impedence.

Additional possible limiting factors are the material properties of dielectrics. If surface flashover is the principal cause of ion emission, then the maximum velocity of the beam front would be less than 0.2 times the velocity of

light[11]. The ion energy seen in experiments to date was insufficient to reach this limit.

IV. CONCLUSIONS

Experiments have detected collective acceleration of protons by intense electron beams in dielectric guides. The ion energy has been shown to increase with guide length (out to 6 beam diameters) and injected current density. With high impedence diodes, this method of acceleration should scale to higher energy beams.

REFERENCES

(1) A. Greenwald, R. Lowell, and R. Little, Bull. Am. Phys. Soc., 21, 1147, (1976).

(2) J. A. Pasour et. al., this conference.

(3) See Particle Accelerator Conf., IEEE Trans. NS-24, 1622-1670 (1977).

(4) J. R. Uglum, R. G. Little, S. H. Face, Spire Corporation Report FR-76-10039, (unpublished).

(5) H. Alfven, Phys. Rev., 55, 425, (1939).

(6) R. G. Little, R. Lowell, J. Uglum, IEEE Trans. on Nuc. Sci., NS-21, #6, 249, (1974).

(7) R. G. Little, R. Lowell, J. Uglum, IEEE Trans. on Nuc. Sci., NS-22, 2351, (1975).

(8) R. B. Miller and D. C. Straw, J. Appl. Phys. 47, 1897 (1976).

(9) G. A. Vorober and V. S. Korolev, Sov. Phys. Tech. Phys., 21, 1222 (1976).

(10) Private Communication Shyke Goldstein.

(11) Private Communication B. B. Godfrey.

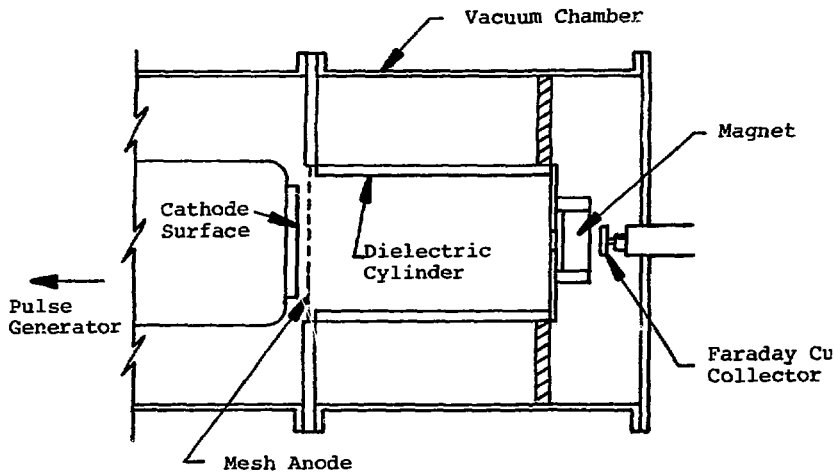

Figure 1. Apparatus for Ion Acceleration Experiment with Dielectric Cylinder Beam Guide

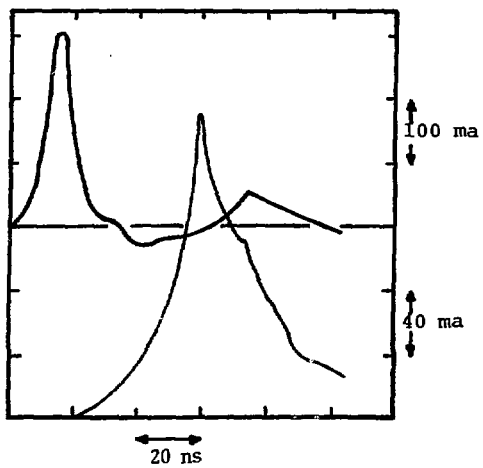

Top Trace:
Mesh Detector
(50% Transmission)
10 cm from Guide

Bottom Trace:
Solid Plate Detector
30 cm from Guide

Figure 4. Detector Ion Current (Through 1.27 cm^2 Aperture)

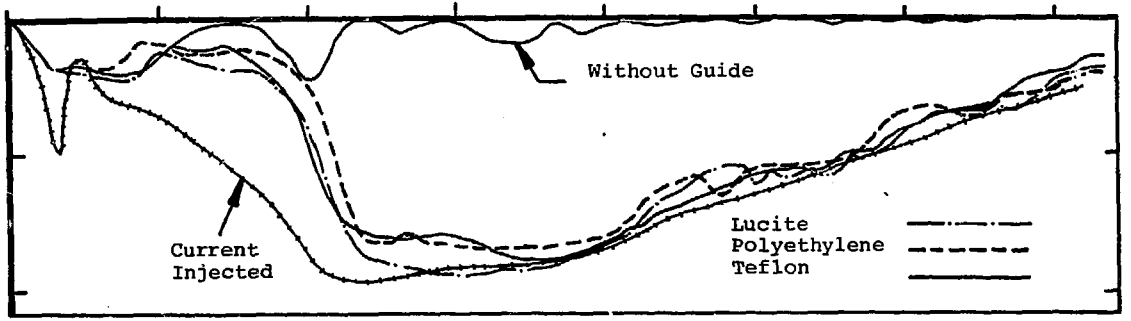

Figure 2. Current Transmitted by Dielectric Guides
(20 ns per Division, 5 kA per Division.)

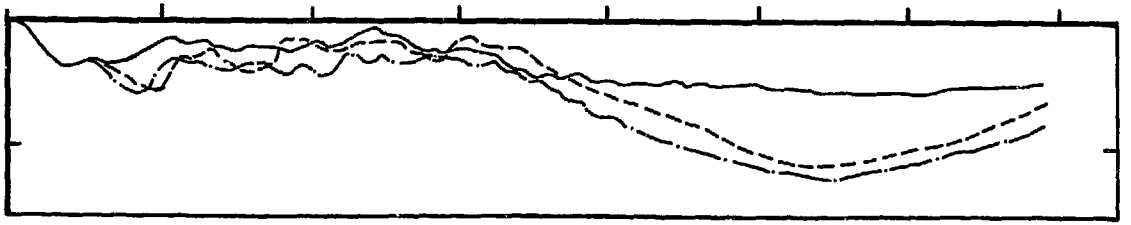

Figure 3. Current Transmitted by Dielectric Guides
With Screen Over Surface (50% Transparency)
(20 ns per Division, 5 kA per Division.)

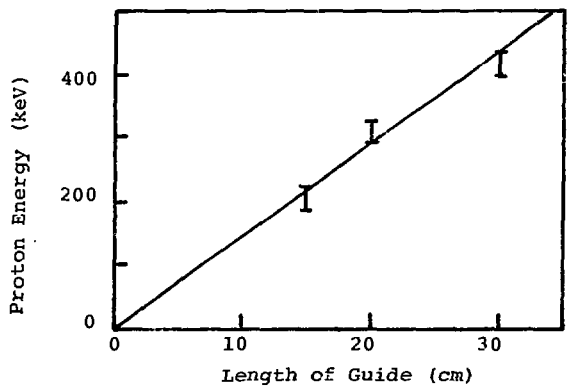

Figure 5. Proton Energy (From Time-of-Flight Measurements)

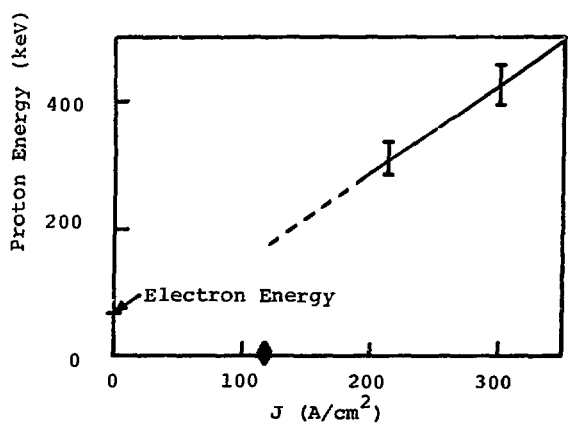

Figure 6. Proton Energy vs. Current Density

ON TRANSVERSE STABILITY IN AN ELECTRON RING ACCELERATOR

I. Hofmann*

Max-Planck-Institut für Plasmaphysik+

D-8046 Garching, Germany

Abstract

Suppression of coherent transverse instabilities is a basic requirement for stable operation of an electron ring accelerator experiment. Landau damping of the unstable radial electron-ion modes and the resistive wall modes may be insufficient after final compression of the ring owing to the curvature and image effects. A specific choice of image focussing and ion loading is then required in order to avoid a large reduction of ring quality. The theoretical implications of this situation, which affects the stable working range of a heavy ion electron ring accelerator, are studied for parameters relevant to the Garching "Pustarex" experiment.

I. Introduction

Performance studies of the electron ring accelerator scheme for collective acceleration of ions have been the subject of several papers in the past few years [1,2]. The negative mass instability [3,4] has been recognized as the main limiting factor for the total number of electrons and hence the "holding power" of rings, which yields the effective

*On leave of absence to the Lawrence Berkeley Lab.,Berkeley/CA

+This work was performed under the terms of agreement on association between Max-Planck-Institut für Plasmaphysik and Euratom.

accelerating field strength $E_H = 0.64\ \eta \frac{eN_e}{4\pi^2 \varepsilon_o R \rho}$. The reduction factor η ranges from 0.2 to 0.75 and gives the fraction of the maximum electric field in the ring, which can be utilized for collective acceleration if polarization effects are taken into account [5]. Calculations have suggested that values of E_H between 50 and 100 MV/m should be achievable provided that appropriate beam sources are available and other collective instabilities such as the resistive wall instability and the electron-ion resonance can be avoided [1]. With the calculated limitations in E_H the main interest in the ERA lies in its potential use as a device for the stripping of ions to high Z and collective acceleration.

The new Garching ERA experiment "Pustarex" [6,7] is expected to yield an effective $E_H \approx 8$ MV/m. This should result in an energy gain per nucleon of 4 MeV/m for He (Z = 2) or 1.5 MeV/m for Xe (Z = 25). There are several potentially dangerous mechanisms which might result in radial beam growth: the radial electron-ion dipole resonance, for which experimental evidence was given in a previous experiment [8], the resistive-wall instability, and the coherent and incoherent $\nu_r = 1$ resonance. Species-species and image forces have been considered in previous literature to affect Landau damping and stability criteria for axial coherent dipole modes [9]. These criteria, however, are not directly applicable to the radial dipole mode [10], which appears to be the most dangerous transverse mode for "Pustarex" with a total number of electrons $N_e \approx 5 \cdot 10^{12}$. A modification is necessary taking into account the centrifugal force term and curvature.

In the present study the possibilities afforded by Landau damping using the correct dispersion relation are examined for parameters relevant to the "Pustarex" experiment. The conditions for circumventing the electron-ion resonance are discussed for different ion species. Landau damping of the resistive-wall instability, which is found to depend on the presence of ions, seems difficult to be realized. Therefore, walls with conductivities should be used that keep the growth rate small. It is found that special care is required for the relatively long period ($\lesssim 1$ msec) during which the ring stays in the "waiting room", where ion space charge is slowly accumulated owing to collisions with the relativistic electrons.

II. Dispersion Relation

Electrons and ions are described by the Vlasov equations, from which we derive an equilibrium solution in terms of the constants of motion valid in a stationary ring symmetric with respect to θ. Frequency spread is introduced into the system by assuming that the electron gyro-frequency Ω_e and radial betatron frequency ν_r are functions of the canonical angular momentum P_θ, and hence the quantity

(1) $S(P_\theta) \equiv \Omega(P_\theta) \left[1-\nu_r(P_\theta)\right]$

is a function of P_θ. The normalized ion oscillation frequency Q_i is assumed to depend on the amplitude A of single particle oscillation, provided that ions execute anharmonic oscillations in the potential well built up by the electron space charge. A corresponding variation of ν_r due to nonlinearities in the guide field may be neglected here because this varia-

tion is very small if the ring is in an almost homogeneous guide field region.

Coherent dipole oscillations of the two-species ring are described by the linearized Vlasov equations. For the "slow wave" - the "fast wave" is stable - the dispersion relation is found to be (the procedure taking into account toroidal terms is outlined in [10] for an electron ring)

$$(2)\quad 1+\left[\,U+(1+i)V\,\right]\int\frac{F_e^0(u)}{S(u)-\omega}\,du=\frac{\bar{\Omega}^2\bar{Q}_i}{4\bar{\nu}_r}\int\frac{Q_1^2(u)F_e^0(u)}{S(u)-\omega}du\int\frac{A^2\frac{\partial F_i^0(A^2)}{\partial A^2}}{\bar{\Omega}Q_i(A^2)-\omega}\,dA^2.$$

The equilibrium radius of particles varies with $u \equiv P_\theta - \bar{P}_\theta$, and hence the shift of ν_r^2 due to the ion space charge, $\Delta\nu_r^2 = Q_1^2(u)$, is itself a function of u if the ion space charge density is nonuniform. U is the coherent frequency shift due to electron species-species and image effects for infinite conductivity, and V > 0 the correction due to the finite resistivity of surrounding walls.

Unstable solutions of equ.(2) are associated with Im ω > 0 and damped solutions with Im ω < 0, in which case the path of integration has to pass the singularities in the complex ω-plane from below. We observe that for zero frequency spread, no ions and V = 0 equ.(2) yields the frequency of the slow stationary coherent electron wave

$$(3)\quad \omega_e = S + U.$$

III. Stability Criteria

Evaluation of equ.(2) requires assumptions on the form and width of the distributions $F_e^0(u)$ and $F_i^0(A^2)$. In the

following we shall adopt as functional dependence

$$F_e^0 \sim (1-y^2)^2 \qquad y \equiv \frac{u}{\Delta u/2},$$

$$A^2\frac{\partial F_i^0}{\partial A^2} \sim (1-y^2)^2 \qquad y \equiv \frac{A^2}{\Delta(A^2)} - 1 \tag{4}$$

which has the desirable feature of zero slopes at the edge. We start by discussing stability of a pure electron ring with $V > 0$ and then consider the influence of ions.

1. Resistive wall instability ($Q_1^2 = 0$)

This mode has been extensively studied for beams in straight vacuum tanks with various cross-sections, and stability criteria have been derived for different distribution functions [11]. For the case of radial dipole oscillations of a ring U has to be calculated properly [10] and one obtains the stability criterion

$$\frac{\Delta S}{2} > \frac{4}{3}|U+(1+i)V| \tag{5}$$

with U, ν_r for a circular cross-section ring (radius ρ) as

$$U = \frac{\Omega}{2\nu_r}\mu\left[-\frac{2R^2}{\rho^2}\frac{1}{\gamma^2}+\ln\frac{8R}{\rho}+4\,\frac{\varepsilon_e^{coh}-\beta^2\varepsilon_m^{coh}}{(1-\bar{S})^2}\right],$$

$$\nu_r^2 = 1-n-\mu\left[\frac{2R^2}{\rho^2}\frac{1}{\gamma^2} - \ln\frac{8R}{\rho} + 4\,\frac{\varepsilon_e^{inc}-\beta^2\varepsilon_m^{inc}}{(1-\bar{S})^2}\right], \tag{6}$$

where the $\varepsilon_{e,m}^{inc}$, $\varepsilon_{e,m}^{coh}$ are, respectively, incoherent and coherent image coefficients tabulated in [10] and $\bar{S} = \frac{\bar{R}}{R}$ gives the ratio of the wall radius to ring radius. In general, one has $V > 0$ with a maximum $\frac{V_{max}}{\Omega} \simeq 5\cdot10^{-2}$ at a surface resistivity $R_s \simeq 1$ Ohm for "Pustarex". We introduce the Landau damping coefficient

(7) $K \equiv \frac{\Delta S}{\Delta E} \frac{E}{\omega_e}$,

using equs.(1) and (3) and evaluate the stability criterion in terms of the required energy spread $\frac{\Delta E}{E}$ for a ring with $N_e = 5 \cdot 10^{12}$, $\frac{R}{\rho} = 10$ and $\mu = 3 \cdot 10^{-3}$ in the compressed state with $\gamma = 27$ (except for case (a), which holds during compression).

	focussing:	U/Ω	|K|*	ΔE/E ≳	V>0 on resistive wall
	walls far away ($\bar{S} \gtrless 1$)		(free space value)		
(a)	$S \gg U$	$\sim 5 \cdot 10^{-3}$	1....2	13 U/S	stable, if V limited by (5)
(b)	$S \lesssim U$			0.7	no stabilization
	squirrel cage				
(c)	outside $\bar{S} = 1.25$	$2.5 \cdot 10^{-2}$	$\lesssim 2$	1.3	no stabilization
(d)	inside $\bar{S} = .75$	$1.2 \cdot 10^{-2}$			
	resistive cylinder with $R_s \ll 1$ Ohm		only electric image contribution		
(e)	inside $\bar{S} = 0.8$	$\sim 5 \cdot 10^{-3}$	4.5	0.15	stabilization feasible
(f)	outside $\bar{S} = 1.2$	$15 \cdot 10^{-2}$	3	0.45	no stabilization

*see [10] for the different contributions to K

Table 1: Evaluation of $\frac{\Delta S}{2U} = K \frac{\Delta E}{E} \frac{S+U}{2U} \gtrsim \frac{4}{3}$, (V = 0) for resistive wall mode

We conclude that Landau damping of the radial dipole oscillation is possible only in cases (a) and (e), while in all other cases oscillations will be stationary or growing if V > 0. The required spread ΔE is understood as the full width of the energy distribution. For the distribution (3) it is about twice as large as the full width half maximum value $(\Delta E)_{f.h.}$. The physical understanding of the above table is that

(8) $\frac{\Delta S}{2} > \frac{4}{3}U$

is a necessary condition for Landau damping. It implies that the tails of the distribution are long enough to ensure that particles stay in phase with the coherent wave, whose frequency is shifted by U/Ω.

2. Electron-ion instability ($V = 0$, $Q_1^2 > 0$)

The case with no self-fields and no frequency spread has been studied in [12] for parameters relevant to the "Pustarex" experiment. The dispersion relation for the axial dipole mode, which has the same structure as equ.(2), was solved analytically in [9] for a semi-circular distribution (with infinite slopes at the edges). For the present distribution numerical solutions for ω from equ.(2) have been obtained for a realistic set of parameters. The stability boundary is fairly well described by the formula derived in [9], except for a factor $\frac{2}{3}$, which matches the threshold spread to the value specific to our distribution (see (8)). Hence we rewrite equ.(24) from [9] in our notation:

$$(9)\quad \left[\left(\frac{(\Delta S)_{f.h.}}{\Omega}\right)^2 - \left(\frac{2}{3}\cdot\frac{2U}{\Omega}\right)^2\right]^{1/2} (\Delta Q_i)_{f.h.} \geq \frac{Q_1^2 Q_i}{\nu_r},$$

which is a necessary and sufficient criterion for stabilization in the center of the resonance band about the point

$$(10)\quad \omega_e = Q_i\Omega \qquad \text{(resonance condition for } Q_1^2 \to 0\text{)}.$$

We observe that the right side of equ.(9) is related to the growth rate of the undamped mode, i.e.

$$(11)\quad \frac{Q_1^2 Q_i}{\nu_r} \approx \left(2\frac{\mathrm{Im}\omega}{\Omega}\right)^2.$$

If $Q_1^2 > 0$, equ.(9) amounts for the threshold dispersion already encountered in (8)

(12) $(\Delta S)_{f.h.} = \frac{\Delta S}{2} > \frac{4}{3}U,$

otherwise there is no damping of the instability irrespective of how small the ion loading is.

From Table 1 we conclude that damping of the electron-ion instability can be achieved only in cases (a) and (e). Assuming that ΔS is twice the limit in (12), the ion loading compatible with stability at resonance $\omega_e = \Omega Q_i$ is limited by

(13) $Q_1^2 \equiv \mu f 2\left(\frac{R}{\rho}\right)^2 \lesssim 10^{-2}\,\frac{\Delta Q_i}{Q_i},$

which for $\frac{\Delta Q_i}{Q_i} = 10^{-1}$ leads to an ion loading $f \equiv z\frac{N_i}{N_e} \lesssim 0.15\%$. If (e) is not feasible there remains only the possibility of such a choice of parameters as to avoid moving through the resonance region with a given ion species after the ring has been loaded with this species. In a heavy-ion ERA a number of resonance bands exists which are associated with rest gas ions and with the various charge states of the heavy-ion species that is to be accelerated. Charge stripping of the heavy ions leads to a change in Q_i according to the expression

(14) $Q_i^2 = \mu \cdot \frac{Z}{A}\,\frac{m\gamma}{M_p}\,2\left(\frac{R}{\rho}\right)^2,$

in which a homogeneous circular charge distribution is assumed.

Dommaschk [13] calculated Q_i assuming a quadratic Lorentzian line for the transverse electron distribution with ρ replaced by the radius at half maximum. He finds a reduction factor $\sigma \approx \frac{1}{2}$ for Q_i. Hence for "Pustarex" one has

(15) $Q_i \approx \sigma \cdot 10^{-1} \sqrt{\frac{Z}{A}}$,

and one may visualize two theoretical alternatives of how to avoid resonances:

(A) $\frac{\omega_e}{\Omega} > Q_i \quad (Z = 1 \ldots Z_{max})$,

(B) $\frac{\omega_e}{\Omega} < Q_i \quad (Z = 1 \ldots Z_{max})$,

which conditions have to be satisfied at a time when a definite charge state exists in the ring. Charge stripping in "Pustarex" is done in the "waiting room", where the magnetic field index n is about $\lesssim 5 \cdot 10^{-3}$. Thus, the only way of adapting $\frac{\omega_e}{\Omega}$ is through appropriate image focussing (squirrel cage etc.). (A) is valid for strong and (B) for rather weak image focussing. Unfortunately, there exists a lower limit for image focussing, which derives from the requirement that $\nu_z^2 > 0$ and $\nu_r^2 < 1$. Because of $\nu_z^2 + \nu_r^2 = 1 + 2\mu\left(2\frac{R^2}{\rho^2}\left(f - \frac{1}{\gamma^2}\right)\right)$, the second requirement is the more stringent if guide field (gradient) errors are such as to prohibit slow crossing of $\nu_r^2 = 1$, which may be induced by a slowly increasing f (see, for instance, [14] with application to "Pustarex"). In the following table the parameters relevant to alternatives (A) or (B) are presented for a number of ion species. We note that for (A) the critical charge state is Z_{max}, whereas it is Z = 1 for (B). The finite width of the resonance band given approximately by

(16) $\delta\left(\frac{\omega_e/\Omega}{Q_i}\right) \approx \pm \left(\frac{Q_1^2}{Q_i}\right)^{1/2}$

requires a safety gap between $\frac{\omega_e}{\Omega}$ and Q_i. It may also be necessary to take into account jitter in ring parameters. One then needs a somewhat larger gap than assumed in Table 2, which requires smaller $\bar{S}$ for (A), whereas for (B) the values

are already at the limit imposed by $\nu_z^2 > 0$.

		H	He	N^+, N_2^+ (rest gas)	Ne	Ar	Xe
B:	critical Z	1	1				
	Q_i	$5\cdot10^{-2}$	$25\cdot10^{-2}$	$14\cdot10^{-2}$, 10^{-2}			
	inner squirrel cage with $\bar{S}=0.65$: $\nu_z^2=n$ $\omega_e/\Omega=n/2+10^{-2}=1.25\cdot10^{-2}$	stable	stable				
	inner resistive cylinder with $\bar{S}=0.65$: $\nu_z^2=n$ $\omega_e/\Omega=n/2+5\cdot10^{-3}=0.75\cdot10^{-2}$	stable	stable	stable			
A:	critical Z				6	9	25
	Q_i				$25\cdot10^{-2}$	$24\cdot10^{-2}$	$22\cdot10^{-2}$
	outer squirrel cage with $\bar{S}=1.25$: $\omega_e/\Omega=n/2+3.25\cdot10^{-2}=3.5\cdot10^{-2}$				stable	stable	stable

Table 2: Evaluation of image focussing to circumvent the electron-ion instability in "Pustarex" ($N_e = 5\cdot10^{12}$, $\frac{R}{\rho} \approx 10$, $\gamma = 27$, $n = 0.5\cdot10^{-2}$)

3. Two-species ring with finite resistivity

Numerical solution of the full equation (2) with $V > 0$ and $Q_1^2 > 0$ has shown the following results for the combined modes:

a) Within the resonance band of the electron-ion mode (defined for $V \approx 0$) an additional $V > 0$ results in a growth rate of about the sum of the independently obtained rates if there is insufficient Landau damping; for damping the required $\frac{\Delta S}{2}$ has to be in excess of $\frac{4}{3}$ U by an amount which is of the order of the sum of the independent growth rates for either mode.

b) Off of the electron-ion resonance band the ions only have a minor effect upon the growth rate of the undamped resistive wall mode. The ΔS required for damping depends, however, on which side of the resonance band the system stays: for $Q_i \ll \omega_e/\Omega$ the ions cannot follow the resistive wall mode and there is only a shift of S and ω_e/Ω by $-Q_1^2/2\nu_r$; for $Q_i \gg \omega_e/\Omega$ only the single particle frequency S is shifted by $-Q_1^2/2\nu_r$, whereas ω_e/Ω remains unaffected by the ions captured in the electron ring. If we assume that Q_1^2 is independent of u (i.e. constant ion space charge density in the ring), equ.(5) is replaced by the more restrictive condition

$$(17)\quad \frac{\Delta S}{2} > \frac{4}{3}\left|U + \frac{Q_1^2}{2\nu_r} + (1+i)V\right|,$$

which will suppress damping if f is in the per cent range. In a different model $Q_1^2(u)$ is allowed to drop quadratically to zero towards the edge of the distribution $F_e^0(u)$ owing to a more realistic centrally peaked ion space charge density. In this case damping of the resistive wall mode is again provided by criterion (5).

Acknowledgement

The author is indebted to Dr. W. Dommaschk for reading the manuscript.

References

1. D. Möhl, L. J. Laslett, and A. M. Sessler, Part. Accelerators 4, 159 (1973)
2. L. J. Laslett, IEEE Trans. Nucl. Sci. NS-20, No. 3, 271 (1973)
3. C. E. Nielsen, A. M. Sessler, and K. R. Symon, Proc. 2nd Int. Conf. on High Energy Accel., CERN, Geneva (1959), p. 239
4. R. W. Landau and V. K. Neil, Phys. Fluids 9, 2412 (1966)
5. I. Hofmann, Proc. 9th Int. Conf. on High Energy Accel., Stanford (1974), p. 245
6. C. Andelfinger, E. Buchelt, W. Dommaschk, J. Fink, W. Herrmann, I. Hofmann, D. Jacobi, P. Merkel, A. Schlüter, H.-B. Schilling, U. Schumacher, M. Ulrich, MPI f. Plasmaphysik, Garching, Rep. IPP 0/30 (1976)
7. C. Andelfinger et al., IEEE Trans. Nucl. Sci. NS-24, No. 3, 1622 (1977)
8. C. Andelfinger, W. Dommaschk, I. Hofmann, P. Merkel, U. Schumacher, M. Ulrich, Proc. 9th Int. Conf. on High Energy Accel., Stanford, 218 (1974)
9. L. J. Laslett, A. M. Sessler and D. Möhl, Nucl, Instr. and Meth. 121, 517 (1974)
10. I. Hofmann, MPI f. Plasmaphysik, Garching, Rep. IPP 0/33 (1976), to be published in Part. Accelerators
11. L. J. Laslett, V. K. Neil, and A. M. Sessler, Rev. Sci. Instr. 36, 436 (1965)
12. W. Dommaschk, MPI f. Plasmaphysik, Garching, Rep. IPP 0/19 (1973)
13. W. Dommaschk, unpublished note RPR-N-27, MPI f. Plasmaphysik, Garching (1974)
14. I. Hofmann, to be published in Nucl. Instr. and Meth.

AUTOACCELERATION OF ELECTRON BEAM AND MICROWAVE RADIATION IN THE DIAPHRAGMED WAVEGUIDE

A. A. Kolomensky, G. O. Meskhy, B. N. Yablokov

P. N. Lebedev Physical Institute
Leninsky Prospect, 53, Moscow 117924, USSR

ABSTRACT

One can increase considerably the energy of a portion of beam electrons by means of the autoacceleration mechanism. In our experiments, an electron accelerator with parameters 0.5-1.0 MeV, 20-30 kA, 40-50 ns was used. A hollow beam was passed through a diaphragmed waveguide. At its output, the electron spectrum and microwave spectrum were measured simultaneously. About 10% of the electrons increase their energy as compared with the maximum input energy, whereby 3% increase their energy more than by a factor of two. The energy multiplication for the tail electrons turns out to be 3-4 times the initial value. About 10% of the beam input power is spent on the increase of electron energy. The pulse microwave power generated is in the range 2.7-2.9 GHz and its total measured power was ~ 0.4 GW, which corresponds to approximately 20% of the input beam power. Experiments show that effects of autoacceleration and microwave generation are interdependent and should be studied together.

The method of autoacceleration and certain of its specific schemes were proposed and developed originally in our laboratory [1-4]. This method makes it possible to use the energy of a high-current beam to accelerate a certain portion of the particles of the beam itself up to considerable energies. The electric field excited by the interaction of the beam with various passive elements such as resonators, long lines and waveguides serves this purpose. Calculations and numerical experiments have shown that the maximum particle energy gain per unit length occurs

when a round diaphragmed waveguide is used as a passive structure [4].

Experiments in autoacceleration have been conducted by us on accelerator "Impulse" [5], which has the following electron beam parameters: electron kinetic energy up to 800 keV, pulse current up to 30 kA, pulse duration ~ 50 ns. The beam power is of the order of 10^9-10^{10} W and energy stored in the beam ~ 1 kJ.

The autoacceleration effect was determined by the change in the electron energy spectrum and already in experiments [6] it was shown that at least 2% (10^{13}) of the particles had increased their energy by more than a factor of two. About 6% (50 MW) of the beam power entering the waveguide was spent on the additional particle acceleration. A 10-cm diaphragmed waveguide terminated with cut-off wavelength tubes was used. A 3-cm diameter electron beam with uniform cross-sectional particle distribution had the following characteristics: energy ~ 300-700 keV, current up to 2 kA in a pulse of 50 ns duration. The waveguide length was varied from 30 to 90 cm and the maximum effect was obtained with a waveguide of 30 cm length.

Important features of the autoacceleration method are the processes of beam excitation and absorption of the powerful UHF-radiation. In this connection, we have conducted a series of experiments devoted to the generation of UHF-radiation in a diaphragmed waveguide during the autoacceleration of an electron beam. The general scheme of experimental apparatus is shown in Fig. 1. In contrast to previous experiments, the electron beam was formed in a diode of coaxial geometry. The cathode consisted of a stainless steel cylinder of 30 mm diameter and 40 mm length and the anode a tube of 43 mm i.d. The diode was located in the magnetic field of a solenoid providing hollow beam formation and confinement. The beam of ~ 5 mm thickness had a diameter of ~ 30 mm which corresponds to the cathode diameter.

The waveguide consists of stainless steel diaphragms (4.0 mm thickness, 47 mm hole diameter) and rings (18.7 mm length, 94.5 mm i.d.) held together by special rods. In control experiments, we use electrons passing through a smooth, stainless-steel tube placed in the waveguide and short-circuiting the diaphragms.

The electron beam parameters were determined by the geometric dimensions of the system. The electron energy was chosen as ~ 400-500 keV, which corresponds to the phase velocity of the cold waveguide ($v_{ph} \simeq 0.87$ c); the beam current was 2-3 kA in passing through the waveguide and 6 kA in the case of the smooth tube.

The accelerator is switched on when current through the solenoid is decreasing and the magnetic field reaches a selected value. The diode and waveguide are located inside a thin-wall vacuum chamber. At the waveguide output there is a wave-type transformer to extract the UHF-power and at the cut-off transformer tube a measuring unit in which aluminum foils can be placed to measure particle current impinging on the foil and current passing through the foil. The measuring unit is also installed in the magnetic field in order to decrease the effect of electron scattering in the foil and improve measurement accuracy. The method of electron energy spectrum measurement was described in [7].

The UHF-power extracted from the diaphragmed waveguide passes through a standard waveguide of rectangular cross-section and is absorbed by the load. A part of this power is branched into the measurement channel, reduced by a calibrated attenuator and measured by a narrow-band calibrated detector.

Measurements of the UHF-power extracted from the waveguide have shown that the frequency spectrum generated lies within the limits 2.5-3.2 GHz (as averaged over many pulses)--see Fig. 2. The maximum power is generated in the 2.7-2.9 band. The full power generated on average in

the whole frequency spectrum is equal to 300-400 MW, i.e., about 20% of the electron beam power at the waveguide input. The level of UHF-power extracted depends on the waveguide length, as can be seen from Fig. 3a. For a waveguide of 14 cm length, no generation was observed. An analogous dependence of the UHF-power level was obtained for various values of axial magnetic field confining the electron beam (Fig. 3b). Considerable generation of UHF-power (at a level of several MW) occurred when electron current through the waveguide exceeded 1.5 kA and the magnetic field was 3.0-3.5 kG. It should be noted that the level of UHF-power varies considerably from pulse to pulse and reaches in some cases ~ 100 MW and more in the 2800 ± 30 MHz band. The envelope oscillograms of UHF signals at the detector show that the UHF-power increases quite rapidly during 2-3 ns, ~ 25 ns after the beam appears at the end of the waveguide. The UHF pulse duration varies from 10 to 20 ns. Such a delay in the appearance of UHF-power permits only the tail end of the beam to accelerate, the electron energy of which is considerably below the maximum. Moreover, the beam current passing through the waveguide to this moment is less than the maximum current (Fig. 4). But in spite of this, foil absorption measurements (Fig. 5) indicate that about 10% of the beam particles have increased their energy relative to the maximum energy at the waveguide input and 3% of the particles by more than a factor of two. The autoacceleration effect becomes significant when the waveguide length reaches 40-45 cm. A further increase in this length does not lead to an increase in the autoacceleration effect. This is also indicated by the level of extracted UHF-power (Fig. 3a). A significant number of particles increasing their energy by a factor of two and more appear when the waveguide length is ~ 40 cm. If this length is decreased to 20 cm, there are practically no particles with doubled energy, although the UHF signal level is 20% of the maximum value. Power balance considerations indicate

that about 10% of the beam power at the waveguide input is spent on increasing the energy of beam particles.

The next stage in our experiments was connected with an investigation of the role of pulse current shape at the waveguide input. When a pulse-sharpening switch was installed before the electron gun, the rise-time of the current pulse decreased to ~ 5 ns at a level of 70-80% of the maximum value (Fig. 4). For such a current pulse shape, the time elapsed from the moment current appeared at the end of the waveguide to the appearance of UHF signal was reduced to 20 ns. The UHF-power level remained practically unchanged. The absorption curve obtained in the case of the small current-pulse risetime (Fig. 5) indicates that the number of particles increasing their energy has increased.

Our experiments show that in the process of electron beam interaction with a periodic structure, the effects of electron autoacceleration and UHF-power generation are interrelated and should be investigated together.

The results obtained show that by means of the autoacceleration method one can vary such electron beam characteristics as spectrum, maximum energy and pulse power. This will make it possible to broaden considerably the possibilities of present and future high-current electron accelerators.

REFERENCES

1. L. N. Kazansky, A. V. Kisletsov, A. N. Lebedev, Atomnaya Energiya, 30 (I), 27 (1971).
2. A. A. Kolomensky, Particle Accelerators, 5 (2), 73 (1973).

3. N. E. Belov, A. V. Kisletsov, A. N. Lebedev, Atomnaya Energiya 36 (3), 201 (1974).
4. V. G. Gapanovich, A. A. Kolomensky, A. N. Lebedev, Proc. 4th All-Union Conf. on Acceler., Moscow, 1974, 1 , 100, Nauka (1975).
5. L. N. Kazansky, A. A. Kolomensky, G. O. Meskhy, B. N. Yablokov, Atomnaya Energiya 42, 113 (1977).
6. A. A. Kolomensky, E. G. Krastelev, G. O. Maskhy, B. N. Yablokov, JTP Lett., 1, 968 (1975).
7. E. G. Krastelev, G. O. Meskhy, B. N. Yablokov, Prib. i Techn. Eksp., No. 3, 39 (1976).

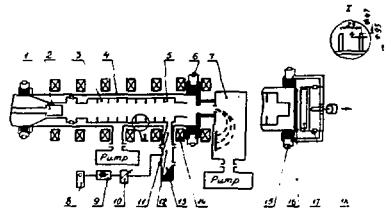

Fig. 1. Schematic diagram of experimental apparatus. (1) cathode; (2) anode; (3) waveguide; (4) vacuum chamber; (5) wave-mode transformer; (6) shunt; (7) 180° spectrometer; (8) oscillograph; (9) - (13) UHF-detector, attenuator, output, pro , load; (14) solenoid; (15) total current shunt; (16) foils; (17), (18) Faraday cup.

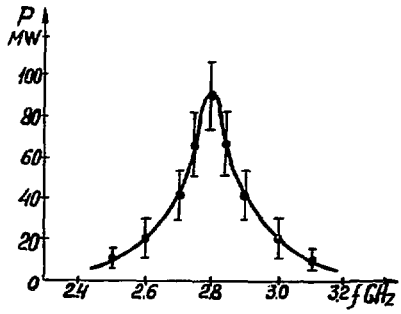

Fig. 2. Mean level of UHF-power output versus frequency (V = 400 - 500 kV, I = 2.5 - 3.0 kA, waveguide length - 80 cm).

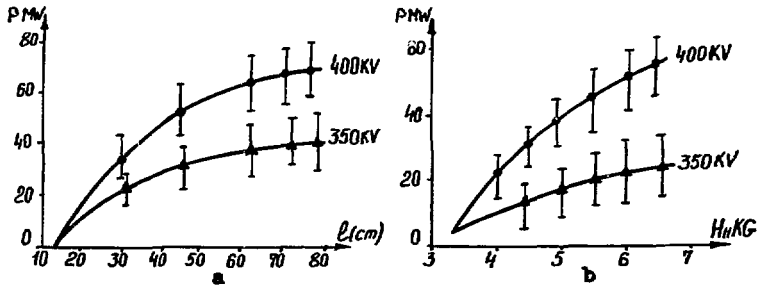

Fig. 3. Mean level of UHF-power output (2800 ± 30 MHz) versus waveguide length (a) and magnetic field (b).

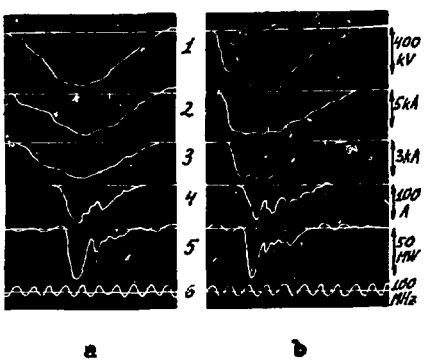

Fig. 4. Oscillograms: (a) ordinary regime without pulse-sharpening switch, (b) regime when pulse sharpening switch is on. (1) diode voltage, (2) waveguide input current, (3) waveguide output current, (4) current beyond 1-mm foil, (5) UHF-power pulse.

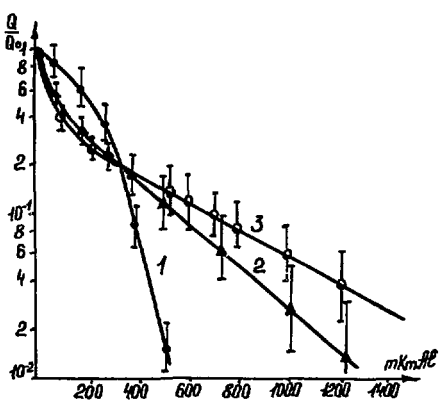

Fig. 5. Absorption curves: (1) control curve, (2) electrons passing through a waveguide of 80 cm length in ordinary regime, (3) in short pulse front regime.

THEORETICAL AND EXPERIMENTAL INVESTIGATIONS OF THE AUTOACCELERATOR

T. Lockner, J. Siambis, and M. Friedman
Naval Research Laboratory, Washington, D.C. 20375

ABSTRACT

Theoretical and experimental work on the coaxial autoaccelerator is presented. The theoretical investigation of instabilities in the autoaccelerator is divided into two areas: resonant and nonresonant interactions. The coaxial autoaccelerator is found to be stable against resonant instabilities such as the longitudinal bunching mode and transverse beam breakup mode because it does not behave as an efficient slow wave structure. From the large class of nonresonant instabilities, the klystron instability has been examined in detail. A stability criterion has been obtained which indicates stability for the projected operating parameters in the experiment. A long pulse (800 ns risetime) beam generator is described capable of producing a ramp charging beam pulse of 1.5 MV peak voltage and 50 KA peak current. The beam generator is equipped with a self break oil switch capable of reducing the peak beam current by a factor of four in less than 5 ns. Experiments on the generation and propagation of beams with peak voltages and currents of 1.1 MV and 35 KA are discussed. Initial experimental results on one-cavity beam autoacceleration, in agreement with theoretical predictions, will be presented. Operation of a six cavity system is anticipated in the near future.

I. INTRODUCTION

The autoacceleration of intense, low v/γ relativistic electron beams is a collective acceleration method whereby the leading portion of the beam stores part of its energy in magnetic fields, inside cavity structures, and the trailing part of the beam is driven inductively by the

collapsing of the stored magnetic fields[1-4]. This method utilizes the well established technology of producing intense relativistic electron beams with particle energies less than 10 MeV in order to generate intense electron beams with particle energies in the multi-10 MeV range, an energy range associated with complex physics, engineering and financial problems. Early attempts to realize this concept followed two approaches. The first approach was that of the coaxial cavity with a beam pulse of constant current[1,3,5,6]. In these experiments the phenomenon of autoacceleration was successfully demonstrated in agreement with the scaling laws for the case of a one cavity device. For a flat current beam profile, however, the scaling laws do not lead to a practical device with many cavities, because of severe successive shortening for both the cavities and the accelerated beam. The second approach was that of an iris loaded cylindrical waveguide driven by a long ramp current pulse[4]. This approach failed because of the resonant-traveling wave instabilities inherent in the geometry of the iris loaded waveguide[7]. The successes and failures of these two approaches have led to the synthesis of an autoaccelerator system[8,9] that is both stable and scalable as will be presented in the following sections.

II. THE AUTOACCELERATOR

The essential features of the autoaccelerator geometry are shown in Fig. 1. A foilless diode produces a thin hollow beam of radial width δ. The beam is guided by a uniform magnetic field $B_o \geq 15$ KG and flows axially at a radius r_b near the wall of the drift tube r_d, such that $\delta \ll r_b < r_d$. In order for the beam to flow freely in the drift tube, it is required[10] that $\omega_{ce}/\omega_{pe} \gg 1$, where ω_{ce} and ω_{pe} are the beam electron cyclotron and plasma frequencies, respectively. The drift tube is surrounded by N coaxial cavities each of length ℓ_c and outer radius r_c. Gaps of length, $\ell_g \ll \ell_c$, connect the cavities to the drift tube. The coaxial cavities support principally the TEM mode[5] with a transit time τ_c,

inductance per unit length L_c and characteristic impedance Z_c given by[8]

$$\tau_c = 2\ell_c/c \; ; \; L_c = (\mu_o/2\pi) \; \ell n \; (r_c/r_d) \qquad (1)$$

$$Z_c = cL_c = 60 \; \ell n \; (r_c/r_d) \; , \text{ ohms} \qquad (2)$$

where c is the velocity of light and μ_o is the vacuum magnetic permeability, all in MKS units.

The time profile for the current and the voltage of the beam produced by the diode are shown in Fig. 1. The current rises, nearly linearly, from zero to its maximum value I_c in a time T which is the charging portion of the cycle. At time T the diode is suitably switched, within a time $\tau_s < \tau_c$, the beam current drops from I_c to $I_b < I_c$ and the auto-acceleration cycle is initiated. The voltage of the charging beam at the diode output V_{INJ} rises from about 100 KV to the maximum charging voltage of 1.5 MV. During the beam rise time an inductive voltage ΔV

$$\Delta V = \ell_c L_c \, dI/dt = 1/2 \; (\tau_c/T) \; I_c Z_c \qquad (3)$$

exists across each gap decelerating the charging beam. At the time the current reaches the value of I_c, the magnetic energy stored in each cavity is

$$W_m = L_c I_c^2/2 \qquad (4)$$

Next the diode beam current is switched and drops to I_b in a time shorter than τ_c, which causes the magnetic energy stored in the drift tube to collapse back into the drift tube and an accelerating voltage appears at the gap

$$V_g = (I_c - I_b) \; Z_c \; . \qquad (5)$$

The total voltage due to the N cavities will be in series and the duration of the accelerating voltage at each gap will be τ_c. For typical experi-

mental parameters of ℓ_c = 1m, Z_c = 80 Ω, N = 10, I_c = 50 KA, I_b = 10 KA, the accelerated beam will have 32 MeV energy and 7 x 10^{-9} sec beam duration.

III. STABILITY THEORY

The stability of electron and ion beams accelerated in periodic linear structures to high energies is a very important design constraint particularly when a high current is desired as well[7]. The instabilities that occur in the beam flow in these periodic structures have been traditionally divided into two types of interactions[11]: (i) the non-resonant interactions[12], such as virtual cathode phenomena[10] and instabilities[13], klystron instabilities[12,14], resistive wall and inductive wall instabilities; (ii) the resonant interactions, such as the traveling wave type longitudinal bunching mode[11] (TM_{01} mode) and transverse beam breakup mode[11] (TM_{11} mode).

The resonant instabilities have been examined by means of a coupling of modes method[11]. That is the dispersion characteristics of the linear periodic accelerating structure are established in the absence of the beam. Next, the beam dispersion characteristics are established for a uniform cylindrical pipe in the absence of the periodic accelerating elements. Then the intersection of the two uncoupled dispersion characteristics yields the real frequency and wavelength for the resonant interaction. The growth rate or e-folding length of the instability can also be obtained by reconsidering the coupled system in the neighborhood of the coupling resonance.

Figure 2 shows dispersion diagrams and resonance intersections for the longitudinal bunching mode for two cases. The first case, lower nearly horizontal curve, is the fundamental spatial harmonic for the iris loaded waveguide structure of Ref. 4. The slow wave branch of the longitudinal bunching mode (0.98) intersects the iris structure dispersion

relation at $\omega = \omega_r = 5.1 \times 10^9$ and $k_r = 17$ radius/m which is in excellent agreement with the experimentally observed instability. The e-folding length for this instability has been found in Refs. 7 and 15 by solving the problem again near the resonance condition and by taking into account the coupling. The dispersion characteristics of the coaxial autoaccelerator are shown in the upper curve of Fig. 2 where there is shown the first, tenth, twentieth, and thirtieth spatial harmonics. It is apparent from this diagram that the coaxial structure is not an efficient slow wave generator, in the sense that the first slow wave for the TM_{01} type mode occurs after the sixteenth spatial harmonic. The beam negative energy slow wave branch appropriate for the longitudinal bunching instability (0.83) intersects the nineteenth, twentieth and higher spatial harmonics of the periodic structure. In order for these harmonics to satisfy boundary conditions on the structure, they must excite the fundamental and lower spatial harmonics at much higher levels than their own, hence they decay even when driven by the beam.

Figure 3 shows dispersion diagrams and resonance intersections for the transverse beam breakup mode (TM_{11} mode) for the same two cases as in Fig. 2, but only for thin pencil beams on axis. The thin hollow beam near the drift tube wall will not be subject to this instability mode because of mode geometrical effects. The resonant intersection for the thin pencil beam in the iris loaded waveguide experiment of Ref. 4 is shown with a large dot in the lower left hand corner of the figure. This instability was measured experimentally in Ref. 4 and the growth rate was obtained analytically in Ref. 7. On the other hand, for a thin pencil beam in the coaxial autoaccelerator, the resonant intersection occurs at very high spatial harmonics ($n \geq 30$) which should severely limit the growth and any adverse breakup effects of the instability (see dotted line on upper right hand side of figure).

In conclusion it can be said that for the case of the iris loaded cylindrical waveguide system, which behaves as an efficient slow wave structure, we find that the beam negative energy slow waves couple to the autoaccelerator fundamental modes and instability results in agreement with existing experimental results and other theoretical predictions. For the case of the coaxial cavity autoaccelerator, which does not behave as a slow wave structure, we find that the beam negative energy slow waves only couple to very high spatial harmonics of the autoaccelerator structure propagating modes, thereby leading to stability against the resonant-traveling wave instabilities in this case.

From the large class of nonresonant instabilities the klystron instability has been examined in detail[12]. The geometry of the coaxial autoaccelerator resembles the geometry of a multicavity klystron[14]. The multicavity klystron is an amplifier where a signal impressed on the beam as a velocity modulation, at the gap of the first cavity, is amplified many-fold through current bunching and strong coupling to subsequent cavities. In this work stability criteria have been derived so that the coaxial autoaccelerator can be designed to operate in a parameter range where the klystron instability is suppressed. The high frequency, $\omega > \omega_{pe}$, form of the stability criterion is given by

$$\frac{\omega_c}{\omega_{pe}} \frac{Z_c}{2Z_D} < 1 \qquad (6)$$

where ω_c and Z_c are the coaxial cavity characteristic frequency and impedance respectively and Z_D is the effective local diode impedance for the beam. A preliminary experiment that illuminates the klystron instability has been performed[12] and the results are shown in Fig. 4. In this experiment the drift tube is surrounded by four coaxial cavities. The

length of each cavity was shortened from about one meter, typical of autoaccelerator cavities, to 15 cm. As a result, the cavity resonant frequency now is much higher, f_c= 500 MHz as compared to the autoaccelerator cavities where it is f_c= 75 MHz. The diode voltage is shown in Fig. 4a. Figure 4b shows the probe current measured in a magnetic loop inside the fourth cavity. This figure shows a large amplitude signal of frequency f = 500 MHz, equal to the fundamental resonant frequency of the cavities. When the beam current reaches approximately 4 KA, then the beam plasma frequency $f_{pe} \approx f_c$ and the klystron oscillation reduces substantially to low level noise amplitude and remains so for the remainder of the beam pulse, where $f_{pe} > f_c$. The ratio of the characteristic impedance of the cavity, $Z_c \approx 80$ ohms, to the effective local diode impedance of the beam, $Z_D \approx 50$ ohms, is $Z_c/2Z_D \approx 0.8$. Applying these values to Eq. 6, it is concluded that for $f_c > f_{pe}$, the klystron oscillations should be suppressed as is apparent from Fig. 4b. For the autoaccelerator experiment, f_c is much smaller and the beam plasma frequency is generally much higher so that the range where the klystron instability is active is limited to a very small portion of the very early, low current, part of the beam.

In conclusion, it must be pointed out that although the coaxial autoaccelerator is stable to the instabilities considered above, there may be other instabilities that the experiments may confront us with in the near future, as often happens when a new parameter regime is obtained experimentally.

IV. THE PULSE GENERATOR AND EXPERIMENTAL SETUP

The E-beam generator consists of a 75 KJ LC generator, a 30 Ω transmission line and an oil switch capable of reducing the voltage by a factor of 4 in 5 ns. A schematic diagram is shown in Fig. 5. This generator is capable of driving a 30 Ω load to a peak voltage and current of 1.5 MV and 50 KA, respectively, with a 1/2 cycle risetime of 800 ns.

Presently the machine is operated at 900 KV and 30 KA as shown in Fig. 6. In normal operation the self break oil switch is set to fire from 600 to 800 ns into the beam pulse. From the fall time and the transmission line impedance, the switch inductance is found to be less than 40 nh.

The pulse generator drives a foiless diode whose impedance is nominally 30 ohms. The foiless diode generates an annular beam propagating approximately 2mm inside a stainless steel drift tube (I.D. = 4.76 cm). The drift tube is surrounded by many coaxial cavities and opens to each one by means of an azimuthal slit. The cavity and drift regions are in a uniform axial magnetic field of 15 KG.

V. CAVITY RESULTS

Preliminary autoacceleration experiments have been performed using a single 70 Ω cavity. Diagnostics include: (a) a magnetic probe at the shorted end of the cavity, (b) an electrostatic probe near the gap, (c) a photodiode X-ray detector looking at the drift tube downstream from the gap.

Figure 7 shows magnetic and electric probe signals for a typical shot. The magnetic probe signal is shown on two time scales to accentuate the principal features of the cavity behavior. In the lower magnetic probe trace, the current rises nearly linearly for over 400 ns. At this time the current drops rapidly and oscillates about a value equal to 1/4 of the peak current. The upper magnetic probe trace shows details of the current drop on an expanded timescale. The 5 ns fall time and the damped oscillation are both clearly visible. The behavior of the cavity after a time τ_c = 6 ns is inconsequential to the beam autoacceleration. It is used only as an indication that the cavity is operating as transmission line theory predicts. It can be shown that for $I_c/I_b \neq 2$, the cavity will oscillate with a period of 2 τ_c. Because of cavity losses, the oscillation will be damped out with the current in the cavity asymp-

totically approaching I_b. This is the observed behavior as shown by the magnetic probe trace in Fig. 7. On the other hand the beam current in the drift tube does not oscillate and after the current drop has the value I_b as measured in the drift tube. The electrostatic probe trace for the same shot is also shown on a timescale of 10 ns/div. The temporal behavior of this probe agrees very well with the magnetic probe. In addition, this probe provides direct qualitative evidence of the electric field at the gap of the cavity. The oscillations of both probes indicate that the gap is not shorting during or after the current drop.

Figure 8 is an X-ray signal trace showing a large increase of X-ray intensity coincident with the current drop and resulting from auto-acceleration. The X-ray detector consists of a photodiode, optically coupled to a plastic scintillator. The detector is oriented to look at a carbon target downstream from the davity gap. The X-ray oscillograph of Fig. 8 shows the signal amplitude rising slowly with the voltage and current of the charging beam. When the beam current is switched and falls there is a significant increase in signal amplitude, lasting a very short time, and indicating a large increase in the electron energy. Several experiments have been performed to verify that the abrupt increase in X-ray intensity is due to the acceleration from the cavity. First, when only a drift tube is used we do not observe an increase in the X-ray signal amplitude during the current fall. Second, if the current fall time (as indicated by the cavity magnetic probe) is longer than 5 ns, the X-ray burst is not seen. Third, unless the diode impedance is less than 35 ohms at the time of the current drop, no increase in the X-ray signal is seen.

The absence of any X-ray bursts for diode impedances greater than 35 ohms, at the time of current drop, can be explained as follows. From

theory, the accelerating voltage across the gap is given by

$$V_g = (I_c - I_b(t))Z_c \tag{7}$$

This equation is valid for a bounce time, ($\tau_c \simeq 6$ ns), i.e., the time for a pulse to propagate to the shorted end of the cavity and back to the gap. The total energy of the accelerated beam will be

$$W_g = q\, I_c\, [Z_c + \alpha(t)\ (Z_D - Z_c)] \tag{8}$$

where Z_D is the diode impedance and $\alpha(t) = I_b(t)/I_c$. We assume that the bremsstrahlung X-ray intensity varies[16] as, ($I\, W^{2.8}$). The ratio I_x of X-ray intensity during current drop to the X-ray intensity at maximum charging current is given by

$$I_x = \frac{I_b(t) W_g^{2.8}}{I_c (q I_c Z_c)^{2.8}} = \alpha(t) \left[1 - \alpha(t) \left(1 - \frac{Z_D}{Z_c}\right)\right]^{2.8} \tag{9}$$

In the experiment discussed here, α goes from 1 to 1/4 in 5 ns, Z_c is fixed at 70 ohms, thus leaving Z_D as the only variable. If Z_D is 35 ohms, the X-ray intensity will increase only by a factor of 1.2, a figure scarcely above noise level in this experiment. In order to obtain a factor of two increase in X-ray intensity, Eq. (9) requires that Z_D = 28 ohms. The experimental situation of Fig. 8 is for a diode impedance Z_D = 25 ohms at the time of current drop. Note that the above analysis assumes that all of the beam electrons are accelerated by the full cavity voltage. This is obviously an idealized case and any departure from this will necessitate an even lower diode impedance for the same I_x. Additional simplifications in the above analysis include the neglect of the attenuation of the X-rays by the drift tube walls and the change in X-ray spectrum as the electron energy increases. For a

measured peak charging current of 30 KA and from Eq. (8), the total electron energy after autoacceleration is found to be $W_g \approx 1.8$ MeV.

Recently a Faraday Cup has been added to the beam diagnostics. A thick carbon target with a 0.51 mm radial slit is placed downstream of the cavity gap. The beam current transmitted through this slit is then attenuated with a 1.5 mm thick carbon sheet and collected on a brass plate. A typical Faracay Cup signal shows a sharp increase in the collected current during the current fall in the drift tube. For a shot with I_c = 22 KA, the peak Faraday Cup current is 10 amperes. Using the given slit size results in a total attenuated current of 2.5 KA. This is a measure of the minimum beam current since it does not include the attenuation by the carbon sheet. Using Eq. (8) gives a total energy of 1.4 MEV for the accelerated electrons. The range for 1.4 MeV electrons in carbon is ~3 mm giving an inferred total accelerated electron current of 5.2 KA. This is in close agreement with the value of I_b = 5.5 KA obtained from other measurements.

The X-ray and Faraday Cup measurements produce signals that are a combination of beam current and electron energy. At current fall, $t = t_o$, the current decreases from peak charging current I_c to beam current I_b in 5 ns, while the accelerating autoacceleration potential increases from zero to $V_g = (I_c - I_b(t))Z_c$, over a time span $t_o < t < 6$ ns. The fact that both X-ray and Faraday Cup signals increase, during the time span t_o t<6<ns, as the beam current falls, proves conclusively that the electron energy is increasing. After this time span the beam energy rapidly falls to a lower level, as clearly seen in the X-ray and Faraday Cup signals. In conclusion, the experimental results, using a single cavity, are in close agreement with theory. Electric and magnetic probe signals show that the cavity gap is not breaking down during the acceleration phase. Both X-ray and Faraday Cup measurements show

that the autoaccelerator is operating as simple theory predicts. Preliminary data interpretations show that peak electron energies in excess of 1.8 MeV have been observed. Future experiments are scheduled to study higher autoaccelerating potentials and more cavities with more sophisticated diagnostics.

REFERENCES

1. L.N. Kazanskii, A.V. Kisletsov and A.N. Lebedev, At. Energ. 30, 27 (1971).

2. A.A. Kolomensky, Part. Accel. 5, 73 (1973).

3. M. Friedman, Phys. Rev. Lett. 31, 1107 (1973).

4. R.J. Briggs, T.J. Fessenden and V.K. Neil, in Proc. of Ninth Int. Conf. on High Energy Accel., 278 (1974).

5. J. Siambis, Phys. Fluids, 19, 1784 (1976).

6. I.A. Grishaev, A.N. Dedik, V.V. Zakutin, I.I. Magda, Yu V. Tkach and A.M. Shendorovich, Sov. Phys. - Tech. Phys. 19, 1087 (1975).

7. V.K. Neil and R.K. Cooper, Part. Accel. 1, 111 (1970).

8. J.K. Burton, D. Conte, M. Friedman, T. O'Connell and J. Shipman, IEEE Trans Nuclear Scien. NS-24, 1628 (1977).

9. U.A. Bashmakov, K.A. Belovintsev, E.G. Bessenov, Ya. A. Vazdik, S.M. Nikolaev and P.A. Cherenkov, Sov. Phys. - Tech. Phys. 18, 696 (1973).

10. M.E. Read and J.A. Nation, J. Plasma Physics 13, 127 (1975).

11. J. Siambis, to be published.

12. J. Siambis and M. Friedman, to be published.

13. M. Friedman, J. Siambis and D.P. Bacon, J. of Appl. Phys. Lett. 28, 308 (1976).

14. C.K. Birdsall and W.B. Bridges, "Electron Dynamics of Diode Regions" (Academic Press, New York, 1966), Chapter 4.

15. V.G. Gapanovich and A.N. Lebedev, Sov. Phys. - Tech. Phys. 20, 532 (1976).

16. H.W. Koch and J.W. Motz, Rev. Modern Phys. 31, 920 (1959).

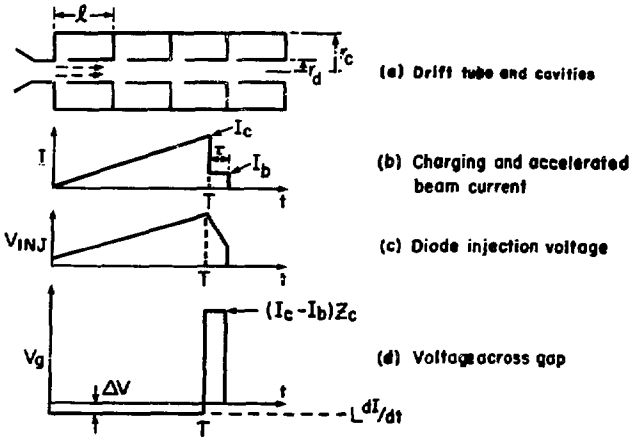

Fig. 1. Schematic of experimental configuration.

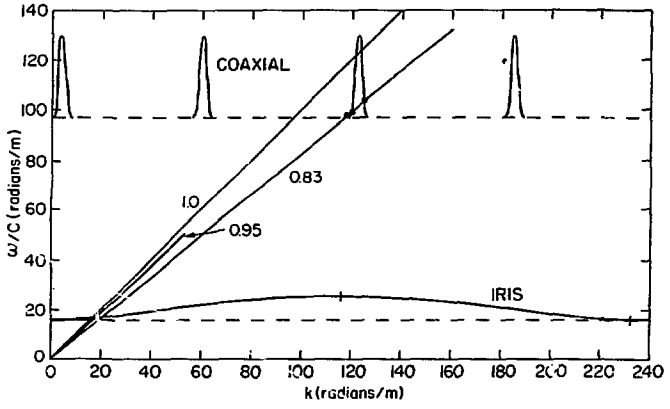

Fig. 2. Traveling wave longitudinal bunching mode.

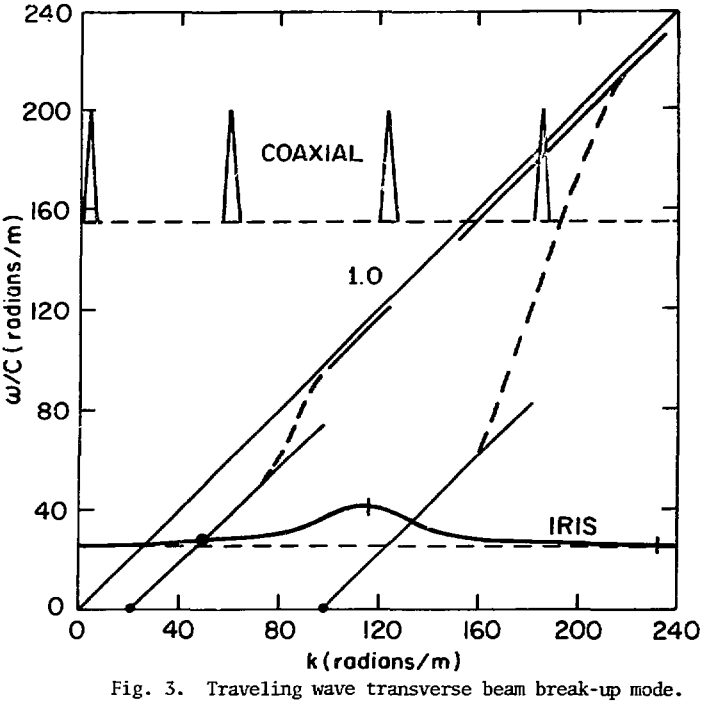

Fig. 3. Traveling wave transverse beam break-up mode.

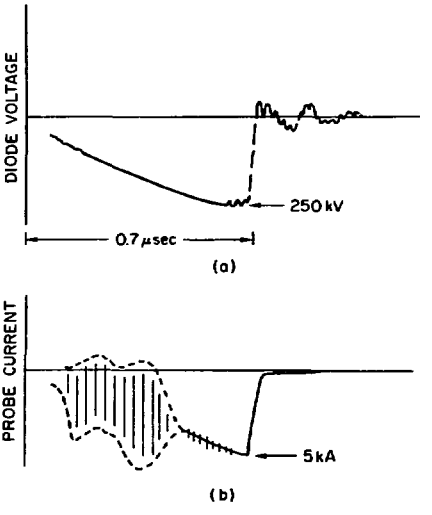

Fig. 4. Observation and stabilization of klystron instability.

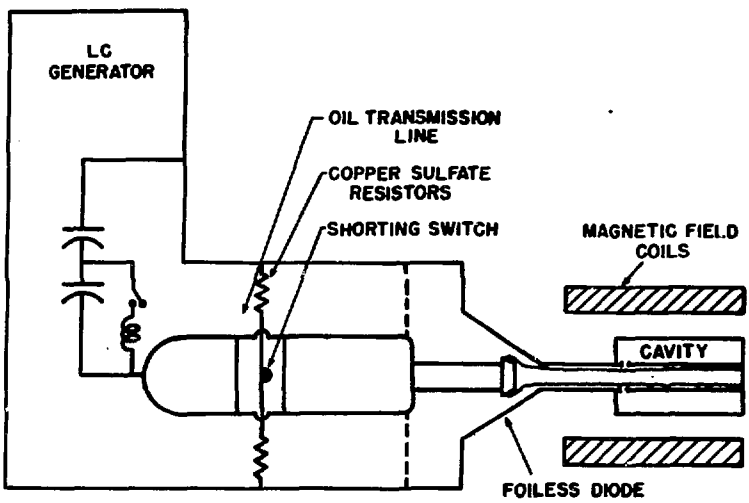

Fig. 5. Schematic of diode pulsed power supply.

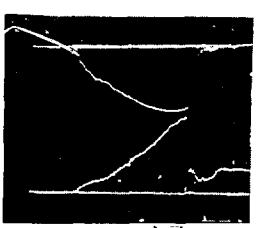

Fig. 6 Diode voltage and drift tube current.

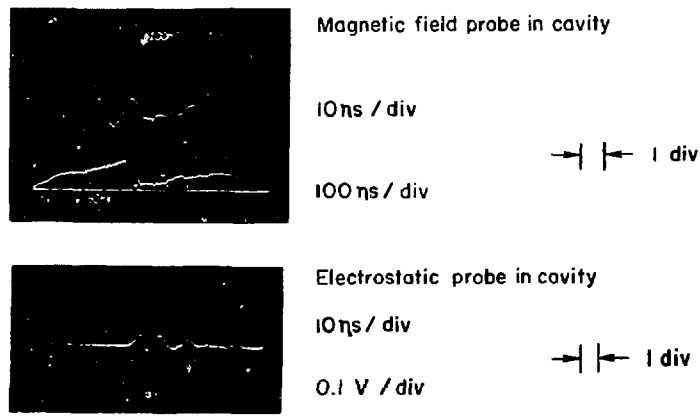

Fig. 7 Integrated magnetic and electrostatic probe signals in the cavity. The magnetic probe is located at the shorted end of the cavity and the electric probe is located 10.5 cm from the accelerating gap.

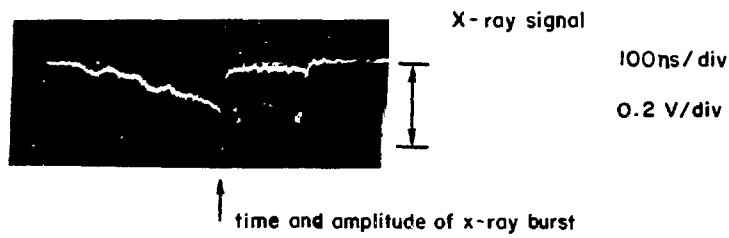

Fig. 8 X-ray detector signal for autoaccelerated beam. Note the narrow pulse in the center of the trace. This is coincident with the beam current drop.

BEAM TRAPPING EXPERIMENTS ON THE UNIVERSITY OF MARYLAND ELECTRON RING ACCELERATOR

R. A. Meger, D. W. Hudgings, and M. J. Rhee
Electrical Engineering Department
University of Maryland, College Park, Maryland 20742

Abstract

The University of Maryland Electron Ring Accelerator experiment involves a collective ion acceleration scheme in which a cusp injected hollow rotating electron beam is used for the acceleration of ions. Essential to this scheme is the slowing and trapping of a nonneutral electron ring in some form of a magnetic mirror system. As a first step in this direction, preliminary experimental results on the interaction of nonneutral E-layer beams with static magnetic mirrors are reported. Also, results from initial experiments on the interaction of E-layer beams and a background neutral gas to be used in ring trapping and ion loading are presented. Detection of a small number of ions in the ERA chamber using cellulose nitrate films is also reported.

1. Introduction

The Electron Ring Accelerator (ERA) concept[1] is a collective ion acceleration technique currently under investigation at Dubna, Garching, and the University of Maryland.[2,3] This technique involves use of the space charge of a nonneutral electron ring to trap and hold ions while the ring is accelerated in a diverging magnetic field. The University of

Maryland ERA differs from other approaches by beginning with a hollow relativistic electron beam injected through a magnetic cusp, forming a rotating electron layer or E-layer. Past experiments have shown such E-layers to propagate with axial velocities of $v_z \sim 0.3c$ and to contain up to 10^{14} electrons. Recent experiments have emphasized the slowing and trapping of such E-layers to form an electron ring similar to those formed in other ERA experiments.

The work reported here involves the use of static magnetic mirrors. To trap a nonneutral E-layer, a static system requires the use of a double mirror configuration where the E-layer is permitted to cross the first mirror but is reflected by the second. While the E-layer is between the two mirrors, a fraction of its axial velocity must be removed to prevent its escape over the first mirror. To provide this loss, two methods are presently under investigation: first, the use of a neutral background gas density in a manner similar to that used for trapping fully neutralized rings,[4] and second, use of resistive boundary layers.[5]

Present results include observations of E-layer reflections off single and double magnetic mirror systems and their interaction with a neutral background gas.

In addition to the experiments with E-layers, some early results on the application of low energy ion diagnostics to the ERA system will be described.

2. Experimental Apparatus

The ERA electron beam accelerator is comprised of a 30 kJ Marx generator with a maximum 1.2 MV output voltage

which feeds a water Blumlein and a tapered oil transmission line. The output pulse is nominally twice the Marx generator output voltage with ~30 nsec full width pulse into a field emission vacuum diode as shown in Fig. 1. The 6 cm radius knife edge cathode produces a hollow electron beam in the nominally 7.5 cm anode-cathode gap. A set of "pancake" magnetic field coils surrounding the diode vacuum vessel provide an axial field of up to 3 kGauss in the diode region. An iron plate located downstream of the slotted brass anode separates the diode field region from the oppositely directed two meter long downstream magnetic field region which is produced by another set of 18 "pancake" field coils. Two additional coils located on either side of the iron plate serve to sharpen the cusp field from a ±90% width of ~12 cm to less than 2.5 cm at the beam radius[6] as well as offsetting some of the coherent particle off-centering caused by the nonideal cusp.[7]

The annular electron beam passes through a thin metal foil behind the anode plate just before entering the cusp region. This foil provides a spread in canonical angular momentum for the beam particles sufficient to stabilize the negative mass instability[8] as well as to lengthen the beam axially in the post cusp region. The beam then passes through the iron cusp section where the strong radial magnetic field converts most of the axial electron velocity into azimuthal velocity. The rotating E-layer then passes through an axial current monitor and enters an 11-inch i.d. lucite vacuum chamber shown in Figs. 1 and 2. This two meter long

copper mesh lined chamber is immersed in the downstream solenoidal magnetic field. Various image current wall structures, both interior and exterior to the E-layer radius, can be inserted within the vacuum chamber to facilitate boundary condition studies.

Two 10 cm radius mirror coils are located between the image current wall structure and the vacuum chamber wall. These battery powered coils provide up to 300 Gauss peak mirror field superimposed on the nominally 1500 Gauss solenoidal field. Both the relative heights and the peak field strengths of the mirrors are adjustable. For the experiments reported here, these coils are located 50 and 100 cm downstream from the cusp.

Beside the axial current monitor just downstream of the cusp, single turn passively integrated dB/dt probes are located at intervals along the tank axis, and small charge collectors and a Cherenkov radiating lucite plate are sometimes placed at various axial positions in the tank. All signal leads are fed through the downstream flange. To detect ions, strips of cellulose nitrate film (Kodak Film LR115, type II) are placed in the downstream region. These films are not sensitive to electrons but show tracks of low energy (<200 keV) protons when etched in a NaOH solution. Thin aluminum foils placed over the films allow for discrimination between energy ranges.

3. Experimental Results

Experiments to date have involved the interaction of E-layers with single and double magnetic mirror systems, and

a background neutral gas, both with and without the mirrors, as well as use of cellulose nitrate films for ion detection.

(a) Magnetic Mirror Experiments.

Recent experiments have emphasized the interaction of E-layers with magnetic mirrors. Beam and system parameters used in these experiments include: electron energy ~2.3 MeV, post cusp current <1 kAmp with ~5 nsec FWHM, and axial magnetic fields of ±1500 Gauss. A conducting boundary wall was located at 7.5 cm radius in all these shots.

In this experiment, E-layers were injected into combinations of one or two mirrors with varying peak mirror strengths superimposed on the 1500 Gauss solenoidal field. The E-layers were observed to reflect off the magnetic mirrors with the amount of the reflected E-layer depending on the beam energy and the strengths of the mirror field. For peak mirror fields of up to 300 Gauss, approximately half of the injected E-layer was reflected back toward the cusp. The mirror fields produced no observable instabilities, either in the vicinity of the mirror or in the reflected E-layer. The beam radius was observed to shrink at a rate consistent with flux conservation in the vicinity of the mirror and to regain its initial radius downstream of the mirror. The fraction of the E-layer transmitted through the mirror decreases with increasing mirror field. Use of two mirrors with the upstream mirror set at a fraction of the downstream mirror strength compounds the reflection: the first mirror appears to reflect the very low axial velocity electron component in the tail of the E-layer, while the second, stronger

mirror appears to reflect a higher axial velocity component. When no energy loss mechanism exists between the mirrors, the reflected beam crosses the upstream mirror with no apparent second reflection.

The effect of the magnetic mirrors is illustrated in Fig. 3. The six oscillograph tracings show the magnetic self-field signals from a pickup loop located 65 cm downstream from the cusp, roughly at the magnetic mirror field minimum. The peak mirror fieldstrengths are as shown to the right of each trace with the left-hand shots having downstream fields of B2 ~ 180 Gauss and the right-hand shots having B2 ~ 300 Gauss. The top traces in each column show the E-layer self-field as a function of time. The traces show ~2 nsec signal risetime to a peak signal of ~15 Gauss followed by a 20 nsec decay. Such signals are typical of shots with 0.5 mil Ti foil in the anode plane. The middle traces in each case show the effect of turning on the second mirror coil located 35 cm downstream of the probe. The signal shows a similar rise and decay time with a second hump appearing 10-20 nsec after the first. This corresponds to the reflected beam superimposed on the incoming beam tail. No apparent detrimental interaction takes place between the two beam components. The bottom traces show the case with the smaller upstream mirror turned on along with the large mirror downstream. Here one sees the hollowing out effect due to reflection of the lower axial velocity component in the E-layer's tail by the first mirror, resulting in greater discrimination between the incident and reflected pulses. No

further reflection of the reflected E-layer off the upstream mirror is observed.

(b) Neutral Background Gas Experiments.

Another experiment that has produced some preliminary results involves the use of a static background gas density in the downstream region. The neutral gas density should provide an energy loss mechanism for the E-layer, possibly leading to some trapping in the double mirror system. The downstream gas density, as supplied by a needle valve in the downstream flange, was limited to ≤100 mTorr nitrogen and somewhat less hydrogen pressures due to leaks through the cusp into the vacuum diode region. For 100 mTorr nitrogen, the head of the beam should be only partially neutralized due to the ~2 nsec beam risetime, thereby minimizing plasma effects. In contrast, the tail of the distribution should be fully neutralized due to its lower fast electron density and the relatively long plasma diffusion and recombination times. The largest effect should appear after reflection, where the head of the beam passes through the plasma distribution it produced on the first pass.

A series of shots were fired with similar beam parameters as in the previous mirror experiment. The magnetic self-field probe measurements made with hydrogen and nitrogen in the pressure range below 100 mTorr showed no apparent effect either with or without the mirror system turned on. In addition, no trapping was observed with the double mirror system and the neutral gas present. The only observed changes appeared on the axial current monitor when both

downstream mirrors were turned on. Figure 4 shows a set of oscillographs from the axial current monitor. All of these shots were taken with ~280 Gauss on the downstream mirror and ~80 Gauss on the upstream mirror. The top trace is typical of shots without a neutral gas background, while the others show the changes introduced by raising the background nitrogen density. The negative spike is the injected beam pulse which is nominally 700 amps and has a <5 nsec width. The positive bump on the 0 mTorr shot is the reflected beam current from both mirrors downstream of the current monitor. With 15 mTorr nitrogen in the tank, the bump appears to divide into discrete signals, and by 38 mTorr the effect is clearly visible. The first positive bump [labeled (a) on the 38 mTorr shot] can be identified as the reflected beam from the smaller upstream mirror, while the second [labeled (b)] is associated with the larger downstream mirror. If the background density is further increased, the first reflected signal is replaced by an overshoot of the trailing edge of the main beam pulse as shown in the 56 mTorr shot. By 100 mTorr, the overshoot [labeled (c)] becomes very pronounced with the first reflected signal no longer clearly defined.

The absence of any observable effects on the magnetic self-field signals due to the gas coupled with the increasing effect on the axial current signal suggests that the neutral gas density is still too low. Raising the gas density beyond the present 100 mTorr limit may yield some interesting results. Such experiments are planned.

(c) Ion Detection Experiments.

The final experimental result deals with the detection of a low energy ion component within the E-layer post cusp beam channel under a variety of machine conditions. Cellulose nitrate films indicate ~10^8 protons/shot reaching the downstream region. These ions showed a cusp field dependence with higher fluxes resulting from lower fields. Use of thin aluminum energy absorbers showed a distribution of ion energies ranging up to the beam energy (2.3 MeV). Early indications are that the ions originate in the diode and do not represent a collective acceleration process. Further work aimed at better measurement of the ion energies and determination of the acceleration process is scheduled for the near future.

4. Discussion

The experimental results reported in this paper are the first efforts to control nonneutral E-layers in the University of Maryland ERA experiment. The results show that use of static magnetic mirrors to reflect E-layers is straightforward. The principal problem arises when trapping of such E-layers is attempted. Thus far, the use of a low density neutral gas has not succeeded in providing sufficient energy loss to result in trapping. Future experiments using higher density static backgrounds or use of puff valves to provide a localized high density region within the mirror well are planned. A second energy loss mechanism using resistive boundaries rather than metal walls offers some advantages over the neutral gas method. Experiments with such resistive

walls are planned.

Acknowledgements

The authors would like to thank C. D. Striffler and M. Reiser as well as the other members of the ERA group for useful discussions, suggestions, and support.

This work was supported by a grant from the National Science Foundation.

References

1. M. Reiser, IEEE Trans. NS-20, 310 (1973).
2. W. W. Destler, et al., IEEE Trans. NS-24, 1642 (1977).
3. C. D. Striffler, R. R. Kulkarni, and T. F. Wang, Proc. of the 2nd Int. Topical Conf. on High Power Electrons and Ion Beam Research and Technology, Oct. 1977.
4. R. E. Kribel, et al., Plasma Phys. 16, 113 (1974).
5. P. Merkel, Part. Accel. 8, 21 (1977).
6. H. Kim, et al., Bull. Am. Phys. Soc. 21, 1129 (1976).
7. M. J. Rhee, W. W. Destler, Phys. Fluids 17, 1574 (1974).
8. W. W. Destler, et al., J. Appl. Phys. 48, 3291 (1977).

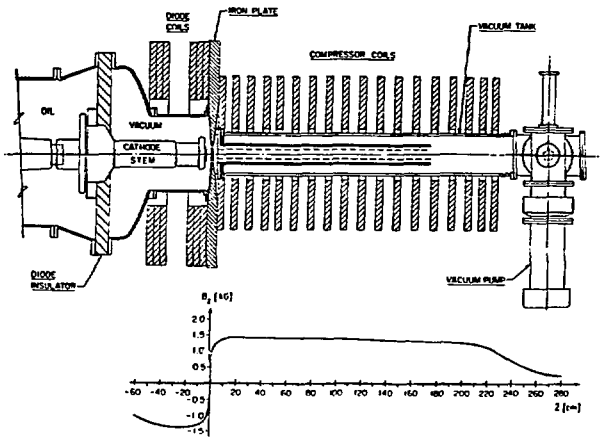

Fig. 1. University of Maryland Electron Ring Accelerator.

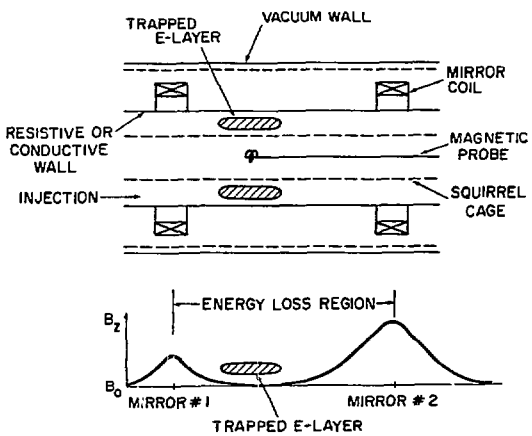

Fig. 2. Top: Schematic of the ERA experimental region showing the mirror coils and wall structures. Bottom: Typical double mirror magnetic field superimposed on the downstream solenoidal field, B_o.

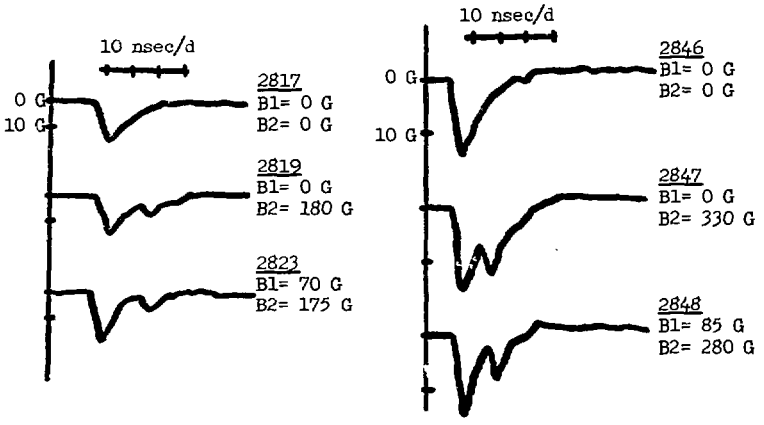

Fig. 3. Tracings of oscillographs from an axial integrated dB/dt probe located between two magnetic mirrors. All shots had similar injected currents. Peak mirror fields (upstream B1, downstream B2) are listed to the right of each trace.

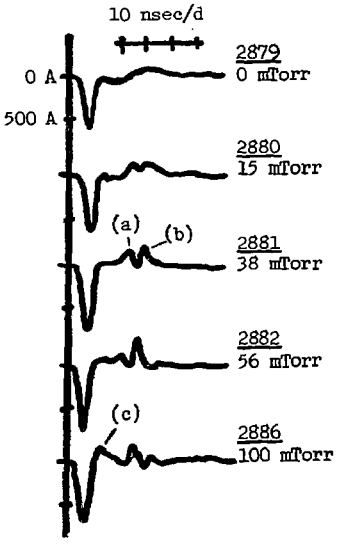

Fig. 4. Axial current traces just downstream of the diode. Neutral background nitrogen pressures are listed to the right of each trace.

Dur

ION ACCELERATION IN A MOVING VIRTUAL CATHODE

R. B. Miller*

Air Force Weapons Laboratory, Kirtland AFB, New Mexico 87117

ABSTRACT

When an intense electron beam is injected into an evacuated drift cavity placed in a strong longitudinal magnetic field, a virtual cathode will form if the beam current exceeds the space charge limiting current. If the drift tube is flared, the virtual cathode can form a substantial distance downstream from the injection plane, and will propagate backward toward the injector, depending upon the time dependent diode voltage and current waveforms. In a recent series of experiments a small amount of neutral gas was introduced into the drift tube and acceleration of gas ions was observed to occur, also in a direction backward toward the injection plane. The acceleration occurs over a very narrow pressure range ($2\text{-}8 \times 10^{-4}$ Torr for H_2 and D_2), and can be entirely suppressed by reducing the magnetic field strength. Using a 2 MeV, 20 kA electron beam nuclear activation of thin (1 mil) anode foils has been observed for a number of different reactions, including $C^{12}(d,n)N^{13}$ and $Cu^{63}(d, 2n)Zn^{63}$ for deuterons, and $Ti^{47}(p,n)V^{47}$ and $Cu^{63}(p,n)Zn^{63}$ for protons.

INTRODUCTION

A class of collective acceleration schemes has been recently proposed [1,2]. The basic concept in these schemes is the controlled motion of a single deep potential well (a virtual cathode). By way of illustration, consider a solid electron beam of radius r_b and kinetic energy $(\gamma_o - 1)mc^2$ with fractional charge neutralization f_e injected into a long drift tube of radius R. The condition for virtual cathode formation is that the beam current exceed the space charge limiting current, i.e.,

* Present address: Sandia Laboratories, Div. 5244, Albuquerque, NM 87115.

$$I(z,t) \geq I_\ell(z,t) = \frac{[\gamma_o^{2/3}(z,t) - 1]^{3/2} mc^3/e}{1 + 2\ell n[R(z,t)/r_b(z,t)]} \quad [1 - f_e(z,t)]^{-1} \qquad (1)$$

In writing Eq. (1) it has been assumed that slow adiabatic variations in the quantities are allowed so that the argument (z,t) denotes the values of the parameters at the axial position z and at time t.

Several possible acceleration schemes (methods for controlling the motion of a virtual cathode) have received analysis [1], and preliminary 2-d numerical simulation results are available [3]. In this paper, we report the results of experiments designed to produce a traveling virtual cathode by a simple, passive technique. The scheme is illustrated in Fig. 1. An intense electron beam is injected into an evacuated ($f_e = 0$), flared ($R = R(z)$) metallic drift tube. The beam radius is held constant ($r_b = r_o$) by placing the system in a strong longitudinal magnetic field B_o. Under these conditions, Eq. (1) simplifies to

$$I(z,t) \geq I_\ell(z,t) = \frac{[\gamma_o^{2/3}(z,t) - 1]^{3/2} mc^3/e}{1 + 2\ell n[R(z)/r_o]} \qquad (2)$$

For a specified time-dependent diode history, it is possible, from Eq. (2) to determine the appropriate drift tube flare R(z) to effect the desired virtual cathode motion.

EXPERIMENTAL DESCRIPTION

The electron beam source used in these experiments was an Ion Physics FX-25, a 2 MeV, 20 kA machine whose operating characteristics have been described previously [4]. Typical diode voltage and current waveforms are presented in Fig. 2. Using Eq. (2) and assuming that the beam propagates at the speed of light, c, until it reaches the virtual cathode region (beam slowing near the virtual cathode position is ignored) the radius of the waveguide can be determined for the desired virtual cathode motion. The result for a constant acceleration rate of $a = 2 \times 10^{15} m/sec^2$ is shown in Fig. 3, assuming a beam radius of 0.64 cm. From these results

it appears that a simple conical waveguide should produce a constantly accelerating virtual cathode over a significant portion of the electron beam pulse. On this basis three conical waveguides each 100 cm in length were constructed of thin wall stainless steel as indicated by the dashed line in Fig. 3. The radii at the entrance and exit ends of the constant-taper sections were i) 0.75 cm, 1.5 cm; ii) 0.75 cm, 3.0 cm; and iii) 1.5 cm, 3.0 cm.

To maintain a constant beam radius, the system was placed in a uniform longitudinal magnetic field with field strengths up to 8 kG possible.* A Pearson current transformer was used to monitor the pulsed magnetic field discharge. Beam diagnostics included diode voltage and current monitors, B-dot loops and electrostatic probes positioned along the flared drift tube section, and a fast risetime Faraday collector which could be continuously positioned throughout the drift tube region. The beam profile was periodically monitored with thin film dosimetry (blue cellophane) during the course of the experiments.

RESULTS AND DISCUSSION

Representative electrostatic probe signals for the case of the (0.75 cm, 1.5 cm) drift tube with a 1 cm diameter solid beam are presented in Fig. 4. The magnetic field strength was 8 kG. The probe waveforms are markedly different from those obtained in the simple vacuum propagation experiments, with the most obvious difference being the sharp spike followed by a negative signal, presumably due to beam electrons striking the probe [5]. This waveform structure is believed to represent the motion of the virtual cathode past the probe position.

The times at which the virtual cathode is detected at the various probe positions for this geometry are plotted in Fig. 5. Also presented

*Vacuum transport of an intense beam is stable and efficient if the external field strength exceeds the equilibrium and stability criteria [5].

for comparison purposes are a solid line representing uniform motion at the velocity of light and a dashed line representing the virtual cathode motion predicted from Eq. (2). The "theoretical" data were generated by digitizing the appropriate diode voltage and current traces, and substituting into Eq. (2) to obtain the position and time for virtual cathode formation. Equation (2) predicts that the virtual cathode should first form at an axial position of 63 cm from the anode; on the other hand, the experimental data indicate that virtual cathode formation first occurs at a distance greater than 68 cm from the anode. In addition, Eq. (2) predicts much faster virtual cathode motion than was observed. These results indicate that Eq. (2) substantially underestimates the limiting current, in agreement with numerical simulations and more recent theoretical work [3].

The possibility of collectively accelerating ions in this geometry as a result of the "backward" motion of the virtual cathode was investigated by introducing a small amount of neutral gas (hydrogen or deuterium) into the drift tube. (The diode pressure was maintained at ~ 5×10^{-5} Torr.) The thin anode foils were then examined for nuclear activation using a 7.5 cm x 7.5 cm NaI scintillation crystal-photomultiplier tube combination. Nuclide identification and counting were performed with a single channel analyzer. A variety of reactions were observed including $C^{12}(d,n)N^{13}$ (Q = -0.28 MeV) and $Cu^{63}(d,2n)Zn^{63}$ (Q = -6.5 MeV) for deuterons, and $Ti^{47}(p,n)V^{47}$ (Q = -3.7 MeV) and $Cu^{63}(p,n)Zn^{63}$ (Q = -4.2 MeV) for protons. (To observe the carbon reaction a 2.5×10^{-3} cm aluminum anode foil was sprayed with Aero-dag. No activation of the anode foil was observed without the thin carbon coating.)

The pressure dependence of the anode activity for the $C^{12}(d,n)N^{13}$ reaction is presented in Fig. 6. Statistically significant activity was not observed for background fill pressures less than 1×10^{-4} Torr or in

excess of 4 x 10^{-3} Torr. For deuterium, peak activity was observed to occur at 3-5 x 10^{-4} Torr, while for the case of hydrogen, the peak pressure was somewhat higher, ~ 7 x 10^{-4} Torr. All of these results were obtained with the strong magnetic field (8 kG). When the field strength was reduced to zero, no anode activation was observed under any circumstance.

The peak ion energies observed (> 6.5 MeV) exceed the $3(\gamma_o - 1)mc^2$ limit previously obtained using the FX-25 machine in the standard neutral gas configuration [4]. This result is evidence for ion trapping in a moving accelerating field structure, although the details of the acceleration process are not clearly understood. In fact, significant acceleration of positive ions was not expected. The numerical simulation results [3] indicate that the on-axis potential should have the approximate shape indicated in Fig. 7. While the accelerating fields on the anode side of the virtual cathode (in a direction to accelerate positive ions toward the anode) are relatively smaller. Since the motion of the virtual cathode is towards the anode it would appear to be much easier to accelerate negative ions to high energy. Several possible mechanisms for the observed ion acceleration are being considered, and the results of these investigations will be presented at a later date.

SUMMARY

In conclusion, the important results of this work can be summarized as follows: i) a traveling virtual cathode has been experimentally observed; ii) Eq. (2) underestimates the space charge limiting current and is not adequate for describing the virtual cathode motion observed in these experiments; iii) collectively accelerated ions with kinetic energy in excess of $3(\gamma_o - 1)mc^2$ have been observed in this configuration indicating ion trapping in a moving accelerating field structure; and iv)

this configuration would appear to be more appropriate for accelerating negative ions to high kinetic energy.

REFERENCES

1. R. B. Miller, Air Force Weapons Laboratory, Tech. Report No. AFWL-DYS-TN-75-115 (unpublished).
2. R. B. Miller, IEEE Proc. Int'l. Conf. Plasma Science, 130 (March 24-26, 1976).
3. R. B. Miller, R. J. Faehl, T. C. Genoni, and W. A. Proctor, IEEE Trans. Nucl. Sci. NS-24, 1648 (1977).
4. R. B. Miller and D. C. Straw, J. Appl. Phys. 47, 1897 (1976).
5. R. B. Miller and D. C. Straw, J. Appl. Phys. 48, 1061 (1977).

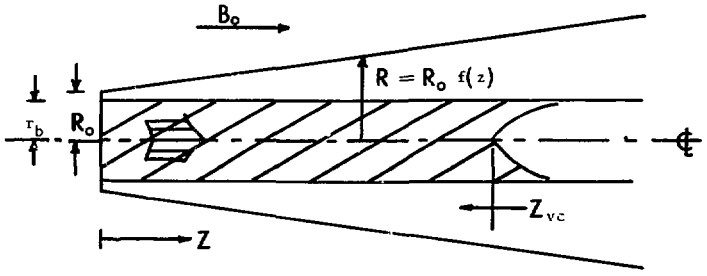

FIGURE 1. SCHEMATIC DESCRIPTION OF THE MOVING VIRTUAL CATHODE EXPERIMENT.

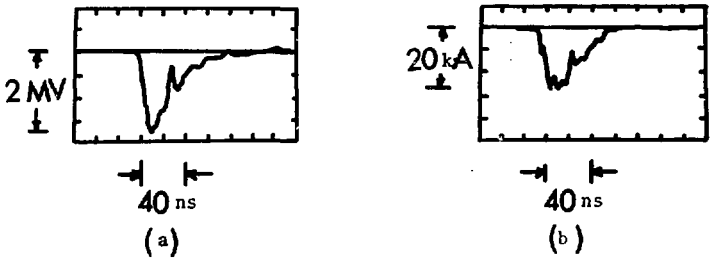

FIGURE 2. TYPICAL FX-25 DIODE VOLTAGE (a) AND CURRENT (b) WAVEFORMS.

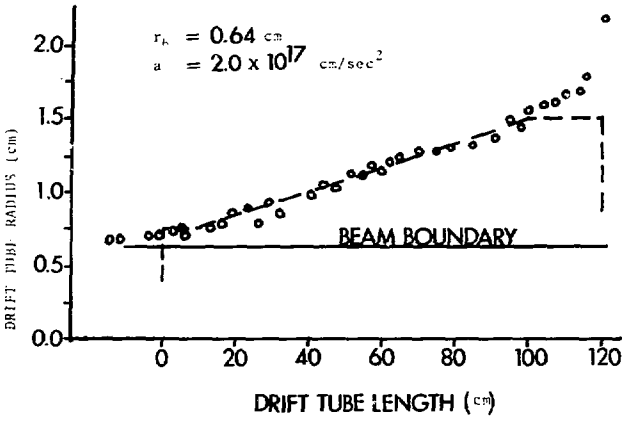

FIGURE 3. TIME DEPENDENT DIODE CHARACTERISTICS USED FOR DESIGNING A WAVEGUIDE TO PRODUCE A CONSTANTLY ACCELERATING VIRTUAL CATHODE.

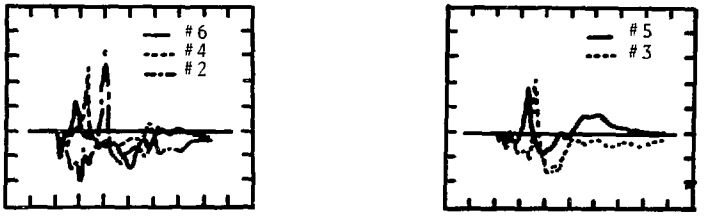

FIGURE 4. REPRESENTATIVE ELECTROSTATIC PROBE WAVEFORMS (PROBE SEPARATION EQUALS (10.64 cm). VERTICAL SCALE: 10v/div; HORIZONTAL SCALE: 20ns/div.

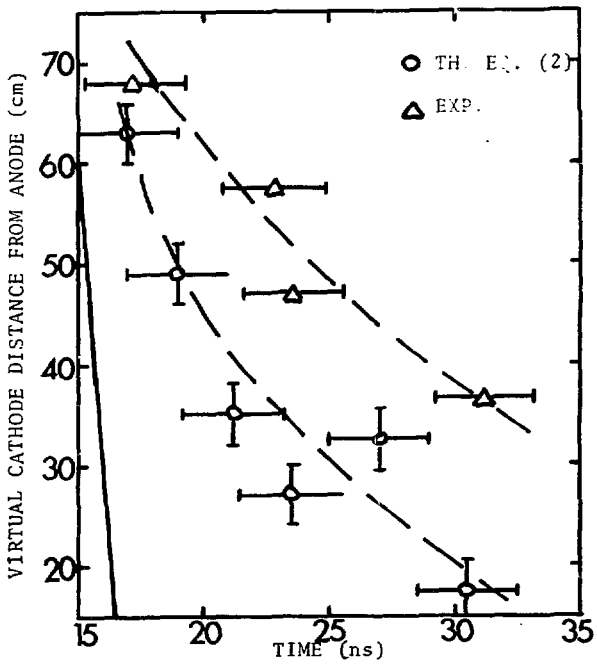

FIGURE 5. POSITION OF THE VIRTUAL CATHODE AS A FUNCTION OF TIME. (0.75 cm - 1.5 cm) waveguide, r_b = 0.5 cm, B_o = 8 kG.

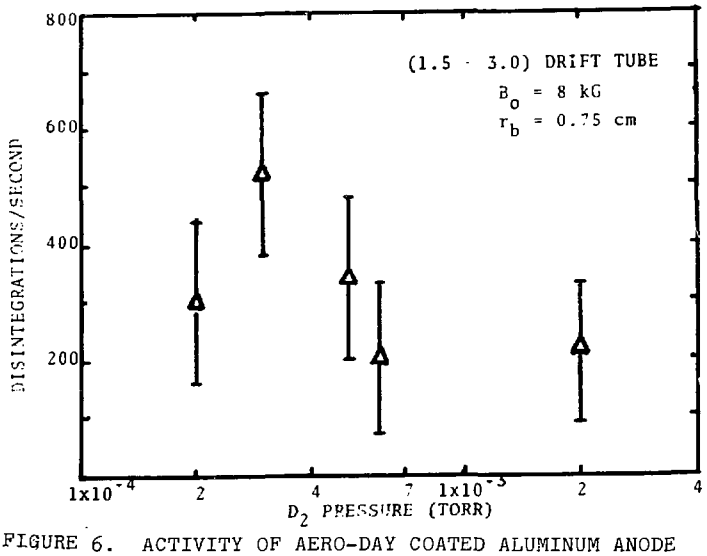

FIGURE 6. ACTIVITY OF AERO-DAY COATED ALUMINUM ANODE FOILS AS A FUNCTION OF DEUTERIUM FILL PRESSURE.

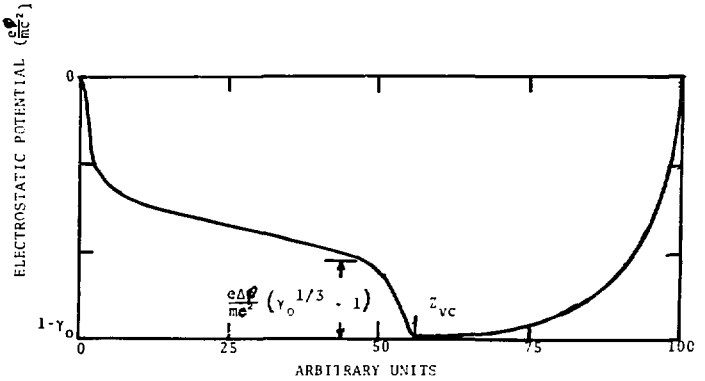

FIGURE 7. CHARACTERISTIC ON-AXIS ELECTROSTATIC POTENTIAL PROFILE AS A FUNCTION OF POSITION IN THE WAVEGUIDE.

COLLECTIVE ION ACCELERATION AND INTENSE ELECTRON BEAM PROPAGATION WITHIN AN EVACUATED DIELECTRIC GUIDE

J. A. Pasour* and R. K. Parker
Naval Research Laboratory, Washington, D. C. 20375

W. O. Doggett** and D. Pershing
North Carolina State University, Raleigh, North Carolina 27607

R. L. Gullickson
Air Force Office of Scientific Research, Bolling AFB, DC 20332

Abstract

Experiments were conducted to extend a previous study[1] of collective ion acceleration and electron beam propagation within an evacuated dielectric guide to higher beam energies. The typical electron beam injection conditions were as follows: current ~ 65 kA, voltage ~ 1.5 MV, $v/\gamma \sim 1.4$ and pulse duration ~ 60 nsec. Beam propagation was found to depend upon space charge neutralization resulting from ions released from the walls of the dielectric guide. The primary energy loss mechanism was found to be erosion of the beam front. With a diode consisting of a small diameter cathode but no anode foil, protons with kinetic energies up to 14 MeV were detected on axis using nuclear activation techniques. The maximum observed yield was ~ 10^{13} protons ($E > 3.8$ MeV).

I. Introduction

Previous experimental studies of collective ion acceleration with linear intense relativistic electron beam (IREB's) have primarily concentrated on neutral gas injection (as first observed by Graybill and Uglum[2]) or vacuum injection through dielectric anodes as pioneered by Luce.[3] An alternative approach involving the injection of an IREB into an evacuated dielectric guide was recently proposed by Little, Greenwald, et al[1,4] who have performed initial experiments on a low-energy acceler-

ator ($V \leq 100$ kV). According to their model, the beam (whose current exceeds the space-charge limit) is stopped by the formation of a virtual cathode and blows out radially, striking the dielectric wall and liberating ions. These ions provide sufficient charge neutralization for the beam to propagate a bit further, so that the potential well at the beam front travels down the guide at a velocity determined by the rate of ion release from the walls. Some of these ions are expected to be accelerated by the potential well, and it should be possible to optimize ion trapping and acceleration by appropriately choosing the system parameters (e.g., guide shape and size, cathode diameter, etc.).

The dielectric guide approach could have advantages over other methods of ion acceleration. Obtaining large ion to electron energy ratios with this technique might prove simpler than in neutral gas injection experiments, where control of the potential well is quite difficult. Also, if ion energy increases with guide length (as predicted by the model), this technique could have a scaling advantage over the Luce diode (although some scaling has been achieved there by placing additional dielectric apertures or "lenses" behind the primary one[5]). The objective of the preliminary experiments to be discussed here was to examine ion acceleration and, to a lesser extent, beam transport in evacuated ($\leq 2 \times 10^{-4}$ Torr) dielectric guides at substantially higher energies ($V \sim 1$ to 2 MV) than in the previous studies.[1,4]

II. Experimental Technique

The experimental configuration for the ion acceleration work, which was performed on NRL's VEBA facility[6], is shown in Fig. 1. The beam was emitted from a pulsed cathode (A) and was injected into Lucite tubes (C) of various diameters (5 to 9 cm ID) and lengths (15 to 90 cm), each with a 6 mm wall thickness. Experiments were performed both with and without an anode foil (B). Attached to the 11-cm-diameter stainless steel outer

cylinder (D) was a Faraday cup (F), whose 12-mm-thick graphite current collector (E) was located ~ 1 cm beyond the end of the Lucite tube. The diode voltage was monitored with a capacitive divider and the diode current was deduced from a $\dot{B}$ loop. Typically, the peak diode voltage was ~ 1.5 MV and the diode current ~ 65 kA. The pulse width (FWHM) was ~ 60 nsec.

Two types of nuclear diagnostics were used to determine the number and energy of accelerated protons (and deuterons on a few shots). A rhodium activation detector[7], located ~ 35 cm above a target attached to the front of the Faraday cup, was used to measure neutron yields from p,n and d,n reactions which resulted from bombardment of both the target and the Lucite tube. The most detailed information was obtained with nuclear activation techniques.[8] Discrimination of ion energies was achieved in two ways: (1) by the use of targets with different reaction thresholds, and (2) by using stacked foil targets and relating the depth of activation to ion energy through range-energy relations. Following a shot, the foils were removed from the vacuum chamber and counted using a 3"X3" sodium iodide detector and a 512-channel pulse height analyzer.

The number N_0 of radioactive atoms produced in the target was calculated from the number of counts recorded together with the detector calibration and the known decay rate of the particular isotope. To accurately compute the number of accelerated ions corresponding to N_0, it was necessary to know the ion energy and the interaction cross section at that energy. The energy spectrum was determined by the activity induced in a stack of thin titanium and copper foils using the technique of Miller and Straw.[9]

III. Electron Beam Transport

Electron beam propagation in a 6.4-cm-dia guide was studied using

the Faraday cup calorimeter. The energy delivered to the calorimeter (as measured with a thermocouple and digital volt meter) is plotted vs guide length for three different cathode diameters in Fig. 2. In all cases, a 12.5-μm titanium anode foil was used with an anode-cathode separation of 28 mm (except for the zero-length case where the gap was 23 mm). It is evident that energy delivery decreased almost linearly with guide length and that the larger cathodes gave best transport. Removing the anode foil more than doubled the energy delivered by the tapered 0.3-cm-dia cathode.

The energy delivered to the Faraday cup was also computed on some shots from the digitized Faraday cup current and diode voltage traces. The result derived from the energy integral agreed to within ~ 10% of the calorimetric value, indicating that most of the electrons reaching the calorimeter had essentially their injected kinetic energy. Furthermore, the peak current delivered was generally of the same order as the diode current, but the pulse width decreased with guide length. This result indicates that most of the energy loss resulted from beam-front erosion, and that propagation over longer distances might have been possible given a longer diode pulse duration.

IV. Ion acceleration

A general idea of the optimum geometry for ion acceleration was obtained by first monitoring the rhodium activation detector as geometrical parameters were varied. Upon the production of significant neutron yields, a thick target (carbon or copper) was activated and counted. From the reaction thresholds (3.2 MeV for $^{13}C(p,n)^{13}N$ and 4.2 MeV for $^{63}Cu(p,n)^{63}Zn$), it was thus possible to determine a minimum proton energy. An approximate numerical yield could also be obtained by assuming the protons had a particular energy (typically 5 MeV).

The general trends that emerged from these initial measurements

were as follows:

(1) Cathode diameter was very important, with a cathode tapered from 12.7-mm dia to 3.2-mm dia giving the best results. A 12.7-mm dia cathode also gave significant acceleration, but cathodes of 4.1 cm (Fig. 1a), 5.7 cm, and 6.7 cm dia produced no detectable yields.

(2) Diode geometry was relatively important. The highest reproducible yields were obtained without an anode foil, but nearly equivalent results were obtained on a few shots with a 12.7 μm titanium foil. Also, best results were obtained with the cathode 2.1 cm from the dielectric tube entrance, and the performance deteriorated gradually as the gap was increased or decreased.

(3) Variation of neutron production with guide diameter and length was studied with the configuration of Fig. 1b and a thick carbon target. In addition to measuring total neutron yield, data were obtained with a parafin and cadmium shield placed over the guide so that primarily neutrons originating in the target were detected. This generally reduced the yield by a factor of two or more. About 2×10^8 neutrons were produced with a 6.4-cm-dia, 15-cm-long guide. This number was ~ 6 times that with a 5-cm-dia guide of the same length, and ~4 times that with a 7.6-cm-dia guide. With a 30-cm-long tube, the results were more erratic, but the yield was generally smaller, especially that portion arising from the target.

(4) A ribbed guide was fabricated with 5-mm-wide grooves cut azimuthally at 1-cm intervals in the inner wall of a 6.4-cm-dia, 15-cm-long Lucite tube. It was thought that the grooves might impede the release of ions from the wall by increasing the surface area over which breakdown occurred, hence slowing the beam-front propa-

gation and facilitating ion trapping to improve yields. Although the arrival of the beam at the Faraday cup was delayed by ~ 20 nsec compared to the smooth tube, neutron yields were generally smaller.

For comparison of the dielectric guide acceleration results with the earlier vacuum diode work,[3] the geometry of Fig. 1c was used. The anode consisted of a polyethylene disk inserted in a graphite holder. The beam was injected through a 6-mm-dia hole in the polyethylene, and a target was placed 15 cm downstream. Although the results were very irreproducible (probably because the 5-mm anode-cathode gap caused diode impedence collapse), target activation and neutron production of approximately the same magnitude as with the dielectric guide were observed.

Stacked foil targets were used with the tapered cathode, foiless anode configuration and 6.4-cm-dia guides to provide ion energy spectra. Fig. 3 consists of histograms showing the energy spectrum for two particular shots, one (Fig. 3a) with a smooth guide and the other (Fig. 3b) with a ribbed guide. Each energy interval corresponds to a single foil, and the ordinate represents the number of protons in each interval divided by the width of that interval. The highest energy obtained on a given shot falls somewhere inside the energy range corresponding to the deepest activated foil in the stack.

Generally, it was possible to fit the data with an exponential of the form $I_p(E) = I_0 \exp(-aE)$, with $a = 1.0 \pm 0.1$ MeV^{-1}. On several shots, there was apparently an additional component to the spectrum, as is particularly evident in the high-energy tail of Fig. 3a. One possible explanation for this behavior is that the lower-energy component (with a peak ~ 3 times the electron energy) is associated with the break-up of the potential well as the virtual cathode is neutralized by ions from the guide wall.[10] The high-energy component might be comprised of ions that are actually trapped and pulled along for some distance by the propagating

beam front.

To increase above background the level of any activation arising from higher-energy protons, a series of seven shots was taken in rapid succession using a target stack consisting of a 1.3-mm-thick carbon foil backed by a series of 50-μm-thick copper foils. Activity was detected on the first copper foil, indicating protons of energy between 14.4 and 15.3 MeV. The highest peak electron energy on any of the seven shots was 1.6 MeV, so that an ion to electron energy ratio of at least 9 was achieved.

By comparing the results of the neutron activation detector with the target activation, it was typically found that more protons were accelerated into the guide wall than onto the target. While the maximum number of protons with energy above 3.8 MeV reaching the target on any stacked foil shot was $3X10^{12}$, a total yield of 10^{14} protons with energy above 3.2 MeV was inferred from the rhodium activation detector (assuming all neutrons were produced from p,n reactions and the thick target yield for the $^{13}C(p,n)^{13}N$ reaction in Lucite was the same as in graphite).

To study the spatial distribution of ion release and acceleration, 75-μm-thick mylar strips were coated with a 0.3 mg/cm^2 layer of CD_2 and used to line the Lucite tubes. Since the cross-section for d,n reactions on carbon is much larger than that for p,n reactions, it should be possible to determine where most of the accelerated ions originate and where they strike the wall. Although there was some shot-to-shot variation, most of the accelerated ions came from the first half of the drift tube. A segmented mylar liner, which was placed in the downstream portion of the drift tube as shown in Fig. 4., was used to determine the distribution of ions accelerated into the wall. Inspection of the histograms shows both an axial and azimuthal variation. More activity was produced in the center band than in either the upstream or downstream band, and

section #7 had more than 7 times the activity of the nearby #13. These results indicate that the electron beam and ion acceleration mechanism do not manifest either axial uniformity or azimuthal symmetry.

V. Conclusions

These initial experiments with high-energy, electron-beam propagation within an evacuated dielectric guide have provided a general indication of the beam transport and ion acceleration properties exhibited by this configuration. The observed features of beam transport were consistent with the qualitative model proposed by Little and Greenwald.[1,4] Since the primary energy loss mechanism was erosion of the beam front, the dielectric guide may well provide an efficient means for transporting electron beams of long duration. To obtain significant ion acceleration, however, a cathode of smaller diameter than that optimum for beam transport was required. As a result, any potential scaling of ion energy with guide length was masked by the low beam transport efficiency within the longer guides. Although a large fraction of the accelerated protons were intercepted by the dielectric liner, the forward directed component still contained approximately 10^{13} protons. The maximum observed ratio of proton to electron energy within this component was nearly 10. Since these results compare favorably with those obtained in early neutral gas and vacuum diode experiments, further study of this mechanism seems justified.

VI. Acknowledgments

The authors thank A. Greenwald for his many discussions and suggestions during the course of this work. We also appreciate the help of F.C. Young in providing and setting up the nuclear diagnostics and of D. Price in assisting in the operation of the experiment.

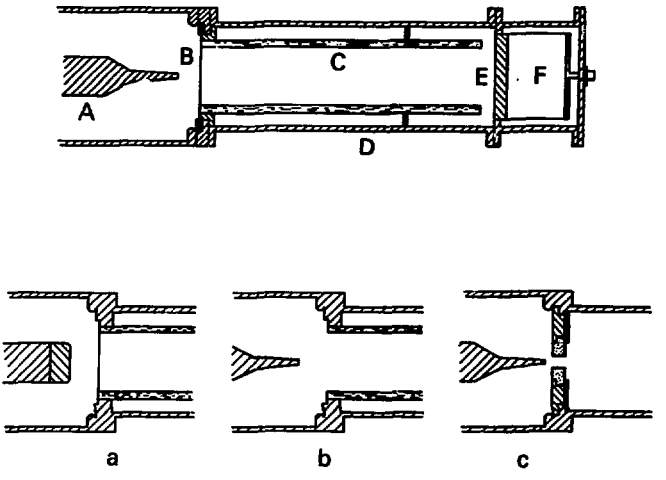

Fig. 1. Experimental configuration: A, cathode; B, anode foil; C, dielectric guide; D, outer conductor; E, graphite current collector; F, Faraday cup. Fig. 1a: propagation configuration. Fig. 1b: acceleration configuration. Fig. 1c: Luce-type diode.

References

*NRC Research Associate
**Supported by AFOSR under Contract F49620-76-C-0007

1. A.Greenwald, R. Lowell, and R. Little, Bull. Am. Phys. Soc. 21, 1147 (1976) and paper this conference.
2. S.E. Graybill and J.R. Uglum, J. Appl. Phys. 41, 236 (1970).
3. J.S. Luce, H.L. Sahlin, and T.R. Crites, IEEE Trans. NS-20, 336 (1973).
4. R.G. Little, J.R. Uglum, and R.A. Lowell, IEEE Trans. NS-22, 235 (1975).
5. J.S. Luce, Ann. N.Y. Acad. of Sciences 251, 217 (1975).
6. R.K. Parker and M. Ury, IEEE Trans. NS-22, 983 (1975).
7. F.C. Young, IEEE Trans. NS-22, 718 (1975).
8. F.C. Young, J. Golden, and C.A. Kapetanakos, Rev. Sci. Instrum. 48, 432 (1977).
9. R.B. Miller and D.C. Straw, AFWL-TR-75-236, Air Force Weapons Lab., April, 1976.
10. R.B. Miller, private communication.

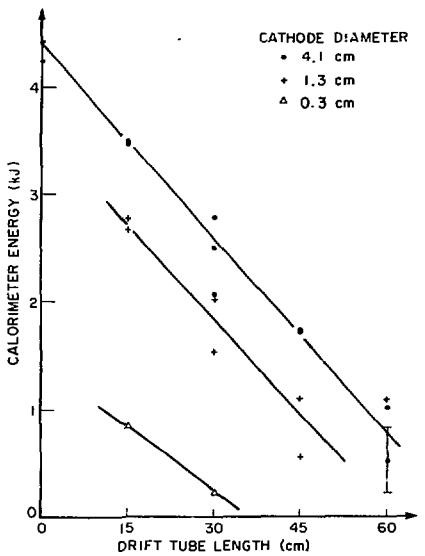

Fig. 2. Electron beam energy transport vs guide length and cathode diameter.

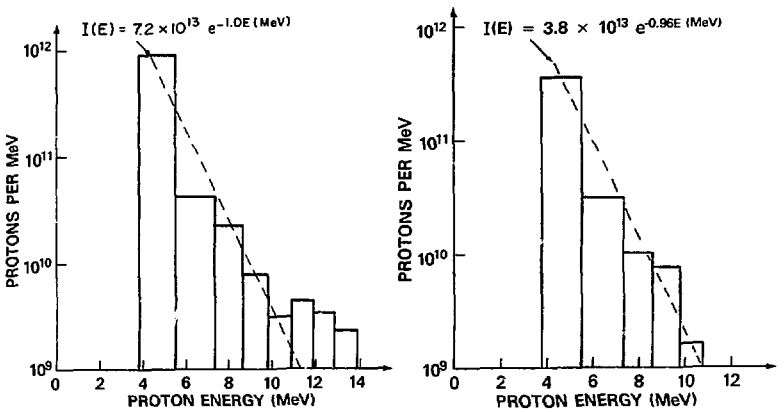

Fig. 3. Proton energy spectra from stacked foil targets with (a) a smooth guide and (b) a ribbed guide.

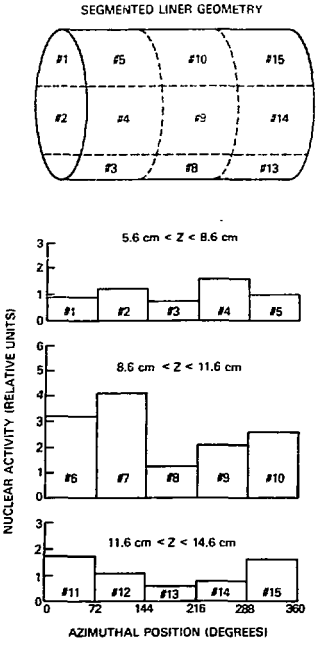

Fig. 4. Segmented liner geometry and relative activity induced in each segment showing radial proton acceleration.

TOROIDAL COLLECTIVE ACCELERATOR FOR HEAVY IONS*

Norman Rostoker

Department of Physics
University of California
Irvine, California 92717

Electrons can be confined in a "bumpy torus" so that they are effectively trapped by mirror magnetic fields and do not circulate around the torus. This has been confirmed by experiments at Maxwell Laboratories. Based on this result, we propose a heavy ion accelerator in which ions are confined and focused by the net space charge of the electrons. Then an inductively applied toroidal electric field of about 10 Volts/cm will accelerate ions without accelerating electrons. The reason for this is that, whereas the electron dynamics is adiabatic, the ion dynamics is not and the magnetic fields have little effect on ions. In this paper, this conjecture is proven, self-consistent equilibria for electrons and ions are obtained and stability problems are investigated. A conceptual design is evaluated in which Uranium ions are accelerated to produce 100 Terawatt pulses at 100 GeV. The major radius of the torus required is 3 - 5 meters, and the design is based on existing technology.

Introduction

Consider electrons magnetically confined in a torus as illustrated schematically in Fig. 1. The electrons produce a potential $\Phi(r)$ shown in Fig. 1 that can be used to confine/focus ions. The acceleration of ions would be conven-

tional and accomplished with an externally produced toroidal electric field.

The essential point of this paper is that it is possible to accelerate only ions and not electrons around the torus because the electron orbits are adiabatic and the ion orbits are not, as illustrated in Fig. 1. This principle applies equally well in linear geometry; it was first proposed[1] and experimentally verified[2] for magnetically insulated ion diodes. In the present application the magnetic field design involves multiple mirrors or a bumpy torus. For electrons, the motion is adiabatic. From the adiabatic invariance of the magnetic moment $\mu = \frac{1}{2} mv_\perp^2/B$ and conservation of energy, we can show that all electrons are trapped that have mid-plane velocities outside the loss cone whose angle is given by

$$\sin^2\theta_o = \frac{B_o}{B_m}\left[1 + \frac{2eE_zL}{mv_o^2}\right] \qquad (1)$$

B_o is the mid-plane magnetic field. B_m is the maximum magnetic field a distance L from the mid-plane. $mv_o^2/2$ is the mid-plane energy and E_z is the applied electric field. If $2eE_zL/mv_o^2 \geq (B_m/B_o) - 1$ or $eE_zL \geq \mu(B_m - B_o)$, $\theta_o = \pi/2$ and all particles will escape the mirror. However, if $eE_zL << \mu(B_m - B_o)$ the applied electric field will have a negligible effect on containment. In recent experiments at Maxwell Laboratories[3] electrons were confined in a slightly bumpy torus. When a toroidal electric field of .5 Volts/cm was applied the resultant current was less than 50 amperes; according to potential measurements the confined charge was

100 μ-coulombs, which should have resulted in a toroidal current of 10 k-amps if most of the electrons were not trapped. Thus the essential features of the electron dynamics have been established experimentally.

There are many possible instabilities to be considered. However, H.I.P.A.C. experiments[4] at the AVCO corporation showed that a toroidal electron ring of density $n_o = 4 \times 10^9 cm^{-3}$ could be confined for 10 millisec. These experiments involved an ion charge density of 10 - 20% of the electron charge density. Thus the main instabilities that need to be considered are those that arise from accelerating the ions.

In this paper we shall discuss theory of single particle ion dynamics, self-consistent equilibria for electrons and ions, and some stability problems. A conceptual design of a heavy ion accelerator will be described.

Single Particle Ion Dynamics

Consider ion motion in cylindrical geometry

$$M\ddot{x} = Ze(-2\pi n_o e x + \frac{1}{c}\dot{y}B_z)$$
$$M\ddot{y} = Ze(-2\pi n_o e x - \frac{1}{c}\dot{x}B_z) \qquad (2)$$

The electric field is due to a uniform cylinder of electrons of density n_o. For constant B_z, these equations can be solved. The result is

$$r^2 = x^2 + y^2 = r_o^2\left[\Omega_+^2 + \Omega_-^2 - 2\Omega_+\Omega_-\cos(\Omega_+ - \Omega_-)t\right] / (\Omega_+ - \Omega_-)^2 \qquad (3)$$

where r_o is the initial radius and

$$\Omega_{\pm} = \left\{-\Omega_c \pm \sqrt{\Omega_c^2 + 4\Omega_i^2}\right\}/2$$

$$\Omega_c = ZeB_z / Mc$$

$$\Omega_i = [2\pi n_o Ze^2 / M]^{\frac{1}{2}} \qquad (4)$$

This solution has previously been employed[5] to calculate the ion magnetic moment μ_i and to show that $\mu_i/Z\mu_e << 1$. In this paper we consider a slowly varying $B_z = B_o(1 + \alpha \sin kz)$ and $B_r = -\alpha \frac{kr}{2} B_o \cos kz$. We solve the equation of motion

$$M\ddot{z} = ZeE_z - \frac{Ze}{c} v_\theta B_r \qquad (5)$$

using the conservation of $P_\theta = Mrv_\theta + \frac{Zer}{c} A_\theta$ to eliminate v_θ. For r(t) we use the solution given by Eq. (3). Equation (5) can be expressed as

$$\frac{d^2Z}{d\tau^2} = \frac{E_z}{B_o} + \alpha \frac{KR_o^2}{4} \cos KZ \left[1 - \alpha - (r^2/r_o^2) - \alpha(r^2/r_o^2)\sin KZ\right] \qquad (6)$$

In Eq. (6), $R_o = \Omega_c r_o/c$, $Z = \Omega_c z/c$, $\tau = \Omega_c t$, and $K = kc/\Omega_c$. This equation has been solved numerically with r^2/r_o^2 given by Eq. (3) and with r^2/r_o^2 replaced by

$$\langle r^2/r_o^2 \rangle = (\Omega_+^2 + \Omega_-^2)/(\Omega_+ - \Omega_-)^2 \quad . \qquad (7)$$

The close agreement of the two solutions justifies the approximation $r^2/r_o^2 \rightarrow \langle r^2/r_o^2 \rangle$. Then a first integral of Eq. (6) can be obtained. From this we conclude that $dZ/dt \neq 0$ or no reflection will occur as long as

$$\alpha \leq 1 - \langle r^2/r_o^2 \rangle \cong 1/2 \qquad (8)$$

This treatment shows that a multiple magnetic mirror that is quite adequate for trapping electrons has no effect on the ions. Electrons will not accelerate in the z-direction if $eE_z L < \mu_e \alpha B_o$ and ions will accelerate for any E_z as long

as $\alpha \leq 1/2$. The present treatment does not consider anything but an externally applied constant E_z-field. There may also be internal E_z-fields. This would require a completely self-consistent treatment and is beyond the scope of the present paper.

Self-Consistent Equilibria

The force balance problem is illustrated in Fig. 2. The centripetal force for the ions cannot be supplied by the toroidal magnetic field because $n_i Mv^2/R >> B^2/8\pi R$. It is supplied by a field E_x produced by polarization of the boundary as illustrated in Fig. 2. The force on the ion beam per unit length is $F_i = N_i Mv^2/R$. There must be an equal and opposite force on the electron beam. This force will cause the electron beam to drift downward and polarize the surface producing a uniform electric field E as shown in Fig. 2. This electric field causes a drift toward the inside surface of the torus and changes the surface polarization. An equilibrium position can be found when the polarization field E is in the x-direction and $N_e eE_x = N_i Mv^2/R$. If Δx is the displacement of the center of the electron beam, $E_x = 2\, N_e e\Delta x/b^2$ where b is the minor radius of the torus. For force balance

$$\frac{2(N_e e)^2}{b^2}\,\Delta x = \frac{N_i Mv^2}{R}$$

or

$$\frac{\Delta x}{a} = \frac{2N_i}{N_e}\,\frac{M}{m}\left(\frac{b}{a}\right)^2\left(\frac{c}{\omega_p a}\right)^2 \beta_i^{\,2}\,\frac{a}{R} \qquad (9)$$

is the shift of the center of the electron beam. a is the

electron beam radius, $\beta_i = v/c$, $\omega_p^2 = 4\pi n_e e^2/m$, and R is the major radius of the torus.

The equations of motion for electrons and ions to the lowest order in the aspect ratio b/R, are of the form[6]

$$m_j\left(\frac{dv_x}{dt} + \frac{v_z^2}{R}\right) = e_j\left[E_j + E_r\frac{x}{r} + \frac{1}{c}v_y B_z\right]$$

$$m_j\frac{dv_y}{dt} = e_j\left[E_r\frac{y}{r} - \frac{1}{c}v_x B_z\right] \qquad (10)$$

E_j is an electric field that arises from the shifts of the electron and ion beams and the resultant surface polarizations as illustrated in Fig. 2. If we assume $m_j\frac{v_z^2}{R} = E_j$, we obtain two equations for Δx_e, the displacement of the center of the electron beam, and Δx_i, the displacement of the center of the ion beam. The solutions are that Δx_e is given by Eq. (9) and

$$(\Delta x_e - \Delta x_i)/a \cong (c/\Omega_i a)^2 (a/R)\beta_i^2 \qquad (11)$$

Self-consistent equilibria for the electron and ion beams are of the form

$$F_j = \frac{m_j}{2\pi} n_j \delta\left[\frac{1}{2}m_j(v_x + \omega_j y)^2 + \frac{1}{2}m_j(v_y - \omega_j x)^2 + U_j(r)\right]\delta(v_z - v_j) \qquad (12)$$

where $U_j(r) = -\frac{1}{2}m_j\omega_j r^2 + e_j\Phi(r) - \frac{e_j}{c}\omega_j r A_\theta - c_j$ (13)

The beam radius a_j is defined by $U_j(a_j) = 0$. These equilibria are of the rigid rotor type with constant density n_j for $0 \le r \le a_j$, and $n_j = 0$ for $r > a_j$. The centers of the beams are shifted from the minor axis of the torus according to Eqs. (9) and (11). For electrons $\omega_e = \omega_p^2/2\omega_c$ where $\omega_c = eB/mc$, and for ions $\omega_i = -\frac{\Omega_c}{2} + \Omega_i$. The potentials are $\Phi(r) \cong (n_e - Zn_i)\pi e r^2$ and $A_\theta \cong B_o r/2$.

Stability Problems

The types of instabilities studied for the H.I.P.A.C. experiments were the diocotron instability,[7] the magnetron instability,[8] and the ion resonance instability.[9] All of these instabilities can be avoided if $q = \omega_p^2/\omega_c^2$ is sufficiently small ($q \leq .1$), a/b is not too small ($a/b \geq .5$), and the ion density is not too large ($n_i/Zn_e \leq .1$). These instabilities were evidently controlled in the H.I.P.A.C. experiments.[4] When ions are accelerated there are various streaming instabilities that must be considered. A preliminary investigation (that does not consider the geometry) indicates that these instabilities can be controlled by designing the system with a sufficiently high electron temperature.[5] The temperatures of electrons and ions change during acceleration so that detailed kinetic theory calculations are required.

Conceptual Design of a Heavy Ion Accelerator

Consider an accelerator to produce 100 GeV ions of U^{60+}, $ZeER/2 = Mv^2/2 = 100$ GeV. For $Z = 60$, $E = 10^7$ Volts/cm and $R = 3.3$ meters. The following parameters are required to produce 100 Terawatts and 1.9 Megajoules of ions.

Torus

Minor radius	$b = 1.5$ cm	Magnetic energy	150 k-Joules
Major radius	$R = 3.3$ m	Toroidal field	$E_z = 10$ Volts/cm
Magnetic field	$B_z = 50$ k-Gauss		

Electron Beam

Density $n = 10^{13} cm^{-3}$; temperature $T_\perp = 200$ keV.
Beam radius $a = 1$ cm.
Total number of electrons $7.2 \times 10^{16} \equiv 11.5$ Milli Coulombs.
Electric field energy 37.5 k-Joules.
$\omega_c = 9.0 \times 10^{11}$ sec^{-1} ; $\omega_p = 1.77 \times 10^{11}$ sec^{-1} ; $q = \omega_p^2/\omega_c^2 = .038$.
Electron beam shift $\Delta x_e = .15$ cm.

Ion Beam

Total number of ions	$1.2 \times 10^{14} \equiv 1.15$ Milli Coulombs.
Ionization time	40 millisec.
Acceleration time	9 millisec.
Ion current	12.5 k-amps.
Pulse length	94 nanosec.
$\Omega_c = 1.2 \times 10^8$ sec^{-1} ;	$\Omega_i = 1.6 \times 10^9$ sec^{-1}.
Ion beam shift	$\Delta x_e - \Delta x_i = .6$ cm.
Power (5 switches)	100 Terawatts.
Ion energy	1.9 M-Joules.

After forming the electron beam with a rising B_z-field, Uranium atoms would be injected and ionized by the beam. We have assumed the toroidal field E_z would be provided by a transformer. The required flux change is $\Delta\Psi/c = 2\pi R^2 B_m/c = 2\pi R E_z \Delta t$. $E_z = 10$ Volts/cm and $\Delta t = 9$ millisec. If $B_m = 20$ k-Gauss for iron, $R = cE_z\Delta t/B_m = 4.5$ meters. Thus, it is the transformer specifications that determine the minimum size. After the ion beam has been formed and accelerated, there remains the problem of extraction. Our present thinking involves a plasma gun to fire a plasma stream into the electron cloud. This would neutralize the space charge of the electron beam at a particular location. The Uranium ions would then move tangential to their previous circular path into a suitably placed drift tube. To obtain a beam

power of 100 terawatts, it would be necessary to switch out the beam simultaneously at 5 locations and guide 5 beams to a target. Further study of this and other extraction schemes is clearly necessary, particularly because the extraction method will mainly determine the beam quality.

References

1. N. Rostoker, IEEE Trans. Nucl. Sc. NS-19, No. 2, 301 (1971).
2. P. Dreike, C. Eichenberger, S. Humphries, and R. N. Sudan, J. Appl. Phys. 47, 85 (1976).
3. W. Clark, P. Korn, A. Mondelli, and N. Rostoker, Phys. Rev. Lett. 37, 592 (1976).
4. J. D. Daugherty, J. Eninger, and G. S. Janes, AVCO Everett Research Report 375, October 1971; G. S. Janes, R. H. Levy, H. A. Betne, and B. T. Feld, Phys. Rev. 145, 1925 (1966).
5. A. Irani and N. Rostoker, UCI Technical Report #77-1, January 1977; to be published in Particle Accelerators.
6. A. Mondelli and N. Rostoker, Proc. Int. Topical Conference on Electron Beam Research and Technology, Albuquerque, New Mexico, 312 (1975).
7. R. H. Levy, Phys. Fluids 8, 1288 (1965).
8. O. Buneman, R. H. Levy, and L. M. Linson, J. Appl. Phys. 37, 3203 (1966).
9. R. H. Levy, J. D. Daugherty, and O. Buneman, Phys. Fluids 12, 2616 (1969).

*Work supported by the National Science Foundation.

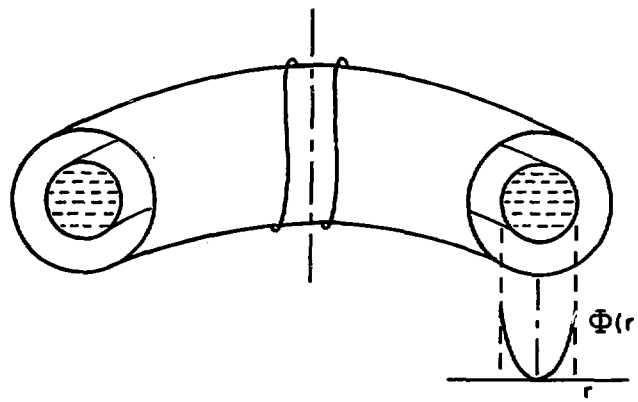

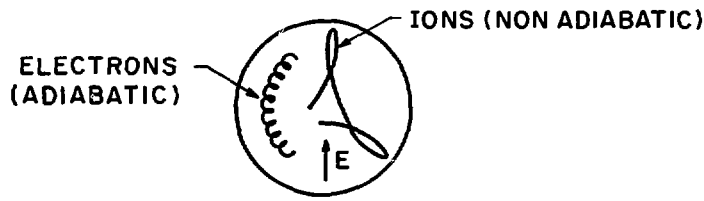

FIG. 1 ELECTRON AND ION ORBITS

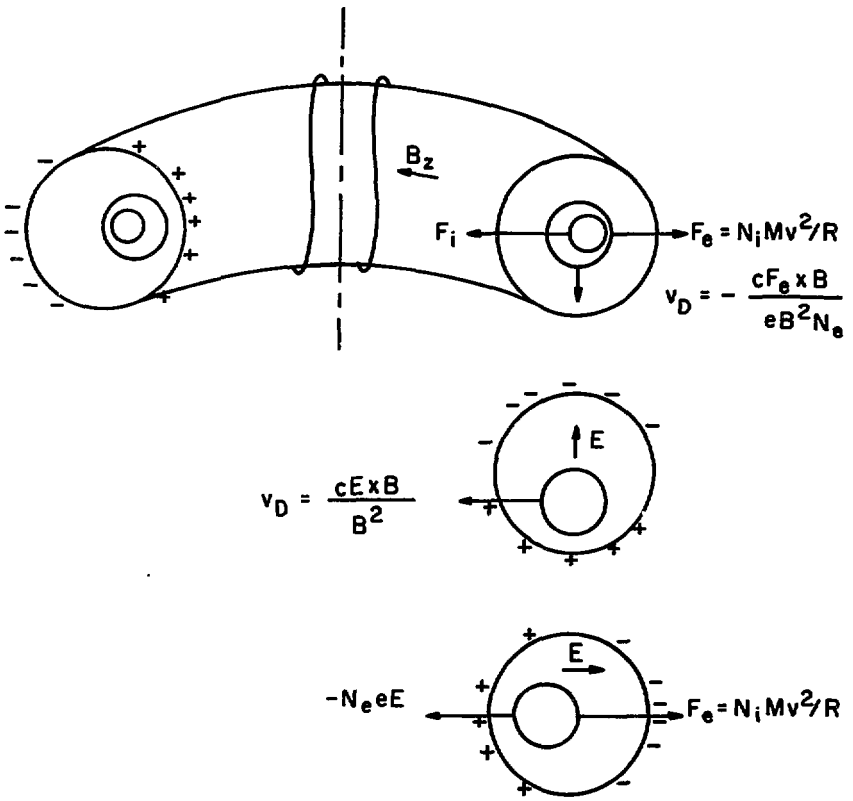

FIG. 2 FORCE BALANCE OF BEAMS IN A TORUS

MICROWAVES AND UNNEUTRALIZED E-BEAMS

MICROWAVE GENERATION IN THE REFLEX TRIODE

Howard E. Brandt, Alan Bromborsky, Henry B. Bruns and R. Alan Kehs

Harry Diamond Laboratories, Department of the Army, 2800 Powder Mill Rd.
ATTN: DRXDO-RBC, Adelphi, MD 20783

Abstract

In recent experiments at the Harry Diamond Laboratories and at the Naval Research Laboratory[1], intense microwave emission has been observed during reflex triode operation. A fully relativistic, time-dependent one-dimensional simulation code, based on the technique formulated by Birdsall and Bridges[2], was written to investigate the collective electron oscillations and to predict the microwave energy spectral density. Predicted and measured reflex triode microwave energy spectral densities in the X-band region are in reasonable agreement with one another and confirm the validity of the model. Computer experiments indicate that microwave generation could be greatly enhanced by feeding the radiated energy back into the oscillating space-charge cloud.

Introduction: The reflex triode was originally conceived by S. Humphries, Jr. (Laboratory of Plasma Studies, Cornell University), in the grounded cathode version as an intense pulsed ion source[3,4]. However, the phenomenon of Barkhausen oscillations in radio tubes operated with the same type of potential distribution as the reflex triode has been known for over 50 years[5,6]. Hence, it is reasonable to expect that, under certain conditions, the reflexing electrons in the triode would emit radiation associated with a Barkhausen type of oscillation. Furthermore, it has been determined that if the angular scattering in the triode anode foil is less than a certain critical amount, quasistatic solutions for

the current density and potential do not exist[7]. The nonexistence of quasistatic solutions indicates that time-dependent potential distributions analogous to those simulated by Birdsall and Bridges[2] will be present in the reflex triode. A preliminary computer simulation of the electron motion in the reflex triode indicated that dominant frequencies of electron oscillations should take place in the X-band region of the microwave spectrum. Thus, microwave diagnostics were used, when a reflex triode experiment was performed at the Harry Diamond Laboratories.

Description of Experiment: Figure 1 shows the reflex triode attached to the FX-45 pulsed power source which is a 60-ohm coaxial transmission line charged by a Van de Graaf generator and discharged via a triggered spark gap. For the reflex triode experiment, the line was positively charged to a potential between 3.5 and 3.7 MV, at which charge it stored approximately 1 kJ of energy.

The triode consisted of a carbon cathode and a 2.5 μm thick Mylar anode foil supported as shown in figure 1. A slow pulsed (∿300-Hz) magnetic field of peak amplitude between 0.3 and 0.4 Tesla was applied along the anode-cathode axis. The final section of the vacuum coaxial line (I.D. 6.25 cm, O.D. 33.75 cm) outer conductor and a cathode support structure were fabricated from circuit board in order to maximize the intensity of the applied magnetic field and minimize eddy current losses. The cathode diameter was 5 cm, the cathode-ground plane gap was 9.5 cm, and the anode-cathode gap was set at both 1 cm and 2 cm.

Experiment diagnostics included standard machine voltage and current monitors, carbon activation targets, a scintillator time-of-flight system for the ion beam extracted from the virtual cathode, and a dispersive line and monopole antennas for microwave measurements.

In detail, the microwave diagnostic system consisted of calibrated dispersive lines, attenuators, couplers, and detectors for quantitative

measurements in the X- and Ku-bands. The microwave output of the reflexing electrons was observed through a 15-cm-diameter lucite window in the triode vacuum chamber. The end of a section of full-size X-band waveguide was aligned 1 m from, and at right angles to, the axis of the anode-cathode gap. Furthermore, the waveguide was orientated to accept only vertically polarized radiation. The waveguide, 49 ft long, was connected to the data screen room where X-band couplers, attenuators, and detectors were used to sample the signal. At this point on the waveguide, the signal was coupled into a half-size X-band waveguide 240 ft long. The output of the waveguide was measured by using couplers and detectors sensitive to the X- and Ku-bands. In addition to the dispersive line system that was used for quantitative measurements, a monopole antenna was used to feed three microwave filters and make qualitative measurements of the presence of radiation in the L-, C-, and S-bands. Finally, several measurements were made where two open-ended waveguides oriented at right angles with respect to one another were used to feed X-band detectors. The relative signal strengths detected would then determine the degree of polarization of the radiation.

Experimental Results: For a 1-cm nominal anode-cathode gap and a machine charging voltage of 3.5 MV, the anode-cathode voltage waveform was triangular and exhibited a peak amplitude of 1 MV, a rise time of 10 ns, and a fall time of 4 ns. The microwave detector output typical of this type of operating condition is shown in figure 2. The trace in figure 2 has been retouched to be rendered clearly visible. Also, the output of each detector has been delayed by a different amount so that both traces could be displayed on the same oscilloscope screen at a reasonably high sweep speed (20 ns/div).

The 49 ft of waveguide joining the exposure room and the detector in the data screen room has caused a significant amount of dispersion between

some frequency peaks in the microwave pulse. Also, in the detected output of the dispersive line (figure 2, delayed X-band), not only have the main frequency components in the pulse separated from one another due to dispersion, but the pulse envelopes corresponding to the dominant frequencies present have widened. This widening is obvious since there are peaks in the undelayed X-band only 3 ns wide whereas the peaks in the delayed X-band are 6 ns wide. Because of this pulse widening, the data were analyzed by measuring (1) the time delays between peaks in the undelayed and delayed outputs and (2) the energy represented by the area under each peak in the delayed output. The energy in each peak was referred to the waveguide input by using the measured waveguide attenuation curve.

The reduced data corresponding to the pulse shown in figure 2 are shown in figure 3. The total energy detected between 9 and 13 GHz for the pulse shown in figure 2, when referred to the source region, was 9 mJ/Ster. Frequency peaks occurring between X-band cutoff ($\sim$7 GHz) and 9 GHz could not be observed in figure 2 since they occurred beyond the right-hand boundary of the oscilloscope trace.

Microwave radiation in L-, C-, and S-bands was detected by using a monopole antenna ($\sim$0.5 cm in length) and microwave filters.

Other shots show roughly the sort of structure present in figure 3, with the energy in the 9 to 13 GHz band going as high as 11 mJ/Ster.

The polarization measurement for the X-band region indicated at least 75% vertical polarization, with the major peaks in the spectrum being even more strongly polarized. This polarization shows that the approximation of one-dimensional electron motion is fairly good for the conditions of the actual experiment.

Description of Theory: The computer simulation of electron motion in the reflex triode (unpublished) is basically a relativistic

generalization of the one-dimensional fully time dependent diode codes developed by Birdsall and Bridges[2], and is applicable when the following assumptions hold:

1. The electromagnetic problem is one-dimensional; that is, the applied magnetic and electric fields are such that the space charge field of the electrons may be approximated as a function of time and one spatial variable.
2. The anode foil is thin enough, and the electron energies are high enough so that angular scattering in the anode foil can be neglected[7].
3. The number of superparticle space charge sheets used in the computer simulation is large enough, and the time step small enough, to adequately represent the electron space charge distribution.
4. The ion space charge will not significantly affect the electron motion. This condition will not be true in the reflex triode once the ion currents are established. However, for our experiment, conditions suggest that the effect of ions can be ignored during the rise time of the machine voltage pulse (several nanoseconds). Future simulations will include ions.

Seven parameters completely define the electron dynamics of a reflex triode simulation run. Geometric parameters are (1) the distance from the anode to the near and far cathodes and (2) the area of the emitting cathode. The machine parameter is the waveform of the voltage applied to the anode-cathode gaps as a function of time. The material parameter is the stopping power of the anode foil as a function of electron energy. Internal code simulation parameters are (1) the time step between electric field calculations and particle pushes and (2) the available current for injection into the anode-cathode region. Time

steps are chosen to be a small fraction of an anode-emission-cathode light transit time. Typically, a time step of 0.26 ps was used, giving a Nyquist cutoff frequency of 2000 GHz. The available current was used to define the charge density on each super particle sheet as the product of the available current times the time step, divided by the emission cathode area.

The energy spectral density of the emitted microwave radiation was computed in the far field dipole approximation by using the calculated current density of the space-charge cloud. One consequence of this treatment was an interference form factor for the oscillating space-charge cloud geometry with zeros in the region of interest (7.2 and 13.2 GHz in figure 6).

Theoretical Results: One of the basic questions in constructing a time-dependent code is how to model the electron emission process at the cathode. For our code, a plasma cathode of negligible temperature was assumed such that a superparticle sheet would enter the anode-cathode region from the emission-cathode plane each time step when the electric field vector at the cathode plane was in the correct direction. Thus, if one fixed the time step, the emission processes at the cathode were defined by a single parameter, the charge on each superparticle, or, for the parameters used in our code, the available current. Because, at our level of understanding, the available current could not be determined a priori, a sensitivity analysis was done for several constant applied voltages. Over a very wide range of available currents, the mean and peak space charge in the triode region saturated. Furthermore, the mean and peak space charge at saturation was directly proportional to the applied voltage. Thus, the electron emission process, for the high fields considered, is completely characterized by charge saturation.

Next, the oscillatory behavior of the space charge was investigated. Figure 4 shows the extremals of the potential function over one dominant period after the system achieved oscillatory equilibrium, for an applied voltage of 1 MV. The position of the plateau in the slope of the potential is taken to be the location of the virtual cathode. The virtual cathode oscillated about a mean position 1.1 cm from the anode foil with a peak-to-peak amplitude of 0.8 cm and a frequency of 9.8 GHz which also corresponds to the main microwave peak. Figure 5 shows the computed charge density as a function of distance from the emission cathode and time, during the same dominant cycle of virtual cathode movement. Due to the time-dependent nature of the system, some charge propagates into the region beyond the virtual cathode and even reaches the ground plane on the virtual cathode side of the anode. Figure 5 shows also the natural bunching of charge that occurs during the complex space-charge oscillations of the system. This bunching is not assumed a priori, nor is it a mathematical artifact of the charge density representation, since several hundred superparticle sheets are used at each instant of time in computing the density function displayed. In actuality, the bunching is due to the time dependence of the system and occurs whether the applied potential rises to its maximum value in one time step, as in a constant potential run, or in 10 ns, as in the simulation of the actual machine voltage pulse.

Since the most easily measured observable quantity that results from the collective space-charge oscillations in the triode is the spectrum of microwave radiation emitted, the energy spectral density of the radiation was computed. Figure 6 shows the microwave energy spectral density computed for an anode-cathode gap of 9.5 mm and an applied voltage in the form of a ramp that rises to a peak amplitude of 1 MV in 10 ns. The fine structure and energy in the 9 to 13 GHz band of the energy

spectral density is a sensitive function of the gap spacing such that, for the same applied voltage waveform, the energy in the band varies as given by Table I.

TABLE I. Energy in 9 to 13 GHz Band versus Gap Spacing

Anode-Cathode Gap (mm)	Energy in Band (mJ/Ster)
9.0	32
9.5	18
10.0	27

A gap spacing of 9.5 mm was chosen as yielding a best fit to the data displayed in figure 3 in the sense, that if the amplitudes of the theoretical points are all reduced by the same multiplicative factor, the trends of both data and theory agree, except for those data points that can be identified as being a superposition of separate frequencies in the delayed X-band output. For example, the data point at 11.2 GHz corresponds to the second peak in the delayed X-band output in figure 2. This peak has a complex structure and would eventually disperse into two or more peaks if the dispersive line were long enough. The points designated "Reduced Theory" in figure 3 were obtained from the data displayed in figure 6 by integrating the energy spectral density over obvious peaks. The amplitude descrepancy between the data and theory points displayed in figure 3, if it does not result from a basic inaccuracy in the assumptions of the model, could be explained by the sensitivity of radiated energy to applied voltage.

Table II shows that a small error in measuring the applied voltage could lead to a large error in the radiated energy. Hence, the disagreement between experiment and theory in figure 3 could be accounted for by a 20% error in the measurement of the applied voltage.

TABLE II. Output Energy in the 7 to 13 GHz Band as a Function of Applied Voltage (1-ns Square Pulse)

Applied Voltage (MV)	Energy in Band (mJ/Ster)
0.2	0.02
0.4	0.65
0.6	3.09
0.8	30.0
1.0	67.9

Finally, a computer experiment was performed to obtain an indication of the effect of feedback on the microwave output of the reflex triode. The experiment consisted of adding an external sinusoidal electric field, with an amplitude of 10 MV/m and a frequency of 9.8 GHz, to the fields generated by the applied voltage. The results of the experiment are that the microwave energy spectral density for a constant applied voltage of 1 MV increases by a factor of 40 at the pump frequency. However, due to the nonlinearity of the system, the output at the first harmonic of the pump frequency increases by a factor of 240; and at the second harmonic, by a factor of 400.

Conclusions: The agreement between the experiment performed and the numerical simulation is good considering the extreme nonlinearity of the system simulated. This nonlinearity results in a wide variation in the microwave output of the triode when the applied voltage and gap spacing are varied by a small amount. Unfortunately, the experiment was performed before the code sensitivity study was completed; as a result several experimental parameters, such as anode-cathode gap and applied anode-cathode voltage, were not measured as accurately as necessary. Also, future simulations must include ions in the code and might possibly need to include electron angular scattering in the anode

foil. For the parameters of the experiment performed, the inclusion of angular scattering is not necessary.

Fortunately in the experiment-model correlation, the walls of the vacuum tank (figure 1) were more than 50 cm from the anode-cathode gap. Wall geometry also prevented radiation from being effectively reflected into the space-charge region. This prevention is inferred from the results of Mahaffey's experiment[1] where the anode-cathode region was close to the wall of the cylindrical vacuum tank, which was aligned along the anode-cathode axis. The results of the NRL experiment[1] were that significant amounts of microwave radiation were present in the X- and Ka-bands, even though the applied voltage was only 350 kV and the cathode diameter was 10 cm. Evidently, radiation feedback occurred in the Naval Research Laboratory experiment.

If one hopes to produce microwave radiation efficiently from a reflex triode, the space-charge region will probably have to be enclosed by a cylindrical reflector-resonator, designed to introduce radiation feedback into the system in a controlled manner. It is such a system that we are currently trying to model using the superparticle simulation approach. These results will determine the design of future experiments.

References:

1. R. A. Mahaffey, P. Sprangle, J. Golden, and C. A. Kapetanakos, High Power Microwaves from a Nonisochronic Reflecting Electron System, Phys. Rev. Lett., Vol. 39, No. 13, p. 843, 1977.
2. C. K. Birdsall and W. B. Bridges, Electron Dynamics of Diode Regions, Academic Press, New York, 1966.
3. S. Humphries, Jr., J. J. Lee, and R. N. Sudan, Advances in the Efficient Generation of Intense Pulsed Proton Beams, Laboratory of Plasma Studies, Cornell University, LPS 154, Aug. 1974.

4. S. Humphries, Jr., R. N. Sudan, and W. C. Condit, Jr., The Production of Intense Megavolt Ion Beams with a Vacuum Reflex Discharge, Laboratory of Plasma Studies, Cornell University, LPS 161, Jan. 1975.

5. H. Barkhausen and K. Kurz, "Shortest Waves Obtainable with Valve Generators," Phys. Zeit, Vol. 21, p. 1-6, Jan. 1920.

6. B. J. Thompson and P. D. Zottu, "An Electron Oscillator with Plane Electrodes," Proceedings of the Institute of Radio Engineers, Vol. 22, No. 12, p. 1374, Dec. 1934.

7. Thomas M. Antonsen, Jr., and Edward Ott, "Foil Scattering in a Reflex Triode Intense Ion Beam Accelerator," Appl. Phys. Lett. Vol. 28, No. 8, p. 424-426, 15 Apr. 1976.

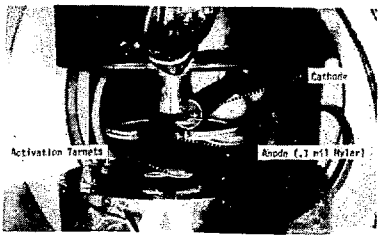

Fig. 1. Reflex Triode attached to FX-45 pulse line.

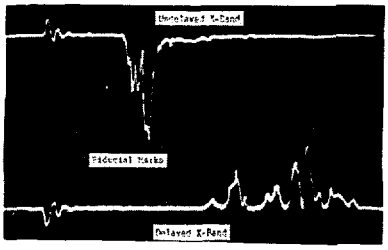

Fig. 2. Output of microwave detectors. Vertical sensitivity 20 mV/div. Sweep speed 20 ns/div.

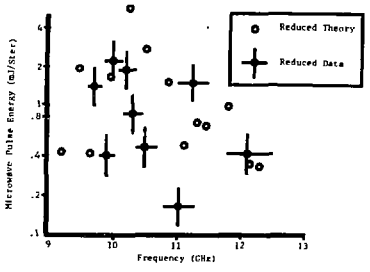

Fig. 3. Comparison of energy in peaks of computed and measured microwave spectrum between 9 and 13 GHz for an anode cathode gap of 9.5 mm.

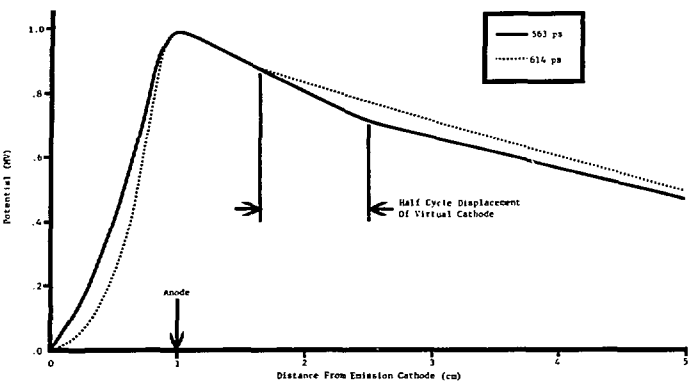

Fig. 4. Extremal forms of potential function for a constant applied voltage of 1 MV.

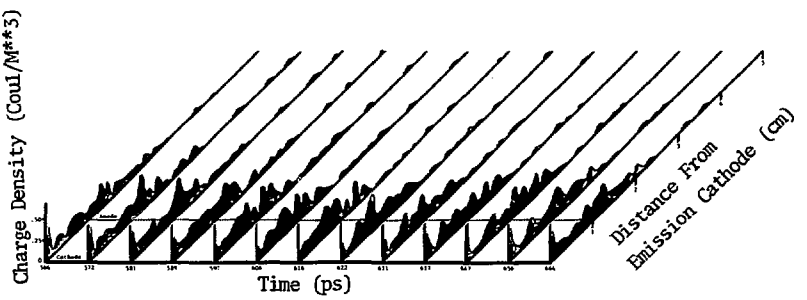

Fig. 5. Space charge density over one dominant cycle as a function of distance from emission cathode for a constant applied voltage of 1 MV.

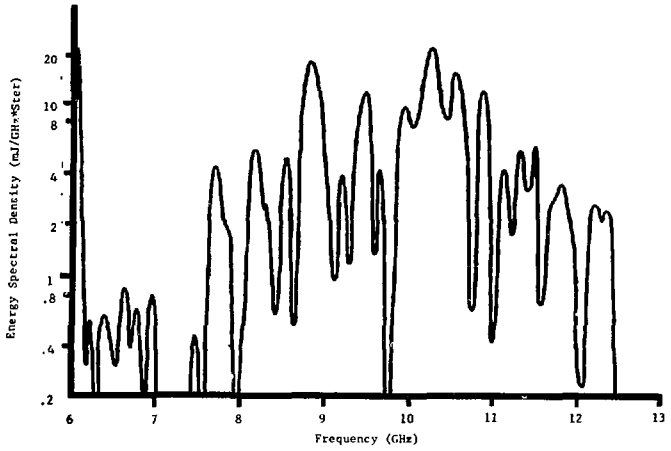

Figure 6. Microwave energy spectral density for an anode-cathode gap of 9.5 mm and time dependent applied voltage approximating machine pulse.

MICROWAVE GENERATION AND FREQUENCY CONVERSION USING INTENSE RELATIVISTIC ELECTRON BEAMS

J.M. Buzzi, H.J. Doucet, B. Etlicher, P. Haldenwang,
A. Huetz, H. Lamain, and C. Rouillé

Laboratoire de Physique des Milieux Ionisés,
Groupe de Recherche du Centre National de la Recherche Scientifique,
Ecole Polytechnique, 91128 Palaiseau Cedex, France

and

J. Cabé, J. Delvaux, J.C. Jouys, C. Peugnet

Commissariat à l'Energie Atomique, S.E.C.R.
21120 Is-s-Tille, France

ABSTRACT

Some aspects of the microwave generation and frequency conversion by relativistic electron beams are studied.

(a) Electron synchrotron maser : the excitation of microwaves by an annular relativistic electron beam propagating through a circular wave guide immersed in a longitudinal magnetic field is analyzed. This theoretical model is somewhat more realistic than previous one because the guiding centers are not on the wave guide axis.

(b) Microwave reflection is observed on a R.E.B. front propagating into a gas filled waveguide. The frequency conversion from the incident X band e.m. waves and the reflected Ka band observed signal is consistent with the Doppler model for $\beta = 0.7$. This value agrees with the average beam front velocity as measured from time-of-flight using two B_θ probes. The reflection is found to occur during the current rise time.

(c) With a low impedance device (2 Ω, 400 keV) a GW Xband emission has been observed using thin anodes and a gas filled waveguide. This emission is probably due to the self-fields of the beam and could be used as a diagnostic.

ELECTRON SYNCHROTRON MASER: THEORY

The basic theory of the synchrotron maser is well known[1,8], however, from the experimental point of view, there is still a need for a model describing more accurately the actual experimental situations.

Therefore we consider the following model : (a) the electron beam is flowing through a circular waveguide immersed in a constant longitudinal magnetic field B_o. (b) We assume that the electron beam can be represented by a distribution of rigid rotators[7] all having the same energy and Larmor radius r_L with their guiding centers centered on a circle of radius r_b (see Fig. 1). (c) We use a perturbation theory for the description of the beam-waveguide interaction. Hence this model is an extension of the model of S.P. Sprangle[7] to the case of non-centered rigid rotators.

Note that the equilibrium electron density in our model is given by

$$n_o(R) = N_o a^2 \left\{(R^2 - R_m^2)(R_M^2 - R^2)\right\}^{-\frac{1}{2}} \text{ for } R_m^2 \leq R^2 \leq R_M^2$$

$$= 0 \quad \text{elsewhere,}$$

with $R_m = r_b - r_L$ and $R_M = r_b + r_L$. N_o is defined as the average electron density given by

$$N_o = (1/\pi a^2) \int_o^{2\pi} \int_o^a n_o(R) R\,dR\,d\phi$$

Using the weak coupling approximation where TE/TM mode interactions are neglected and only $TE_{\ell n}/TE_{\ell n}$ or $TM_{\ell n}/TM_{\ell n}$ coupling terms are taken into account, on obtain[9] for TE modes

$$\omega^2 - k^2c^2 - \omega_{\ell n}^2 = \omega_p^2 \tau_{\ell n} \sum_{p=-\infty}^{+\infty} J_{\ell-p}^2(\mu) S_p \qquad (1)$$

with $\omega_p^2 = N_o e^2/\varepsilon_o m_o \gamma_o$, $\mu = \beta_{\ell n} r_b/a$ and :

$$\tau_{\ell n} = \left| (1 - \ell^2/\beta_{\ell n}^2) J_\ell^2(\beta_{\ell n}^2) \right|^{-1}$$

where $\beta_{\ell n}$ is the nth zero of $J_\ell'(x)$. Moreover,

$$S_p = \left\{ J_p^2(\lambda)\pi_p^2 + J_p'^2(\lambda)\omega'^2 \right\}/(\psi_p^2 - \omega_b^2) - 2\, J_p'(\lambda) J_p(\lambda) \pi_p/\psi_p (\psi_p^2 - \omega_b^2) \ldots$$

$$\ldots - (\omega^2 - k^2c^2)\, \beta_\perp^2\, J_p'^2(\lambda)/\psi_p^2$$

with : $\lambda = \beta_{\ell n} r_L/a$, $\omega' = \omega - k v_{//o}$, $\psi_p = \omega' - p\omega_b$, $\omega_b = eB_o/m_o\gamma_o$

$\pi_p = p\omega'/\lambda - \lambda\omega_b$, and $\omega_{\ell n} = \beta_{\ell n}\, c/a$.

For the TM modes, one obtains

$$\omega^2 - k^2c^2 - \Omega_{\ell n}^2 = \omega_p^2\, (kc - \beta_{//}\omega)^2 \mathcal{E}_{\ell n} \sum_{p=-\infty}^{+\infty} J_{\ell-p}^2(\xi)\, T_p \qquad (2)$$

with $\xi = \alpha_{\ell n} r_b/a$ and :

$$\mathcal{E}_{\ell n} = \left| J_\ell'^2\, (\alpha_{\ell n}) \right|^{-1}$$

where $\alpha_{\ell n}$ is the nth zero of $J_\ell(x)$. Moreover,

$$T_p = \left(\frac{p^2}{\nu^2} J_p^2(\nu) + J_p'^2(\nu) \right) / \left(\psi_p^2 - \omega_b^2 \right) - 2 \frac{p}{\nu} J_p(\nu) J_p'(\nu) \omega_b / \psi_p (\psi_p^2 - \omega_b^2) \ldots$$

$$\ldots + J_p^2(\nu) \left[\omega' - (\omega^2 - k^2c^2) p\omega_b / \Omega_{\ell n}^2 \right] / (kc - \beta_{//}\omega)^2 \psi_p - J_p^2(\nu)/\psi_p^2$$

with $\nu = \alpha_{\ell n} r_L/a$ and $\Omega_{\ell n} = \beta_{\ell n} c/a$. As in Sprangle's analysis[7] we obtain cyclotron and synchronous mode interactions but we keep the hybrid mode $1/\psi_p(\psi_p^2 - \omega_b^2)$ because of its stabilizing effect on the synchronous instability.

Looking for solutions of equations (1) or (2) at the intersection $(\omega_\pm, k_\pm)$ of the dispersion relation of the waveguide mode with $\psi_m = 0$, neglecting non-resonant terms, one obtains for TE modes

$$\omega \approx \omega_\pm + \delta\omega ,$$

with

$$(\delta\omega/\omega_{\ell n})^3 - 3\, q_{TE} \frac{\omega_p^2}{\omega_{\ell n}^2} (\delta\omega/\omega_{\ell n}) F_\pm^{-1} + 2\, \beta_\perp F_\pm^{-1} \frac{\omega_p^2}{\omega_{\ell n}^2}\, r_{TE} = 0 ,$$

where $F_\pm = \gamma_{//}^2 \left\{ 1 \pm \beta_{//} \sqrt{1 - \omega_{\ell n}^2/m^2\gamma_{//}^2\, \omega_b^2} \right\}$, $\omega_\pm = m\omega_b F_\pm$

with the condition $m\omega_b > \omega_{\ell n}/\gamma_{//}$ and

$$r_{TE} = \frac{\tau_{\ell n}}{4\, m}\, \lambda\, J_{\ell-m}^2\, (\mu)\, J_m'^2\, (\lambda)$$

$$q_{TE} = \frac{\tau_{\ell n}}{3}\, J_{\ell-m}\, (\mu)\, J_m'\, (\lambda) \left[J_{\ell-m}(\mu)\, J_m(\lambda) \lambda \left(\frac{m^2}{\lambda^2} - 1 \right) \ldots \right.$$

$$\ldots - \frac{\lambda^2}{m}\left(\frac{\ell-m}{\mu}\right) J'_{\ell-m}(\mu)\, J'_m(\lambda)\Big]$$

Therefore, the instability condition for TE modes is given by

$$-\frac{\omega_p^2}{\omega_{\ell n}^2}\, q_{TE}^3 / F_\pm + \beta_\perp^2 r_{TE}^2 > 0 \qquad (3)$$

The term r_{TE} represents the destabilizing effect of the synchronous mode interaction which is of relativistic origin. The term q_{TE} is more complicated because it contains the stabilizing synchronous factor (proportional to $(m^2/\lambda^2 - 1)$) and the cyclotron factor (proportional to $(\ell - m)/\mu$). It can be shown that q_{TE} can be destabilizing only if

$$\begin{cases} \ell - m > 0 & \mu < \theta_{\ell-m,1} \qquad (4a) \\ \ell - m < 0 & \mu > \theta_{\ell-m,1} \qquad (4b) \end{cases}$$

Moreover in the case (4a), for $r_b \to 0$, the cyclotron instability occurs if

$$r_L / r_b < \sqrt{\ell - m}\,/\, m \qquad (5)$$

For the TM modes, one obtains

$$(\delta\omega)^3 - 3\, q_{TM} H_\pm \omega_p^2\, \delta\omega + 2\, \omega_p^2 \omega_b H_\pm r_{TM} = 0$$

with $H_\pm = (1 - \Omega_{\ell n}^2 / m^2\gamma^2\omega_b^2)/F_\pm$ and

$$\begin{cases} r_{TM} = \dfrac{\mathcal{E}_{\ell n}}{4}\, m\, J_{\ell-m}^2(\xi)\, J_m^2(\nu) \\ q_{TM} = \dfrac{\mathcal{E}_{\ell n}}{3}\, m \left\{ J_{\ell-m}^2(\xi) J'_m(\nu) I_m(\nu) - J_m^2(\nu) J'_{\ell-m}(\xi) I_{\ell-m}(\xi) \right\} \end{cases}$$

where $I_n(x) = n\, J_n(x)/x$. The instability condition for TM mode is

$$-\frac{\omega_p^2}{\Omega_{\ell n}^2} H_\pm\, q_{TM}^3 + r_{TM}^2 > 0 \qquad (6)$$

Again, the term r_{TM} is the destabilizing effect of the synchronous interaction, but for TM modes, its origin is not relativistic. As regards q_{TM}, we have the stabilizing term (proportional to $J_{\ell-m}^2(\xi)$) due to the synchronous interaction and the cyclotron term proportional to $J_m^2(\nu)$.

q_{TM} can be destabilizing under the conditions defined by 4a and 4b.

Moreover, the cyclotron instability occurs for $r_b \to 0$ if

$$r_L/r_b < (\ell-m)/m \qquad \ell-m > 0 \qquad (7)$$

Since q and r are functions only of r_b and r_L, its interesting to calculate these functions for various modes and harmonic interactions. Examples are given in Fig.2 for the TE_{01} mode and the TE_{21} mode interacting with the first gyrofrequency harmonic. Note that r_b can vary from 0 to a, whereas r_L must satisfy the two conditions

$$\begin{cases} r_L + r_b \leq a \\ r_L < m/k_i^{\ell n} \end{cases}$$

As shown in Fig.2, the TE_{01} mode frequently observed experimentally[10-12] is essentially subject to the synchrotron maser instability. As regards the TE_{21} mode which is closer to the fundamental TE_{11}, the instability can be of relativistic or cyclotron origin.

BEAM FRONT SCATTERING EXPERIMENT

In a recent experiment[13], microwave reflection on a relativistic electron beam has been observed and explained by a beam front scattering phenomena. In the present work, microwave reflection is observed on a relativistic beam front propagating in a gas. The experimental set up is described on Fig.3. The diode (750 keV, 40 Ω, 50 μ thickness T_i foil) and the waveguide are immersed in a uniform static magnetic field B_o.

The incident microwave signal is provided by a pulsed magnetron (50 kW, 800 ns pulse duration, tunable between 8.6 and 9.6 GHz). The microwaves are injected into the circular waveguide through the rectangular-to-circular transition, which is a bidirectionnal 3 dB coupler. Therefore, half of the magnetron power leaves the device through the conical antenna and is monitored by an X-band detector at the end of a 50 m delay line. The second half of the magnetron power propagates towards the electron beam, mainly in the TE_{01} mode. The reflected signal is measured in the K_a-band with crystal detectors and a 13 m delay line.

Frequency conversion from the reflection in a waveguide by a mirror moving at speed v is given by :

$$f_1 = f_o \, (1 + 2 \, \beta\beta_g + \beta^2) \, \gamma^2 \qquad (8)$$

with $\beta = v/c$, $\gamma = (1 - \beta^2)^{-\frac{1}{2}}$ and $\beta_g = v_g/c$ where v_g is the group velocity of the incident wave. Since in our experiment, the incident wave lies in the X-band and the expected reflected wave lies in the Ka band, we see from Eq. 8 that we need a value of β close to 0.7. We have chosen to adjust the value of the beam front velocity by changing the background gas pressure in the waveguide, holding constant all other parameters : the diode voltage, the current rise time and the magnetic field (5 kG).

In order to measure the beam front velocity, two B_θ probes were located on the surface of the waveguide with a spacing of 68 cm between probes. Time-of-flight measurements between the two probes allows the determination of an average beam front velocity. Figure 4 shows the variation of this beam front velocity as a function of the air pressure. Taking into account the delay in the cables, we have determined the beam current while measuring the beam front velocity with the two B_θ probes. We found that this velocity measurement is made when the beam current in the drift tube is half of the peak value.

Without magnetron, no signals are detected during the rise time of the current. When the magnetron signal is applied, very short microwave pulses are detected in the Ka band during about 3 ns when the current reaches about 2/3 of its maximum value. This signal is attributed to the reflection on the beam front. Since the β values for the reflection in the Ka band are very limited around 0.7, one should expect that the pressure is a very critical parameter. As a matter of fact, the Ka band detectors no longer indicate any reflected signal when the pressure lies outside the range 350-450 μ, in agreement with the beam front velocity measurement (see Fig. 4). We have also varied the magnetron frequency f_o and measured the reflected frequency f_1 with a Ka-band delay line. The results are presented in Fig. 5 and compared tothe theoretical curves given by Eq. 8 for the TE_{01} and TE_{31} modes. Fairly good agreement is found for β

close to 0.7. Therefore, the corresponding velocity of the mirror is close to the beam front velocity.

In conclusion, we have observed the reflection of microwaves on a relativistic electron beam front propagating in a gas. The "mirror velocity" deduced from the relativistic Doppler shift for various incident frequencies agrees with the beam front velocity measured with B_θ probes. We have also shown that the reflection occurs during the rise time of the beam current. However, the reflected power has not yet been measured and the reflection coefficient is unknown. The specific mechanism for the change of the waveguide cut off due to the beam front in a gas has not been determined. These two points, particularly the importance of the ionization front, are presently under investigation. If ionization processes participate in the reflection mechanism, the reflection coefficient could be rather small[14].

X BAND GIGAWATT EMISSION WITH HIGH γ/γ BEAM

In an experiment intended to observe beam front scattering in a low impedance electron beam device a very strong emission of microwave had been observed[15] ($\sim$ 1 GW at 10 GHz). The scheme of the experiment is presented on Fig. 6. The cathode is a 4cm diameter graphite disk and the anode a 6μ thickness aluminized Mylar Foil. The diode is working at 400 kV with an impedance of 2Ω. After the anode the beam can propagate in a 5cm diameter 80cm length waveguide connected to a conical horn. The air pressure in the waveguide was changed from 5μ to 1 Torr. Calorimetric measurements made at the end of the 5cm waveguide indicate that the transmitted energy grows constantly from 5μ (less than 1 % of the diode energy) to 1 torr (75 % of the diode energy). Microwaves in the X-band emitted by the conical horn are monitored by a small external antenna connected to a 60 m delay line. The detected microwave emission is first growing with the background pressure, reaches a maximum value ($\sim$ 1GW) for 10μ, then decay with the pressure. An interesting fact is that the larger emission pulses have well defined frequencies 9,11 and 14 GHz. These frequencies

are practically independent of the background gas pressure. Since there is no external magnetic field and since $\omega/\gamma \gg 1$, the self-fields of the beam are probably responsible of the microwave emission. However the specific physical process occuring in our case is not known. The most important self-field can be electric (as electron oscillations in a reflex diode[16]) or magnetic (B_θ field along the beam path for example) and experiments are in progress to determine if the process is a diode or a beam propagation phenomena. In both cases one can expect that the microwave emission can be an interesting diagnostic for high ω/γ beam.

REFERENCES

1. R.Q. Twiss, Australian J. Phys. 11, 564 (1958)
2. J. Schneider, Phys. Rev. Letters 2, 504 (1959)
3. G. Bekefi, J.L. Hirshfield and S.C. Brown, Phys. Rev. 122, 1037 (1961)
4. M. Friedman, D.A. Hammer, W.M. Manheimer, and S.P. Sprangle, Phys.Rev. Lett. 31, 752 (1973)
5. E. Ott and W.M. Manheimer, IEEE Trans. On Plasma Sci. PS-3, 1 (1975)
6. S.P. Sprangle and W.M. Manheimer, Phys. Fluids 18, 224 (1975)
7. S.P. Sprangle, J. Appl. Phys. 47, 2935 (1976)
8. See also "Sources based on relativistic electron beams" IEEE Trans. on Microwave theory and techniques MTT-25, 513 (1977)
9. B. Etlicher, A. Huetz, J.M. Buzzi, D. Lequeau and H.J. Doucet, PMI report 836, september 1977, submitted for publication
10. Y. Carmel, J.A. Nation, Phys. Rev. Lett. 31, 806 (1973)
11. V.L. Granatstein, M. Herndon, P. Sprangle, Y. Carmel and J.A. Nation, Plasma Physics 17, 23 (1974)
12. V.L. Granatstein, P. Sprangle, R.K. Parker and M. Herndon, J. of Appl. Phys. 46, 2021 (1975)
13. V.L. Granatstein, P. Sprangle, R.K. Parker, J. Pasour, M. Herndon and S.P. Schlesinger, Phys. Rev. A 14, 1194 (1976)
14. M. Lampe, E. Ott, W.M. Manheimer, S. Kainer, IEEE Trans. on Microwave Theory and Techniques MTT-25, 556 (1977)

15. J.M. Buzzi et al., IEEE Transaction on microwave theory and techniques, MMT-25, 559 (1977)
16. R.A. Mahaffey, P. Sprangle, J. Golden and C.A. Kapetanakos, NRL Memorandum Report 3504, May 1977.

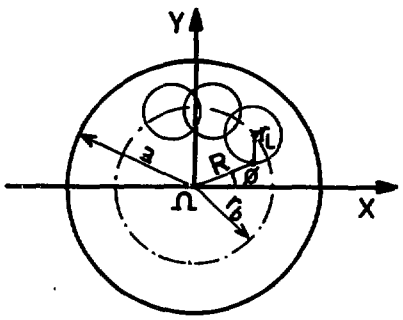

Figure 1

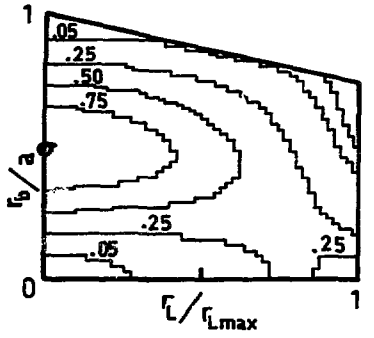

Fig.2a Altitude chart of $q_{TE}/(q_{TE})max$ for the TE_{o1} mode interacting with the first harmonic $(q_{TE})max = 0.174$

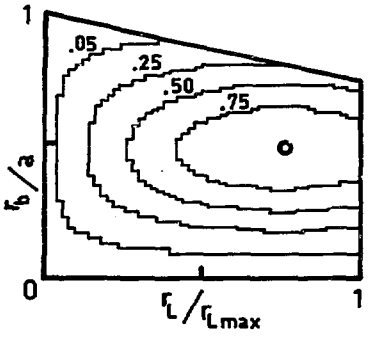

Fig.2b Altitude chart of $r_{TE}/(r_{TE})$ max for the TE_{o1} mode interacting with the first harmonic $(r_{TE})max = 3{,}11 \times 10^{-2}$

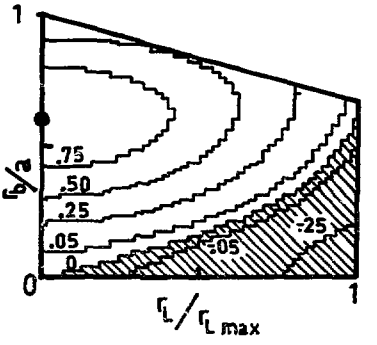

Fig.2c Altitude chart of $(q_{TE})/(q_{TE})$ max for the TE_{21} mode interacting with the first harmonic $(q_{TE})max = 0.209$. The shadded area is subject to cyclotron instability.

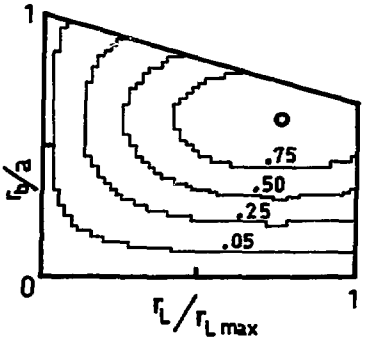

Fig.2d Altitude chart of $r_{TE}/(r_{TE})$ max for the TE_{21} mode interacting with the first harmonic (q_{TE}) max $= 3.73 \times 10^{-2}$.

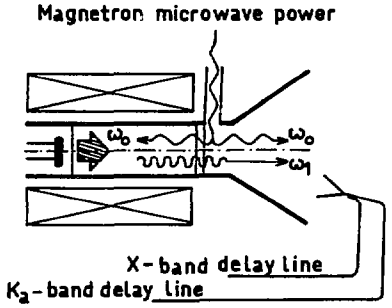

Fig. 3

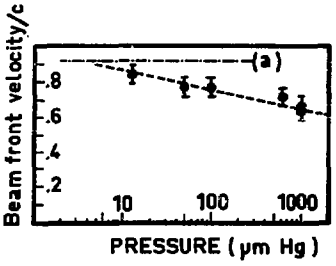

Fig. 4

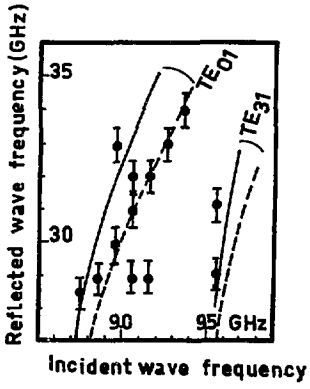

Fig. 5

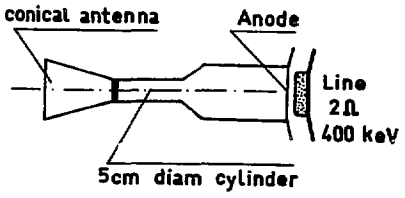

Fig. 6

COHERENT MICROWAVE SCATTERING FROM INTENSE RELATIVISTIC ELECTRON BEAMS - A POWERFUL, TUNABLE SOURCE OF MILLIMETER AND SUBMILLIMETER RADIATION

V.L. Granatstein, R.K. Parker, J.A. Pasour, P. Sprangle, and A.T. Drobot
Naval Research Laboratory, Washington, D.C. 20375

ABSTRACT

Microwaves have been backscattered from magnetized, intense, relativistic electron beams to produce high-power outputs at a frequency far above that of the incident radiation. Two phenomena have been studied: (1) reflection from a refractive-index discontinuity near the beam front, and (2) stimulated magneto-Raman scattering from plasmons in the body of the beam.

With the beam front technique, a 250 kW, incident wave at 9.3 GHz was reflected to yield a 5 MW output at 50 GHz. The center frequency of the output radiation could be tuned over an octave by changing the beam-front velocity.

Stimulated scattering offers the advantage of still larger frequency shifts but requires a very high-power, incident, pump wave. A 2 cm pump wave with power ~ 100 MW has been scattered to produce an output of 1 MW at 400 μm. Experiments are in progress in which the multigigawatt output from an S-band magnetron of unique design will be scattered from a 2 MeV, 0.2 TW, electron beam. Analysis of the saturation processes in stimulated Raman scattering indicates that several percent of the beam power may be converted to scattered radiation ($\lambda \sim 1$ mm) in this experiment.

INTRODUCTION

The development of coherent radiation sources operating at millimeter and submillimeter wavelengths presents a challenge to two disparate technologies. Attempts to extend laser technology into this wavelength

range using optically-pumped molecular lasers will ultimately be constrained by the consequences of the Manley-Rowe relationship which states that the laser efficiency must be less than the radio of output to pump frequencies. Alternatively, experience has shown that conventional electron beam microwave devices cannot be extended into this wavelength range without a severe reduction in output power. In this case, the constraints are more practical than theoretical. As the characteristic dimension of the slow wave structure or cavity is reduced, the electron beam power that can be handled becomes severely limited.

Recent experiments[1,2,3] with coherent microwave scattering from an intense relativistic electron beam suggest an alternate approach. In these experiments, low frequency microwaves have been coherently backscattered from counterstreaming electron beams to produce an output wave which has been doubly Doppler shifted to a much higher frequency. Since the output frequency is higher than that of the pump wave, the Manley-Rowe relationship is favorable. Moreover, the output wavelength is independent of the characteristic dimensions of the interaction volume.

The coherent scattering mechanisms studied in these experiments fall into two types; mirror-like scattering from the rapidly rising front edge of the beam and stimulated scattering from induced electron density oscillations in the body of the electron beam. The two types of scattering are illustrated in Fig. 1. Both types of scattering are enhanced by cyclotron resonance phenomena.

In both methods, the frequency of the backscattered wave, ω_s is related to the frequency of the incident wave, ω_i by the relationship

$$\omega_s = (1 + \beta)^2 \gamma^2 \omega_i \ , \qquad (1)$$

where β and γ are the normalized velocity and normalized total energy of the electrons, respectively, i.e., $\beta = v/c$ and $\gamma = 1 + (T/mc^2) =$

$(1 - \beta^2)^{-\frac{1}{2}}$.

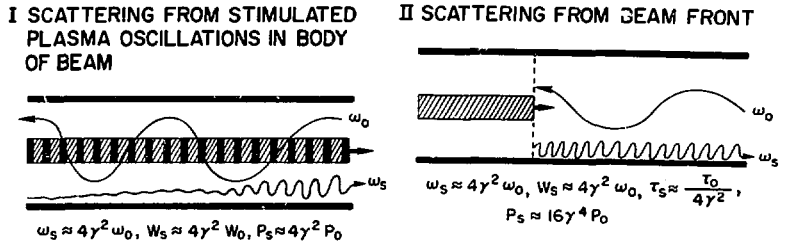

Fig. 1 Two types of backscattering of an input wave ω_o from a counterstreaming relativistic electron beam.

Here T is the electron kinetic energy. It should be appreciated that the Doppler shift can be large; for example, with 2 MeV electrons $\gamma \simeq 5$ and $\beta \simeq 1$ so that $\omega_s \simeq 100\ \omega_i$ and an incident wave with a wavelength of 3 cm would yield a backscattered wave at 300 μm. Moreover, the output wavelength is adjustable by changing either ω_i or the electron energy. Thus, devices based on coherent scattering promise to provide continuously-tunable, coherent sources at submillimeter wavelengths where no such sources are presently available.

Unlike other common mechanisms for frequency conversion (e.g. harmonic generation in nonlinear components, or submillimeter generation in optically-pumped molecular lasers), coherent scattering promises energy and power gain. The energy of the backscattered output wave, W_s, is related to the energy of the input wave, W_i, by

$$W_s = (1 + \beta)^2 \gamma^2 R W_i \ , \qquad (2)$$

where R is the reflectivity of the beam (i.e. the fraction of incident photons which result in backscattered photons). Clearly when the reflectivity approaches unity, energy gain may be achieved that is almost as large as the Doppler frequency shift. Moreover, in beam-front

scattering, relativistic time compression also occurs and the power gain will be larger than the energy gain by an additional factor of $(1 + \beta)^2\gamma^2$.

MAGNETO-RESONANT BEAM FRONT SCATTERING

The interesting features of an electromagnetic wave interaction with a reflector moving at relativistic speeds was first recognized by Albert Einstein in 1905.[4] In 1952, Landecker[5] described how the front of a magnetized relativistic electron beam could provide such a relativistic reflector. However, an experimental demonstration of beam front scattering was not made until 1976. A group at NRL demonstrated the conversion of a 3 cm incident wave into a 1 cm output wave with output power being twice as large as incident power.[1] In more recent studies at NRL,[2] the velocity of the beam-front electrons has been increased by steepening the rise time of the accelerating voltage pulse. This has resulted in a demonstration of converting a 3 cm incident wave into a 6 mm output wave with power in the output wave exceeding incident power by an order of magnitude.

The experimental configuration used in these recent beam-front scattering studies is shown schematically in Fig. 2. The relativistic electron beam was generated by applying a 1-MV-peak, 60-nsec-duration voltage pulse to a cold-cathode, field-emission diode. The electrons were injected through a 13-mm-diameter aperture in a graphite anode into an evacuated, 22-mm-diameter drift tube in a uniform, axial, magnetic field. A Lucite pulse-sharpening switch was inserted into the cathode shank to decrease the cathodic voltage rise time from 15 nsec to 5 nsec and the beam current rise time from 7 nsec to ~ 3 nsec. The peak beam current was ~ 2 kA both with and without the switch. From the damage pattern on a Lucite disk placed in the drift tube, the beam profile was

found to be relatively uniform over its 12-mm diameter.

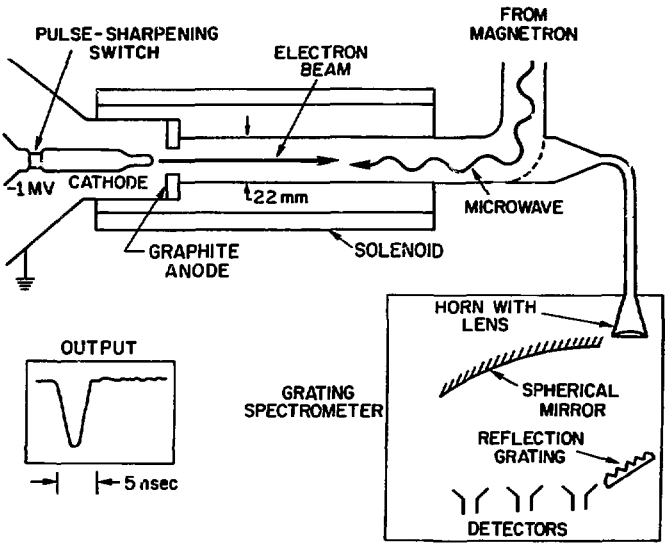

Fig. 2 Beam front scattering experiment. (Inset: oscilloscope trace of output signal.)

The counterstreaming microwave signal was supplied by a 9.3-GHz magnetron. The 500-kW, 50C-nsec-duration pulse was transported into the drift tube through a 90° bend in rectangular waveguide and a rectangular-to-circular transition. Consequently, the incident wave was linearly polarized and propagated in the fundamental waveguide mode (TE_{11}). The high-frequency output passed through 4-mm-diameter holes in the sidewall of the 90° bend, and a tapered transition to a Ka-band (26.5 - 40 GHz) waveguide, which led to a multichannel grating spectrometer. Broad-band crystal detectors connected to 1-cm-wide rectangular horns were used to monitor the output, which was found to consist of two perpendicular components (suggesting a circularly-polarized reflected wave).

When the diode voltage and magnetron pulses were synchronized and

the magnitude of the external magnetic field was properly adjusted, a strong high-frequency output pulse was observed. A typical oscilloscope trace of the output, obtained without the pulse-sharpening switch, is inset into Fig. 2.

Representative data, taken at two values of magnetic field, 6.8 kG and 7.0 kG, are shown in Fig. 3. From the spectral profiles in Fig. 3, it can be seen that the output wavelength was slightly shorter at the higher value of magnetic field.

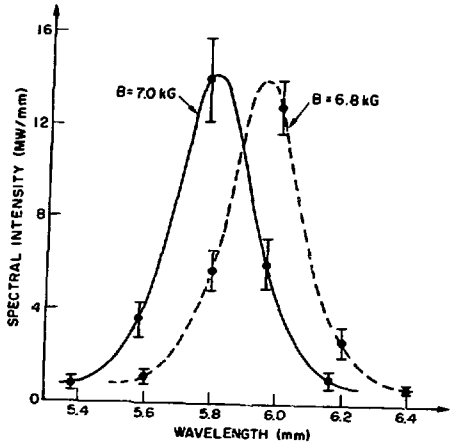

Fig. 3 Spectral intensity profiles with two different axial magnet fields.

According to the analysis presented by Landecker,[5] reflection from a cold, uniform, semi-infinite electron beam propagating along an external field occurs near the cyclotron resonance. In a waveguide geometry, the resonance occurs at the intersection of the empty-waveguide mode (TE_{11})

$$\omega^2/c^2 - k_z^2 - b_{11}^2 = 0 \qquad (3)$$

and the fast beam-cyclotron mode

$$\omega - vk_z - \Omega_o/\gamma = 0 \,, \qquad (4)$$

where $b_{11} = 1.84/r_g$, r_g is the guide radius, and $\Omega_o = eB_o/m$ is the non-relativistic electron cyclotron frequency. Given a particular incident-wave frequency and external magnetic field, this condition determines the electron velocity required for reflection. Then the Doppler-shifted reflected-wave frequency is found from Eq. (1). For example, given a 9.3-GHz incident wave and magnetic fields of 6.8 and 7.0 kG, the wavelength of the reflected wave should be 6.3 and 6.0 mm, respectively. These values are in reasonable agreement with the experimental observations, indicating that reflection does occur near magnetic resonance.

Over the wavelength range in Fig. 3 of approximately 5.5 - 6.2 mm, the attenuation of the output section was quite constant (~ 30 dB), and the various calibration data used to compute the absolute intensities plotted in Fig. 3 have a maximum cumulative uncertainty of less than ± 2 dB. Consequently, the total integrated power, to within a factor of 1.6, is 5 MW or an order of magnitude larger than the incident power. The spectral width (FWHM) of the output is $\Delta\lambda/\lambda = 5\%$.

The beam front scattering process thus appears to be attractive for producing very high-power, high frequency pulses. However, it has a feature which may be a drawback in many practical situations: the output pulses produced are very short in duration. The scattering only occurs for the time it takes the beam front to propagate through the limited length of the interaction region, L, and in addition there is a relativistic time compression. Thus the duration of the output pulse is only $L/v(1 + \beta)^2\gamma^2$, typically on the order of one nanosecond as may be seen from the insert in Fig. 2.

STIMULATED RAMAN SCATTERING

The second type of scattering, stimulated scattering from induced density fluctuations in the body of the electron beam, is not characterized by short output pulses, and can in fact produce an output pulse as

longlasting as the electron current pulse. This scattering process involves an instability in which the pondermotive force (radiation pressure force) generated by interaction between the incident and scattered e.m. waves modulates the beam electron density. This modulation in turn produces stronger scattering. The growth of the instability depends on the strength of the incident pump wave, and for e-folding lengths on the order of centimeters, one normally requires pump wave power at a level ≥ 10 MW/cm^2.

The production of submillimeter radiation by stimulated scattering of a microwave signal from a relativistic electron beam was first proposed by Pantell.[6] Subsequent analyses of submillimeter wave production by stimulated scattering in the presence of a constant magnetic field demonstrated that the process could be strengthened by a resonance effect when the frequency of the incident pump wave is close to the electron cyclotron frequency as seen in the rest frame of the electron beam.[7,8]

The ratio of the Debye length in the electron beam to the scattered wavelength has also been shown to be an important beam frame parameter.[8,9] When this ratio is large, stimulated Compton scattering may occur. The recent experiment by Elias et al.[10] in which a relativistic electron beam was used to amplify an infrared wave ($\lambda = 10.6$ μm) has been shown[11,12] to constitute a demonstration of stimulated Compton scattering. When the Debye length to wavelength ratio is small, however, the stimulated scattering process changes in character and can best be described as being stimulated Raman scattering. The scattering interaction is now accompanied by a growing electrostatic oscillation at the beam plasma frequency ω_p. Moreover, the growth rate of the scattering instability is large compared to that experienced in stimulated Compton scattering.

An experiment has been carried out at NRL to investigate stimulated Raman scattering in the presence of a constant magnetic field.[3] The experimental arrangement is shown in Fig. 4. A voltage pulse (60 ns, 2 MV) is applied to a cold, field-immersed cathode. A resultant, 30 kA, annular, electron beam is injected axially into an evacuated drift tube along the lines of the externally applied magnetic field. The beam passes through a region where the magnetic field is periodically rippled by a structure of alternating iron and aluminum rings which are placed inside the bore of the solenoid magnet and surround the drift tube. The magnetic field ripple has an axial period of 3.8 cm and a peak-to-peak magnitude

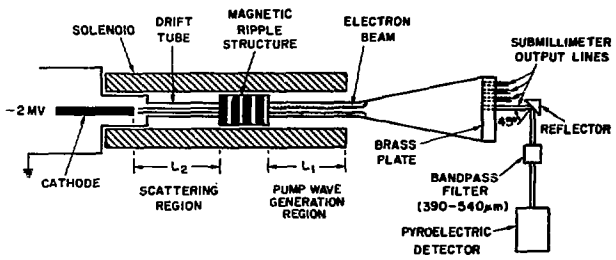

Fig. 4 Stimulated magneto-Raman scattering experiment at NRL[3] (stimulated Raman scattering experiments are also underway at Columbia University).

$\Delta B_z/B_z \sim 10\%$. As the electrons pass through the rippled magnetic field, a large fraction of their streaming energy is converted into motion transverse to the axis. The electrons with large transverse energy then enter an unrippled field region, L_1, where strong conversion of transverse electron energy to microwave radiation has been shown to occur[13,14] through the cyclotron maser mechanism. For the parameters in the present experiment, microwave radiation has been measured[15] with a peak value of several hundred megawatts ($E_o \simeq 10^5$ V/cm) at $\omega_o/2\pi \simeq 14$ GHz.

This 2 cm radiation propagates along the drift tube into a conical section where it is reflected from a brass plate that terminates the cone. The reflected wave backstreams up the drift tube where it can interact again with the electron beam. The 2 cm microwaves can act as an incident pump wave and drive a stimulated scattering instability. The interaction which will produce a scattered wave at the highest frequency takes place in a region, L_2, where the axial component of electron velocity is largest.

The submillimeter scattered wave is monitored through a series of goldplated tubes passing through the brass plate. Each tube passes the radiation through a wave filter with passband 390 - 540 μm, and into a calibrated pyroelectric detector. By measuring the submillimeter power in each tube a radial profile can be deduced, and the total submillimeter radiation striking the brass plate can then be calculated.

Total radiated power striking the brass plate in the 390 - 540 μm passband was found to be ~ 1 MW when the applied magnetic field was adjusted to 13 kG, and the position of the magnetic ripple structure optimized. The magnetic resonance at 13 kG had a half-width of ~ 3 kG. Reducing the magnitude of the voltage applied to the cathode from the usual 2 MV level had the effect of rapidly diminishing the submillimeter output; for voltage magnitude $\leq$ 1.5 MV no submillimeter output could be detected.

Dependence of the submillimeter radiation on the position of the ripple structure was studied. As the ripple structure was moved downstream from the cathode, the scattering region L_2 was lengthened, while simultaneously shortening the region L_1, in which the pump wave is generated. Thus, one expects an initial increase in the submillimeter

output as the scattering became stronger, followed by a decreasing submillimeter output as the pump wave weakened. The experimental results are shown in Fig. 5 where the total power striking the brass plate in the 390 - 540 μm passband is plotted vs. L_2. For 7 cm < L_2 < 41 cm (55 cm > L_1 > 21 cm), the expected behavior was observed with the submillimeter output having a maximum at L_2 = 30 cm (L_1 = 32 cm).

The initial increase in the submillimeter output as the ripple structure was moved downstream indicates the importance of the scattering region, L_2, to the production of submillimeter radiation, and supports the view that the dominant process involved scattering of electromagnetic waves from a fast streaming electron ensemble. Further support comes from the observation that when the magnetic field at the cathode was made nonuniform so as to give the electrons in region L_2 a larger transverse energy and a corresponding smaller streaming energy, the submillimeter output signal disappeared.

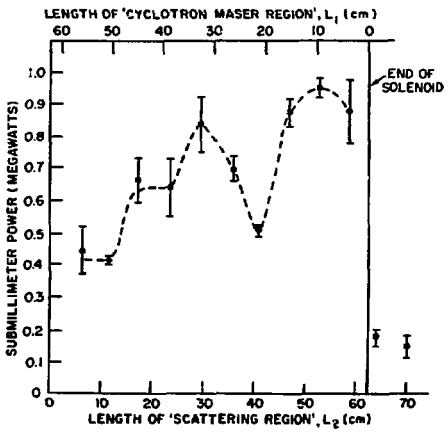

Fig. 5 Total radiated power in 390 - 540 μm passband versus length of scattering regions.

A relativistic analysis of stimulated, magneto-resonant, Raman scattering has been performed, and calculations have been carried out for the following set of parameters: $\omega_o/2\pi$ = 14 GHz; E_o = 8 x 10^4 V/cm; axial magnetic field B_o = 16 kG; γ_z = 5.3; $\omega_p/2\pi$ = 3.5 GHz; and $v_p \to \infty$.[9] The predicted growth rate for the scattered wave at 440 μm wavelength was $\Gamma = 10^{10}$ sec^{-1}, implying an e-folding length for the submillimeter radiation of 3 cm. The parameters used in this calculation are close to those realized in the experiment described above. Thus, the observation of a substantial rise in submillimeter radiation as L_2 is increased from 7 cm (~ 2 e-folding lengths) to ≥ 30 cm (≥ 10 e-folding lengths) is consistent with the model of stimulated magneto-resonant Raman scattering. Stimulated Raman scattering experiments have also been carried out at Columbia University.[16]

The experimental configuration depicted in Fig. 4 has a distinct disadvantage in that both pump wave generation and stimulated scattering occur in the same e-beam. This does not allow for separate optimization of each process and complicates interpretation of the experimental results. Furthermore, the pump wave may be significantly attenuated as it travels back through the perturbed electrons in the pump wave generation region before entering the scattering region. To overcome these disadvantages, the new experimental configuration pictured in Fig. 6 is presently being assembled at NRL. Two synchronized pulsed-power systems are being employed. The pulse-forming network from a Febetron 701 flash x-ray system (peak power = 3.6 GW) will be used to drive an S-band magnetron that will furnish a multi-gigawatt pump wave with λ_o = 9.4 cm.

The magnetron being developed for this purpose is based on a hybrid inverted coaxial design.[17] Like the usual inverted coaxial magnetron,[18,19] this configuration has a grounded cathode. However, an additional

coaxial cavity has been inserted between the cylindrical output waveguide and the anode slow-wave structure. This hybrid approach is ideally suited for high peak-power generation because the number of anode cavities (power generating sections operating in parallel) which can be stably oscillated in the π mode is comparatively large. Problems with RF vacuum breakdown are reduced by coupling alternate anode sections to the coaxial cavity through separate coupling slots. The symmetry of this feed drives TE_{011} mode oscillations in the cavity which because of its high Q acts in turn as a frequency and mode stabilizer for the anode circuit. The power within the cavity is then coupled to the TE_{01} mode in the output cylindrical waveguide by again using a series of symmetrical axial slots in the intervening wall. The field configuration of the TE_{01} mode is optimum for strong interaction with an annular electron beam.

The larger VEBA accelerator (peak power = 0.2 TW) will provide the annular electron beam in which stimulated magneto-resonant Raman scattering may take place. The backscattered output radiation is expected to be at $\lambda_s \approx 1$ mm. Potentially, a significant fraction of the VEBA electron beam may appear in the scattered wave. (Note that $P_o\ \omega_s/\omega_o \sim$ 0.1 TW.) Saturation of the stimulated scattering process is expected to occur in this experiment because of electron trapping. Quantitative calculations of the saturation level of output power are in progress, and preliminary results indicate that several percent of the beam energy may be converted to scattered radiation.

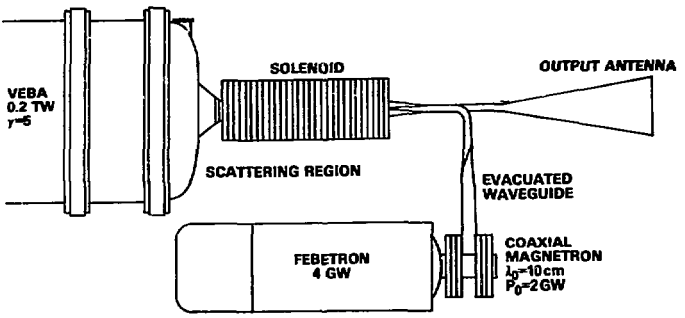

Fig. 6 Proposed ultra-high-power millimeter-wave Dopplertron.

REFERENCES

1. V. L. Granatstein, P. Sprangle, R. K. Parker, J. Pasour, M. Herndon and S. P. Schlesinger, Phys. Rev. A14, 1194 (1976).

2. J. A. Pasour, R. K. Parker, V. L. Granatstein, M. Herndon and S. P. Schlesinger, Bull. Am. Phys. Soc. 21, 1112 (1976); also, J. A. Pasour, V. L. Granatstein and R. K. Parker, submitted to Phys. Rev. A.

3. V. L. Granatstein, S. P. Schlesinger, M. Herndon, R. K. Parker and J. A. Pasour, Appl. Phys. Lett. 30, 384 (1977).

4. A. Einstein, Ann. Phys. 17, 891 (1905).

5. K. Landecker, Phys. Rev. 66, 852 (1952).

6. R. H. Pantell, G. Soucini and H. E. Puthoff, IEEE J. Quantum Electron. QE-4, 905 (1968).

7. V. P. Sukhatme and P. E. Wolf, IEEE J. Quantum Electron. QE-10, 870 (1974).

8. P. Sprangle and V. L. Granatstein, Appl. Phys. Lett. 25, 377 (1974).

9. P. Sprangle, V. L. Granatstein and L. Baker, Phys. Rev. A12, 1697 (1975).

10. L. Elias, W. Fairbank, J. M. J. Madey, H. A. Schwettman, and T. Smith, Phys. Rev. Lett. 36, 717 (1976).

11. F. A. Hopf, P. Meystre, M. O. Scully, and W. H. Louisell, Opt. Commun. 18, 413 (1976), and Phys. Rev. Lett. 37, 1342 (1976).

12. A. Hasegawa, K. Mima, P. Sprangle, H. H. Szu, and V. L. Granatstein, Appl. Phys. Lett. 29, 542 (1976).

13. M. Friedman and M. Herndon, Phys. Rev. Lett. 28, 210 (1972); Phys. Rev. Lett. 29, 55 (1972); Phys. Fluids 16, 1982 (1973).

14. V. L. Granatstein, P. Sprangle, M. Herndon, R. K. Parker and S. P. Schlesinger, J. Appl. Phys. 46, 3800 (1975).

15. V. L. Granatstein, M. Herndon, R. K. Parker and S. P. Schlesinger, IEEE Trans. MTT-22, 1000 (1974).

16. P. Efthimion and S. P. Schlesinger, Bull. Am. Phys. Soc. 21, 1113 (1976); also, T. C. Marshall, M. R. Mross, P. Efthimion and S. P. Schlesinger, Bull. Am. Phys. Soc. 21, 1113 (1976).

17. G. K. Farney, private communication.

18. J. Feinstein and R. J. Collier, "Crossed-Field Microwave Devices," (E. Okress, ed.), Academic Press, New York, 1961, p. 123-134.

19. J. F. Hull, "Crossed-Field Microwave Devices," (E. Okress, ed.), Academic Press, New York, 1961, p. 291-300.

ZERO FREQUENCY PUMPED STIMULATED RAMAN SCATTERING BY AN INTENSE RELATIVISTIC ELECTRON BEAM

S. P. Schlesinger and P. C. Efthimion
Columbia University, New York, N.Y. 10027

Further investigations into the physical processes involved in the generation of high powered mm and cm radiation resulting from stimulated Raman scattering by an intense relativistic electron beam in a rippled magnetic field are presented and compared for two different configurations. An estimate of growth rate magnitude and the dependence on pumping power both seem consistent with a theory.

During the last few years investigators have observed high-powered millimeter and submillimeter radiation from intense relativistic electron beams undergoing stimulated Raman scattering processes[1-3]. In this coherent interaction, a low frequency electromagnetic pump wave is backscattered from a relativistic electron beam to yield radiation whose frequency is much larger than that of the pump wave[4]. In order to obtain an e-folding length of a few centimeters, the pump wave must induce transverse oscillations of electrons with velocity $v_\perp \approx 0.1C$. This corresponds to a pump wave $\approx 10^9$W in the beam frame.

Presently, there are two methods of providing an adequate pump wave: (1) generate an electromagnetic wave to serve as the pump[1] and (2) arrange for the electron beam to propagate in a long spatially rippled magnetic field with a wavenumber η[2,3]. This paper is concerned with scattering by means of the second method. The spatially rippled magnetic field has a zero frequency and a wavenumber η in the lab frame. However, the rippled magnetic field amplitude and wavenumber appear as an electro-

magnetic wave in the beam frame. An expression for the backscattered frequency (ω_s) as a function of the period of the rippled field (L) is derived from the conservation of energy and momentum during the scattering process, as well as the appropriate relativistic transformations:

$$\omega_s \simeq 2\gamma^2 \eta V = 2\gamma^2 (2\pi/L) V, \qquad (1)$$

where V is the velocity of the electron beam, and $\gamma \triangleq (1-(V/C)^2)^{-1/2}$ is the relativistic factor. With L $\simeq$ 1 cm and $\gamma \simeq 2$, 1-2 mm radiation should be generated.

In this paper, we compare the radiation characteristics of two zero frequency pumped Raman scattering experiments: (1) an experiment employing a 1.4 cm period rippled magnetic field[2] and (2) one using a 6 mm pitched helical undulator[3]. For the 1.4 cm period experiment, the drift tube is a coaxial waveguide with alternating brass and iron rings internally loaded in the center conductor. The electron beam parameters are 750 KV($\gamma \simeq 1.7$) and 10KA. The helical configuration has the beam propagate in a smooth iron tube with a deep-grooved helical screw of 6 mm pitch machined in the outer wall. In this case, the beam parameters are 860 KV($\gamma \simeq 2.5$) and 12KA. In both configurations, $\Delta B/B = 0.05$ as long as the homogeneous magnetic field is below the 13KG saturation level of the iron. The millimeter waves were measured by a 4mm delay line and a pyroelectric detector employing wire mesh fitters to estimate wavelength.

The millimeter radiation generated by these two configurations is shown in Fig. 1[2,3]. For both experiments, the radiation has two fundamental characteristics: (1) the shortest wavelength radiation exponentially grows with magnetic field and (2) longer wavelength radiation exhibits a magneto-resonance. The shorter wavelength indication has a

frequency $w \simeq 2\gamma^2\eta V$ and thus it is the backscattered wave. Up to 12 KG, the radiation power appears to exponentially grow with no indication of saturation. Perhaps a further increase in magnetic field will result in a power increase above the 0.5-1.5 MW already achieved.

It appears that the exponential change in radiation power in both experiments is merely a manifestation of increasing the quiver velocity ($v_\perp$) and thus enhances the growth rate of the Raman scattering process. For the case of an electron beam in a long rippled magnetic field, the quiver velocity ($v_\perp$) in the beam frame is

$$v_\perp = \frac{eVB_r}{\gamma m(\eta V - \frac{\Omega}{\gamma})} \qquad (2)$$

where B_r is the radical amplitude of the magnitue field ripple, m and e are the electron rest mass and charge, and $\Omega = eB/mc$. When the homogeneous magnetic field is increased while the iron used to form the ripple field has not saturated, the radical amplitude of the ripple field will increase. Thus a sweep of homogeneous magnetic field will change the growth rate, and the radiation power changes by an exponential amount. This effect is presently being investigated in an experiment where the ripple field amplitude may vary independently of the homogeneous field[5].

It is interesting to compare the expected e-folding length predicted by the growth rate for stimulated Raman scattering derived by Sprangle, et al.[6], with the observed radiation. For the case of the 1.4 cm period undulator, the interaction length of the experiment is 70 cm. We now ask the question, at what value of magnetic field will the back-scattering wave power be over some reasonable range, say ~ 10-100KW? Estimating the noise level to be 0.1-1KW[7], a 20dB amplification of the noise level is required to generate the 10-100KW of millimeter radiation.

This 20 dB gain corresponds to $\Gamma = 1.6 \times 10^9$ sec^{-1}, and from Eq. (2) and Sprangle's grow rate expression we obtain $B \sim 8$KG. From Fig. 1, 10-100KW of radiation is observed surprisingly close to the prediction.

Returning to Fig. 1, note the longer wavelength radiation has an order of magnitude greater power and exhibits a magneto-resonance similar to that predicted by theory. The 8MW of 2 mm radiation is the largest power observed from a stimulated Raman scattering process to this date. However, this radiation does not peak according the the relationship[4]

$$\eta V = \frac{\Omega_c}{\gamma} , \tag{3}$$

but appears to follow the empirical relation[2]

$$\eta V - \frac{\Omega_c}{\gamma} \simeq \omega_{co} , \tag{4}$$

where ω_{co} is a TM cutoff frequency of the drift tube. It is possible that the observation of two high-powered radiation frequencies may be due to the triangular shape of the beam voltage pulse. A beam with such a voltage characteristics will have the relativistic factor γ varying over the entire pulse which can result in multiple radiation frequencies. Preliminary experiments with a rectangular shaped voltage pulse appear to produce higher power levels at just one wavelength. Further research into the effect of pulse shape as well as independently varying ΔB and B is currently underway[5].

*Work supported by AFOSR Grant No. F44620-75-C-0055.

REFERENCES

1. V. L. Granatstein, S. P. Schlesinger, M. Hendon, R. K. Parker, and J. A. Pasour, Appl. Phys. Lett. 30, 384 (1977).
2. P. C. Efthimion and S. P. Schlesinger, Phys. Rev. A. 16, 633 (1977).
3. T. C. Marshall, S. Talmadge, and P. C. Efthimion, Appl. Phys. Lett. 31, 320 (1977).
4. P. Sprangle, V. L. Granatstein, and L. Baker, Phys. Rev. A. 12, 1697 (1975).
5. T. C. Marshall, F. Sandel, and R. M. Gilgenbach, see following paper in this publication.
6. V. L. Granatstein and P. Sprangle, IEEE Trans. on Microwave Theory and Techniques, MTT-25, 545 (1977).
7. H. Motz, J. Appl. Phys. 22, 527 (1951).

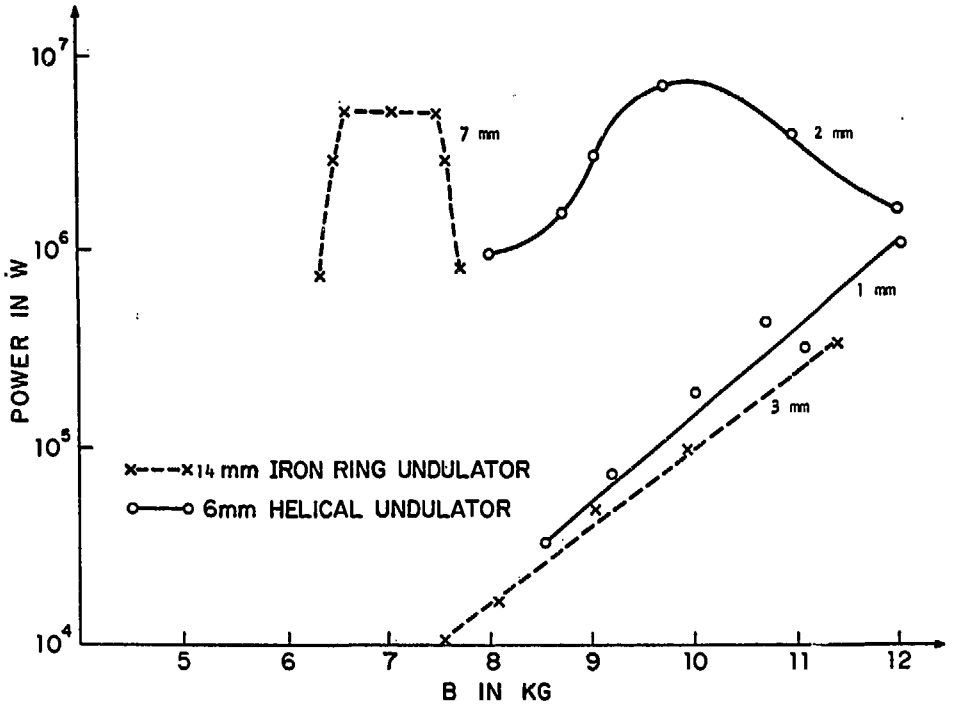
POWER IN W
10^7
10^6
10^5
10^4
7 mm
2 mm
1 mm
3 mm
×---×14 mm IRON RING UNDULATOR
o——o 6mm HELICAL UNDULATOR
5
6
7
8
9
10
11
12
B IN KG

Fig. 1

MILLIMETER WAVE GENERATION THROUGH STIMULATED SCATTERING WITH AN INTENSE RELATIVISTIC ELECTRON BEAM AND A CONTROLLED ZERO-FREQUENCY PUMP*

T. C. Marshall, F. L. Sandel, and R. M. Gilgenbach
Plasma Laboratory, Columbia University, New York, New York 10027

Several megawatts of radiation, at $1 < \lambda < 2$mm, have been generated by the interaction of a cold beam with a rippled magnetic field, in a scaled-up version of an earlier experiment. In one mode of operation, the beam propagates in an evacuated cylindrical waveguide along a solenoidal field ($B_o \approx 10$ kG) which includes a periodic iron structure, or undulator. The short-wavelength radiation output maximizes at B_o which depends on waveguide diameter and beam γ. A new pulsed-current, non-ferro-magnetic undulator with adjustable ripple period (≤ 1 cm) gives similar performance but with a sharper magnetic resonance; the field ripple amplitude can be increased up to 6%. The output power increases exponentially with ripple amplitude.

Experimental research on a multimegawatt source of radiation at wavelength $\approx 1 - 2$ mm, using an intense relativistic electron beam (5 - 10 kA, 900 kV, 15 nsec pulse), has recently been published [1,2]. The process by which radiation is generated is believed to be a parametric pumping of the beam modes by a periodic rippled magnetic field. This method which is called the "Zero-Frequency Pump" is related to the stimulated Raman scattering process [3] which has been suggested as the cause of submillimeter radiation observed in a related experiment [4]. Our experiment also bears resemblance to the "free electron laser" [5], in that both use a periodic rippled magnetostatic guide field. In both

* Work supported by AFOSR Grant No. F44620-75-C-0055.

cases, the expected wavelength of the radiation is $\lambda \approx \ell_o/2\gamma^2$, where ℓ_o is the ripple period and γ is the beam energy parameter, $(1 - V^2/c^2)$.

This work describes progress on a series of experiments to unfold the details of the wave-interaction process. In the previous work the field ripple was created using a periodic iron structure (rings or a helix) placed adjacent to the waveguide wall near which the REB propagated. Thus there was no control of the field ripple parameter apart from the strong guiding magnetic field ($B_o \approx 10$ kG). In the present experiment, the field ripple is independently controlled with an electromagnetic field-rippled device, or "undulator".

The experimental layout is given in Fig. 1. The electron beam is propagated in an evacuated cylindrical drift tube, which is also a quasi-optical light guide for the millimeter waves. The solenoid is 100 cm long, and the undulator is 32 cm long; the latter is made up of an assembly of aluminum plates and insulating spacers, having a ripple period $\ell_o = 0.8$ cm. An exploded view is shown in Fig. 2. The ripple period can be changed by removing or adding spacers and plates (thickness $\approx$ 1 mm) from each section. The assembly fits over the drift tube (1" O.D.), and is insulated from it by a vacuum-sealing sleeve. A slot on the drift tube wall permits the field from the undulator, which is driven by a pulsed current source, to enter the region containing the beam electrons. The undulator current (~ 10 - 20 kA) is made to reverse in each adjacent turn of the undulator, so it can be regarded as a series of tightly spaced single-turn cusp coils. The current in the undulator feed lines is not perfectly compensated in the axial direction, and thus an additional compensating current is needed to cancel an unwanted transverse magnetic field which otherwise perturbs the beam equilibrium.

A high-pass filter is used to reject microwave noise, and a system of reflecting meshes is used to determine the mean wavelength. The

detector is a calibrated Molectron pyroelectric element. Additional power calibration has been done by measuring the temperature rise of a carbon-pyramid "matched load" (Fig. 1, part B) using thermistors in a sensitive bridge circuit [6]. The ripple field component $\delta B_\perp$ has been measured using a small magnetic loop, and shows a sinewave type behavior (Fig. 2) along the axis of the drift tube; near the wall, $\delta B_\perp$ can be as large as 400 G.

Figure 3 shows data taken from photographs of the signal as observed on a Tektronix R 7912 500 MHz storage scope. Although the diode voltage holds constant for 10 - 15 nsec, appreciable signal output occurs only for 2 - 5 nsec, suggesting that perhaps 5 - 10 nsec is necessary for the signal to grow several e-folding periods ($\approx$ 1 nsec). Figure 3(a) shows that the process has a magnetic resonance, in this case when $\omega/c \approx$ (TM_{01} guide cutoff frequency). Setting B_0 at resonance, we observe an exponential dependence of power output upon the field ripple (Fig. 3(b)) amplitude (this is the "pump" for the electron "quiver" velocity in the parametric pumping process). The data therefore bears out theoretical calculations of the linear growth rate [3,7], both as to magnitude and parametric dependence. Further experimental work in the near future will determine the power spectrum, investigate the dependence of wavelength upon beam γ and consider a signal feedback technique such as was used in the non-relativistic ubitron experiment [8].

REFERENCES

1. T. C. Marshall, S. Talmadge, and P. Efthimion, Appl. Phys. Lett. 31, 320 (1977).
2. P. C. Efthimion and S. P. Schlesinger, Phys. Rev. A 16, 633 (1977).
3. V. L. Granatstein and P. Sprangle, IEEE Trans. Microwave Theory and Tech., MTT-25, 545 (1977).
4. V. L. Granatstein, M. Herndon, R. K. Parker, and S. P. Schlesinger, Appl. Phys. Lett. 30, 384 (1977).

5. D. A. G. Deacon, L. R. Elias, J. M. J. Madey, G. J. Ramian, H. A. Schwettman, T. I. Smith, Phys. Rev. Lett. 38, 892 (1977).
6. P. Efthimion, P. R. Smith, and S. P. Schlesinger, Rev. Sci. Instr. 47, 1059 (1976).
7. P. Diament, Bull. Am. Phys. Soc. 22, 648 (1977).
8. C. E. Enderby and R. M. Phillips, IEEE Proc. 53, 1648 (1965).

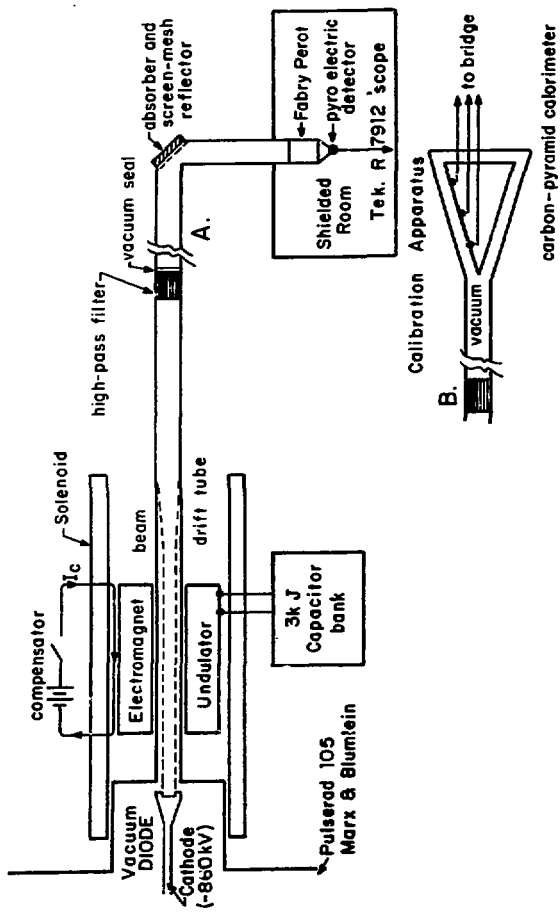

Fig. 1

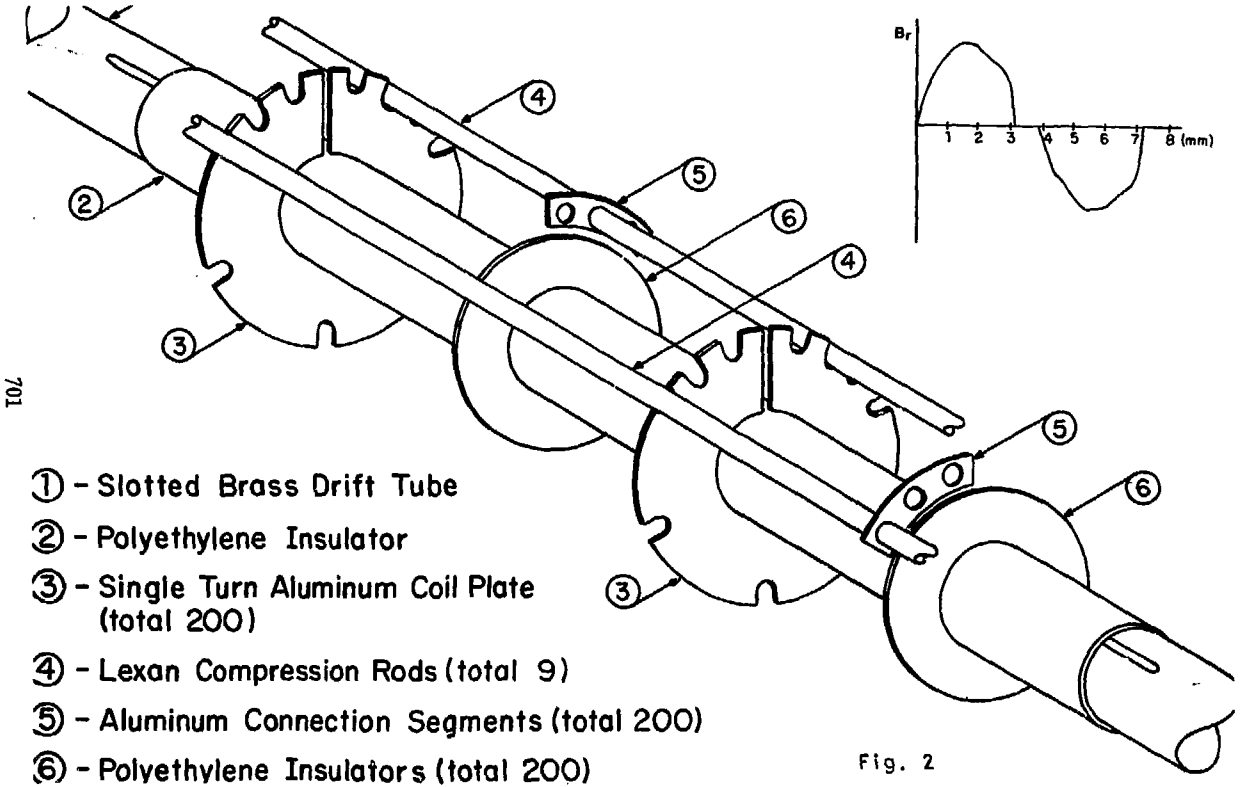
Br
1 2 3 4 5 6 7 8 (mm)
① - Slotted Brass Drift Tube
② - Polyethylene Insulator
③ - Single Turn Aluminum Coil Plate (total 200)
④ - Lexan Compression Rods (total 9)
⑤ - Aluminum Connection Segments (total 200)
⑥ - Polyethylene Insulators (total 200)

Fig. 2

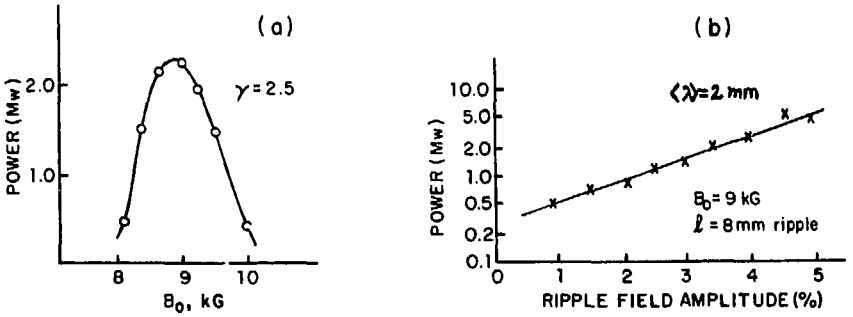
(a)
POWER (Mw)
2.0
1.0
γ = 2.5
8
9
10
B_0, kG
(b)
⟨λ⟩= 2 mm
10.0
5.0
2.0
1.0
0.5
0.2
0.1
POWER (Mw)
B_0 = 9 kG
ℓ = 8 mm ripple
0
1
2
3
4
5
RIPPLE FIELD AMPLITUDE (%)

Fig. 3

THEORY OF THE CYCLOTRON MASER INSTABILITY

P. Sprangle, K. R. Chu, A. T. Drobot, and V. L. Granatstein

Naval Research Laboratory, Washington, D.C. 20375

ABSTRACT

The cyclotron maser instability has a two-fold importance; first, there is fundamental scientific interest in the physical processes involved in this instability; second, this mechanism is the basis for a new class of powerful millimeter and submillimeter wave generators (gyrotrons) which are finding application to r.f. heating of plasmas in controlled fusion research devices. In this paper, both the scientific aspects and the design procedures for devices based on the cyclotron maser instability are reviewed.

I. Introduction

The electron cyclotron maser instability is generated by a beam of electrons following helical trajectories around the lines of an axial magnetic field. Through a relativistic bunching mechanism, the electron ensemble interacts unstably with an electromagnetic wave whose frequency is near the Doppler shifted electron cyclotron frequency or its harmonics. Initially, the phases of the electrons in their cyclotron orbits are random, but phase bunching can occur because of the dependence of the electron cyclotron frequency on the relativistic electron mass. Those electrons that lose energy to the wave become lighter, rotate faster, and hence accumulate phase lead while those electrons that gain energy from the wave become heavier, rotate slower, and accumulate phase lag. This can result in phase bunching such that the electrons radiate coherently and amplify the wave. Early descriptions of the physical process are to be found in the works of Twiss [1], Schneider [2], Gapanov [3], and Lamb [4]. The first deliberate experimental study was made by Hirshfield and

Wachtel [5]. An extensive description of the early work is to be found in some recent review papers [6]. The highest recorded millimeter wave power, both peak and average, have been achieved through the cyclotron maser process. High peak powers were achieved in a series of experiments using intense relativistic electron beams (V ~ 1 MV, I ~ 30 kA). Power levels of 900 MW at λ = 4 cm [7], 350 MW at λ = 2 cm [8], 8 MW at λ = 8 mm [9], and 2 MW at λ = 4 mm [9] were obtained. However, the efficiency of converting electron beam energy to radiation was only ~ 1%. The initiative in developing high average power cyclotron masers has been taken by workers at the Gorkii State University (USSR) [10,11] who have called their devices "gyrotrons". Zaytsev, et al. [10] have generated the following CW powers: 12 kW at λ = 2.78 mm with 31% efficiency; 2.4 kW at λ = 1.91 mm with 9.5% efficiency; and 1.5 kW at λ = 0.92 mm with 6.2% efficiency. These results represent an advance in CW power capability by orders of magnitude.

II. Linear Theory

We first present a brief summary of the linear theories [12-17] on cyclotron masers. The electron beam and waveguide configuration is shown in Fig. 1. The beam of electrons are gyrating about the axial magnetic field B_0 with velocity $V_{0\perp}$ and drifting along B_0 with velocity $V_{0/\!/}$. The guiding centers of all the particles lie midway between the two conducting plates. Thus, the beam thickness is twice the Larmor radius. We assume that the field components within the waveguide are those of a TE_{0n} mode (i.e., E_y, B_z, and B_x are the only nonvanishing field components), hence, all quantities are independent of y. The functional dependence of the fields on z and t has the form $\exp(i(k_0 z - \omega t))$. The set of Vlasov-Maxwell equations yields the following dispersion relation:

$$\omega^2 - c^2(k_o^2 + k_n^2) = \delta_{n\ell}(\omega_b^2/\gamma_o)$$

$$\left\{ \frac{(\omega - k_o v_{o\parallel}) Q_{n\ell}}{(\omega - k_o v_{o\parallel} - \ell\Omega_o/\gamma_o)} - \frac{\beta_{o\perp}^2 (\omega^2 - c^2k_o^2) W_{n\ell}}{(\omega - k_o v_{o\parallel} - \ell\Omega_o/\gamma_o)^2} \right\} \quad (1)$$

where $k_n = \pi n/2a$ is the perpendicular wave number, $n = 1, 2, 3, \ldots$ is the waveguide mode number, $\delta_{n\ell} = (1 + (-1)^{n+\ell})$, $\omega_b^2 = 4\pi|e|\sigma_o/m_o a$ is the modified plasma frequency, σ_o is the surface charge density of the beam in the x-y plane, $\ell = 1, 2, 3$ is the cyclotron harmonic number, $\gamma_o = (1 - v_{o\perp}^2/c^2 - v_{o\parallel}^2/c^2)^{-1/2}$, $\Omega_o = |e|B_o/m_o c$, $\beta_{o\perp} = v_{o\perp}/c$, $Q_{n\ell} = x_n(\ell^2/x_n^2 - 1) \cdot (d(J_\ell(x_n))^2/dx_n$, $W_{n\ell} = (dJ_\ell(x_n)/dx_n)^2$, $x_n = \beta_{o\perp} ck_n/(\Omega_o/\gamma_o)$ and J_ℓ is the Bessel function of order ℓ. It is straightforward to show from Eq. (1) that (i) the first term in the bracket on the right hand side is always stabilizing while the second term is always destabilizing; (ii) the frequency of the unstable wave in the rest frame of the electrons is slightly greater than the cyclotron frequency, $\gamma_o(\omega - k_o v_{o\parallel}) \geq \Omega_o$; (iii) there exists a threshold condition for instability such that

$$\beta_{o\perp} > \beta_{\perp, crit}$$

where $\omega_o = c(k_o^2 + k_n^2)^{1/2}$ and $\beta_{\perp, crit} = \ell(\Omega_o/\gamma_o)(Q_{n\ell}/W_{n\ell})^{1/2}[(2/27) \delta_{n\ell}\omega_b^2 Q_{n\ell}/(\gamma_o\omega_o\ell\Omega_o/\gamma_o)]^{1/4}/ck_n$; and (iv) the growth rate is a maximum when the wave group velocity V_g equals the beam axial velocity $V_{o\parallel}$. Figure 2 shows the dispersion diagram for the cyclotron maser instability when $v_o = 0$, $\omega_o = ck_n = \ell\Omega_o/\gamma_o$ and $\ell = n = 1$. Note that the cyclotron mode splits into two branches of negative and positive energy polarity. The negative energy cyclotron mode couples to the positive energy TE guide mode and the growth rate maximizes at $k_o = 0$.

III. Nonlinear Analysis

We have noted in Section II that the linear growth rate for the excited TE_{on} mode maximizes when the axial beam velocity and the wave group velocity are equal. Hence, we choose to carry out a nonlinear analysis for this situation [18,19]. For convenience, we transform to a frame in which both the axial beam velocity and wave group velocity vanish Since the group velocity is zero in this frame (cutoff frame), we note that the axial wave number of the wave is also zero. The electric field, in the cutoff frame, of the vacuum waveguide mode has the form

$$E_y(x,t) = -E_o(t) \cos(\omega_o t + \alpha(t)) \sin(k_n(x - a)). \qquad (2)$$

In Eq. (2) the frequency ω_o is a constant, while the amplitude, $E_o(t)$, and the frequency shift, $\partial\alpha(t)/\partial t$, are weak functions of time (i.e., $\partial \ell n (E_o(t))/\partial t$, $\partial\alpha(t)/\partial t \ll \omega_o$). The amplitude $E_o(t)$ can be expressed as $E_o(t) = \varepsilon_o \exp \int_o^t \Gamma(t')dt'$, where ε_o is the initial field amplitude and $\Gamma(t)$ is the time dependent growth rate.

To first order in the small parameters $\Gamma(t)/\omega_o$ and $\dot{\alpha}(t)/\omega_o$, the vector potential is given by

$$A_y(x,t) = (c/\omega_o) \left\{ (1 - \dot{\alpha}/\omega_o) E_o \sin(\omega_o t + \alpha) + (\dot{E}_o/\omega_o) \cos(\omega_o t + \alpha) \right\} \sin(k_n(x - a)), \qquad (3)$$

The time evolution of $E_o(t)$ and $\alpha(t)$ is determined by the particle current density, $J_y(x,t)$, through the wave equation for $A_y(x,t)$:

$$\left(\frac{\partial^2}{\partial x^2} - \frac{1}{c^2}\frac{\partial^2}{\partial t^2}\right) A_y = -4\pi \frac{|e|\sigma_o}{cN} \sum_{i=1}^{N} V_y(\phi_i,t)\delta\left[x - x(\phi_i,t)\right]$$

where σ_o is the surface number density in the y-z plane, N is the number of particles, ϕ_i is the initial velocity space angle of the i-th particle measured with respect to the x axis and x (ϕ_i,t) is the x position of the i-th particle. Substituting Eq. (3) into Eq. (4) multiplying the result by $\sin(k_n(x-a))$, integrating across the waveguide from x = -a to x = a and taking the temporal average we arrive at following expressions for $\dot{\alpha}(t)$ and $\Gamma(t)$:

$$\dot{\alpha}(t) = \frac{\omega_o}{(\omega_o^2 + c^2k_n^2)} \left[c^2k_n^2 - \omega_o^2 + \left\{ \frac{2|e|\sigma_o}{a} \omega_o(\omega_o + \dot{\alpha}) \cdot \right.\right.$$

$$\left.\left. \int_t^{t+2\pi/(\omega_o+\dot{\alpha})} dt' \langle v_y(\phi_o,t') \sin\left(k_n(x(\phi_o,t') - a)\right) \sin\left(\omega_o t' + \alpha(t')\right) \rangle \right\} \cdot \right.$$

$$\left. \left\{ \int_t^{t+2\pi/(\omega_o+\dot{\alpha})} E(t') \sin^2(\omega_o t' + \alpha(t'))\, dt' \right\}^{-1} \right], \qquad (5)$$

$$\Gamma(t) = \frac{\omega_o}{\omega_o^2 + c^2k_n^2} \left\{ \frac{2|e|\sigma_o}{a} \omega_o(\omega_o+\dot{\alpha}) \cdot \int_t^{t+2\pi/(\omega_o+\dot{\alpha})} dt' \langle v_y(\phi_o,t') \right.$$

$$\left. \sin\left(k_n(x(\phi_o,t') - a)\right) \cos\left(\omega_o t' + \alpha(t')\right) \rangle \right\}$$

$$\left\{ \int_t^{t+2\pi/(\omega_o+\dot{\alpha})} E(t') \cos^2(\omega_o t' + \alpha(t'))\, dt' \right\}^{-1} . \qquad (6)$$

In the above equations, $\langle\ \rangle = (2\pi)^{-1} \int_o^{2\pi} d\phi_o$ is the ensemble average over the initial particle phase. The right hand side

of Eqs. (5) and (6) contain implicitly the details of the particle dynamics which are related to the fields through the relativistic equation of motion.

Two mechanisms are responsible for the saturation of the wave, namely, depletion of the free energy in rotational motion and phase trapping of the gyrating particles in the wave.

(i) Free Energy Depletion

The linear dispersion relation, Eq. (1), gives rise to a threshold condition for instability $\beta_{o\perp} > \beta_{\perp,crit}$. That is, the maximum free energy per particle available to the wave is

$$\epsilon_{free} = (\gamma_{o\perp} - \gamma_{\perp,crit})m_o c^2 , \qquad (7)$$

where $\gamma_{\perp,crit} = (1 - \beta_{\perp,crit}^2)^{-1/2}$. If the beam particles were to lose all of the free energy given by Eq. (7), the energy conversion efficiency would be

$$\eta = \frac{\langle\Delta\gamma\rangle_s}{\gamma_{o\perp}-1)} \approx \frac{(\gamma_{o\perp} - \gamma_{\perp,crit})}{(\gamma_{o\perp} - 1)} \qquad (8)$$

where $\langle\Delta\gamma\rangle_s \tilde{=} \gamma_{o\perp} - \gamma_{\perp,crit}$ is the average change in gamma at saturation and $\gamma_{o\perp} \geq \gamma_{\perp,crit}$. If $\gamma_{o\perp}$ is slightly greater than $\gamma_{\perp,crit}$, the expression in Eq. (8) will represent a good approximation to the actual conversion efficiency. In this case the particles lose all their free energy before thermalizing or trapping takes place and the wave linearly stabilizes. If, however, $\gamma_{o\perp}^{-1} >> \gamma_{\perp,crit}^{-1}$, the following case applies.

(ii) Phase Trapping

The frequency of the wave must be slightly greater than the relativistic electron cyclotron frequency, Ω_o/γ_o, for an instability to develop. Therefore, initially we have

$$\omega - \Omega_o/\gamma_o = \Delta\omega \geq 0 , \qquad (9)$$

where $\Delta\omega$ is the frequency shift which can be obtained from the linear dispersion relation. Now, as the instability develops the average gamma of the particles, $\langle\gamma_\perp\rangle$, decreases until $\omega - \Omega_o/\langle\gamma_\perp\rangle = -\Delta\omega$. At saturation $\langle\gamma_\perp\rangle$ is minimum and:

$$\omega - \Omega_o/\langle\gamma_\perp\rangle_s = -\Delta\omega \tag{10}$$

where $\langle\gamma\rangle_s$ is the average value of $\gamma_\perp$ at saturation. Comparing Eq. (9) with Eq. (10), we find that at saturation the average change in the gamma of the particles, $\langle\Delta\gamma_\perp\rangle_s = \gamma_{o\perp} - \langle\gamma_\perp\rangle_s$, is given by:

$$\langle\Delta\gamma_\perp\rangle_s \approx 2\gamma_{o\perp}\Delta\omega/\omega. \tag{11}$$

The efficiency of conversion of kinetic energy to field energy, η, when electron phase trapping is responsible for saturation, is therefore

$$\eta \approx 2\ (\Delta\omega/\omega)\ \gamma_{o\perp}/(\gamma_{o\perp} - 1). \tag{12}$$

To examine the validity of these qualitative arguments, the nonlinear coupled equations (5) and (6) together with the particle equations of motion are solved numerically for a wide range of parameters. The distribution function was represented by a sufficient number of test particles to insure convergence.

A run was initiated by uniformly distributing the particles in the velocity space angle, $0 \le \phi_o \le 2\pi$ and assigning them the same perpendicular velocity, $v_\perp = v_{o\perp}$. A small

amplitude electric field was introduced as a perturbation and allowed to grow self consistently. From the results of the single wave simulations we have made composite graphs of the transfer efficiency from particle kinetic energy to wave electromagnetic energy at saturation as a function of several parameters. A comparison between these results and the analytic predictions shows good qualitative agreement.

As an example of a typical result, we follow the time evolution of field and particle quantities. The initial conditions chosen for this example are: $\mu = \omega_b/(\sqrt{\gamma_{o\perp}}\ \omega_o) = 0.05$, $\gamma_{o\perp} = 1.05$, $\omega_o = ck_n = \Omega_o/\gamma_{o\perp}$ and $n = 1$. In Fig. 3, the nonlinear frequency shift and growth rate are shown as functions of the normalized time $\tau = \omega_o t$. In the linear regime ($150 \lesssim \tau < 350$) the wave grows exponentially and both the growth rate and frequency shift assume the values predicted by linear theory. At saturation, we find $\omega_o + \dot{\alpha}(\tau) - \Omega_o/\langle\gamma_\perp\rangle \simeq -\Delta\omega$, in good agreement with the preceeding qualitative arguments.

We have found that the energy efficiency curves for a given set of parameters always display a maximum. For example, with $\mu = 0.1$, the efficiency curve shown in Fig. 4 has a peak of 40 percent when $\gamma_{o\perp} = 1.1$. The peak results from the competition between the two saturation mechanisms described in Section VI. As can be seen in Fig. 4, the efficiency curve has a cutoff at $\gamma_{o\perp} = \gamma_{\perp,crit} = 1.0185$. This is in excellent agreement with the analytical prediction of Eq. (1). For beams that have initial energies characterized by $\gamma_{o\perp} - 1 \gtrsim \gamma_{\perp,crit}^{-1}$, we find that the excited wave extracts free energy from the beam until $\langle\gamma_\perp\rangle = \gamma_{\perp,crit}$ and the system

becomes linearly stable without particle trapping taking place. The simulations confirm this, since the velocity phase space plots show no evidence of trapping at the time of saturation. In this regime a rough expression for the average change in $\gamma_\perp$ at saturation is $\langle \Delta\gamma_\perp \rangle_s \simeq \gamma_{o\perp} - \gamma_{\perp,crit}$ and implies an efficiency monotomically increasing with $\gamma_{o\perp}$; this is shown as a dashed curve on Fig. 4. In the other regime where $\gamma_{o\perp}^{-1} >> \gamma_{\perp,crit}^{-1}$, the saturation mechanism is dominated by particle trapping and we find that $\langle \Delta\gamma_\perp \rangle_s \simeq 2\gamma_{o\perp}\Delta\omega/\omega_o$. This implies an efficiency curve monotomically decreasing with $\gamma_{o\perp}$ as shown in Fig. 4. The two saturation mechanisms described here predict an efficiency maximum as a function of $\gamma_{o\perp}$.

We now present the results of our nonlinear analysis for a wide range of parameters. In Fig. 5, energy efficiency as a function of $\gamma_{o\perp}$ is shown for various values of μ, μ = 0.025, 0.05, 0.15 and 0.35. In this figure the initial wave frequency ω_o was set equal to ck_n with n = 1. Furthermore, the initial relativistic cyclotron frequency, Ω_o/γ_o was set equal to ck_n. These initial conditions on ω_o, ck_n and $\Omega_o/\gamma_{o\perp}$ were selected because they occur near the maximum linear growth rate. All of the curves in Fig. 5 display a maximum in efficiency in the beam frame as a function of $\gamma_{o\perp}$. This characteristic of the curves explains the relatively low (high) efficiency achieved with high (low) energy beams in

gyrotron experiments. From Fig. 5 we also note that the efficiency increases at low values of $\gamma_{o\perp}$ as μ is decreased. This property of the curves can be explained by noting that as μ decreases, $\gamma_{\perp,crit}$ decreases, resulting in a sharp increase in efficiency as a function of $\gamma_{o\perp}$ near $\gamma_{\perp,crit}$. The maximum efficiency seems to level off at ~40 percent for low values of $\gamma_{o\perp}$, when $\omega_o = ck_n = \Omega_o/\gamma_{o\perp}$.

IV. Design of a Cyclotron Maser Amplifier

The preceding linear and nonlinear analyses provide a theoretical framework for the design of an actual cyclotron maser amplifier. For the exposition of the basic physics, the parallel plate geometry proves to be most convenient. In order to apply the present analyses to the design of a cyclotron maser amplifier, we have reformulated the problem in cylindrical geometry so as to incorporate geometric effects. The design consideration basically involves the optimization of all the free parameters of the system. In the present case, there are five parameters to be specified, namely, the beam guiding center position r_o, the wave number k_o, the number of particles per unit axial length N_b, the beam energy γ_o , and the magnetic field B_o. The parameters r_o and k_o are to be chosen to maximize the beam-wave coupling on the basis of the linear dispersion relation. N_b is specified according to several factors:[20] the wave power desired, the estimated efficiency, the total electron energy and axial velocity. With r_o, k_o, and N_b specified, the energy conversion efficiency η can be calculated with the numerical code in the parameter space of $\gamma_{o\perp}$ and B_o. The point in the

(γ_{o1}, B_o) space where η peaks will then be the optimum choice for the design. To illustrate the applications of the theory developed, we present the results of the optimum parameter calculations for a 35 GHz, 340 kW cyclotron maser amplifier based on the interaction of the TE_{o1} waveguide mode and the fundamental cyclotron harmonic of the electron beam[20]. The ratio of perpendicular to parallel velocity is assumed to be 1.5, an optimum value for the engineering of the electron gun[21]. Linear theory shows that maximum coupling occurs at $r_o = 0.48\ r_w$ and $k_o = 1.96\ cm^{-1}$ (or $k_o = 0$ in the beam frame), where r_w is the wall radius. The output wave power requires $N_b \simeq 7.4 \times 10^9$/cm. Figure (b) shows the numerically calculated beam frame efficiency as a function of γ_{o1} and B_o. In Fig. 6, the magnetic field B_o is denoted by a dimensionless parameter $X = \Omega_o/(\gamma_{o1} k_n c)$. The point of maximum efficiency, 70 percent in beam frame or 51 percent in lab frame, will thus be chosen for the design. Table I lists the set of design parameters (in lab frame) based on the point chosen. It is seen in this design that the cyclotron maser amplifier is indeed an efficient device for the production of intense microwaves.

REFERENCES

1. R. Q. Twiss, Australian J. Phys. 11 (1958) 564.
2. J. Schneider, Phys. Rev. Lett. 2 (1959) 505.
3. A. V. Gapanov, Izv. VUZ., Radiofizika 2 (1959) 450.
4. W. Lamb, Jr., and M. Borenstein, Phys. Rev. A5, 1298 (1972).
5. J. Hirshfield and J. Wachtel, J. Phys. Rev. Lett. 12 (1964) 533.
6. V. A. Flyagin, A. V. Gapanov, M. I. Petelin, and V. R. Yulpatov, IEEE Trans. MTT-25 (1977) 514; J. L. Hirshfield and V. L. Granatstein,

IEEE Trans. MTT-25 (1977) 522.

7. V. L. Granatstein, M. Herndon, P. Sprangle, Y. Carmel, and J. A. Nation, Plasma Physics 17, (1975) 23.
8. V. L. Granatstein, M. Herndon, R. K. Parker, and S. P. Schlesinger, IEEE Trans. MTT-22 (1974) 1000.
9. M. Friedman and M. Herndon, Phys. Fluids 16 (1973) 1982.
10. N. I. Zaytsev, et al., Radiotekhnika i Electronica 19 (1974) 1056.
11. D. V. Kisel, et al., Radio Engineering and Electronic Physics 19 (1974) 95.
12. M. Friedman, D. A. Hammer, W. M. Manheimer, and P. Sprangle, Phys. Rev. Lett. 31 (1973) 752.
13. H. Jory, Research and Development Technical Report, ECOM-01873-F (1968) Varian Associates.
14. V. L. Bratman and A. E. Tokarev, Radiofizika 17 (1974) 1224.
15. V. V. Zhelznyskov, Izv. VUZ., Radiofizika 3 (1960) No. 1, 57.
16. E. Ott and W. M. Manheimer, IEEE Trans.Plasma SC., Vol. PS--3 (1975)1.
17. K. R. Chu and J. L. Hirshfield, Phys. Fluids (in press).
18. P. Sprangle and W. M. Manheimer, Phys. Fluids 18 (1975) 224.
19. P. Sprangle and A. T. Drobot, IEEE Trans. MTT-25 (1977) 528.
20. K. R. Chu, A. T. Drobot, V. L. Granatstein, and J. L. Seftor, IEEE-MTT, to be published.
21. J. L. Seftor, A. T. Drobot, and K. R. Chu, IEEE-ED, to be published.

Table I - Efficiency Optimized Operating Parameters for a 340 kW, 35 GHz Cyclotron Maser Amplifier

N_b (axial density)	7.4×10^9/cm
V (electron energy)	70.82 keV
I_b (beam current)	9.48 Amp
η (efficiency)	51.0 %
P_b (beam power)	671.5 kW
P_w (wave power)	342.5 kW
B_o (magnetic field)	12.87 kG
k_o (wave number)	1.96 cm^{-1}
r_w (wall radius)	5.37 mm
r_o (guiding center position)	2.52 mm
r_L (Larmor radius)	0.61 mm
$v_\perp/c$ (perpendicular velocity)	0.401
v_{oz}/c (parallel velocity)	0.268
G (power gain)	2.0 dB/cm

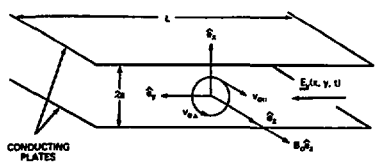

Fig. 1 - The electron cyclotron maser configuration in plane geometry.

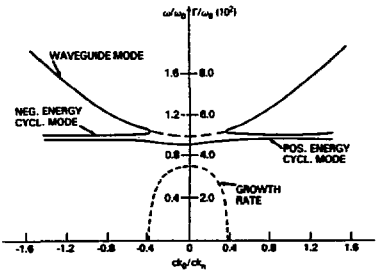

Fig. 2 - Typical dispersion curve for cyclotron maser instability. This case is for $\gamma_{o\perp} = 1.2$, $\omega_b \sqrt{\gamma_{ol}} = 0.05 \cdot \omega_o$, $\omega_o = ck_n = \ell\Omega_o/\gamma_{o\perp}$ and $\ell=n=1$.

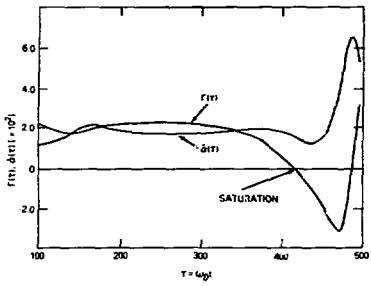

Fig. 3 - The nonlinear phase shift and growth rate as a function of time for a typical simulation.

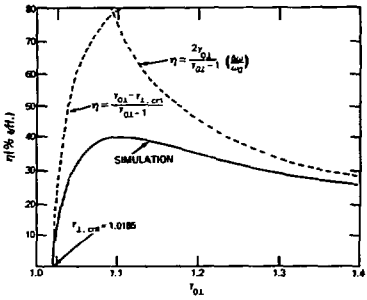

Fig. 4 - The efficiency of the cyclotron maser as a function of energy found from the two mechanisms of saturation and from simulations.

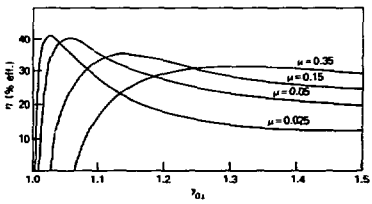

Fig. 5 - The beam frame efficiency of the electron cyclotron maser as a function of energy for various densities when $ck_n = \Omega_o/\gamma_{0\perp}$.

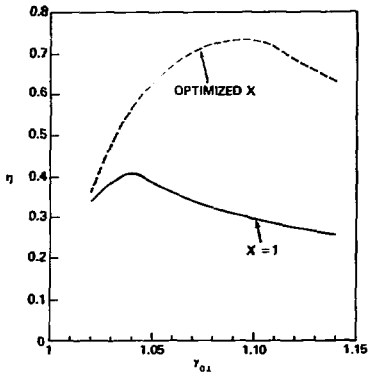

Fig. 6 - η versus $\gamma_{0\perp}$ for grazing intersection case ($X = 1$, solid curve) and for optimized near grazing intersection case ($X \leq 1$, dashed curve). A point on the dashed curve, is obtained by varying X but keeping $\gamma_{0\perp}$ fixed until η reaches a maximum. The peak of the dashed curve is therefore the peak of η in the $(\gamma_{0\perp}, X)$ parameter space. The parameters used for this figure are $r_o = 0.48 r_w$, $N_b = 7.4 \times 10^9/cm$ and $k_c = 0$.

MASER ELECTRON CYCLOTRON RESONANCE IN VACUUM AND PLASMA WITH REB

P. S. Strelkov

Lebedev Physical Institute, Moscow, USSR

The problem of beam space charge in microwave generator with REB is discussed. The intense REB is injected in plasma and the degree of space charge neutralization is measured. The stimulated cyclotron radiation of spiral beam in vacuum and in plasma is observed. The microwave power in plasma is more than the power in vacuum by a factor of about one hundred. This fact is explained by neutralization of beam space charge in plasma. The investigation of maser electron cyclotron resonance in vacuum is described in the last part of the report. We hope to make this maser with plasma and to increase the microwave power.

1. Introduction

The recent advent of intense relativistic electron beams (REB) has been accompanied by widespread interest in applying such beams to the generation of ultra high power microwaves. Intense REB have certain features impeding microwave generation with REB. In the first place, it is necessary to take into account the relativistic properties of electrons. Secondly, microwave generators require a beam with known electron trajectory. It is difficult to create such high-current beams in the diode of an accelerator. And finally, the REB space charge results in limiting transported current. Moreover, the potential of the space charge results in a variation of electron energy in the cross section of the beam and therefore the efficiency of transformation energy from the beam to a wave decreases.

In the present report, we are concerned mainly with the space charge problem of REB. First, we consider charge neutralization of the electron beam in the plasma. Then, we consider experiments on excitation of stimulated cyclotron radiation by means of the electron beam and investigations with the microwave generator, i.e., maser on electron cyclotron resonance 1 (MCR). The aim of our research is to create an MCR generator filled with plasma. It is well known that the space charge of an electron beam in plasma can be equal to zero and the beam current may be more than in vacuum because the power of the generator will increase.

2. The maximum current in vacuum.

In the MCR generator a beam of radius r travels along the lines of magnetic field in a metallic chamber of radius R and length L. Let the angle between the velocity of the electrons and the lines of magnetic field equal θ. If $L \gg R$, the maximum current of the beam in vacuum is:

$$I_o = \frac{mc^3}{e(1+2\ln R/r)} \left[\gamma^{2/3} - (\gamma^2 \sin^2\theta + \cos^2\theta)^{1/3}\right]^{3/2} \qquad (1)$$

for W = 350 keV, $\gamma = 1.7$, $\theta = 45^o$, $R/r = 2.7$, $I_o = 430$ A. This is valid for a solid beam only. It is known that the transported value of maximum current for an annular beam is more than the current of a solid cylinder beam. If the external radius of the annular beam is equal to the radius of the chamber and the thickness of the beam is very small, then the maximum current may have any large value. But, as the electrons have a transverse velocity in the MCR, the thickness of the annular beam is more than the Larmor electron diameter and, therefore, the maximum current has a finite value always. (In our experimental case, $2r_L = 0.6$ cm, $\Delta r = 0.9$ cm, $r = 1.5$ cm, i.e., it is possible to consider the beam solid.

The maximum stable current in plasma is:

$$I_{\text{l}} = \frac{mc^3}{e(1+2\ln R/r)} \cdot \frac{(\gamma^2-1)^{3/2}\cos^3\theta}{\gamma^2\sin^2\theta+\cos^2\theta} \qquad (2)$$

In our experimental case (see Eq. 1), I_{l} = 2.7 kA. If the angle θ = 0, the ratio $I_{\text{l}}/I_0 \sim \gamma$ for $\gamma \gg 1$ and I_{l}/I_0 = 140 for γ = 10. When $\theta \neq 0$, for example, $\theta = 45^0$, $I_{\text{l}}/I_0 \approx$ const $\geq 3\sqrt{3}$ for any γ (γ = 10 I_{l}/I_0 = 7.5). We hope to use a current in the generator of more than I_{l} where plasma density will be more than the beam density ($n_p > n_b$).

3. The space charge neutralization of the beam.

In our experiments [2,3], a beam with W ~ 400 keV, I_i = 1 - 17 ka, is injected into plasma, which is produced beforehand in a homogeneous magnetic field (H ~ 5 kOe). The diameter of the beam and plasma are equal, $r_p = r_b$ = 1.5 cm. (Fig. 1). The radius of metallic chamber is R = 7.5 cm, length L = 100 cm. We can vary the density of plasma from $n_p \approx 10^{10}$ up to $n_p \approx 2.10^{13}$, i.e., it is possible for $n_p \approx n_b$ and $n_p \gg n_b$. The beam space charge in plasma is measured with a capacitive voltage divider [10]. If the beam is steady state, the condition of space charge neutralization is simply $n_p = n_b$. Since the pulse duration is small, ~ 20 - 100 nsec, the electrons of plasma do not have sufficient time to move along the lines of magnetic field to the metallic ends of the chamber. It is clear that the condition of neutralization is $n_p > n_b$. On the other hand, if plasma density is high and the value of the return plasma current is equal to the beam current $I_p = I_b$, the space charge of the whole system equals zero. It is known that the return plasma current is equal to the beam current when $c/w_p r \to 0$. The exact calculation gives $I_p = 0.9\ I_b$ when the density of plasma is $n_p = 2.10^{12}$ for our experimental conditions.

Now we report the first experiment, in the case when the injected

current I_i is less than I_o, $I_i < I_o$, and so the beam current does not depend on the plasma density and the beam density is constant also, n_b = const = 2.10^{10}. Figure 2 shows the theoretical dependence of net current ($I = I_p + I_b$) and the experimental points for net current and for the beam charge vs. the density of plasma. One can see that the theoretical curve for net current and experimental results coincide. Then, one can see that space charge neutralization takes place with density n_p = $2.10^{11} >> n_b$, when $I_p = 0.7\ I_b$. In this case, the space charge neutralization is explained only by return plasma current.

It was shown in our works [2,4] that the return current has cut off when $t > T_1$ because electron emission from the collector is absent. The beam puts charge in the chamber only during the time of electron travelling through the chamber (T_2), but the return plasma current carries out charge all the time (T_1), when it exists. Since $T_1 > T_2$, we obtain the condition $I_p < I_b$ for space charge neutralization.

We consider now the second case, when the injected current I_i is more than I_o. In this case, the beam current is not constant and increases, with plasma density increasing, because plasma neutralizes the space charge. Figure 3 shows the dependence of the beam potential vs. the density of plasma for different injected current. The curves 1 and 2 correspond to the condition $I_i < I_o$; for cases 3, 4, 5, and 6, $I_i > I_o$. The potential is P = 0.75 U in vacuum for $I_i > I_o$ and this fact coincides with the simple theory. The potential is $P \approx U \equiv w/e$ in the region of small density of plasma and then falls. The potential decrease begins at the high plasma density for large ratio I_i/I_o. The beam current $I_b < I_i$ always, when $P \sim U$, i.e., a virtual cathode exists in the system.

We do not give a full explanation of the dependences 3, 4, 5, and 6 in Fig. 3. But, it is clear that transport of a large current is

required for a high degree of space charge neutralization and therefore for high density of plasma. It is clear also that the potential equals zero at the plasma density $n_p = 2.10^{13}$, when $n_p >> n_b$ and $I_p = I_b$ for injected currents. Thus, we know the degree of space charge neutralization when the beam is injected into the plasma and we can transport current $I_b/I_o \approx 10$. Next, we consider the processes of electron radiation.

4. Stimulated cyclotron radiation.

When the electrons of a beam move in the magnetic field and have the transverse velocity, cyclotron radiation takes place. The condition of effective interaction of electrons with the radiation field is

$$\frac{w_H}{\gamma} + K_{||} U_{||} = w_{res} \qquad (3)$$

Here, $\frac{w_H}{\gamma} = \frac{eH}{mc\gamma}$, $K_{||}$ is the longitudinal compenent of wave number, $U_{||}$ is the longitudinal component of velocity and w_{res} the frequency of the resonator. In our experiments, 5 electrons pass through a metallic foil and therefore have transverse velocity. We use two foils: the first foil is Ti, $\Delta = 50_\mu$, and gives $(\overline{\theta^2})^{1/2} = 48^o$, according to calculations; and the second foil is Al, $\Delta = 10\ \mu$, and gives $(\overline{\theta^2})^{1/2} = 10^o$. The magnetic field is homogeneous and the resonator is a cylindrical metallic chamber (Fig. 1). The X-band electromagnetic radiation from the chamber is registered only across the chamber axis through a Teflon window of $\phi = 8$ cm. The frequency of radiation was measured as w_H/γ and the dependence of the radiation power on the magnetic field had a resonance character. But we cannot find an exact correspondence of the experimental results with the condition (3). It can be explained that the chamber is not an exact cylindrical resonator, because it has large windows, probes, etc. Figure 4 shows the dependence of microwave power on the

plasma density for two foils. One can see that the power in the case of the Ti foil is more than the power in the case of the Al foil both in vacuum and in plasma. It can be explained that in the first case the electrons have a large transverse velocity. Figure 4 shows that the radiated power increases in plasma and achieves a maximum when the plasma density is $n_p = 5.10^{12}$. The space charge of the beam is equal to zero in plasma when $n_p = 5.10^{12}$ and in this case the current of the beam is $I_b = 2.5\ I_o = I_i$. The power is greater than that in vacuum by a factor of about 100.

This result, from our point of view, is very important and is attributable to the effect of space charge neutralization, as a result of which the beam becomes uniform in energy in the cross section and all the electrons participate in the excitation of the cyclotron wave. We note also that the frequency of radiation in plasma decreases as the γ of electrons increases in plasma and $w \sim \frac{w_H}{\gamma}$.

5. Maser electron cyclotron resonance.

We have described experiments in which resonator was not specially calculated and consequently the beam energy conversion efficiency was very small, ~ 0.2%. Now we consider the next experiments with a special resonator with calculated type of wave mode TE_{13} for $\lambda = 3$ cm. The electrons acquire transverse energy in the diode of the accelerator (Fig. 5). It was measured that the frequency was equal to $f = 10$ gHz and $\Delta f < 0.7$ gHz. Figure 6 shows the dependence of density power radiation vs. diameter of radiated horn. Each experimental point corresponds to one accelerator shot. The parameters of the accelerator pulse vary a little from one pulse to another, but we can see good coincidence of the experimental points with the theoretical curve for mode TE_{13}. The microwave power is equal to 15 MW and the beam energy conversion efficiency is

$\approx$ 10%. The energy conversion efficiency depends very strongly on angle Θ. There is a single optimum angle for each current. The generation is observed only for certain values ($H \sim H_{opt}$) of magnetic field, and $\Delta H/H_{opt} \sim 0.1$. The value H_{opt} increases when Θ increases. These results prove that maser cyclotron microwave radiation is observed.

Our future plan is to create plasma in this maser, to increase beam current and therefore to increase the radiation power.

References

1. A. V. Gaponov, M. I. Petelin, and V. K. Yulpatov. Izvestia Vusov Radiophisika 10, 1414 (1967).
   A. V. Gaponov, V. A. Flyagin, M. I. Petelin, and V. K. Yulpatov. Trans. IEEE, MIT-25, 6, 514 (1977).
2. O. D. Klok, V. I. Krementsov, P. S. Strelkov, and A. G. Shkvarunets. JETP 67, 1401 (1974).
3. V. I. Krementsov, P. S. Strelkov, and A. G. Shkvarunets. Phizika plasmi 21, 936 (1976).
4. A. G. Shkvarunets, V. I. Krementsov, and P. S. Strelkov. Phizika plasmi 3, 770 (1977).
5. V. I. Krementsov, M. S. Rabinovich, A. A. Ruchadze, P. S. Strelkov, and A. G. Shkvarunets. JETP 69, 1218 (1975).

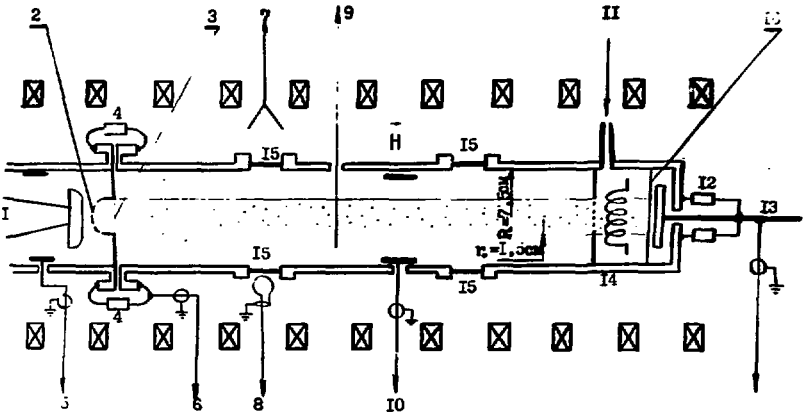

Fig. 1. Experimental set-up: (1) cathode of accelerator, (2) anode, (3) metallic foil, (4) shunt, (5) capacity divider to measure the voltage, (6) pulse of chamber current, (7) 3-cm microwave channel, (8) loop to measure the plasma oscillation, (9) probe to measure plasma density, (10) capacitive divider for measuring the beam potential, (11) leak valve, (12) pulse of beam current, (13) beam collector, (14) electron gun to produce the plasma, (15) Teflon windows of 8 cm diameter, (16) foil (Ti).

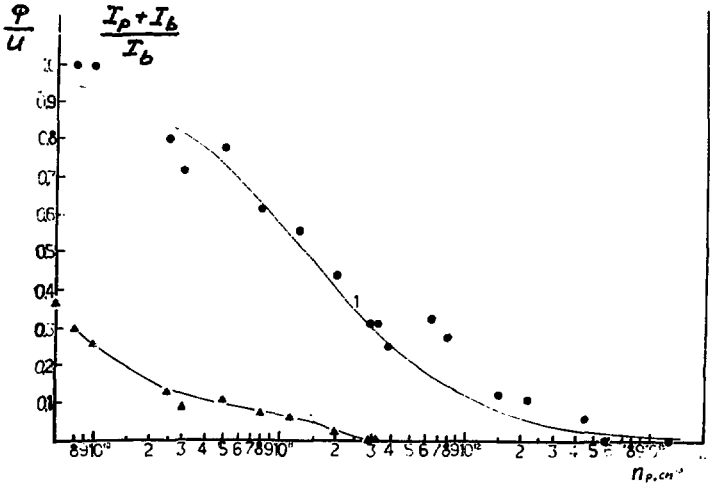

Fig. 2. The space charge and current neutralization, when $I_i < I_o$: (1) the theoretical curve $I_p + I_b/I_b$ on the experimental points; (2) the experimental dependence beam potential on the plasma density; eu = w = 380 keV, I_i = 0.7 kA, I_o = 1.2 kA, H = 5.4 kOe, r = 1.5 cm, R = 7.5 cm.

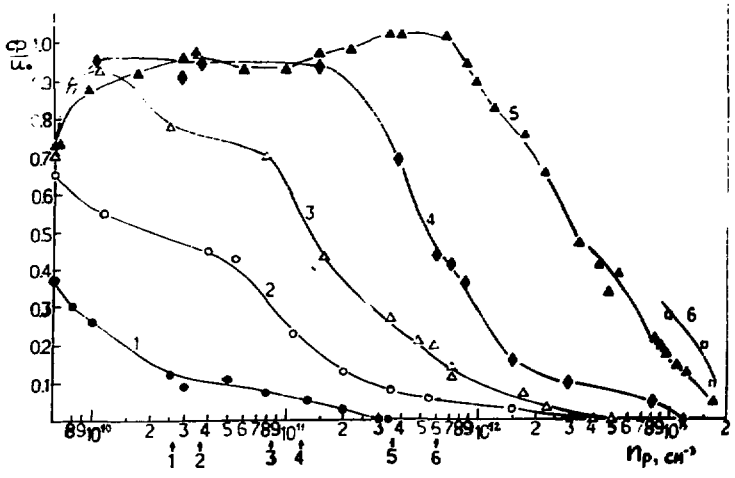

Fig. 3. The dependence of beam potential P/U on the density of plasma n_p for any injected currents; w = 380 keV, I_o = 1.2 kA. (1) I_i = 0.7 kA; (2) I_i = 1 kA; (3) I_i = 2.2 kA; (4) I_i = 3.4 kA; (5) I_i = 10 kA; (6) I_i = 17 kA.

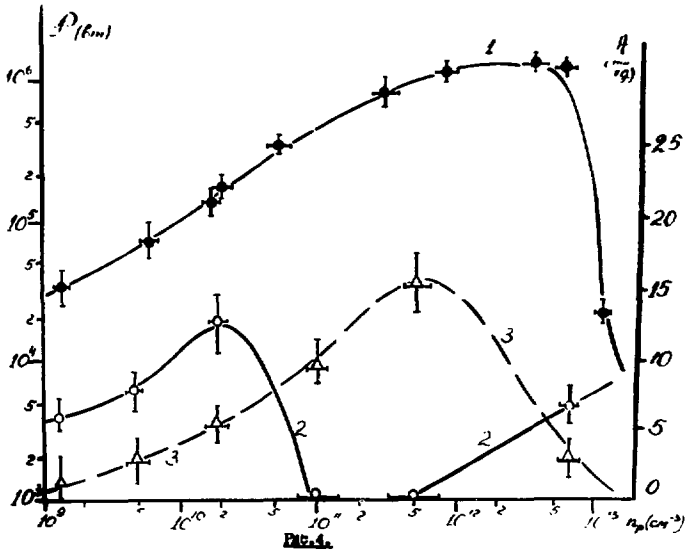

Fig. 4. Maximum radiation power P in the pulse vs. the plasma density in a magnetic field H = 4.8 kOe. (1) The power in watts of short-wave radiation (f = 9 gHz) for foil Ti, Δ = 50μ; (2) the same, only for foil Al, Δ = 10μ; (3) long-wave radiation (f ~ 1.5 gHz) power in relative units (foil Al, Δ = 10μ).

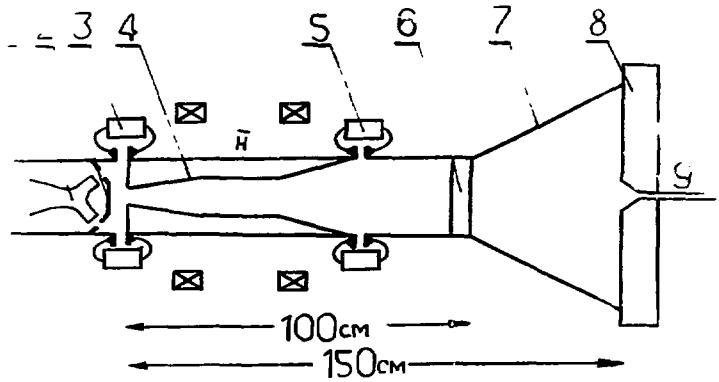

Fig. 5. MCR generator: (1) cathode, (2) anode, (3),(5) shunts, (4) resonator, (6) Teflon window, (7) radiative horn, (8) microwave absorber, (9) X-band waveguide.

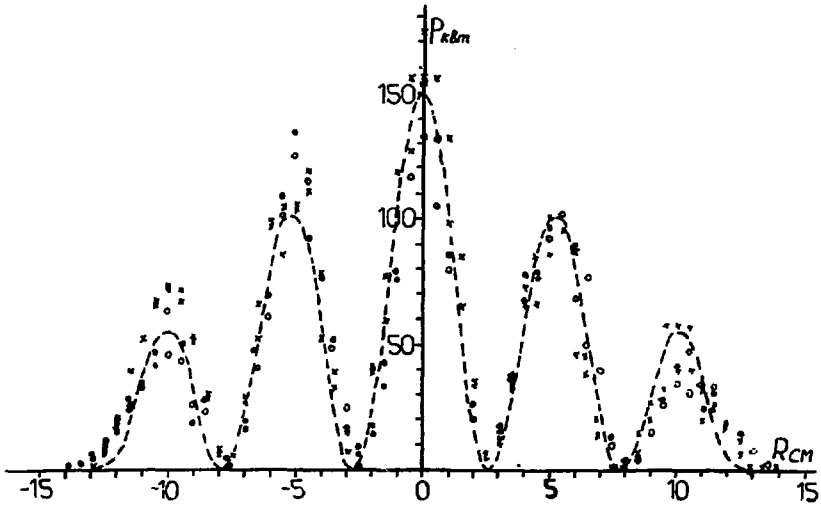

Fig. 6. The distribution of radiation power P on the radius radiated horn, P is power on the detector. The curve is a theoretical curve for mode TE_{13}; x - experimental points measured with band filter; o - without filter.

LIMITING CURRENTS FOR INJECTION OF AN UNNEUTRALIZED MAGNETIZED RELATIVISTIC ELECTRON BEAM INTO A CYLINDRICAL DRIFT TUBE

J. R. Thompson and M. L. Sloan

Austin Research Associates, Austin, Texas 78758

ABSTRACT

Results of an investigation of the steady state injection of a uniform unneutralized, magnetized, relativistic electron beam into a cylindrical drift tube are presented. The space-charge limited current and the asymptotic kinetic energy of electrons on axis is determined both numerically and analytically as a function of the input kinetic energy $(\gamma_o-1)mc^2$ and of the ratio of beam-to-wall radii. A previously cited "interpolation formula" is obtained in the pencil beam limit, but more accurate limiting current expressions are developed for other cases (such as the fat beam limit) where the interpolation formula is as much as 20 percent in error. The corresponding axial electron energy is also found to be significantly smaller than the previously cited value of $(\gamma_o^{1/3}-1)mc^2$ except in the strong pencil beam limit.

I. INTRODUCTION

We consider a small but relevant subclass of the general limiting current problem, which has been discussed repeatedly

in the literature (c.f.[1] and the bibliography given there). Specifically we consider a cold, unneutralized electron beam of radius a, propagating along an effectively infinite magnetic guide field, within an evacuated coaxial drift tube of radius $b \geq a$. At the anode plane, which is connected electrically to the drift tube wall, the electron number density n_o, axial velocity $\beta_o c$, and particle energy $(\gamma_o - 1)mc^2$ are assumed independent of radius r. We consider only the limitation on beam current which derives from the conditions for propagation in a steady state equilibrium; previous work[2] has indicated that such an electron beam is absolutely stable in a sufficiently large magnetic guide field.

The exact numerical solution of this limiting current problem was obtained long ago[3] for nonrelativistic ($\beta_o << 1$) beams, but relativistic solutions have only been published for the special cases of pencil beams ($\ell n\, b/a >> 1$) or ultra-relativistic beams ($\gamma_o >> 1$) for which the radial variation in the downstream quantities γ, β, n are unimportant. We describe herein relativistically correct numerical solutions to the limiting current problem (indeed our emphasis is on the relativistic case where β_o is not small compared to unity) for arbitrary values of b/a, as well as analytical approximations which provide a high degree of accuracy.

II. GOVERNING EQUATIONS AND NATURE OF NUMERICAL SOLUTIONS

By exploiting the constants of the motion, $r = r_o$, $n\beta = n_o\beta_o$, and $\gamma - (e\phi/mc^2) = \gamma_o$, one may write the Poisson equation far downstream of the injection plane in the form

$$\frac{1}{r}\frac{d}{dr}\, r\, \frac{d\gamma}{dr} = \frac{4\nu}{a^2}\, \frac{\gamma}{\sqrt{\gamma^2-1}}\,, \qquad r \le a \tag{1}$$

subject to the boundary conditions that γ be regular at the origin and obey

$$\left(\gamma + \ell n\, \frac{b}{a}\, r\, \frac{d\gamma}{dr}\right)_{r=a} = \gamma_o \tag{2}$$

which follows from integrating the radial Poisson equation through the vacuum gap from a to b. Here

$$\nu \equiv \frac{\pi n_o e^2 a^2 \beta_o}{mc^2} = \frac{I_e}{mc^3/e} \tag{3}$$

is dimensionless current, independent of r, z.

In principle, if one specifies a value for the γ of the electrons at the center of the beam, $\gamma_c = \gamma(r = 0)$, then Eq. (1) determines $\gamma(r)$ throughout the beam as a function of γ_c, ν, a. Applying the boundary condition, Eq. (2) then allows one to solve for ν as a function of γ_c, γ_o, b/a. The resulting dependence of ν on γ_c for fixed values of γ_o, b/a is illustrated in Fig. 1. The maximum value of ν is the desired ν_L (the corresponding electron current is the limiting current), and the corresponding value of γ_c is γ_{cL}. It is of interest

in some applications to know γ_{cL} as well as ν_L, with a fair degree of accuracy.

A representative spectrum of the numerical solutions is listed in Table I. The montonic dependence of ν_L and γ_{cL} on separate variation of γ_o or b/a may be observed.

III. APPROXIMATE ANALYTICAL SOLUTIONS

There are several theoretical approaches to the limiting current problem, which yield approximate solutions that are useful in different regions of parameter space.

A. Iteration of Integral Equation

Equations (1) and (2) may be combined into a single integral equation, which is indicated below in iterative form

$$\gamma^{(N)}(x) = \gamma_o - 4\nu \ln \frac{b}{a} \int_o^1 \frac{dy\, y}{\beta^{(N-1)}(y)} - 4\nu \int_x^1 \frac{dw}{w} \int_o^w \frac{dy\, y}{\beta^{(N-1)}(y)} \qquad (4)$$

where $x = r/a$, $\beta = (1-\gamma^{-2})^{1/2}$, and the superscripts in parentheses indicate the order of the iteration. A zero-order guess is made for $\gamma^{(o)}(x)$ or $\beta^{(o)}(x)$, which may then be inserted in the RHS of Eq. (4) and the integrals performed to give a new, first-order solution $\gamma^{(1)}(x)$, after which the procedure may be repeated. If the zero-order guess is a constant, the iteration may be readily carried out to second

order, yielding the following equations:

$$\gamma^{(o)}(x) = \gamma_k = (1-\beta_k^2)^{-1/2} \tag{5}$$

$$\gamma^{(1)}(x) = \gamma_c + (\gamma_e - \gamma_c)x^2 \tag{6}$$

$$\nu = \beta_k(\gamma_e - \gamma_c) \tag{7}$$

$$\gamma_e = \left(\gamma_o + 2\gamma_c \ln \frac{b}{a}\right) \Big/ \left(1 + 2 \ln \frac{b}{a}\right) \tag{8}$$

$$\frac{\left[\gamma_o - \gamma^{(2)}(x)\right](\gamma_e - \gamma_c)}{\nu} = 2 \ln \frac{b}{a} (\gamma_e\beta_e - \gamma_c\beta_c)$$

$$+ \left[\gamma_e\beta_e - \gamma^{(1)}(x)\beta^{(1)}(x)\right] + \gamma_c \ln \frac{\gamma_e(\beta_e+1)}{\gamma^{(1)}(x)\left[\beta^{(1)}(x)+1\right]}$$

$$- \gamma_c\beta_c \ln \frac{\gamma_c\gamma_e(\beta_c\beta_e+1)-1}{\gamma_c\gamma^{(1)}(x)\left[\beta_c\beta^{(1)}(x)+1\right]-1} \tag{9}$$

Here γ_c, γ_e represent the value of γ for central and edge electrons. There remains the freedom to specify one further equation which will determine what constant γ_k is, in terms of γ_o, b/a, ν. [Equations (6)-(9) follow from Eqs. (4) and (5).] For example, if one selects $\gamma_k = \gamma_o$, then Eqs. (7) and (8) give

$$\nu = \beta_o(\gamma_o - \gamma_c) \Big/ \left(1 + 2 \ln \frac{b}{a}\right) \tag{10}$$

and hence,

$$\nu_L = \beta_o(\gamma_o - 1)/\left(1 + 2\ \ell n\ \frac{b}{a}\right) = \nu_o; \quad \gamma_{cL} = 1 \qquad (11a,b)$$

which is a previously published result.[4]

Another possibility is to select $\gamma_k = \gamma_c$, with Eqs. (7) and (8) then giving

$$\nu = \beta_c(\gamma_o - \gamma_c)/\left(1 + 2\ \ell n\ \frac{b}{a}\right) \qquad (12)$$

and hence

$$\nu_L = \frac{(\gamma_o^{2/3} - 1)^{3/2}}{1 + 2\ \ell n\ \frac{b}{a}}; \quad \gamma_{cL} = \gamma_o^{1/3}; \quad \nu_o = 0 \qquad (13a,b,c)$$

where Eq. (13a) is the previously mentioned and widely cited interpolation formula.[5] The corresponding value of γ_{cL} in Eq. (13b) has also been previously published.[6]

The above results of Eqs. (10)-(13) are essentially first order iterations, since no use was made of the second order Eq. (9). Consequently, they will have only limited accuracy, but may be expected to bracket the correct solutions.

An example which contains second order accuracy is to let γ_k be such that $\gamma^{(2)}(x=1) = \gamma^{(1)}(x=1) = \gamma_e$. Eqs. (9) and (8) then give

$$\nu = \frac{(\gamma_o - \gamma_c)^2/\left(1 + 2\ \ell n\ \frac{b}{a}\right)^2}{\left[\left(\gamma_c + \frac{\gamma_o - \gamma_c}{1 + 2\ \ell n\ \frac{b}{a}}\right)^2 - 1\right]^{1/2} - (\gamma_c^2 - 1)^{1/2}} \qquad (14)$$

Another example containing second order accuracy is to let γ_k be such that $\gamma^{(2)}(x=0) = \gamma^{(1)}(x=0) = \gamma_c$. Then Eq. (9) gives the result[7]

$$\nu = (\gamma_e - \gamma_c)^2 \left\{ (\gamma_e \beta_e - \gamma_c \beta_c) + \left(\frac{\gamma_c}{1 + 2\ \ell n\ \frac{b}{a}} \right) \right.$$

$$\left. \times \left[\ell n\ \frac{\gamma_e (\beta_e + 1)}{\gamma_c (\beta_c + 1)} - \beta_c\ \ell n\ \frac{\gamma_c \gamma_e (\beta_c \beta_e + 1) - 1}{2(\gamma_c^2 - 1)} \right] \right\}^{-1} \qquad (15)$$

with γ_e specified by Eq. (8).

Since Eqs. (14) and (15) are of second order accuracy, they may be used to explore the validity of Eq. (13). One finds that Eqs. (14) and (15) reduce to Eq. (12) only in the pencil beam limit for which $\gamma_e - \gamma_c << \gamma_c$, or $\gamma_o^{2/3} << 1 + 2\ \ell n\ b/a$, which is the lower left hand portion of Table I.

Although Eqs. (14) and (15) do not yield closed form algebraic solutions for ν_L and γ_{cL}, they are still fairly useful since they may be numerically maximized in minutes with a scientific hand-calculator.

B. Variational Principle

A variation principle which generates the differential equation (1) and the boundary condition (2) is

$$I[\gamma(x)] = \int_0^1 dx\ x \left[\frac{1}{2} \left(\frac{d\gamma}{dx} \right)^2 + 4\nu \sqrt{\gamma^2 - 1} \right] - \left. \frac{\gamma(x)[2\gamma_o - \gamma(x)]}{2\ \ell n\ \frac{b}{a}} \right|_{x=1} \qquad (16)$$

where I is a functional of $\gamma(x)$, which is to be extremized with respect to possible trial functions $\gamma(x)$. The simplest trial function of modest accuracy is that of Eq. (6), which gives from Eq. (16) a function $I(\gamma_c, \gamma_e, \gamma_o, b/a, \nu)$. The two free parameters γ_c, γ_e are determined from $\partial I/\partial \gamma_c = 0$, and $\partial I/\partial \gamma_e = 0$, while the limiting current condition is $(\partial^2 I/\partial \gamma_c^2)\ (\partial^2 I/\partial \gamma_e^2) - (\partial^2 I/\partial \gamma_c \partial \gamma_e)^2 = 0$. These three equations represent a closed form parametric solution for the limiting current parameters, which is listed in detail elsewhere.[8] The results are fairly accurate, as illustrated in Table II.

C. Ultrarelativistic Perturbation Expansion

We now restrict our attention to the case of a sufficiently highly relativistic beam that $\gamma_o \gg 1$ and $2\gamma_{cL}^2 \gg 1$. Then using the expansion

$$\frac{1}{\beta} = \frac{\gamma}{\sqrt{\gamma^2 - 1}} = 1 + \frac{1}{2\gamma^2} + \ldots \quad , \tag{17}$$

Eq. (1) may be solved iteratively to yield

$$\gamma(r) = \gamma_c + \frac{\nu r^2}{a^2} + \frac{1}{2\gamma_c} \ell n \left(1 + \frac{\nu r^2}{\gamma_c a^2}\right) + \ldots \quad . \tag{18}$$

Then the boundary condition, Eq. (2), gives

$$\gamma_o = \gamma_c + \nu\left(1 + 2\ \ell n\ \frac{b}{a}\right) + \frac{1}{2\gamma_c}\left[\ell n \left(1 + \frac{\nu}{\gamma_c}\right) + \frac{2\nu}{\nu+\gamma_c}\ \ell n\ \frac{b}{a}\right] + \ldots . \tag{19}$$

The peak value of ν (i.e., ν_L) may be found by differentiating

Eq. (19) with respect to γ_c and setting $\partial\nu/\partial\gamma_c\Big|_{\gamma_o, b/a} = 0$, to obtain

$$2\gamma_{cL}^2 = \ell n\left(1+\frac{\nu_L}{\gamma_{cL}}\right)+\frac{\nu_L}{\nu_L+\gamma_{cL}}\left(1+2\ \ell n\ \frac{b}{a}\right)+\frac{2\nu_L\ \gamma_{cL}}{(\nu_L+\gamma_{cL})^2}\ \ell n\ \frac{b}{a}+\ \ldots\ . \tag{20}$$

Equations (19) and (20) may now be solved simultaneously to determine the limiting current parameters ν_L and γ_{cL}.

Under the pencil beam limit, $2\ \ell n\ \frac{b}{a} >> \gamma_o^{2/3} >> 1$ and $\nu_L << \gamma_{cL}$, and one recovers an expanded version of Eq. (13).

On the other hand, in the fat beam limit (the upper right portion of Table I), $3+2\ \ell n\ \frac{b}{a} << \gamma_o^{2/3}$ and $\nu_L >> \gamma_{cL}$, so that Eqs. (20) and (19) become

$$2\gamma_{cL}^2 = \ell n\ \frac{\nu_L}{\gamma_{cL}} + 1 + 2\ \ell n\ \frac{b}{a} + \ \ldots\ , \tag{21}$$

$$\nu_L = \left(\gamma_o - 2\gamma_{cL} + \frac{1}{2\gamma_{cL}} + \ \ldots\right)\Big/\left(1+2\ \ell n\ \frac{b}{a}\right)\ . \tag{22}$$

To obtain γ_{cL}, Eq. (22) may be inserted in Eq. (21), which may then be solved iteratively. To second order, one finds

$$\gamma_{cL} = \frac{1}{\sqrt{2}}\left\{\ell n\left[\frac{\sqrt{2}\ \gamma_o}{\sqrt{\ell n\left(\frac{\gamma_o - 1.5}{1+2\ \ell n\ \frac{b}{a}}\right)+1+2\ \ell n\ \frac{b}{a}}} - 2 + \frac{1}{\ell n\left(\frac{\gamma_o - 1.5}{1+2\ \ell n\ \frac{b}{a}}\right)+1+2\ \ell n\ \frac{b}{a}}\right] + 1 + 2\ \ell n\ \frac{b}{a} - \ell n\left(1+2\ \ell n\ \frac{b}{a}\right)\right\}^{1/2} \tag{23}$$

The value of γ_{cL} in the fat beam limit may be seen to be much less than in the pencil beam limit, for a given value of γ_o.

In Table II, the numerical solutions illustrated in Table I are used to gauge the accuracy of the various analytical approximations. It may be seen that the "interpolation formula" significantly underestimates the limiting current, while Eq. (13b) grossly overestimates γ_{cL}.

ACKNOWLEDGMENT

This work was partially supported by the Air Force Office of Scientific Research (AFSC), Contract F49620-76-C-0002, and by the Ballistic Missile Defense Advanced Technology Center, Contract DASG60-76-C-0045.

REFERENCES

1. L. S. Bogdankevich and A. A. Rukhadze, Soviet Physics Uspekhi, 14, 163 (1971).
2. H. V. Wong, et al., Phys. Fluids 16, 902 (1973).
3. L. P. Smith and P. L. Hartman, J. Appl. Phys. 11, 220 (1940).
4. C. L. Olson and J. W. Poukey, Phys. Rev. A, 9, 2631 (1974).
5. Reference 1, p. 167.
6. R. J. Briggs, Phys. Fluids 19, 1257 (1976).
7. Eq. (15) was independently derived by W. A. Proctor and T. C. Genoni.
8. M. L. Sloan and J. R. Thompson, submitted to Phys. Fluids.

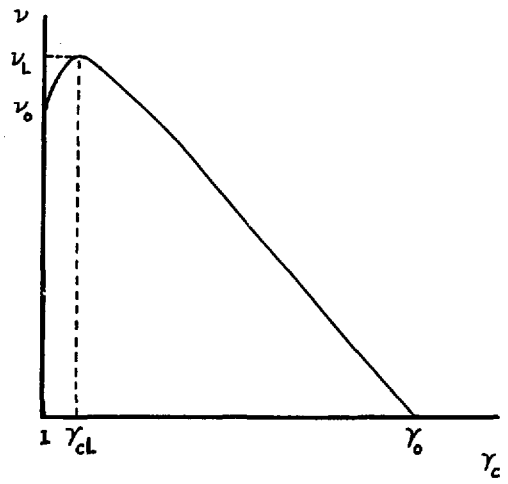

FIGURE 1: "Current" ν as a function of the relativistic factor γ_c of center electrons with γ_o, b/a fixed.

TABLE I. Numerical Solutions for $\frac{\nu_L}{\gamma_{cL}}$

	$\gamma_o = 2$	$\gamma_o = 5$	$\gamma_o = 7$	$\gamma_o = 100$
$\frac{b}{a} = 1$	$\frac{0.553}{1.12}$	$\frac{3.12}{1.26}$	$\frac{4.98}{1.31}$	$\frac{97.06}{1.68}$
$\frac{b}{a} = 2$	$\frac{0.221}{1.14}$	$\frac{1.27}{1.31}$	$\frac{2.05}{1.37}$	$\frac{40.61}{1.74}$
$\frac{b}{a} = 5$	$\frac{0.118}{1.18}$	$\frac{0.695}{1.41}$	$\frac{1.12}{1.48}$	$\frac{22.90}{1.89}$
$\frac{b}{a} = 20$	$\frac{0.069}{1.21}$	$\frac{0.407}{1.50}$	$\frac{0.659}{1.61}$	$\frac{13.75}{2.14}$

TABLE II. Tests of Accuracy of Analytical Approximations

	$\gamma_o = 5, \frac{b}{a} = 2$			$\gamma_o = 7, \frac{b}{a} = 4.985$			$\gamma_o = 100, \frac{b}{a} = 1$	
	ν_L	γ_{cL}	γ_{eL}	ν_L	γ_{cL}	γ_{eL}	ν_L	γ_{cL}
Numerical Computer Results	1.273	1.313	--	1.125	1.480	--	97.06	1.676
Interpolation Formula, 1st Order Eq. (13)	1.12	1.71	3.09	1.03	1.91	3.12	93.12	4.64
1st Order Eq. (11)	1.64	1.00	2.68	1.41	1.00	2.42	99.00	1.00
2nd Order Eq. (14)	1.31	1.27	2.83	1.13	1.47	2.78	98.28	1.15
2nd Order Eq. (15)	1.26	1.38	2.90	1.12	1.53	2.83	96.96	1.82
(Variational Principle)	1.28	1.31	2.90	1.13	1.49	2.83	97.82	1.33
Eqs. (22) - (23) (Ultrarelativistic Fat Beam)	1.35	1.11	--	1.09	1.39	--	97.13	1.59

TECHNOLOGY

MICROSECOND INTENSIVE E-BEAMS

E. A. Abramyan, B. A. Altercop, and G. D. Kuleshov

Institute of High Temperatures, USSR Academy of Sciences,
Korovinskoye Chaussee, Moscow, 127412, USSR

Summary

The scientific and technical problems which can be solved by use of long pulse $\tau \sim 10^{-6}$ - 10^{-3} sec, high power 10^5 - 10^7J electron beams and the technical possibilities of generating such beams are discussed. Some physics and technical aspects of the forming, transport and stability of beams and different types of the pulse power sources are considered. A prospective design of a compact multichannel acceleration 1 MeV, 1 kA range tube is proposed.

The recent advances in relativistic electron beam (REB) acceleration engineering are mainly concerned with the construction of high-current nanosecond accelerators. Taking into account that high-power REB application is considered to be one of the basic directions in the CTF problem solution, maximum research activities are directed toward the development of nanosecond superhigh-power REB generation technique. However, there is no doubt that the potential capabilities of REB as a tool for research and engineering is significantly wider. Thus, in justice to the successes and tendencies of further power increase in the nanosecond range, in this report we focus the attention on the necessity of developing the microsecond-range acceleration technique.

In the schematic diagram of Fig. 1 the coordinates "beam output energy - pulse length" represent a situation facing the intense electron current accelerators. On the one hand, there is a large quantity of

installations operating in the range of 10 to 100 nsec with the beam output energy per pulse from several kilojoules to 3 MJ. On the other hand, there are stationary plants generating 1 MW beams with a comparable output energy level at the time of 10^{-3} - 10 sec.

The intermediate microsecond range has been most inadequately developed, although, as will be seen from below, there are problems for which optimal solution is concerned with progress in intense microsecond-range electron accelerators.

An "intermediate" position of the beams in the range being observed stipulates a number of peculiarities in the technique of their generation as well as in the nature of their interaction with the medium and electromagnetic fields.

LONG-PULSE BEAM APPLICATIONS

With certain restrictions for the energy characteristics of the pulsed storage systems, the microsecond beam generation becomes possible at a limited level of their power output. The expediency and preferability of such combination of the parameters clear up when the processes to be investigated are optimized over the time or power within that range, or when the enhanced requirements are claimed to the beam quality. The possibility for simulation and study on quasi-stationary and stationary electron currents of this range at high levels, which can be realized at present stage of the technical development only in pulsed modes, is of certain interest.

Among various versions of the collective ion acceleration method a proposal by Sloan and Drummond [1] seems to be particularly attractive. According to their idea, the acceleration is accomplished with the wave electric field of the magnetized-beam space charge, when cyclotron resonance with the electron beam making use of the anomalous Doppler effect

and Cherencov resonance with the ion beam are performed.

An analysis of this process shows [2] that the optimal beams for this method may prove to be of the microsecond duration. Thus, for the pulse duration $\tau \sim 10^{-3} - 10^{-6}$ sec, at the length L~4 to 5m, an electron beam with the current $I \sim 10^3 - 10^5$A, and with the energy $\xi \sim 10^5 - 10^6$ ev is able to accelerate a proton current I_p~1-100A with the initial energy $\xi_p \sim 10^5$ev up to the evergy $\xi \sim 10^6 - 10^8$ev. In the acceleration circuits based on the REB scanning, when the ion acceleration occurs due to the shift of a potential hole formed by local disturbance of the beam density, the quasi-stationary REB application seems to be very prospective as well, owing to the principal possibility of forming a quasi-continued sequence of the potential holes for the ion trapping and acceleration.

Another problem is the construction of powerful SHF-generators [3]. An application of long-pulsed beams with the current $I=10^3 - 10^5$A, the energy $\xi \sim 10^6$ev and $\tau > 10^{-6}$sec, in the vacuum and plasma operated devices represents a unique possibility for achieving quasi-continued intensive SHF-rays, expands the frequency range owing to the ability of producing a desired frequency by modulating the beam at the interaction space input.

A third problem is concerned with the energy transmission over long distances. In this case, the current energy content is of major importance. As the investigation on the economical and technological aspects of this problem shows [4], attractive here appears to be a utilization of REB with the following parameters: $\tau \sim 10^{-3}$sec, $I \sim 10^3$A, $\xi \sim 10^6$ev.

Along with the encountered problems, long-pulsed REB find increasing application in such spheres as plasma heating in magnetic confinement CTF devices, novel methods for cutting and cleaving rocks, electron-beam treatment of materials, etc. REB utilization for excitation of the gas-dynamic and electrical ionized lasers makes it possible to sufficiently increase the capacity and pressure of the active medium, and ensure high

efficiencies of the irradiation.

Long-pulsed REB may prove to be especially effective when a problem to be solved requires bulk power supply in the presence of the restrictions on power output. These restrictions may arise from physical and technical conditions related to each specific problem. For example, they might be stipulated by the requirement of indestruction of a sample in the investigation on the kinetics of such processes as phase transitions, or in electron-beam treatment, and might be limited by dielectric strength of technological components, etc.

THE DYNAMICS FEATURES OF INTENSE MICROSECOND BEAMS

The dynamics features of electron currents for the range being considered are determined by the physical processes having commensurable characteristic times, which quantities as well as their influence on the beam behavior, depend on both its parameters and the external conditions. Substantial differences in behavior of the beams of various length begin to clear up when the energy exchange occurs between the electrons of the beam and the medium over or near which they propagate. The medium state alteration, which magnitude relates to the duration of the beam interaction, may lead to a qualitative change in the dynamics of electron current when its length is increased. Typical are the processes of neutralization of the charge and current of the beam passing through the gas and plasma.

Under these conditions, the influence of the plasma ion movement, and so on, appears to be a new circumstance in the beam current increase. The minimal pressure which allows the ions being generated to neutralize a space charge of the beam having the current density $j[A/cm^2]$: $P_{min} \simeq 3 \cdot 10^{-9} j/\beta M[torr]$ where $\beta = \frac{u}{c}$, u is the velocity of the beam electrons, c is the velocity of light, M is the molecular weight. The time required for the beam charge neutralization at $P > P_{min}$: $\tau_i \sim 10^{-8}/\beta MP(torr)[sec]$. For instance,

during a relativistic beam transfer with $j \sim 10^2$ A/cm in air $P_{min} \sim 10^{-8}$ torr and at $P < 10^{-3}$ torr, $\tau_i > 10^{-6}$ sec. The time τ_i is calculated with account for the ionization accomplished only with the beam electrons. In the gas ionization a significant contribution is also paid by the beam-induced fields, the ions and secondary electrons knocked on from the atoms and having the energy which is several orders smaller by that of the beam electrons. The time $t \sim \tau_i$ being over, the secondary electrons are no longer pushed out from the beam by the space charge and may cause a gas breakdown resulting in a high-conductive plasma channel formation. The space charge neutralization creates the conditions for gas focusing of the beam, when the electrostatic repulsion is replaced by compression with the own magnetic field. If the beam radius exceeds the skin thickness $a > \lambda s = (c^2 \tau / 4\pi\sigma)^{1/2}$ where σ is the plasma conductivity, the inverse current reducing the beam magnetic field is initiated in the plasma due to induction emf. The inverse current, however, damps with the time $t \sim \tau s = 4\pi\sigma a^2/c^2$ or at the distance $l = v\tau s$ from the front of the beam. Taking into account the gas heating with the beam, the plasma temperature is assumed to be $T \sim 10^{4o}$K. Then, $\tau s \approx 10^{-7} a^2$ sec. In this case, for microsecond beams with a smooth front and $a \sim 1$ to 3cm the characteristic time for the beam current change $\tau > \tau s$ and the inverse current do not affect essentially the dynamics of the beam.

In regard to the effective transfer of the beam, the problem of its stability acquires a great importance. The growth of short-wave perturbations leads, in general, to a diffusion washing-out of space-power distribution of the beam particles, whereas the perturbation instability with a characteristic dimension of one order or more for the beam radius causes macroscopic alterations in the beam profile (overbalances, coiling), which may result in particle throw-out onto the chamber walls. The

review on these questions is provided in papers [4, 5]. Here we will point out one of the most dangerous large-scale instabilities - the so-called hose instability. In the absence of the external magnetic field in the plasma the beam compensated over the charge and current is unstable in relation to coiling. The instability is caused by a centrifugal force affecting the flow when its trajectory is bent. The characteristic time for this instability development [6] is $\tau_h \sim \frac{a}{c}(Nm_i/nm_e\gamma)^{1/2}$ where $m_{e,i}$ is the electron (ion) mass; n, N are the beam and plasma densities, respectively, at $n/N \leq 10^{-6}$, $a \approx 2$cm, $\tau_h \geq 10^{-5}$sec. The instability is suppressed by a sufficiently strong magnetic field limiting the transverse shifts of the beam, or by the increase spread in the particle velocities. Furthermore, it is revealed only in beams with the radius $a < \tau(KT/m_i)^{1/2}$. When the beam current compensation in a plasma channel with the external magnetic field is incomplete the spiral instability develops with the typical rise time [5] $\tau_r \sim ca^2/I(4\pi Nm_i)^{1/2}$. Thus, when $I \sim 1$kA, $a \sim 3$cm, $N \sim 10^{16}$cm^{-3}, $\tau_r \sim 10^{-4}$sec. The instability is suppressed if the external magnetic field satisfies the condition $B > \frac{L}{c}j$, where L is the size of the system, j is the current density.

THE MICROSECOND BEAM ACCELERATION TECHNIQUE

Let us consider some questions on construction of the electron-beam accelerators having the following parameters: the energy ~1MeV, the beam output energy per pulse 0, 1 - 10MJ, the current 1 - 10kA, the pulse length 1 - 1,000mcsec.

The Emitters. The utilization of the FE cathodes making up one of the characteristic units of high-current nanosecond accelerators for the range being considered appears to be difficult. The main obstacle is the acceleration gap short-circuiting with the plasma resulting from operation of such an emitter. On the other hand, the emitters available from

development of stationary electron-beam thermocathodes either show small emission density (~1A), or are not prospective for application in high-current accelerators due to the increased sensitivity to operating conditions (e.g., oxide cathodes). An acceptable level for the emission density ($\sim 10^2 A/cm^2$) can be attained with several types of the rare-earth-based cathodes (e.g., iridium-cesium ones) or with pure-metal cathodes for the direct heating, being operated in "overheating" mode, approaching to the emission mode. Switching-on of the heating of such a cathode for a part of a second allows achievement of high level of the pulsed heating-up and emission, and short-duration switching ensures sufficiently long performance in the single pulse generation mode.

The Acceleration System. In the microsecond range a great dependence of dielectric strength on the duration of the voltage affecting the vacuum space requires the selection of the acceleration gap, when it is a diode-based one, being measured by tens of centimeters for the operating voltage ~1MV. Although, in principle, such an option seems to be achievable, the dimensions of the system, and that of the cathode, in particular, a specific emission density of which, in this case, is limited by the space charge at the level of several A/cm^2, turn out to be excessively large, but the reliability of the whole device is not found to be high.

The utilization of the compact multichannel acceleration tube (Fig. 2) appears to be prospective for the parameters being considered.

This construction apparently will allow achievement of high longitudinal potential gradient due to the use of narrow channels (~1mm), of dielectric with conductivity $\sim 10^4 - 10^6 \Omega cm$ in combination with the fine segmentation spacing (10 - 100μ), and longitudinal magnetic field, which lines of force constitute an angle with a cone surface of the channels. Furthermore, the limiting effect of the beam space charge is

considerably restricted because of the division of the total electron current into a large number of rays which do not interact in the acceleration zone. As a result the average current density in such a construction may account for ~100A/cm^2, so that the beam parameters described above may be obtained in the acceleration device with the typical size of ~10cm.

High-Voltage Power Sources. The power content of 1 - 10MJ and the electron-beam power output of 10^8 - 10^{10}W propose the utilization of high-voltage power sources, including, as a rule, the electric energy accumulators - the capacitive and inductive ones. We will consider three circuits being of practical interest and permitting increase of the beam homogeneity in a simple way:

(1) A Marx generator circuit with the pulse shape correction (Fig. 3a). When the acceleration tube is fed directly by the Marx generator, the pulse shape approaches to an exponential one, and consequently, the instability of the beam energy within the pulse duration is great.

A correction circuit, which consists of the opposite charged capacitor C, rechargable inductivity L, and controlled commutator S_1, connected in series with the Marx generator stages C_2, allows simple achievement of the voltage shape correction in the circuit and obtainment of a pulse with the quasi-constant voltage level [7]. In order to eliminate a shunting effect of the generator charge circuit in high-voltage pulse generation mode remaining quick charge of the capacitive accumulator of large energy capacity it is expedient to use components with a variable resistance. For example, charging may be accomplished via gas-filled resistors, the pressure variation of which permits switching them from a conducting state (charge mode) to a nonconducting state (pulse generation mode) [8]. It is noticable that one or more generator stages may be used as a correcting circuit condenser, which provides the the possibility for modification of the operating generators without

fundamental alterations. The efficiency of the stored energy into beam energy transfer in this scheme exceeds 50% at the instability of the beam energy of ±3,5%.

(2) An inductive storage system with the acceleration tube operating in the recuperation mode is shown in Fig. 3b. The inductive accumulators have not been so widely spread as the Marx generators because of the unsolved problems of commutation in their circuits. A transition to longer times (from nanoseconds to microseconds) reduces the commutator demand for operating speed and simplifies the task solution making use of conventional circuits.

We would like to point out a possibility of high-voltage pulse generation in circuit with the inductive accumulator, where the commutator and the acceleration tube are replaced by a single electron-ray device (Fig. 3b) with the electron energy recovery [9].

In the energy accumulation mode the current from the source G_1 is short-circuited over the inductivity L and the acceleration tube, and the resistance of the latter and as a consequence, the energy losses in it may be small enough, if the electrode is fed with high voltage from the auxiliary source G_2, and the electrode itself is made transparent for the accelerated electrons in the "cathode-electrode" section. These electrons are decelerated at the "electrode-collector" section, which is under a small positive potential relative to the cathode. The voltage drop at the tube is determined by a potential difference between the collector and the cathode, and the beam current is determined by the electrode potential value, which may be sufficiently high. When the energy accumulation mode is completed in the inductance, a locking potential is applied to the tube control electrode, the inductance circuit current is decreased, and a high-voltage pulse is generated on the inductance terminals, which is

applied to the "cathode-collector" section. The programmed change of the control electrode voltage makes it possible to obtain a voltage pulse of the desired shape, and consequently, a required electron-beam power spectrum.

(3) A circuit with the shock transformer and the line (Fig. 3c). In the circuit utilizing the shock transformer where the inductively coupled loops are resonantly adjusted ($L_1C_1=L_2C_2$) at the coupling coefficient~0,6 and at high Q-factor value of the loops [10], the energy stored in low-voltage capacitor C_1 of the primary circuit may be simply transferred, at high efficiency, into the capacitor C_2 of the secondary loop with a multiple voltage increase $V_2 \approx V_1\sqrt{C_1/C_2}$. The programmed change in the current over the acceleration tube shunted to the capacitor C_2 makes it possible to keep on the constant voltage level at the pulse section. An increase in the efficiency and a beam output stabilization for the pulse duration may be achieved by means of replacing the line with the point parameters L_iC_i, utilized instead of the capacitance C_2, permitting formation of a square-wave voltage pulse at the tube, which is connected via the discharge switch S_2 at the time when the secondary voltage approaches its maximum. The line discharge duration is selected to be less than the typical period for the voltage change at the oscillation process in the transformer.

It also should be noted that the explosion-magnetic generators can be used as the powerful energy sources to accelerate microsecond electron beams with high output energy.

The promising directions for the considered range of parameters are concerned with application of the electron-beam energy recuperation method [11].

Thus, the consideration of physical and technical possibilities for the achievement and utilization of the microsecond relativistic electron

pulses has revealed the urgency and practical significance for the development of corresponding acceleration technique and of the initiation of physical studies on long-pulsed REB properties.

REFERENCES

1. M. L. Sloan, W. E. Drummond, Phys. Rev. Lett. 31, 1234 (1973).
2. V. P. Indykul, I. P. Panchenck, V. D. Shapiro, V. I. Shevchenko, Physika Plasmy, 2, 775 (1976).
3. M. Friedman, Appl. Phys. Lett., 26 1, (1975).
4. R. S. Symons, paper N2-94, World Electrotechnical Congress, Moscow (1977).
5. B. N. Breizman, D. D. Ryutov, Nucl. Fusion 14, 873 (1974).
6. A. A. Ivanov, L. I. Rudakov, JETP 58, 1332 (1970).
7. E. A. Abramyan, G. D. Kuleshov, N. 540632 Bul. isobr. N.47, 132(1976).
8. E. A. Abramyan, G. D. Kuleshov, N. 544108 Bul. isobr. N.3, 179(1977).
9. I. N. Slivkov, G. I. Dolgachov, PTE 3, 27 (1975).
10. E. A. Abramyan, High-voltage generators of the base of the shock transformer, Intern. pulsed power conf., Lubbock (1976).
11. E. A. Abramyan, E. N. Efimov, G. D. Kuleshov, Energy recovery and power stabilization of pulsed electron beams in Marx generator circuits, this conference.

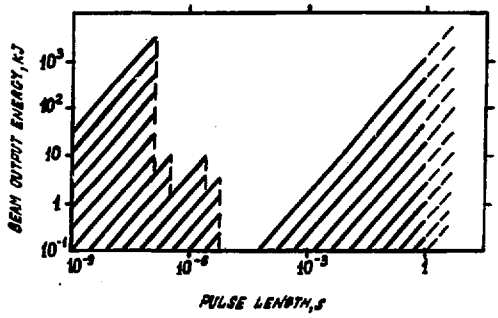

Fig. 1. Electron beam parameters of the modern accelerators.

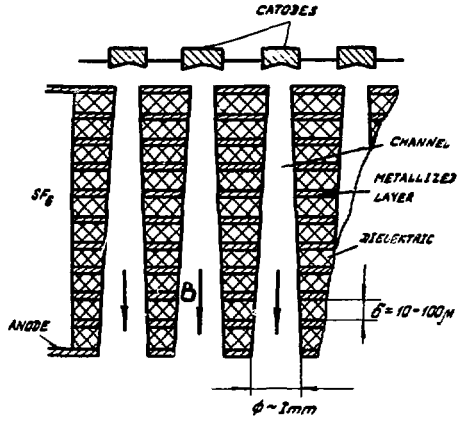

Fig. 2. Schematic design of the multi-channel compact accelerating tube.

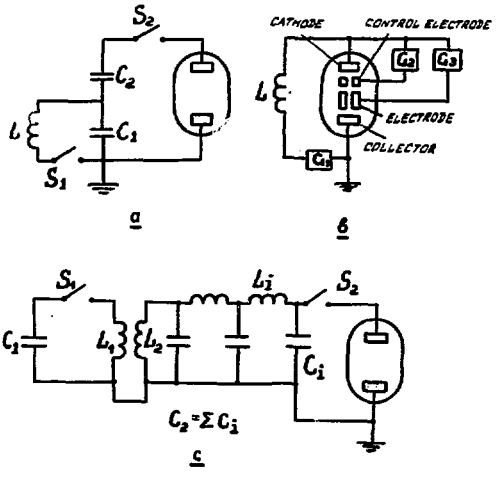

Fig. 3. Some high voltage pulse power supply shemes of the microsecond accelerators.

ENERGY RECOVERY AND POWER STABILIZATION OF PULSED ELECTRON BEAMS IN MARX GENERATOR CIRCUITS

E. A. Abramyan, E. N. Efimov, and G. D. Kuleshov

Institute of High Temperatures, USSR Academy of Sciences
Korovinskoye Chaussee, Moscow, 127412, USSR

Summary

A possibility of increasing the electron beam pulse duration and current in accelerators fed from the capacitive storage systems with the electron-beam energy recovery is described. A simple scheme for correction of the pulse shape of the generator voltage allows keeping in a quasi-constant level of the voltage on the acceleration tube for the pulse time, thus stabilizing the beam parameters: energy, current, and power. The experimental results are given.

The achieved level of the energy and power parameters of high-intensive electron beams is determined to a great extent by the capabilities of the power sources. To achieve high-power charged particle beams, the electric energy storage systems, generally of a capacitive type, will be used in such power sources. The typical characteristic value of the stored energy in such systems used in acceleration technology is higher, up to some megajoules [1]. But such accumulating complexes appear to be unique engineering constructions being on the verge of technical and economic possibilities. This imposes some restrictions on possible combinations of the generated beam parameters: high power level is attained in short-duration pulses.

In this paper we consider some ways of increasing these characteristics without a corresponding increase in energy capacity of the storage systems which are used in pulsed high-voltage power sources, such as Marx generators. Such possibilities can be realized when the beam power is not consumed completely in a certain process of interaction and is in general uselessly dissipated on the target and collector. This circle of problems involves, for example, the studies on the dynamics and stability of the beams, the interaction between the beam and the vacuum plasma, the investigation of the collective ion acceleration mechanisms, SHF-rays generation, etc. In such cases, return of the part of the beam energy remaining after the interaction makes it possible to increase the beam length and power without an adequate increase of the stored energy. The development of electron-beam energy recovery systems [2-4] has now attained the level where the product for beam power and its length can tens of times exceed energy capacity of a storage system used in the power source.

A schematic diagram for a device employing the principle of energy recuperation is shown in Fig. 1.

In the cathode-anode sector the electron current is accelerated up to the energy corresponding to the Marx generator voltage $V \approx nV_0$. Having passed the drift chamber, which is at the anode potential, the beam does not get the target as usual, but reaches braking electric field between the drift chamber and the collector, which has a small positive potential ΔV in relation to the cathode. Being decelerated, the electrons return their energy to the electric field and reach the collector with the energy of $e\Delta V$, which is considerably less than that of the acceleration enV_0.

If the electron energy dissipation in the drift chamber is small enough, whereas the electron-optical system is quite perfect ($\Delta I \ll I$, $\Delta V \ll nV_o$), the beam power $P=IV$ exceeds greatly the total power of both the Marx generator $P_g \approx \Delta IV$ and the auxiliary low-voltage source (e.g. the capacitor C_r) $P_r \approx I\Delta V$.

This allows either increase of the beam current with regard to the value determined by internal resistance of the Marx generator, or increase of the current duration as compared to the value determined by the time constant of the generator shock capacitance discharge with the total current of the beam.

Oscillographic records obtained with the generator set-up equipped with the energy recuperation device illustrate these possibilities.

Fig. 2a shows oscillographic records of the current and voltage in a Marx generator circuit without the beam energy recuperation. Fig. 2b shows at the same scale the oscillographic records for the same parameters in a recuperation circuit. The other two oscillograms (2c and 2d) illustrate an increase in the beam current and energy when recuperation is used with the beam current limited by the Marx generator internal resistance.

The voltage drop at the acceleration tube caused by a discharge of the generator shock capacitance with the beam current may be additionally reduced, and even eliminated at the pulse sector by means of a correcting loop LC_k included in the generator circuit, with the voltage inversion during the recharge of the capacitor C_k via the inductance L [5]. A schematic diagram for the circuit with the correcting loop is shown in Fig. 3.

At the time of switching the polarity of the capacitor charged to the voltage V_k is opposed to that of remaining generator capacitors.

Then, during the recharge of C_k via the inductance L, the change of the voltage polarity over the period of $\tau \approx \tau_i \sqrt{LC_k}$ is followed by more or less complete compensation of the Marx generator voltage drop when it is discharged with the load, and thus, a quasi-constant voltage level at the acceleration tube equal to $V \approx V_k - nV_o$ is kept on. The appropriate selection of the circuit parameters provides constant voltage at the load with several per cent accuracy when the circuit efficiency is in excess of 50%. This scheme of the beam power stabilization may be applied as well in Marx generators, where the energy recovery is not used. A pulse shape for the voltage generated in the circuit with the correcting loop is shown in Fig. 4.

References

1. B. Bernstein, I. Smith, IEEE Trans. Nucl. Sci. NS-20, No. 3, 294 (1973).
2. A. I. Arenshtam, I. N. Meshkov, V. G. Ponomarenko, R. A. Salimov, A. N. Skrinsky, B. M. Smirnov, V. G. Faynshtein, GTF 41, No. 2, 336 (1971).
3. E. A. Abramyan, A. H. Sharapa, PTE, No. 2, 30 (1971).
4. V. I. Perevodchikov, Paper No. 2-96, World Electrotechnical Congress, June 1977, Moscow.
5. E. A. Abramyan, G. D. Kuleshov. No. 540362. Bul. isobr., No. 47, 182 (1976).

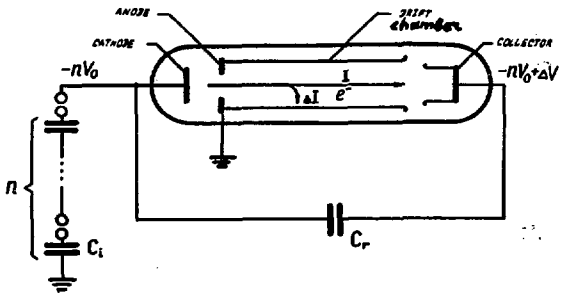

Fig.1 A circuit with electron-beam energy recovery.

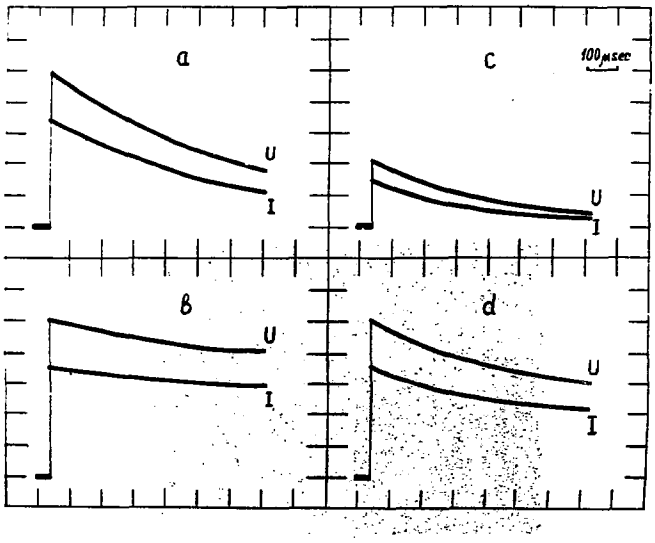

Fig.2 Oscillographic records of the electron beam current (I), and voltage (V) at the acceleration tube:
a) Marx generator with small internal resistance.
b) Marx generator with small internal resistance and with the beam energy recovery.
c) Marx generator with large internal resistance.
d) Marx generator with large internal resistance and with the beam energy recovery.

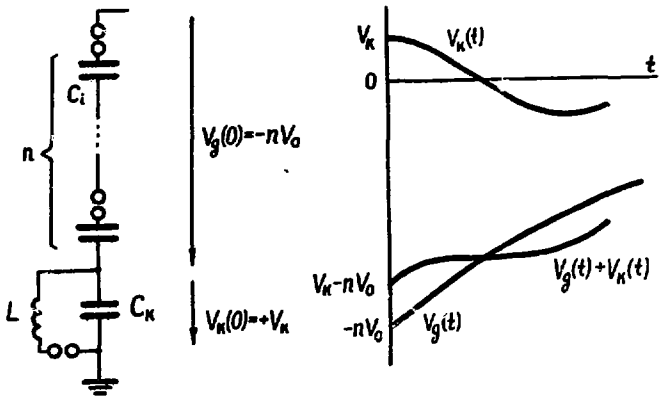

Fig.3. A circuit with the correction of the voltage pulse shape for a Marx generator.

Fig.4. Oscillographic records of the voltage pulse in the Marx generator with a correcting loop.

ON THE PROPERTIES OF CATHODE PLASMA IN THE DIODE WITH MAGNETIC INSULATION

R. B. Baksht, S. P. Bougaev, V. I. Koshelev, and G. A. Mesyats

Institute of High-Current Electronics

Siberian Department of USSR Academy of Sciences, Tomsk

ABSTRACT

In this paper there are given the results of investigations of the cathode plasma properties formed in the magnetic field in the process of the explosive emission. It has been shown that electron beam duration in the diode with the magnetic insulation is determined by the time of closing the gap by the plasma. The measured plasma velocity across the magnetic field with $B \geq 10^4$ G is equal to 0.45 cm/μs and did not depend on the cathode material (C, Al, Cu). The cathode plasma composition is investigated. It has been shown that the cathode material and the cracking products are present in the plasma. The possible mechanism of plasma velocity decrease in the magnetic field is discussed.

The diodes with magnetic insulation have been comparatively long in use to obtain annular electron beams [1]. One of the most important problems in obtaining these beams in increase of their duration. The solution of this problem greatly depends on the study of the properties of the cathode plasma obtained in a magnetic field in the process of the electron explosive emission [2]. The first experiments with the magnetic insulation in vacuum discharges were carried out by Mesyats and Baksht in 1969 [3]. The information about cathode plasma expansion across the magnetic field in diodes with magnetic insulation is based either on calculation of this value using the dependence of the diode resistance on

time [1,4,5], or on measurement of the breakdown formation time [6,7]. The direct measurements of plasma expansion velocity which defines the emission boundary motion is absent.

The experiments were carried out in a diode of cylindrical geometry. The experimental scheme is shown in Fig. 1. A voltage pulse of negative or positive polarity with the amplitude of U_o = 100 - 600 kV and duration $\tau_p \leq$ 5 μs was applied to the diode from the Marx generator. Cylindrical cathodes (C, Al, Cu) with a diameter of d_c = 2.8 - 10 cm, and a length of 3 cm were used. The drift tube with a diameter of d_a = 11.2 cm and a length of 50 cm was used as an anode. A cylindrical cathode of tantalum foil that was heated to the temperature of 1400°C was also used. The vacuum in the chamber was 10^{-5} Torr. The diode and the section of the beam transmission were in an axial magnetic field of B = 5 - 18 kG. Note that for the conditions of the experiment the calculated field of the magnetic insulation of the gap d, without taking into account the motion of the cathode plasma, was 2 kG. The diode voltage U_d was measured by the resistive divider, the diode current of $i_d \leq$ 4 kA by a shunt, and the electron beam current i_b by a Faraday cup.

Photographing the diode by an open shutter camera through the window of the drift tube at various voltage pulse durations has shown that luminescence is first registered on the cathode, and then spread on the gap. Fig. 2 shows the pictures of plasma in the diode with a carbon cathode, with d_c = 6 cm.

On the background of the diffused luminescence of the plasma one can see bright plasma jets (Fig. 2b) moving off the cathode in the direction corresponding to the plasma drift in the crossed electric and magnetic fields. The drift velocity $V_d \simeq$ 1 cm/μs. These jets are also observed on the beam track on the target. With the increase of the magnetic

field, the jets embrace the cathode (Fig. 2c). The data obtained indicate the penetration of the magnetic field into the plasma. The experiment has also shown that under the application and subsequent increase of the outer magnetic field, the number of emission centers in the cathode grows and the plasma luminescence of the cathode becomes more uniform. The reasons for this phenomenon will be discussed below.

The plasma velocity V_p across the magnetic field was measured according to the electron beam expansion as a result of plasma radial motion and was calculated by the delay time t_d of the current appearance on the probes set along the radius, one after another at a distance δ from the cathode.

For the simultaneous registration, a six-ray oscilloscope 6 OP-02M with microsecond sweeps was used. The error of the measurement V_p was 20-60%. The experiments on plasma expansion did not show any essential difference for Al and Cu cathodes. The results of the measurements of t_d for Cu and C cathodes of d_c = 6 cm, at U_0 = 300 kV averaged for 10 pulses, are given in Table 1. The table shows that V_p near the cathode, with the exception of the carbon cathode at B = 6 kG, does not depend on the cathode material, or the value of the magnetic field, and is 0.3 - 0.4 cm/μs. With the increase of the distance from the cathode, V_p grows somewhat as well. For a carbon cathode at B = 6 kG, V_p near the cathode is $V_p \sim 1.5$ cm/μs; at a distance of 6 mm from the cathode, V_p reduces to almost a third of its former value and then it increases again to 1 cm/μs.

The measurements with the carbon and copper cathodes at d = 11 mm have shown that the value d/t_f, where t_f is the breakdown formation time in the diode at B = 6 - 18 kG, is practically independent of the magnetic field, and is 0.45 cm/μs. Within 20% it coincides with the value of V_p taken as an average over the distance close to d. Note that in the conditions of the experiment, d/t_f at B=0 was 1.5 - 3 cm/μs. The heating of

the tantalum cathode to 1400°C did not change t_f(B + 6 kG, d = 6 mm). The mass composition in these conditions was not checked, but it has been shown earlier [8] that at such temperature the tantalum surface is practically pure.

To understand the process of plasma expansion across the magnetic f field, the knowledge of the composition and the concentration of plasma is required. The spectrum of the plasma luminescence has been photographed in the range of 400 - 700 nm with the consecutive exposure of 100 pulses on "ISOPANCHROM 18" film. The characteristic curve was taken in conditions of the pulse illumination of the film. The spectograms obtained indicate the presence in the plasma, as in [9], both of the cathode material (Al I, Al II, Al III, Cu I, Cu II), and the products of cracking of carbohydrates (C_2 - Swan's system, CH - the system of 420.0 nm, H_α, H_β, H_γ, C I, C II), the intensity of the latter considerably exceeding that of the metal lines. The results of the photometering on UPO-451 of some of the lines of the plasma radiation at the copper cathode in axial and radial directions are given in Fig. 3. The position of the slit of the spectrograph UCP-51 is shown in the corresponding figures. On photometering in axial direction (Fig. 3a) the radiation peak is distinctly seen on the cathode edge. In contrast to the axial direction, the intensity of the lines of the metal (Cu I, Cu II) in radial direction (Fig. 3b) drops more sharply inside the gap than with the lines C_2, H_β, C II.

The maximum intensity of the Balmer hydrogen lines did not depend on the cathode material (C, Al, Cu). The width of their contour in the maximum intensity did not exceed the width of the device trace that indicated the absence of the Stark broadening of these lines. This permits estimation of the concentration of plasma as $n < 10^{15} cm^{-3}$. Interferometric measurements using the methods described in detail in [10] on the carbon

and copper cathodes for the times 0.65, 2.0, 3.5 μs from the onset of the current pulse in the diode have shown that at the distance of 300 μm from the cathode $n_e < 10^{16}cm^{-3}$.

Assuming that the electron temperature of the plasma T_e 1 eV and that the plasma regime is close to saturation, the plasma concentration at the density of the electron current of the beam $j_e \leq 10^2 A/cm^2$ was estimated as $n_e \leq 10^{13}cm^{-3}$. This estimate does not contradict the result of n_e measurement.

The time-dependent electron beam structure was investigated by using the probe system and copper and plastic targets. The inside diameter of the hollow electron beam is approximately equal to the cathode diameter. The tract thickness obtained for 5 - 10 pulses on a copper target was about 10 mm. The experiments show that uniformity of electron beam increases with the magnetic field increase. The time-dependent current density investigations using probes and multi-ray oscilloscope showed that its value $j \leq 10^2 A/cm^2$ and it changed during the pulse, as shown in Fig. 4. The current from the cathode edge decreases with the magnetic field increase; that is in agreement with the plasma photographs on cathode (Fig. 2b, c). The current density distribution in the magnetic field, 18 kg (Fig. 4b) at the beginning of pulse, is close to uniform. During the pulse with plasma expansion j_e decreases on the inside beam wall, and it increases on the periphery at the same time. This is defined by the electric strength decreasing of the inside of the beam because of space charge screening.

The data obtained permit the conclusion that the duration of the electron beam in the diode with magnetic insulation is determined by the time of plasma expansion from the cathode to the anode. The decrease of the plasma velocity to $V_p \approx 0.45$ cm/μs is evidently due to the growth of the number of emission centers on the cathode surface with the application

of magnetic field and the current decreases on one center. In [11] it has been shown that decrease of the current removed from the single emission center leads to the drop of plasma velocity. An important role in the motion of plasma may also be played by the vapors of the cathode material and by the products of cracking of carbohydrates, which are not stopped by the magnetic field and may determine the plasma velocity across the magnetic field.

REFERENCES

1. M.Friedman, M.Ury. Rev. Sci. Instrum., 43, 1659, 1972.
2. С.П.Бугаев, Е.А.Литвинов, Г.А.Месяц, Д.И.Проскуровский, УФН, 115, 101, 1975.
3. Р.Б.Бакшт, Г.А.Месяц. "Известия ВУЗов СССР, Физика", 7, 144,1970.
4. Л.В.Дубовой, И.М.Ройфе, Е.В.Середенко, Б.А.Стекольников, В.Б.Шапиро. АЭ, 38, 87, 1975.
5. И.М.Ройфе, Б.А.Стекольников, В.И.Энгелько. ЖТФ, 46, 2563, 1976.
6. Ю.В.Ткач, Я.Б.Файнберг, Н.П.Гадецкий, Б.А.Лемберг, В.В.Дятлова, В.В.Ермоленко, А.В.Сидельникова. Письма ЖЭТФ, 22, 136, 1975.
7. S.C.Luckardt, N.N.Fleischmann. Appl. Phys. Lett., 30, 182, 1977.
8. В.И.Кошелев, Н.А.Ратахин, М.Н.Тимофеев. ПМТФ, 6, 6, 1975.
9. G.Bekefi, T.J.Orzechowski, K.D.Bergeron. Proc. of the Intern. Top. Conf. on Electron Beam Research and Technology. Vol. 1, p.333-345, 1975.
10. С.П.Бугаев, Р.Б.Бакшт, Е.А.Литвинов, В.П.Стасьев. ТВТ, 14, 1145, 1976.
11. Г.П.Баженов, С.П.Бугаев, Г.А.Месяц, С.М.Чесноков. Письма ЖТФ, 2, 462, 1976.

Table 1

Summary of results

B, kG	cm	t_d, us	
		Copper	Carbon
6	0.3	0.77	0.2
	0.6	1.32	0.75
	1.2	-	1.37
12	0.3	0.9	0.79
	0.6	1.22	1.52
18	0.3	0.73	0.9
	0.6	1.39	1.49

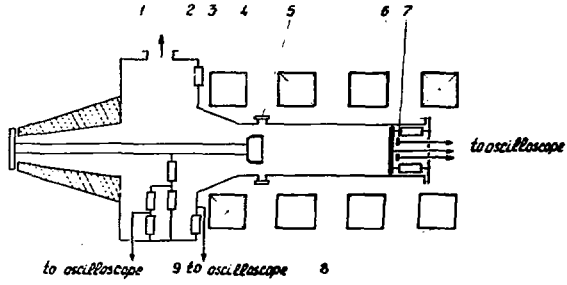

Fig. 1. The experimental scheme.

1 - vacuum chamber, 2 - cathode shank, 3 - current shunt, 4 - cathode, 5 - window, 6 - Faraday cup, 7 - probes, 8 - solenoid, 9 - voltage divider.

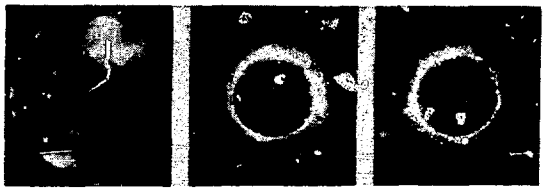

a *b* *c*

Fig. 2. Photographs of plasma in diode.

a - B = 0, b - B = 6, c - B = 18 kG.

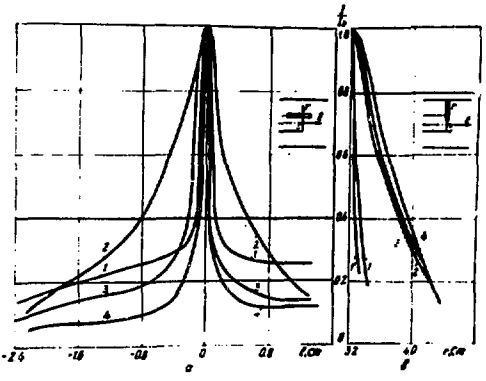

Fig. 3. The graphs of the dependence of the cathode plasma intensity on the distance.

d = 3.2 cm, = 3 us, B = 5.1 kG, = 230 kV.

a - the spectrograph slit parallel to the beam axis.

b - the spectrograph slit perpendicular to the beam axis.

1 - Cu I 521.8 nm, 1' - Cu II 490.9 nm,
2 - H 458.0 nm, 3 - C_2 516.5 nm, 4 - C II 558.9 nm.

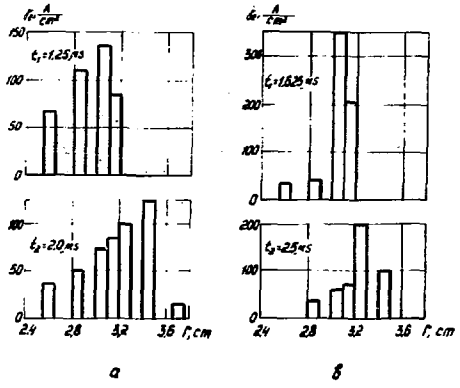

a *б*

Fig. 4. The current density distribution along the radius for some moments of current pulse in diode.

a - r_c = 3 cm, B = 6 kG, U_e = 250 kV, I_e = 2 kA.
b - r_c = 3 cm, B = 18 kG, U_e = 250 kV, I_e = 1,6 kA.

STUDY OF 200KA REB FOCUSSING DEPENDING ON THE "KALMAR" DIODE GEOMETRY

B. A. Demidov, M. V. Ivkin, V. A. Petrov,
E. A. Smirnova, and S. D. Fanchenko
I. V. Kurchatov Institute of Atomic Energy, Moscow, USSR

High-power relativistic electron beam focussing represents an important problem to be solved in order to make the controlled pulsed electron fusion feasible. As shown by L. I. Rudakov [1, 2], a relativistic electron beam with a current 10^7A and a power density in the beam 10^{13}W/cm^2 is required.

The "Kalmar-1" accelerator, producing a relativistic electron beam with a $5\cdot10^{11}$ - $5\cdot10^{12}$W/cm^2 power density, is described. The results on the relativistic electron beam focussing as a function of electrode geometry and voltage prepulse in the high-voltage diode are presented.

I. Accelerator design.

The pulsed electron accelerator "Kalmar-1" is a 70ns electric length water Blumlein line charged by a 2MV output voltage Marx generator with a stored energy of 70kJ. Although the Marx generator is rather simple in design, it provides triggering jitter less than 10-20ns [3]. The Blumlein line, the 1.5 Ohm output impedance coaxial transformer (5), and the high voltage diode (7) are inside a stainless steel 4.2m long container (Fig. 1) with a diameter of 1m. Vacuum is produced in the container, while filling it with distilled water.

The central cylinder of the Blumlein line (3) is fixed to the end-on insulators with hydroshock-proof elastic elements. The Blumlein spark switch constitutes the gap between the cylinder (3) and the mobile

shaft (2), the latter comprising a lens (12), focussing the laser beam to the electrode (3) surface, and a sapphire safety window (11). The neodymium glass laser (pulse energy 2J, pulse duration 20ns) consists of a Q-switched oscillator (13) and two amplification stages (14). In experiments with the laser off the water spark gap was operated as an untriggered switch. A "Vilite" nonlinear resistor was inserted in the Blumlein charging circuit to quench post-oscillations of the Marx generator-Blumlein line system in case of spark gap failure [4].

The high-voltage diode had a 80mm diameter planar anode (8). Cathodes (9) of various geometries have been tested. The prepulse magnitude could be varied from 1% up to 10% of the diode high voltage by the choice of inductance (10). An inductance-less resistor (6) and a Faraday cup have been used to measure the diode current and the beam current, respectively. The voltages at the Blumlein line, at the input and output of the coaxial transformer and between the electrodes of the diode have been measured with voltage dividers (4) described in [5].

X-ray diagnostics included a nine-channel pin-hole camera, a plastic scintillator and thermoluminescent LiF detectors and a ferrous sulfate dosimeter capable of measuring doses from 10^3 up to 10^5 rad [6].

II. Experimental results.

The first series of "Kalmar-1" experiments was done with a 70 mm diameter stainless steel flat cathode.

The experimental results are presented in Fig. 2. Represented here are the diode current (curves 1, 2) and impedance (3, 4) versus the cathode-anode gap δ for the two different prepulse values. The Blumlein line voltage was 0.5 MV. One sees that in the high prepulse regime the diode breakdown would occur for $\delta \leq 4$ mm so that the measured current J values differed but slightly from the short circuit current J_{sc}.

However, for both low and high prepulse conditions it was possible to find some gap value δ^* for which the current was nearly equal to half the short-circuit current J_{sc} as should be observed in the Blumlein-diode impedance matching case. The fact of Blumlein-diode matching is corroborated by Blumlein voltage measurements demonstrating the reflected wave minimum for $\delta=\delta^*$. Figure 3 presents the current and voltage oscilloscope traces together with the diode impedance and output power versus time for a planar-cathode diode. In this operation regime the X-ray pin-hole camera and spall records showed that the relativistic electron beam was sometimes pinched to some 2 mm diameter focus. From shot to shot the relativistic electron beam focus would sporadically wander all over the anode area.

Much experimental efforts have been devoted to find conditions of stable REB focussing to a given point at the anode. Different authors proposed [7, 8, 9] to use partly evaporating plexiglass cathodes, or to produce plasma jets at the cathode center either with a laser or a plasma gun triggered at the appropriate time. At the "Kalmar facility the solution of the stable REB focussing problem was sought via the choice of optimal metal cathode geometry. The following cathode shapes have been tested: pin, ring, convex cone. The best REB focussing (the focus size not exceeding 1 mm, see the pin-hole picture in Fig. 4) has been obtained with a convex 135^{o} metal cone with a 70 mm base diameter. X-ray pictures and anode spall figures have shown that such a cathode geometry provided the REB focussing precisely at the center of the anode with a 100% repetition rate. The current density was 10^7 A/cm^2 with the power density of $5 \cdot 10^{12}$ W/cm^2. Good focussing was obtained with both 1% and 10% prepulse values.

However, the impedance of the convex-cone cathode is rather high and it is difficult to match it with the 1.5 Ohm line output impedance. Therefore, the absolute values of energy delivery to the REB focus was not greater that 1 - 2 kJ.

The highest energy delivery to the focus has been obtained with a 8 mm diameter hollow metal cone cathode of the type previously used at the "Angara-1" device [10]. Using such a cathode, the relativistic electron beam has been focussed to the center of the "Kalmar-1" anode, with focussed beam current 200 kA and focussed beam diameter 2-3 mm. Apart from the spalling of the external side of the anode the focussed REB produced in a single shot a spherical crater 5-5.5 mm deep at the internal surface of the Al anode (in some cases the beam perforated the aluminum anode 6 mm thick). According to computations [11], this corresponds to 3-4 kJ energy delivery to the REB focus. One should note that such an energy delivery to the focus was obtained only in the low prepulse (1%) case, the cathode-anode gap for 500 kV being 2.5-3.5 mm. The oscilloscope traces of current and voltage in the high focus energy-delivery low prepulse regime are presented in Fig. 6 together with diode impedance and output power plotted versus time.

The pinched REB X-ray spectrum was measured using variable thickness absorbers in front of thermoluminescent detectors in the 9-channel pin-hole camera. It was found to correspond to the Bramsstrahlung spectrum of electrons with an energy equal to the diode accelerating voltage. Fig. 7 presents the X-ray dose versus distance from the anode (250 kV voltage, 20 μm thick lead anode on an aluminum substrate). The dose was measured with LiF detectors. It is evident from Fig. 7 that the X-ray source was of some milimeters size. For U = 500 kV the dose was 5 kRad at a 1.5 cm distance, corresponding to 10 kRad directly at the anode.

Initial experiments on the laser triggering of the Blumlein line water spark gap have also been carried out at "Kalmar-1". According to the results reported in paper [12], the laser triggering is capable of shortening the pulse buildup time and diminishing the discharge channel impedance. In the present experiments with the Blumlein voltage equal to 90% of the untriggered breakdown voltage, the laser triggering made it possible to switch on the spark gap precisely at the moment when the Blumlein line charging voltage would reach its maximum. Preliminary results indicate that the voltage loss at the spark gap was reduced by a half and the rise-time of the diode voltage pulse was shortened by 10-15%.

III. Discussion and Conclusions.

Being rather simple in design, the "Kalmar-1" facility made it possible to achieve relativistic electron beam parameters required for electron fusion research. According to [13] the relativistic electron beam is absorbed in a 5-10 μm heavy metal layer so that the 4 kJ energy deposition at the focus of the "Kalmar-1" beam corresponds to a 1 keV per atom "instant" energy release as required in the electron fusion reactor. The experimental data on the diode impedance with low and high prepulse values and for different cathode geometries are of special interest.

From the data of Fig. 2 one can see that the impedance of a diode depends on two factors: the preliminary plasma density and the gap between the anode and the cathode. When the prepulse is high, the diode impedance at a given δ is less by a half than the low prepulse one. The behaviour of curves 3 and 4 in Fig. 2 representing high-prepulse and low-prepulse conditions, respectively, for a planar-cathode diode are in good agreement with the $R \sim \delta^2$ function, following from the well-known Chid-Legmuire law. However, much alike [14], the absolute values of R

in both cases differ several times from those calculated according to this law and depend on the preliminary plasma density. One should note that on high prepulse conditions with gap less than 5 mm a flash-over arises very soon and the diode is short-circuited with plasma. Because of that it is advantagious to operate with a low prepulse, making possible smaller gaps δ and consequently to obtain higher relativistic electron beam currents. Using a hollow cone in a low prepulse regime, it was possible to reduce δ down to 2-3 mm and obtain focussed electron beam currents up to 200 kA. The beam energy calculated as the integrated product of the measured current by the diode voltage was 8 kJ. This is in reasonable agreement with the 3-4 kJ energy delivery estimated by the anode spall. Such a considerable part of energy being deposited in the focus corroborated the model of REB fast pinching to a thin channel.

An additional proof of the model is provided by the observed dose dependence over distance (Fig. 7) suggesting a quasi-point X-ray source all over the current passage time.

Finally it is interesting to pay attention to the temporal behaviour of the diode impedance. It is evident from the curves in Fig. 3 that the planar-cathode diode impedance do not considerably change during approximately 100 ns. Due to this it was possible to match the diode impedance with the coaxial transformer output impedance for a long period. Under the focussed beam conditions a certain diode impedance increase occurs with time (Fig. 6). This phenomenon seems to be explained by the plasma anomalous resistivity in turbulent processes arising during the constriction of the beam to a narrow pinch. The focussed relativistic electron beam current was 200 kA at 0.5 MV in good agreement with the formula proposed by L. I. Rudakov for a relativistic beam [10].

$$I = 0.3\sqrt{U}$$

I and U representing the current in MA and the diode voltage in MV, respectively.

REFERENCES

1. L. I. Rudakov, A. A. Samarskij, Proc. 4th Europ. Conf. Controlled Fusion and Plasma Physics (Moscow, July-August 1973).
2. I. P. Afonin, M. V. Babykin, L. I. Rudakov et al., Second All-Union Meeting on Engineering Problems of Controlled Nuclear Fusion (Leningrad, 1977).
3. B. A. Demidov, M. V. Ivkin, Prib. Tekh. Ehksp. (1975), issue 3, 120.
4. B. A. Demidov, M. V. Ivkin, V. A. Petrov, S. D. Fanchenko, Prib. Tekh. Ehksp. (1975),issue 3, 37.
5. B. A. Demidov, M. V. Ivkin, Prib. Tekh. Ehksp. (1977), issue 2, 115.
6. I. D. Sokolova. "Chemical Methods of Dosimetry in Radiobiology," (in Russian), Atomizdat, 1972.
7. B. I. Liksonov, Gu. L. Sidorov, V. P. Smirnov, Pis'ma ZhETF, 19, 516 (1974).
8. Gu. V. Koba, V. I. Liksonov, V. S. Pen'kina, L. I. Rudakov, Gu. L. Sidorov, V. P. Smirnov, A. D. Suhov, E. Z. Tarumov, Proc. X Intern. Conf. on Nuclear Fusion and Plasma Physics (Tokyo, 1974). IAEA, Vienna (1975), v. 2, 337.
9. P. A. Miller et al. Phys. Rev. Lett. 35, no. 14, 940 (1975).
10. M. V. Babykin, B. V. Vaev, K. A. Baygarin, A. V. Bartov, P. P. Gavrin, B. A. Demidov, E. D. Korop, V. I. Mijiritzkij, A. M. Pasechnikov, S. S. Sobolev, S. D. Fanchenko, Technology of inertial

confinement experiments (Dubna, USSR, 19-23, July 1976) IAEA, Vienna 1977, p. 41.

11. M. M. Widner, S. L. Thompson, "Calculations of anode witness plate damage to pinched REB" Sand-74-351.
12. B. A. Demidov, M. V. Ivkin, V. A. Petrov, S. D. Fanchenko, Prib. Tekh. Ehksp. (1974), issue 1, 120.
13. S. L. Bogolubskij, B. P. Geracimov, V. I. Liksonov, Ju. P. Popov, V. P. Smirnov, L. I. Rudakov, A. A. Samarskij, L. I. Urutzkoev, Pis'ma v ZhETF 29, 203 (1976).
14. G. A. Mesyatz, "Production of high-power nanosecond pulses" (in Russian), Moscow, Sovetskoe radio (1974).

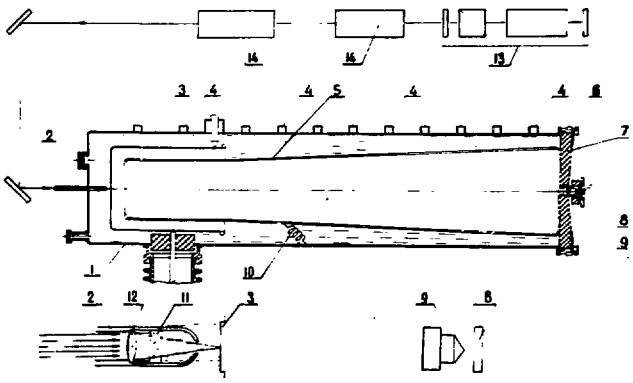

Fig. 1. Accelerator design.

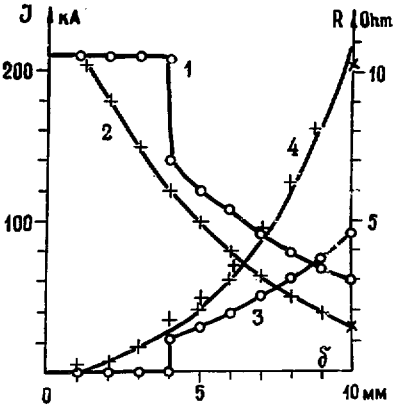

Fig. 2. Diode current versus cathode-anode gap (curves 1 and 2) and diode impedance versus gap (curves 3 and 4). Curves 1 and 3 were obtained with a 1% prepulse, while curves 2 and 4 represent a 10% prepulse.

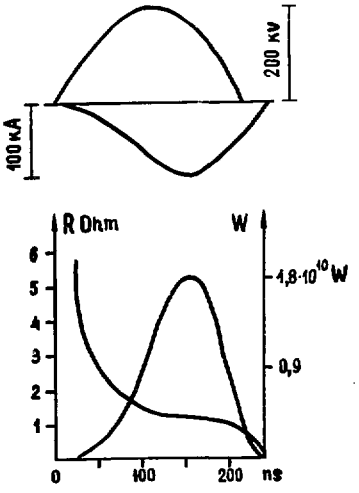

Fig. 3. Current and voltage oscilloscope traces together with the diode impedance and electron beam power as functions of time. Planar cathode geometry.

Fig. 4. Pin-hole X-ray photograph.

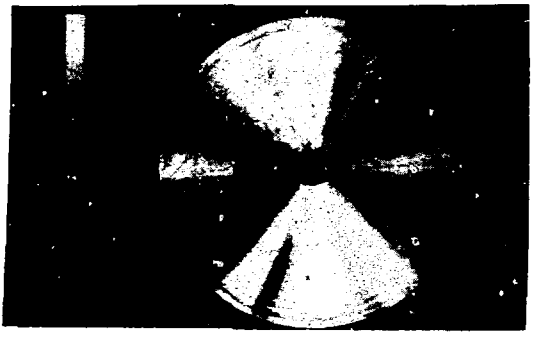

Fig. 5. Al 6 mm thick anode plate damage by the focussed electron beam.

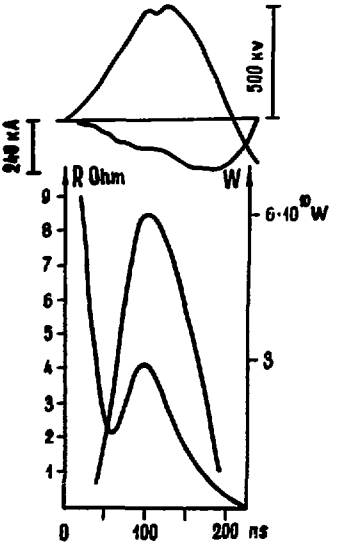

Fig. 6. Current and voltage oscilloscope traces together with the diode impedance and electron beam power versus time. Pinched beam.

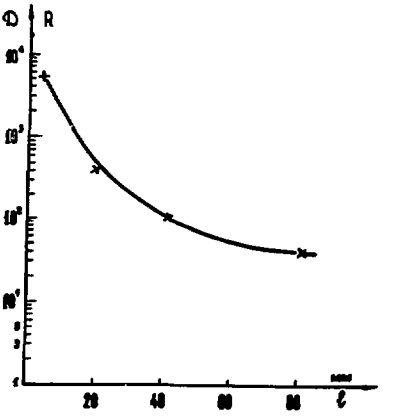

Fig. 7. Radiation dose as a function of distance from the anode.

MAGNETIC INSULATION IN TRIPLATE VACUUM TRANSMISSION LINES*

M. S. Di Capua, D. Pellinen, and P. D. Champney

Physics International Company
San Leandro, California 94577

and

D. McDaniel

Sandia Laboratories
Albuquerque, N. M. 87109

ABSTRACT

Magnetically insulated vacuum feeds have been investigated for use in an electron beam fusion accelerator. The magnetically insulated transmission lines would transfer the power pulses from many accelerator modules to a single diode region or multiple diodes to generate currents of the order of 100 MA. This approach may allow the present limits on power flow through dielectric/vacuum interfaces to be overcome. Experiments are reported on vacuum triplate transmission lines with a 24 ohm wave impedance and peak applied fields up to 1 MV/cm. Both ohmic and field emission loads were used with the center conductor pulsed positive. Measurements were made with a transmission line with a pulse double transit time length longer than the pulse risetime. Diagnostics included total current and boundary current, input and output voltages, and diode calorimetry. Accurate measurements of current, voltage, power, and energy transfer, as a function of several loads are reported and a comparison is made with theoretical models.

*Work performed under contract with Sandia Corporation 06-3645

1. INTRODUCTION

This paper describes the experiments performed to investigate power transfer in a magnetically insulated vacuum triplate transmission line with the center conductor at positive potential. These experiments are relevant to inertially confined electron (ion) beam fusion since the required power flow in a relativistic electron beam accelerator for fusion applications is beyond the present technology if the voltage requirement remains less than 3 MV (Reference 1). Therefore one must seek an improvement in the conventional technology of feeding the diode with an electromagnetic wave, perhaps leading the power from many accelerator modules to a single diode or multiple diodes using magnetic insulation. Either approach may provide much larger power to the target while at the same time isolate the target from the accelerator region in an electron beam fusion device.

To achieve the transport of an electromagnetic power pulse in the vacuum from the generator(s) to the diode at the voltages of interest, one must suppress or inhibit the space charge flow across the electrically stressed vacuum gap. This electron flow may, in principle, be inhibited by suppressing emission through special surface finishes or short pulses, or using magnetic fields which prevent electron flow to the anode (magnetic insulation). A chronology of the developments in magnetic insulation has been surveyed in Reference 2 and current theories as well as recent experiments have been discussed in References 3, 4, 5, 6 and 7.

Therefore there are some fundamental questions concerning vacuum transmission lines which are magnetically insulated by the self current in the line.

These questions are:

1. What is the magnetically insulated impedance Z = V/I of the line and how is it related to Creedon's geometrical factor g of the line (Reference 3)?
2. What combination of transmission line impedance and load impedance allows optimal power and energy transfer to the load?
3. What is the maximum applied electric field magnetic insulation can isolate?
4. Can the energy of the electrons in the space charge flow be recovered?
5. How does magnetic insulation affect the leading edge of the pulse?
6. What are the current and voltage losses associated with the propagation of the power pulse and how do these losses depend on the length of the transmission line?

The results of the experimental program indicate that the magnetic insulation process is considerably more complex than had previously been anticipated. In a vacuum triplate transmission line, there is a power loss associated with the sharpening of the leading edge of the pulse in the triplate. This sharpening might even be beneficial for pellet fusion applications. However, in the triplate geometry there is also an energy loss in the line which causes attenuation of the voltage as well as of the current pulse, resulting in peak power transport in the present experiments with a 50

percent flat optimum which is relatively independent of the load. This optimum arises when the impedance of the line as measured at the input is equal to the impedance of the load. These results as well as some answers to the questions posed above, will be explored in more detail throughout the discussion of the experiments.

These experiments represent an attempt to make basic electrical measurements; the geometry and materials were not optimized, so many of the conclusions should be taken as preliminary rather than fundamental for arbitrary geometries.

2. EXPERIMENTAL APPARATUS

A view of the 7 meter-long apparatus as seen from the load end appears in Fig. 1. It consists of a symmetric arrangement of two parallel plane transmission lines which share a common center conductor. This arrangement is referred to as a triplate in the rest of the paper. The outer conductors of the triplate are formed by the backs of two 20.3 cm-high aluminum "C" beams. These beams are supported from the top and the side of the 1.2 meter-diameter aluminum vacuum chamber with adjustable tie rods which allow their exact positioning, with respect to the inner conductor, under vacuum. The inner conductor is a 5.1 x 10.2 cm rectangular cross section steel tube supported at the input end by the anode stalk of the accelerator and at the output end by a 20 stage electrolytic resistor capable of operating up to 3.2 MV in vacuum. The photograph also shows, in the background, the vacuum electrolytic input voltage monitor at its location. The accelerator used in these experiments is the 1150 Pulserad facility located at Physics International's

San Leandro plant. The facility is a 45 ns, 35 ohm oil dielectric Blumlein accelerator capable of being charged to 5 MV and operated with a positive center conductor.

An important accomplishment of the experimental program has been the development of the diagnostics required to completely characterize the operation of the magnetically insulated vacuum triplate transmission line. The vacuum voltage monitors which have been developed have eliminated the uncertainties of the inductive voltage correction. A vacuum transit time isolator has been incorporated in the apparatus so that diagnostic signals from monitors located in the high voltage electrode can be recorded with oscillographs at ground potential. Therefore it has been possible to measure in these experiments the total current in the center conductor as well as the boundary current in the negative outer conductors; the input and output voltages, the voltage at intermediate points in the center conductor, and the energy delivered to a calorimeter by the field emission load.

A schematic of the triplate transmission line diagnostics appears in Fig. 2. The apparatus is drawn to scale with a cut removed from the center section. I0, I1, I2, and I3 are differentiating monitors which measure the total current at the input and output of the triplate respectively. IB1, IB2, and IB3 are their counterparts in the outer conductor which measure the boundary current. VI, VIM and VL are the input, movable and output voltage monitors. The transit time isolator, located beyond the field emission load, is also equipped with a current monitor, and it brings the leads of

the inner monitors and the calorimeter to ground. A schematic of the current flow in the triplate is shown in Fig. 3.

The waveforms for the total current in the center conductor appear in Fig. 4. The measurements have been displaced in time by a delay corresponding to the propagation of an electromagnetic wave in vacuum, along the triplate, at the velocity of light. In Fig. 4 a current loss of 7 percent arises in the first 30 cm of triplate, between I0 and I1. This loss varied between 0 and 10 percent in all experiments. The current transport is about 64 percent between I0 and I3 which is quite representative of the experiments performed in the neighborhood of the impedance match. The erosion of the leading edge of the current pulse is evident in the I2 waveform and the precursor at the foot of the waveform becomes very well defined in the I3 current. The current transport into a short circuit was consistently 100 percent rather than the 200 percent which would be observed in a conventional transmission line.

The boundary current IB (i.e., the currents flowing on the negative outer conductor) waveforms appear in Fig. 5. The difference between IB and the total current I is the current flowing as high energy electrons in the space between the inner and outer conductors. At peak current 30 percent of the current flows in the space charge at the location of I1, 22 percent at I2 and 45 percent at I3. The significance of the "bump" in the IB1 waveform has not been determined yet. It appears in 3 input monitors in some of the experiments. The increase in the space charge flow at the field emission load end is associated with the

impedance of the load (15 Ω). Experiments with a 11 Ω load showed 10-15 percent of the current in the space charge.

The voltage waveforms for the input, movable, and output monitors are shown in Fig. 6. The movable monitor was located 3 meters down the 7 meter-long triplate. The peak voltage at the load is 74 percent of the input voltage. The load voltage shows the leading edge erosion and the small initial peak associated with the precursor. The waveform for the movable monitor shows a partial erosion of the leading edge and a 15 percent loss in peak amplitude.

The values of input and output impedance, power and energy are summarized in the figure as well as the energy collected in the calorimeter. About 20 percent of the energy which flowed out of the triplate was not collected in the calorimeter.

The voltage in the triplate as a function of position for 4 monitor locations is shown in Fig. 7. The distance along the triplate is shown in the vertical axis and the waveforms were obtained at the 1, 2, 4, and 6 meter locations. The slanted line at the left represents the propagation of a pulse at the speed of light in vacuum. These experiments were performed with a field emission load with a gap of 1 cm. The solid waveform corresponds to the input monitor and the dashed waveform corresponds to the movable monitor. The erosion of the leading edge is already evident at the 1 meter location and at the 2 meter location there is already a noticeable loss in voltage. At the 4 meter location the voltage waveform has departed considerably from

the input waveform and at the 6 meter location the waveforms of the movable monitor and of the load monitor practically coincide.

One way to compare the experimental results with theory is to plot the total current in a magnetically insulated transmission line as a function of boundary current for a constant voltage. One such plot, for a voltage of 1.75 MV, corresponding to the parapotential theory of Creedon (Reference 3) appears in Fig. 8. Other models yield essentially the same result for current in the region where the data points occur (References 3, 6, 7). For very large boundary currents there is practically no space charge flow in the transmission line and the plot reaches an asymptote with a slope equal to one (total current = boundary current). As the boundary current decreases so does the total current until a minimum is reached at the minimum trapping current I_{MIN}. As the boundary current decreases further, the total current again increases reaching a maximum corresponding to saturated parapotential flow in which the boundary of the space charge flow grazes the anode. The data points displayed in the figure correspond to the total and boundary currents measured at the location of I1 (input of the line) for a peak voltage of 1.75 MV. The currents have been divided by the geometrical factor g = 2.5 of the triplate transmission line. The data for the 6 experiments and for 36 other experiments obtained at peak voltages between 1.5 and 1.9 MV shows approximate agreement with theory. The scatter in the data may be due to small uncertainties in the voltage measurements.

ACKNOWLEDGMENTS

The authors gratefully acknowledge the contributions of W. Adams, W. Furrow, M. Klatt, C. Parks, and H. Styles to the successful completion of the experiments and J. M. Creedon and I.Smith in assisting in the interpretation of the data.

REFERENCES

1. "Electron-Beam Fusion Progress Report, January-June 1976," SAND76-0410, Sandia Laboratories, Albuquerque, N.M. (1976).
2. P. D'A. Champney, M. Di Capua, D. Pellinen and I. D. Smith, "Magnetic Insulation in Coaxial Vacuum Transmission Lines," PIFR-937, Physics International Company, San Leandro, CA (1977).
3. J. M. Creedon, "Magnetic Cutoff in High Current Diodes," JAP, 48, 3, pp. 1070-77, (1977).
4. K. D. Bergeron, "Equivalent Circuit Approach to Long Magnetically Insulated Transmission Lines, "SAND-77-0021J, Sandia Laboratories, Albuquerque, N.M. (To be published, JAP) (1977).
5. "Electron-Beam-Fusion Progress Report, July through September 1976," SAND76-0711, Sandia Laboratories Albuquerque, N.M. (1977).
6. A. Ron, A. Mondelli, and N. Rostoker, IEEE Trans. Plas. Sci. PS-1, 85 (1973).
7. R. V. Lovelace and E. Ott, Phys. Fluids, 17, 1263 (1974).

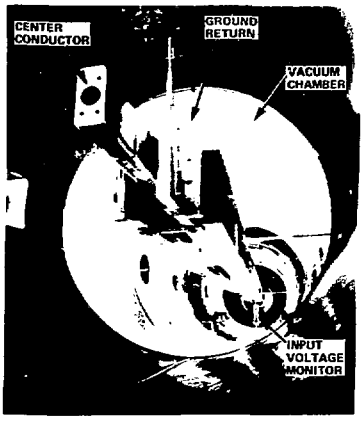

FIGURE 1 7 m-LONG TRIPLATE AND VACUUM CHAMBER (VIEW FROM LOAD END).

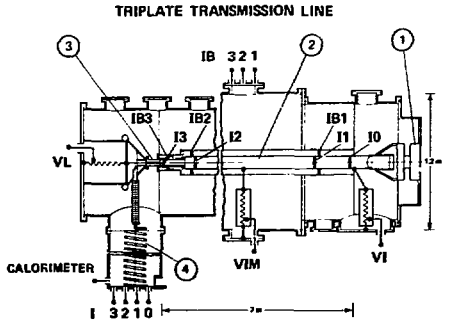

FIGURE 2 SCHEMATIC OF DIAGNOSTICS.

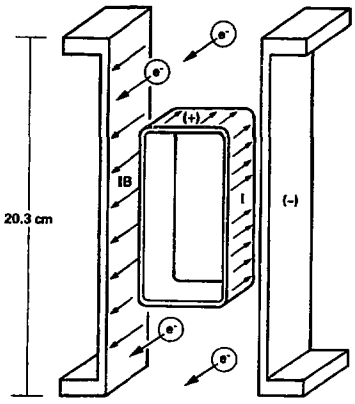

FIGURE 3 ELECTRON FLOW IN TRIPLATE.

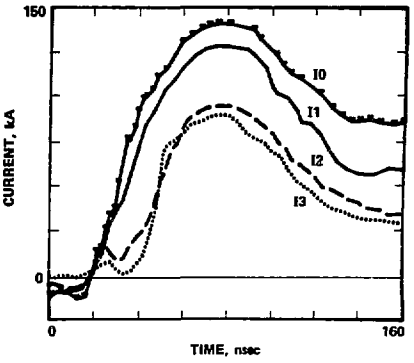

FIGURE 4 TOTAL CURRENT I WAVEFORMS.

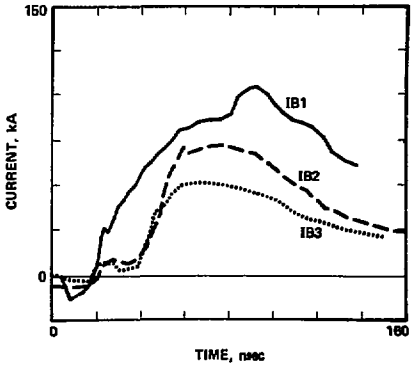

FIGURE 5 BOUNDARY CURRENT IB WAVEFORMS.

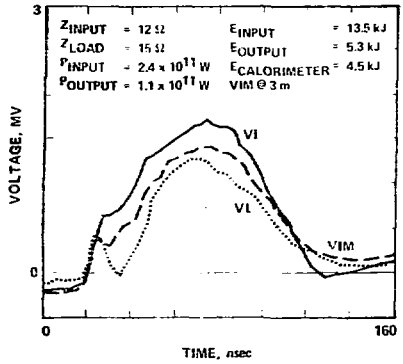

FIGURE 6 VOLTAGE WAVEFORMS.

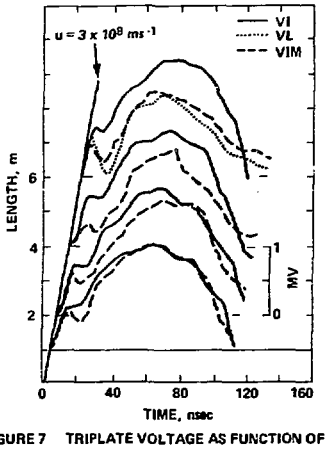

FIGURE 7 TRIPLATE VOLTAGE AS FUNCTION OF POSITION.

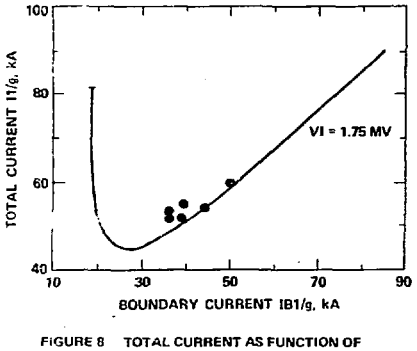

FIGURE 8 TOTAL CURRENT AS FUNCTION OF BOUNDARY CURRENT (VI = 1.75 MV).

REB FOCUSING AND TRANSPORT INVESTIGATIONS

A. A. Kolomensky, E. G. Krastelev, A. N. Lebedev,
V. S. Voronin, and B. N. Yablokov
P. N. Lebedev Physical Institute
Leninsky Prospect, 53, Moscow, USSR

ABSTRACT

Many important physical and technical problems are related to beam transportation in vacuum channels, energy transportation in vacuum transmission lines, and to possibilities of energy and power compression. All these problems require a common approach, e.g., control of high-current electron flows in a two-electrode geometry. We discuss here some related investigations carried out in the P. N. Lebedev Physical Institute.

The theory of beam transportation in a hydrodynamic and kinetic (two-flow) approximation can be found in ref. [1, 2]. To compare the theory and experiments, we use a hydrodynamic model of monoenergetic electrons with a longitudinal velocity $\beta_{||}$ constant across the beam. The theory provides the total current I_e as a function of the magnetic rigidity $r_e B_e$, outer electron energy γ_e and $\beta_{||}$, which usually are not measured directly in an experiment. The value γ_e differs from the fixed total electron energy γ_o by the voltage between the beam surface and the wall. This voltage is proportional to the total current: $\gamma_o = \gamma_e + 2I \cdot \ln(r_o/r_e)/\beta_{||}$. Moreover, the field B_e cannot be identified as an external guiding field B_o. For a pulse time typical for REB's, the skin-depth is much less than the thickness of walls, so it is the total flux $\pi r_o^2 B_o$ which is fixed. Indexes i, e and o signify values on the inner and outer boundaries of a hollow beam and on the conductive wall of an

external coaxial pipe. Using the assumptions mentioned above, one can express the values of $r_e B_e$ and γ_e in terms of measurable parameters $r_o B_o$, γ_o and r_i/r_o (or r_o/r_i). Then, there remains only one free parameter $\beta_{||}$ through which current can be optimized*.

For infinitely large magnetic fields, when the beam thickness tends to zero and there is no potential difference inside the beam, the current is optimized by $\gamma_{||} = \gamma_o^{1/3}$ and has the well-known form $I_{max} = .5(\gamma_o^{2/3}-1)^{3/2}/\ln(r_o/r_e)$. The thickness of the hollow beam increases when the magnetic field decreases. If the increase is due to a decrease in the inner radius (r_e + const), the optimized current becomes less. On the other hand, if the beam expansion is due to an increase in the outer radius and r_i = const, the optimized current increases due to the energy increase at the outer surface. This may explain the experimentally observed maximum of the curve $I(B_o)$. The current increase continues while the magnetic field approaches some value B_{th}, when the beam touches the pipe wall. It should be noted that in a real beam, electrons also move radially, so this contact means loss of internal electrons as well. One should expect that for a finite drift length, the magnetic field below B_{th} would lead to a current decay which is more rapid the longer the drift space. An increase of the magnetic field above B_{th} decreases the outer radius so the losses abruptly decrease. The calculated values of B_{th} and corresponding values of the maximal current are presented in Fig. 1 as a function of the total energy and the parameter r_i/r_o.

All experiments described below were carried out on the "Impulse" accelerator (electron energy up to 800 keV, current 30 kA, pulse half-width 50 ns) [4]. The rise time of the magnetic field was 1 μs and the decay time 17 μs. The inhomogeneity of the magnetic field inside the

* The similar procedure was used in ref. [3] for planar beams.

pipe was less than 1%. The beam was injected at a flat portion of the magnetic field pulse about 1 μs after its maximum. To generate the beam, two types of coaxial cathodes were used [5]--either a cylindrical cathode in a uniform field or a conical cathode placed in a fringed field.

Figure 2 shows the dependence of the current on the magnetic field strength at 7 and 15 cm from the edge of the cylindrical cathode for an electron energy of 400 keV. The theoretical curve is plotted for $\gamma_o = 1.8$ and for a constant inner diameter of the hollow beam which was supposed to be equal to the cathode diameter ($r_o/r_i = 1.4$). Experimental data in Fig. 3 are obtained at a distance of 20 cm from a conical cathode, where the magnetic field was about 80% of the transport region value. The inner diameter in this case was approximately 2.6 cm. The theoretical curves 1, 2 are calculated for $r_o/r_i = 1.65$, $\gamma_o = 1.8$ and 2.0.

The experimental data for $B_o > B_{th}$ seem to be in good agreement with the hydrodynamic model for a constant inner radius case. When the magnetic field decreases, the current reaches its maximum at $B \approx B_{th}$ and then drops. The total diode current still increases and, as damage pictures and bremsstrahlung patterns show, the beam touches the wall. The inner diameter is practically independent of the magnetic field and the diode voltage. For a cylindrical cathode in a uniform field, it is equal to the cathode diameter and for a conical one, to the diameter of the tangent force tube. The values of r_i and r_e measured at 15 cm from the cylindrical cathode are shown in Fig. 4 and are compared with outer diameter values theoretically predicted for the case $r_i = \text{const} = r_{cath}$.

A promising way to focus a beam and to concentrate the power transmitted into a diode is to use converging guiding electrodes operating at high electric strength, i.e., for significant electron emission from the cathode. A theoretical kinetic model of a steady-state magnetically

insulated electron flow between two coaxial cones was considered in [6]. The model takes into account emission and "landing" at the cathode and motion across equipotential surfaces, so it can be considered physically justified and a refinement of the corresponding "parapotential" model [7].

The magnetic self-insulation, i.e., the magnetic field at the cathode, is provided by a conductive cathode current which is to be considered as an external parameter of the problem. The electron trajectories were supposed to be geometrically similar.

One of the results is presented in Fig. 5 as a set of current-voltage dependencies for a fixed cathode current. The magnetic self-insulation is possible when the total current exceeds a certain value I_{min} depending on the applied voltage (this threshold of magnetic insulation is shown by the envelope 2 in Fig. 5). A maximal electron current is realized when the gap is filled up with electrons. The dependence of this maximal current on the voltage is presented by curve 1 which joins the ends of the characteristics. If the total current is between I_{min} and I_p, two steady states are possible which have different thicknesses of the electron layer and different cathode currents. For total currents exceeding I_p, the electron component of the current is relatively small and is suppressed by the magnetic field near the cathode.

It is convenient to characterize the geometry by the impedance Z_o of a corresponding vacuum line (or by aspect ratio $g = 60/Z_o$ for a diode). Measuring the total current in units of a matched current $I_m = V/Z_o$, one obtains for the parapotential model universal dependencies $I_p(V)$ and $I_{min}(V)$. For the kinetic model, the normalized threshold current coincides practically with the parapotential one within a wide range of impedances. The normalized maximal current appeared to be slightly dependent on Z_o, increasing for lower Z's and approaching the maximal current of a plane kinetic flow (see Fig. 6).

Three sub-regions in Fig. 6 separated by the curves I_p/I_m and I_{min}/I_m correspond to different regimes: a) magnetically insulated transmission line (above I_p/I_m) where the electron component of the current is small; b) super-pinched beam in a diode (between I_{min}/I_m and I_p/I_m) where the electron component is large; and c) overlapping of the gap (below I_{min}/I_m) which corresponds to a weak-focusing diode and to the Child-Langmuir law in the limiting case of very low currents.

It is possible to determine the self-insulating current in a relatively simple experiment with cylindrical coaxial diode. While the cathode is short the influence of the magnetic field is small and diode current equals the Child-Langmuir current, being proportional to the diode length. The longer the cathode, the greater the magnetic field, so the current rises more slowly than the Child-Langmuir curve and then saturates at a certain value. This value is the threshold of self-insulation because any deviation from it changes the length of the effectively emitting region.

Measurements of the self-insulating currents were carried out for coaxial diodes with Z_o= 100, 78, 60 and 37 Ohms in the voltage range 250-650 kV for anode diameters 27.7 and 54 mm. Figure 7 shows the dependence of a coaxial diode current on the cathode length. The measurements are compared with a theoretical curve for a space-charge limited magnetically insulated diode. Experimental investigations of the self-insulating current vs. the voltage show that the most points are located between the theoretical threshold of insulation and the maximal currents calculated for Brillouin flow and for a kinetic model. The average value of the self-insulating current is $I = (2.5 \pm 0.2)U/Z_o$, which is in reasonable agreement with both models, but essentially exceeds the result of the one-particle model [8].

A diode consisting of two coaxial cones with common apexes theoretically can deliver an arbitrarily high power density, assuming the magnetic insulation of the gap is provided by an additional conductive axial current. Practical limitations are due to the separation of cone apexes, which cannot be too small to delay shorting by plasma.

A scheme of the experiment is shown in Fig. 8. A coaxial cylindrical line with a "cold" impedance of 60 Ohms is joined to a conical diode of the same impedance. At the apex of the anode cone there is a hole of 2 mm dia. to control the position of the inner electrode and to eject the beam from the diode. The measurements were carried out in the voltage range 250-500 kV. Two types of diodes were used with different electrode diameters but with the same Z_o.

For small separations (1-2 mm), fast shorting of the diode occurred. When the separation was 3-4 mm, the operation time increased to 20-30 ns and then saturated. Typical traces of current, voltage and X-ray emission are shown in Fig. 9. At the beginning the diode operates for a while as a radial diode considered above. There is no current through the hole. An expansion of the cathode plasma (mainly in axial direction) leads to a decrease in the impedance of the top region of the diode. As a result, after a while the electron flow bursts through the hole and during the next 5-10 ns the external current reaches the total diode current value. After 10-20 ns the diode and the gap between the anode and the Faraday cup is filled with plasma. Some typical interferograms showing the process are presented in Fig. 10.

Pin-hole pictures show the existence of two zones of high-energy X-ray emission (see Fig. 11). The central spot of 2 mm dia. corresponds to emission from the target (i.e., from the FC collector) behind the anode hole. The halo is due to X-ray emission from those parts of the

anode where the current density was high immediately before the burst. Of course, these two components of the open shutter pin-hole picture are separated in time as well. The observed density of the external current was about 1 MA/cm^2. Thus, the results of the experiment prove the possibility of strong focusing in a high-Z cone diode (30 Ohms for "Impulse").

In a vacuum dielectric channel, propagation conditions can be provided by the beam itself [9]. The front part of the injected beam is scattered and the electrons charge the dielectric surface and break it. Plasma created by the breakdown is an efficient source of ions which are pulled out by the space charge field and compensate the beam electrically.

In experiments on REB propagation in a dielectric vacuum channel, two modes of injection were investigated [10]. When axial injection was used, the electrons accelerated in a planar diode were introduced axially into a drift tube through an anode grid. The cathode diameter was 25 mm, the accelerating gap 8 mm, and the anode transparency 50%. The inner surface of the 43-mm dia. drift pipe was covered with a dielectric (polyethylene, chlorvinyl) of 38-mm inner dia. For the second injection mode, a coaxial cylindrical diode was used and electrons were accelerated normally to the tube axis. The cathode diameter was 7.5 mm, the inner diameter of the dielectric insert 21 mm.

In both cases, the total current of the diode and the beam current at the end of the pipe were detected. The Faraday cup was separated from the pipe volume by aluminum foils or by 10 μ metallized mylar, so only fast primary electrons were detected. The beam geometry was determined by damage on polyethylene targets. The vacuum in the system was better than $5 \cdot 10^{-5}$ Torr. All measurements were carried out in the voltage range 350-480 kV, the diode current being 11-23 kA. In the uncovered metal

pipe, even at 5 cm distance, the beam current did not exceed 35% of that injected and at 10 cm it was negligible (curve 1 in Fig. 12). When dielectric was inserted, the transport efficiency increased significantly (curves 2 and 3).

When the beam passed through the dielectric channel, both the cross-section and current shape of the pulse changed. As compared with the injection value, the beam current at the end of the pipe was shorter and had a sharper front. Pulse rise-time variations along the pipe are shown in Fig. 12 (curve 3). At 10 cm the pulse front became shorter by a factor of two and subsequently did not change further. In the case of radial injection, the front variations were faster: at 8.5 cm from the cathode, the average rise-time was already 5 ns and the minimum observed rise time 3.9 ns., i.e., 1/6 that of the initial value (~30 ns). In this case, damage patterns indicated that the beam filled the pipe cross-section. At longer distances, the beam propagated along the chamber axis and there was a gap between the wall and the beam.

For axial injection, there were no noticeable inhomogenieties in the beam near the anode. The beam diameter here was approximately 28 mm. At 11.6 cm, the damage pattern had an outer diameter of 22-24 mm and a central spot of 10-14 mm dia. At 15 cm, the spot diameter decreased to 6-8 mm; at 20 cm from the anode, the main part of beam energy was located in the 5 mm dia. spot.

Assuming the plasma is generated by dielectric break-down, the time delay of its formation is the time of charge accumulation. The last is dependent on the rate of current rise and varies with time and with the distance along the pipe. Near the anode the low-energy electrons of the beam front move to the walls, so the delay of plasma formation here can be greater than in the next part of the pipe. Possibly due to that fact,

the main shortening of the current pulse (Fig. 13) occurs in the first 10 cm of pipe length.

To understand the mechanism of plasma formation (breakdown to the metal wall or along the dielectric surface), we have tried to transport the beam through a dielectric pipe, the outer metal tube being removed. In this case, too, the beam propagated and focused itself efficiently. Moreover, the beam propagated even when the pipe was curved, so straight propagation was impossible. These results suggest for surface breakdown, though other mechanisms are also possible.

Thus, when injected into a dielectric channel, the beam itself builds up the conditions for its propagation due to some loss of beam electrons. Main energy losses take place at the front of the beam pulse. The phenomenon can be used for shortening the current rise time. Apparently, the focusing mechanism is the same as in low-pressure gases. In the case of a dielectric channel, however, one may hope to improve the focusing of the beam due to the absence of current neutralization.

References

1. A. V. Agafonov, V. S. Voronin, A. N. Lebedev, and K. N. Pazin, JTP 44, 1909 (1974).
2. V. S. Voronin and A. N. Lebedev, JTP 43, 2591 (1973).
3. V. E. Nechaev and M. I. Fuks, II Symp. Col. Meth. Accel., Dubna, 1977, p. 240.
4. L. N. Kazansky, A. A. Kolomensky, G. O. Meskchi, and B. N. Yablokov, Atomnaya Energiya 42, 113 (1977).
5. V. S. Voronin, A. A. Kolomensky, E. G. Krastelev, A. N. Lebedev, V. A. Papadichev, and B. N. Yablokov, II Symp. Col. Meth. Accel., Dubna, 1977, p.222.

6. O. I. Vasilenko, V. S. Voronin, and A. N. Lebedev, II Symp. Col. Meth. Accel., Dubna, 1977, p. 216.
7. J. M. Creedon, J. Appl. Phys., 46, 2946 (1975).
8. A. A. Kolomensky, E. G. Krastelev, and B. N. Yablokov, Lett. in JTP 3, 603 (1977).
9. R. G. Little et al., IEEE Trans. Nucl. Sci., NS-21, No. 6, 249 (1974).
10. E. G. Krastelev and B. N. Yablokov, Lett. in JTP 3, No. 15 (1977).

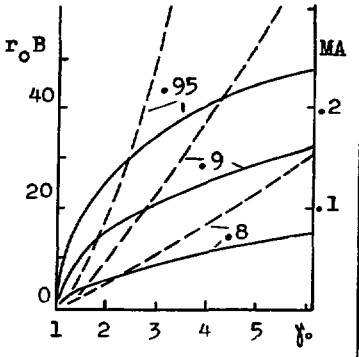

Fig.1. Calculated values of r_oB_{th} (solid, 1.7 kGs.cm units) and I_{max} (dashed) for different r_i/r_o.

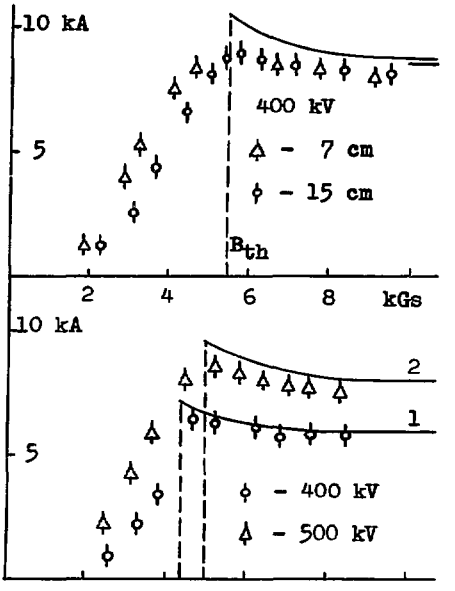

Fig.2,3. Beam current vs.magnetic field.

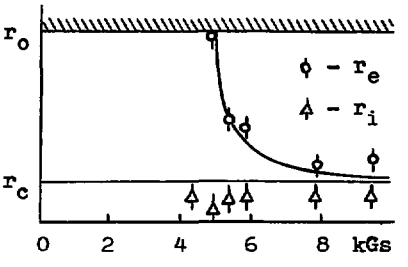

Fig.4. Calculated and measured beam radii.

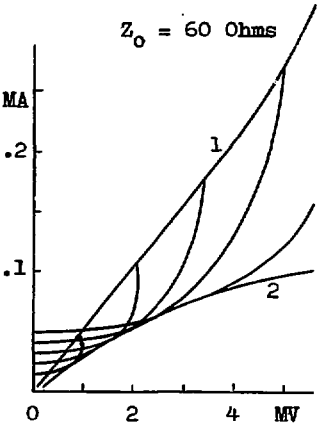

Fig.5. Current-voltage dependencies for kinetic-flow model in conical geometry.

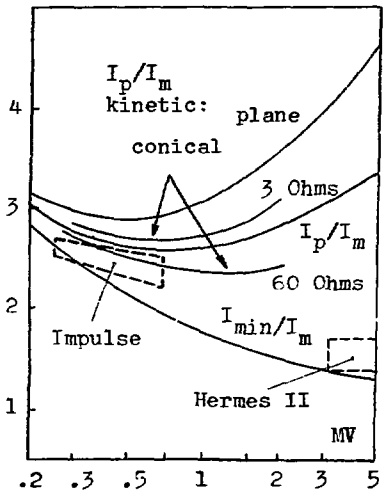

Fig.6.

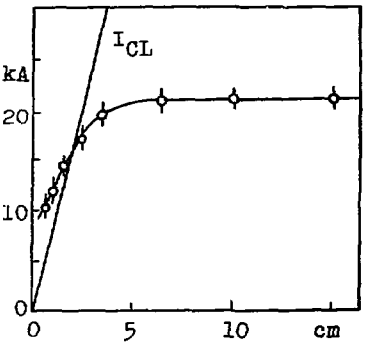

Fig.7. Coaxial diode current vs. cathode length.

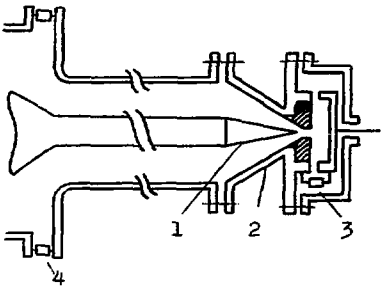

Fig.8. Conical diode layout.
1 - cathode,
2 - anode,
3,4 - current monitors.

Fig.9. Typical traces for conical diode.
1 - voltage (200 kV/div),
2 - current (25 kA/div),
3 - current through hole,
4 - X-ray emission.
Time scale 25 ns/div.

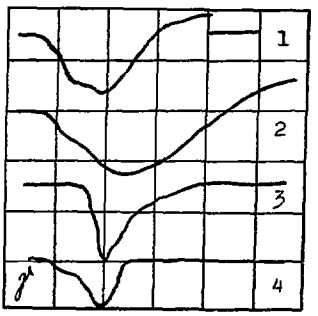

Fig.10. Interferogram of plasma between the anode hole and the Faraday cup.

Fig.11. Radial distribution of X-ray emission from conical diode.

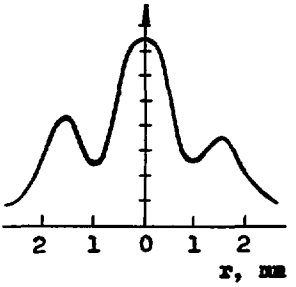

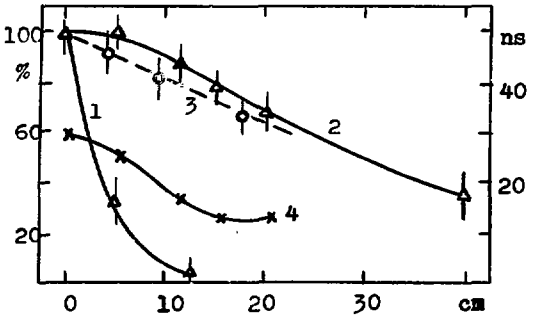

propagation efficiency:
1 - without dielectric
2 - current
3 - charge
4 - current rise-time

Fig.12. Beam propagation through vacuum channel with dielectric walls.

Fig.13. Shortening of current pulse after propagation through vacuum channel with dielectric walls. Upper trace - input current. bottom trace-output current.

SUPER POWER GENERATORS*

T. H. Martin, D. L. Johnson, and D. H. McDaniel
Sandia Laboratories, Albuquerque, New Mexico 87115

ABSTRACT

PROTO II[1], a super power generator, is presently undergoing testing at Sandia Laboratories. It has operated with an 80 ns, 50 ns, 35 ns, and 20 ns positive output pulse high voltage mode and achieved total current rates of rise of 4×10^{14} Amps/sec. The two sided disk accelerator concept using two diodes has achieved voltages of 1.5 MV and currents of 4.5 MA providing a power exceeding 6 TW in the electron beam and 8 TW in the transmission lines.

A new test bed named MITE (Magnetically Insulated Transmission Experiment) has been designed and is now being tested. The pulse forming lines are back to back short pulse Blumleins which use untriggered water switching. Output data showing a ten ns half width power pulse peaking above one terrawatt have been obtained. MITE is a module being investigated for use in the Electron Beam Fusion Accelerator and will be used to test the effects of short pulses propagating down vacuum transmission lines.

Introduction

The high power required for electron beam fusion[2] has resulted in a sequential development of double sided, disk

*This work was supported by the U.S. Energy Research and Development Administration, under Contract AT(29-1)-789.

shaped accelerators at Sandia Laboratories. The sequence is PROTO I[3] - now operational, PROTO II[1] - presently undergoing developmental testing, EBFA I[4] - now in design and EBFA II - being anticipated. MITE is a single module of EBFA I now being tested. PROTO II is the first short pulse (∿ 20 ns), high power (7-10 TW), fast rise (∿ 10 ns), low impedance (∿ 1/4 Ω) radial line accelerator to be developed. The design required several new pulsed power developments such as synchronized Marx generators,[5] triggered SF_6 switches, multiline energy compression, fast risetime synchronized switching,[6] radial line transformers, and ultra low inductance diodes. The accelerator has provided a wide range of half-power pulse durations ranging from 20 to 80 ns. The original accelerator objectives of this program in these areas have now been met within experimental accuracy.

PROTO II

Overall Design

Reference 1 has an in-depth description of PROTO II, a later paper[5] detailed the slower pulsed power data. A photograph of PROTO II is shown in Fig. 1. Eight Marx generators, tested to one megajoule, are located in a annulus formed between a central 7.9 m diameter tank and the outer 13.4 m diameter tank. The tanks are 2.8 m high. Low jitter 400 kV trigger units synchronize the eight Marx generators and tests indicate less than 20 ns jitter for the entire Marx and trigger system. After triggering, the Marx generators transfer their energy to 16 intermediate water dielectric storage capacitors which are then switched through the eight 1.2 m

diameter high voltage feedthrough located around the inner tank wall by SF_6 trigatrons. The triggered SF_6 switches provide time synchronization for the accelerator and transfer the energy into the first water line in about 300 ns. A series of rod switches (16 to 80) then discharge the first water line into the second water line which in turn self-breaks through a sharp edge switch in typically 150 to 200 channels and provides a short rise time pulse into the radially converging transmission lines. Circumferential interconnections between the first water lines average voltage and time differences between the water capacitors and SF_6 switches. The radially converging lines join to two back to back low inductance diodes which provide two oppositely directed 1 m diameter ring electron beams. The lines also provide a transformer with a .125 ohm input and a .25 ohm output for this series of tests. The output of the transformer section attaches to the back to back diode that has been described.[1] This diode was designed to have an inductance of 4.1 nH within the insulator envelope. The effective inductance, determined by short circuit shots in all pulse modes, was found to be within 10% of the design value. The short circuit shots provided a cross-check of the monitor calibration, calculated inductance, and effective output impedance of the accelerator. The electron beam was generated with a 1 m diameter razor blade cathode and a 24 segment prepulse switch, consisting of 1.27 cm by 1.27 cm cylinders and was installed at a 1.32 m diameter. This increased the effective diode inductance by 1.5 nH and reduced the

prepulse by a factor of 5 for the 50 ns pulse mode as shown by the traces in Fig. 2.

20 ns Mode Operation

Sixteen sharpened rods are used between the first water line and the second water line in this mode of operation. The small number of switching points provides inductive isolation between the two lines and exchanges the line energy in a lumped constant fashion. The energy transfers with a typical voltage of $V = V_o (1-\cos \omega t)/2$ waveshape with a zero to peak of 70 ns. When line two is charging, a voltage is applied across the second switch which is a sharp edge blade. A photograph of the channels obtained is shown as Fig. 3. Note the large number of channels per radial section that were obtained. As expected, the switch rise time is limited by the water switch resistive phase and the total switch jitter. Voltage monitors are located opposite line 1, line 2, and the entrance to the radial transmission line. The voltage on line 1 rises to 2.1 MV in 240 ns, then the rod switches break down and charge line 2 in about 40 ns and subsequently cause a prepulse voltage at the transmission line input. After line 2 switches the output peaks at 1 MV or 3.9 TW in 12 ns with an energy of 60 kJ per side. The pulse then passes thru the transmission line transformer sections where the impedance changes and the voltage is increased by 1.4 before impinging on the diode. Each diode has four $\dot{B}$ monitors and $\dot{V}$ monitors. These are integrated, averaged then compared to the opposite diode. The data provides power, energy, and the inductively corrected voltages

for the electron beam. The power and energy are shown in Fig. 4.

The generated pulses arrive at the diode in a slightly asymmetric manner. They average to provide the diode current and voltages. A typical combined current trace is shown in Fig. 5 for monitors 1 m from center and 90 degrees apart. The currents and voltages average out for a small diameter cathode but a large diameter cathode probably emits preferentially. If the arrival time differs by a spread of Δt, then the apparent rise time increase to the diode will be $\sim \Delta t/3$. Therefore, a spread of 15 ns will add 5 ns to the diode rise time. The spread originates primarily in the SF_6 switches and first set of water switches. An analysis of the switch data is shown in Fig. 6. The switching appears to operate as predicted. The larger spreads are caused when one or two gas switches fire early. The cause of these early firings is being investigated.

Varying Pulse Width Mode

Due to the three pulse forming networks and the large number of water switches, several different pulse lengths can be obtained from this type of accelerator. The simplest PFN is described[5] and consists of dumping the water capacitors into a load. Approximately 2 TW peak was generated by charging water line 1 and using 1, 3, or 5 rod switches to shape the pulse. In this mode, 80, 60, or 35 ns pulses can be obtained. The line 2 switch is shorted to the transmission line during these tests. A summary of the normalized accelerator outputs in this mode is shown in Fig. 7.

MITE-EBFA

The MITE pulser uses the same Marx as PROTO II[2,5] with solid dielectric intermediate storage capacitors to drive back to back water insulated Blumlein transmission lines. The solid dielectric capacitors are being investigated as an alternative to the water insulated intermediate energy storage capacitors. These new capacitors offer some distinct advantages over the water capacitors: no polarity effect as in water; compact packaging; no deionized water system is necessary. The primary problem is the uncertainty of capacitor lifetime. Currently, lifetime tests are being conducted at 2.5 MV during the MITE experiments.

The MITE water insulated pulse forming lines are shown in Fig. 8. The line 1 sections are pulse charged to $\sim$ 2.5 MV in $\sim$ 250 ns. The energy stored in line 1 is then transferred to line 2 through self-breakdown single channel water switches. The line 2 sections reach a peak voltage of 2.5 MV in 70 ns. At that time the knife edged Blumlein switches launch two pulses down the two 9 Ω water insulated transmission lines to the vacuum envelope. Monitors at positions 1, 2, and 3 as well as at the vacuum envelope are used to measure voltages and arrival times of the pulses. Measurements of pulse simultaneity show a mean difference of 3.8 ns.

The charging waveforms at position 1 and 2 are similar to those for PROTO II. The Blumlein output waveform at position 3 is shown in Fig. 9. The power waveform shown is for both sides of MITE and was determined from the Blumlein output and line impedance at that point.

The vacuum envelope presently being used is a shortened (22 cm insulator length) version of a REBA[7] diode. The measured inductance of 80 nH is double that of the intended envelope that is being fabricated. Connected to the vacuum envelope are the triplate magnetically insulated vacuum transmission lines. The 28 cm wide lines are spread 1 cm apart with the outer two lines held at ground potential and the centerline pulsed positively. A 1.2 m set of vacuum lines has been tested and a set 7 m long is on order. Experimental results of the lines will be presented in another paper.[8]

EBFA (Electron Beam Fusion Accelerator)

The EBFA design can choose from a wide variety of hardware. Short pulse flat lines like PROTO II and Blumleins like MITE have been demonstrated to operate. This provides a wide range of voltages and pulse lengths. The Marx generators and intermediate storage capacitors are operating well in PROTO II, although further investigation of the triggered SF_6 switches is needed. A variety of pulse durations has been demonstrated and can accommodate a wide variety of fusion experiments. The disk shaped accelerator is operating well and has several operational advantages over concentric coaxial line type of accelerators. Magnetic insulation is being investigated and will be used to alleviate the vacuum interface flashover problem. Combining the above, the EBFA design is shown in Fig. 10. The 30.5 m diameter tank will contain 36 modules. Each module will contain a PROTO II type Marx, intermediate storage capacitors, a Blumlein pulse forming network, transmission lines, a single diode and a

four meter long magnetically insulated transmission line leading to a common experimental chamber. The output voltage will be approximately 2.4 MV and currents of 12.5 MA are expected.

REFERENCES

1. T. H. Martin, J. P. VanDevender, D. L. Johnson, D. H. McDaniel, and M. Aker, Proc. of Int'l. Topical Conf. on E-Beam Res. and Tech., Albuquerque, NM, p. 450 (1975).
2. T. H. Martin, Proc. Int'l. Pulsed Power Conf., Lubbock, TX, ID1-1 (1976).
3. K. R. Prestwich, P. A. Miller, Proc. of Int'l. Topical Conf. on E-Beam Res. and Tech., Albuquerque, NM, p. 423 (1975).
4. T. H. Martin, K. R. Prestwich, Proc. Int'l. Conf. on Energy Storage, Compression and Switching, Torino, Italy (1974).
5. D. L. Johnson, Proc. Int'l. Pulsed Power Conf., Lubbock, TX IE2-1 (1976).
6. J. P. VanDevender, T. H. Martin, Proc. Nat'l. Particle Accelerator Conf., Washington, DC. (1975).
7. D. L. Johnson, Record of 11th Symp. on Electron, Ion, and Laser Beam Tech., Boulder, CO, p. 445 (1971).
8. D. H. McDaniel, J. W. Poukey, K. D. Bergeron, and J. P. VanDevender, Presentation at 2nd Int'l. Topical Conf. on E-Beam Res. and Tech., Ithaca, NY, (1977).

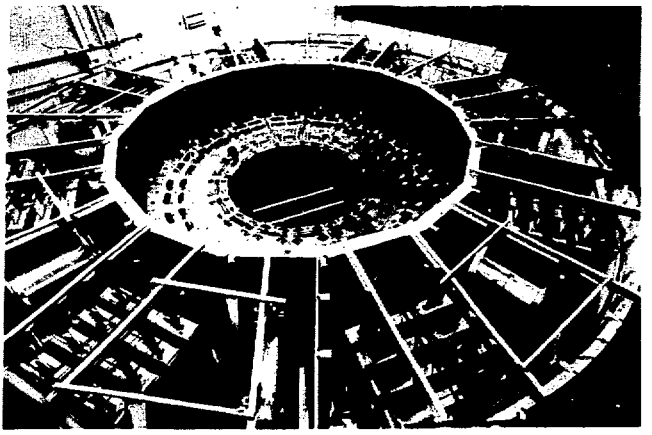

Fig. 1 - the PROTO II Accelerator

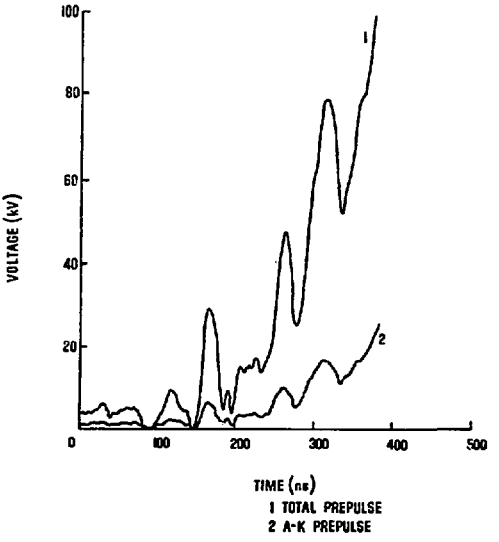

Fig. 2 - PROTO II Prepulse Voltages

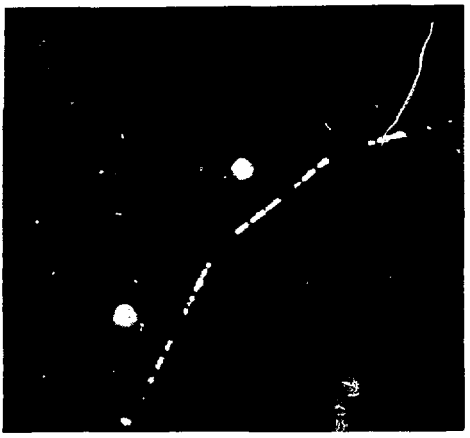

Fig. 3 - Photograph of PROTO II Switching Arc Channels

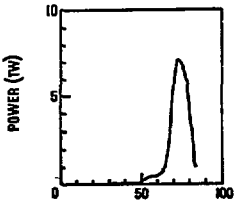

a

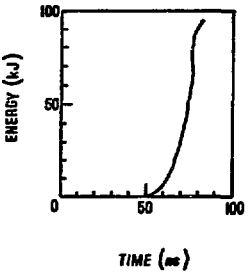

b

Fig. 4a - PROTO II Output Power

Fig. 4b - PROTO II Output Energy

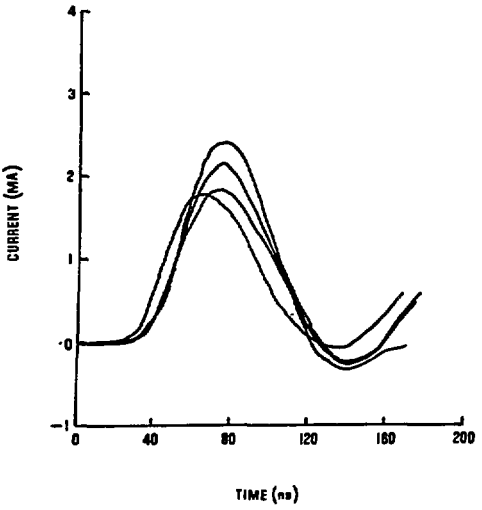

Fig. 5 - PROTO II Diode Currents

PROTO II - SWITCH DATA

	Spread ns	1σ Deviation ns	Predicted Deviation ns
SF_6 Trigatrons	25	6.8	5
Untriggered Rod Switch	10.5	3.2-6	2-6.4

Fig. 6 - Table of PROTO II Switch Results

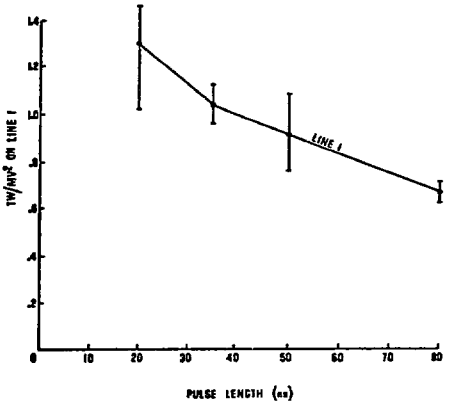

Fig. 7 - PROTO II Output vs. Power Pulse 1/2 Width

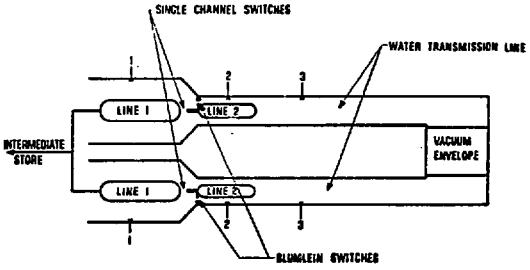

Fig. 8 - MITE Water Insulated Pulse Forming Lines

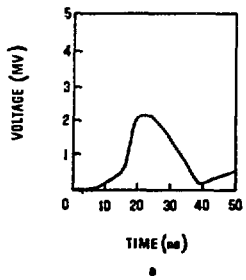

Fig. 9a - MITE Blumlein Output Voltage

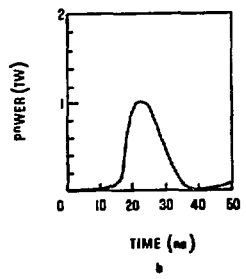

Fig. 9b - MITE Blumlein Output Power

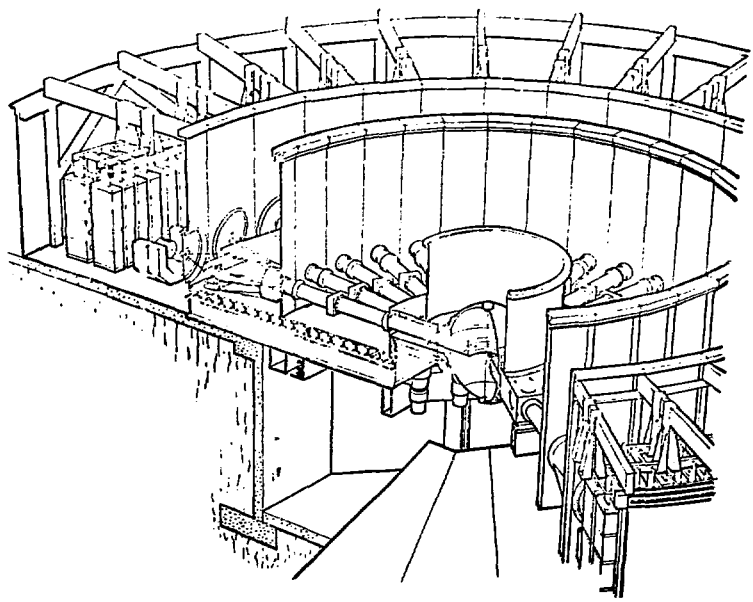

Fig. 10 - *Drawing of Electron Beam Fusion Accelerator (EBFA)*

POWER FLOW STUDIES OF MAGNETICALLY INSULATED LINES*

D. H. McDaniel, J. W. Poukey, K. D. Bergeron,
J. P. VanDevender, and D. L. Johnson

Sandia Laboratories, Albuquerque, New Mexico 87115

ABSTRACT

The designs for relativistic electron beam accelerators with power levels of 20 to 100 TW are greatly restricted by the inductance of a single diode of reasonable size. This fact leads to modular designs of very large accelerators. One concept uses several small insulators at a large radius arranged around the accelerator center. The total effective inductance is then low, but the energy must then be transported by self-magnetic insulated vacuum lines to the target volume. A triplate vacuum line configuration eases many mechanical support problems and allows more A-K gaps or feeds to be packaged around a given radius. This type of vacuum transmission line was chosen for initial experiments at Sandia.

The experiments have been conducted on the MITE (Magnetically Insulated Transmission Experiment) accelerator which is described elsewhere in the proceedings. The water pulse forming lines are connected to a vacuum triplate line through a conventional stacked insulator. Diagnostics on the experiment consisted of 1) input V, 2) input $\dot{I}$, 3) $\dot{I}$ monitors at the input, middle, and output of both the center conductor

*This work was supported by the U.S. Energy Research and Development Administration, under Contract AT(29-1)-789.

and ground plane of the transmission line, 4) magnetic energy analyzer to view peak electron energy in the A-K gap, 5) calorimetry, and 6) Faraday cups to look at electron current flowing across the transmission line. The main goal of this experiment is to obtain input impedance of the transmission line as a function of voltage and to measure electron loss currents. These measurements are compared to theoretical models for the input impedance and energy losses.

Introduction

The next generation of high current particle accelerators will place many 1 TW accelerators in parallel and use magnetically insulated vacuum transmission lines to transport the power from the individual accelerators to the particle accelerating electrodes. In the Electron Beam Fusion Accelerator (EBFA)[1] at Sandia, 36 of these lines are used and each is approximately 7 m long. Since the transit time through the line is approximately the pulse duration, the electron flow must be magnetically insulated by the self-limiting impedance of the line, which is a much more stringent criterion than that encountered in conventional load dominated lines.[2]

Both coaxial and triplate transmission lines have been considered for EBFA. With mean stresses of 2.4 MV/cm, power can be transported to within 1.1 m and .45 m of the pellet in EBFA for coax and triplate configurations, respectively. Consequently, the triplate configuration is being pursued because of its advantageous power flow capability.

The magnetic insulation program has been a cooperative

venture with Physics International Co. Experiments have been performed at Physics International on coaxial[3] and triplate[4] configurations. Additional experiments are now in progress on the coaxial configuration. At Sandia experimental work was undertaken on coaxial lines and semi-empirical theory was developed to explain the input impedance of magnetically insulated transmission lines.[2] Two numerical codes have been developed to study power flow in long self-magnetically insulated transmission lines[5,6] and have been useful in interpreting the experimental results. Recently experimental work has begun on the MITE accelerator[1] using a 1.5 m long triplate transmission line with a geometrical impedance of 8 ohms. The results of the numerical computations and the results of the MITE experiments will be discussed in this paper, and related to the design of EBFA.

Computational Results

Two time dependent numerical codes have been developed to study the properties of magnetic insulation.[5,6] Results will first be discussed for the two-dimensional, time dependent, fully self-consistent, particle-in-cell computer code. A voltage waveform is applied to the input of the simulated transmission line, and the time history of the pulse propagation and electron flow is computed. Figure 1 shows the voltage waveform for a 7 m long, 8 Ω vacuum coax. The input voltage waveform was a trapezoid with a 10 ns rise to a 2.4 MV level and then constant; this shape was chosen to approximate the MITE voltage pulse. The voltage pulse without the magnetic insulation effects is shown by the

dotted line in Fig. 1. The apparent input impedance Z = V/I of the coax for this case was 5.4 Ω, which is 67% the geometrical impedance. The pulse rise time has sharpened, and the front of the pulse has been eroded. The average velocity of the front is 2.2 x 10^8 m/sec. Peak power is transported with 100% efficiency. Since electrons are lost to the anode during the rise time of the pulse, the average energy of the electrons reaching the anode is typically .1% of the maximum potential across the transmission lines. Electrons in the cutoff region behind the front are confined in a sheath which is relatively close to the cathode; there is no leakage of electrons across the gap in the cutoff region. The current flowing in the negative inner conductor and the total current has been computed for input voltages between 1 and 10 MV and the results agree within 2% with that computed from the minimum current allowed in the parapotential[7] theory.

Another simulation was developed using the circuit analysis code SCEPTRE. The physics of electron emission and magnetic insulation are introduced via a conductance in an equivalent distributed network approximation of a lossy transmission line. The functional dependences of the conductance on the local voltage and current are semi-empirical fits to experimental data in short line experiments. The results of this code agree very well with the 2-D simulations and with experiments with coaxial lines.[5] The advantage of this code is that it is possible to study the effects of various load configurations and simulated loss currents

behind the pulse front.

Recent experiments on the triplate lines at Physics International[4] have shown losses resulting in a nearly linear voltage drop along the length of the triplate line. The code has been modified to include a small conductance behind the pulse front. Simple consideration of power balance for a line with a voltage loss yields an expression for the conductance per unit length of $g = \frac{2}{Zv}\frac{dv}{dz}$. For the PI results this suggests an equivalent loss current density of 12 A/cm^2 or 1.2% of the possible Child's law, space charge limited value for this geometry. The solid dots with error bars in Fig. 2 are the experimental values for the peak voltage as a function of length and the open squares are the code results using the 12 A/cm^2 loss current. Hence the azimuthal asymmetries inherent in triplate lines may cause a low level leakage current to flow in the self-magnetically insulated triplate line. Recent 4-chlorostyrene measurements of the emission pattern confirm that the losses are predominantly in the regions with reduced E and B fields.

Sandia Triplate Experiment

A single module of EBFA has been designed and is being fabricated. The module consists of a 7 m long, 8 Ω vacuum triplate line with a low inductance, 36 nH insulator. A 1.5 m long, 8 Ω triplate was adapted to the MITE pulse forming network using a modified REBA diode with an inductance of 85 nH. Figure 3 shows the triplate transmission line and some of its diagnostics. The centerline was constructed of two lines 25.4 cm wide, spaced 5.08 cm apart and

connected electrically. The outer lines were 30.5 cm wide and were spaced 1 cm from the inner set of lines. The lines were terminated in a field emission diode in which the anode is a carbon calorimeter and the cathode is 20 cm of 5 mil thick stainless steel. Input voltage and current are measured on each side of the diode. B-dots are mounted on the input, middle, and output of the inner and outer conductors of the transmission line. Experiments have been conducted with positive polarity on the center conductor. The monitors on the inner line measure total current and those on the outer line measure boundary current, which is total current minus the electron current. Since B-dot monitors suffer from the effects of non-uniform current flow and emission, reliable data were taken only after the uniformity of emission was improved by coating the lines with graphite. A magnetic energy analyzer is mounted within the anode and uses 4-chlorostyrene to record time integrated electron energy distribution at the load. The azimuthal symmetry of electron loss current is measured with 4-chloro placed around the circumference of the inner transmission line. A Faraday cup is installed in the middle of the centerline to measure loss current density to the side of the line. The cup measured losses of between 10 A/cm^2 and 2 A/cm^2 during the pulse rise time, and much less than 4 A/cm^2 during the rest of the pulse.

The initial shots were performed with bare Aluminum lines and damage was severe and spotty. A 4-chloro showed damage patterns that were tear-drop shaped (6 mm x 12 mm)

shaped with doses in excess of 2 x 10^6 rads. More uniform emission was obtained by coating the outer lines with Aerodag. The dose at the top and bottom of the lines was 30 to 50% larger than the dose on the sides. Voltage, L dI/dt, and corrected voltage waveforms are shown in Fig. 4 for a charge level of 2.4 MV on the Blumlein. The high inductance of the diode made it difficult to calculate the corrected voltage available at the input of the transmission line with the fast 15 ns fwhm pulse. These waveforms were taken when the transmission line was running at its self-limiting impedance, i.e., the A-K gap was not drawing sufficient current to insulate the transmission line. The input impedance for this case is 4 Ω at peak power.

In order to obtain data at higher voltages while we awaited delivery of the low inductance tube, the switching configuration in the MITE pulse forming network was changed from that in Reference 1. Figure 5 shows the configuration used to obtain the long pulse. The Blumlein switch on line 2 and the transfer switches between line 1 and line 2 were removed and a three-point Blumlein switch was installed on line 1. Typical output voltage, current, and corrected voltage waveforms and the output of the magnetic energy analyzer are shown in Fig. 6 for a charge voltage of 1.7 MV on the Blumlein. The L dI/dt correction to the voltage is now much lower, allowing a more reliable calculation of input voltage. The input impedance of the transmission line is 4 Ω, and is

the same self-limiting value as that obtained with the short pulse. The magnetic energy analyzer data and the A-K gap geometry indicate the gap impedance to be 7 Ω. Hence although the current transport was 100% to the end of the transmission line, only a third of the current was flowing to the anode from the cathode. The rest must be flowing directly to the anode in the last 2.54 cm between the last B-dot on the cathode and the load A-K gap. Figure 7a shows plots of the total current as a function of corrected voltage with curves for minimum parapotential current and saturated parapotential current. These curves are similar to those obtained in the P.I. experiments. Figure 7b shows plots of the boundary current vs. corrected voltage along with curves for the boundary current necessary for saturated parapotential and minimum parapotential electron flow. The boundary current and the total current are equal up to the arrow. The total current begins to rise at a faster rate and exceeds the value for minimum parapotential current near the end of the pulse. The voltage decreases as the current remains high at the end of the pulse which indicates that the magnetically insulated line is not a constant resistive load for an accelerator. The current transport was excellent for this case and the current loss density was between 10 and 50 A/cm^2 on the top and bottom of the line and < 2 A/cm^2 on the sides between plates.

A summary of the loss current density for various experiments is shown in Table 1. The values of the losses have been normalized to the space charge limited current

densities for the various configurations. The experiments above the dotted line were all for uniform coaxial geometry. The values of loss current are very low and the power transport was excellent for these experiments. The 2-D PIC simulations have indicated no loss current in uniform geometries and is consistent with experiments. Experiments involving non-uniform geometries are listed below the dotted line. The fraction of the anode area over which the loss current was observed is also indicated. The current was lost in the regions in which the ratio of the vacuum fields E_v/B_v at the anode was reduced well below the average E_v/B_v in the lines. Consequently, although the loss currents in a simple triplate line result in an unacceptably low transport efficiency for EBFA, a line designed for a nearly constant value of E/B should be much more efficient. An oval shaped or "closed triplate" cross-section line approximately satisfies this criterion and will be tested in the near future.

REFERENCES

1. T. H. Martin, D. L. Johnson, and D. H. McDaniel, Presentation at 2nd Int'l. Topical Conf. on High Power Electron and Ion Beam Res. and Tech., Ithaca, NY (1977).
2. S. Shope, J. W. Poukey, K. D. Bergeron, D. H. McDaniel, A. J. Toepfer, and J. P. VanDevender, Submitted to J. Appl. Phys.
3. I. D. Smith, P. D'A. Champney, and J. M. Creedon, Proc. of Int'l. Pulsed Power Conf., IIC-8 (1976).

4. M. S. DiCapua, P. D'A. Champeny, D. Pellinen, I. D. Smith, D. H. McDaniel, Presentation at 2nd Int'l. Topical Conf. on High Power and Electron and Ion Beam Res. and Tech., Ithaca, NY (1977).

5. K. D. Bergeron, J. Appl. Phys., 48, 7, p. 3065-9 (1977).

6. J. W. Poukey and K. D. Bergeron, Submitted to Appl. Phys. Lett.

7. J. M. Creedon, J. Appl. Phys, 48, 1070 (1977).

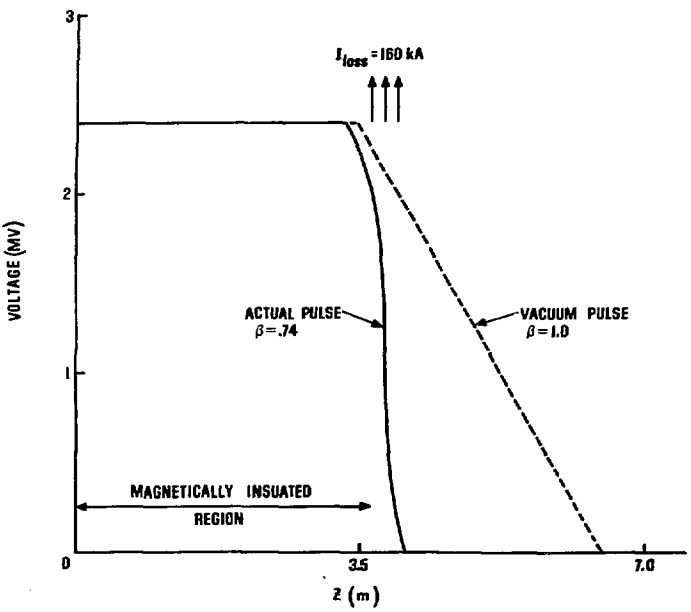

Fig. 1 - 2-D Time Dependent P.I.C. Simulation of Magnetic Insulation

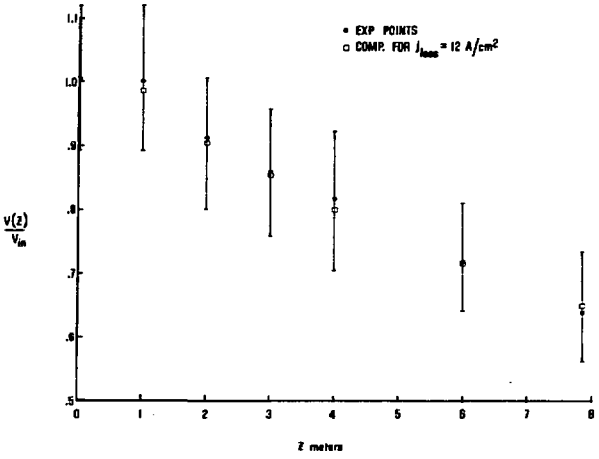

Fig. 2 - Voltage Loss as a Function of Length for a Simple Triplate

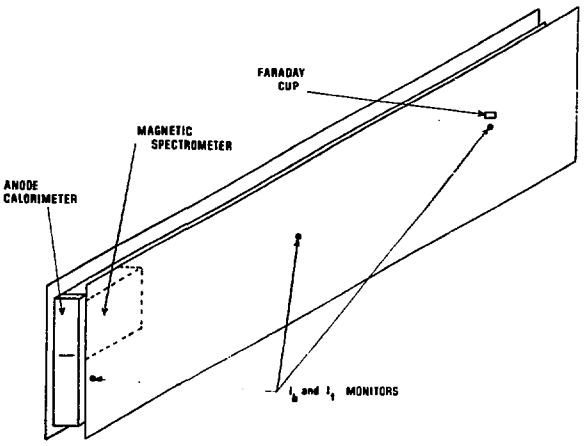

Fig. 3 - MITE Vacuum Transmission Lines and Diagnostics

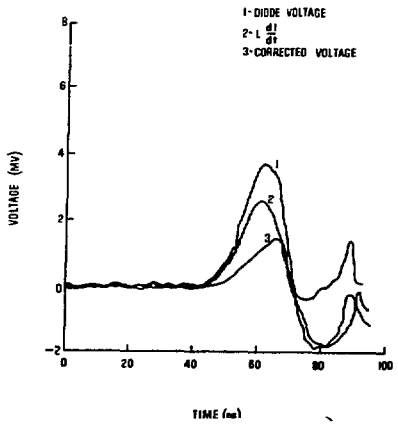

Fig. 4 - Voltage Waveforms for Short Pulse Operation

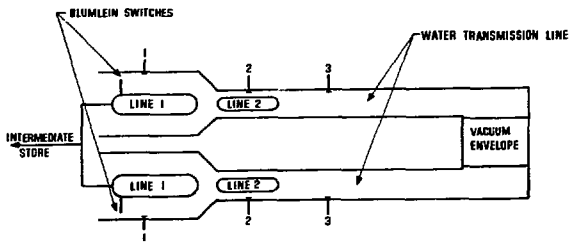

Fig. 5 - Pulse Forming Line Configuration for Long Pulse

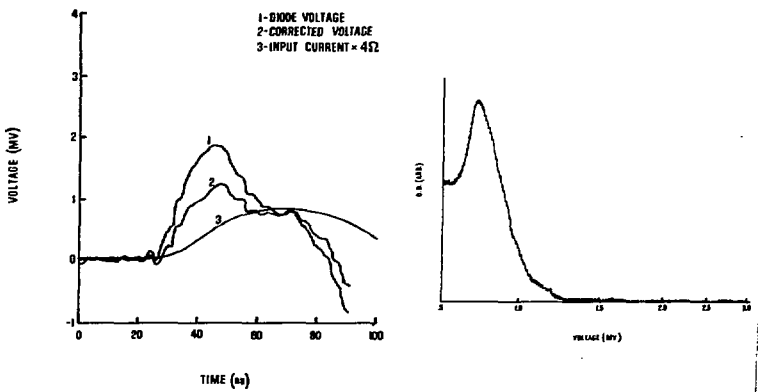

Fig. 6 - Typical Electrical and Magnetic Energy Analyzer Data for the Long Pulse

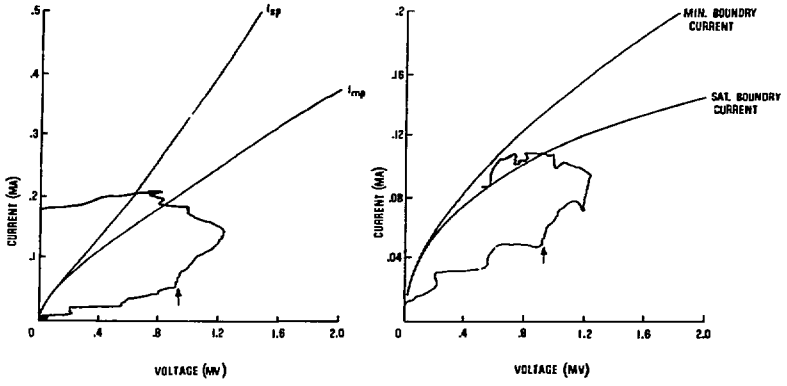

Fig. 7 - Total Current and Boundary Current V-I Plots for a Magnetically Insulated LIne

Table 1

LOSS CURRENT DENSITY SUMMARY

Experiment	Z Ohms	(J_L/J_{CL}) %	Aerodag Coating Negative Electrode
Hydra Coax	11	$\leq .2$	No
PI - Short	24 to 49	$\leq .2 \pm .1$	No
PI - Long	49	$\leq .03 \pm .02$	No
Curved Coax Hydra	11	3.0 (1/4 area)	No
PI Triplate	24	.5 (1/3 area)	Yes/No
MITE Triplate	8	5.0-10.0 (1/6 area)	Yes

PERFORMANCE CHARACTERISTICS OF LARGE AREA ELECTRON ACCELERATORS

S.V. Nablo, W.A. Frutiger, and A.S. Denholm
Energy Sciences Inc., Bedford, Massachusetts 01730

Abstract

The performance characteristics of "planar" electron accelerators using hot cathodes, and operating in the 150-500 kilovolt range will be reviewed. Self-shielded units utilizing barium dispenser cathodes capable of providing variable pulse width (10^{-3}-10^{-6} secs) at variable repetition frequency, with peak window current densities to 15 mA/cm^2 are discussed. Some of the problems peculiar to the diagnosis of these relatively low energy beams will be reviewed with attention to the limitations of available thin film dosimeters suitable for this energy regime. The use of these techniques for the determination of beam quality differences between beams generated by these systems and comparable cold-cathode units will be discussed.

In addition to the plasma physics applications of these energy sources, a number of processes of industrial interest involving cw initiation of chemical reactions have been commercialized over the past two years. The high energy efficiency offered by these all electric systems as compared with their thermal counterparts has generated increasing interest in these energy sources since the crisis of 1973. Self-shielded units up to 1.4 meters long and rated at 200 kV continuous operation at 20 kW will be described. Some of the problems peculiar to the introduction of this type of energy source into the non-laboratory environment will be treated, with discussion of federal and state regulations affecting their use.

1. Introduction

Over the past five years there has been a dramatic improvement in the technology of large area, high intensity electron guns. This has been motivated largely by the development of accelerators for pulsed radiation effects testing,[1,2] large volume gas lasers,[1,2] and for industrial radiation processing.[3] The independent variable characterizing these applications is the peak power of the electron generator or, alternately, the dose rate delivered to the target by the beam. An indication of the broad spectrum of current densities of interest for these applications is shown in Figure 1, in which current density, j_e, is plotted as a function of dose rate. For reasons of optimum energy absorption in the target, most of these units operate in the voltage range from 0.2 to 2.0 MeV. Since there is not a large variation in the electron stopping power of matter over this energy range, the plot of Figure 1 can be taken as characteristic of these machines.

At the upper end of the rate regime plotted in Figure 1, only the cold cathode will supply the very high current densities of interest, and typically only for a very short pulse duration (limited by gap closure). Several of the papers presented at this conference address the status of this technology and it is shown as the "pulsed" regime in Figure 1, occupied largely by radiation effects and fusion physics oriented equipment.

At the intermediate region of this plot, say at dose rates of 10^6-10^9 rads/second, dc machines operation at modest current densities are used, and the performance of compact, self-shielded units up to 250 kV has been described in the literature, both for large volume laser excitation applications,[4] as well as for commercial, large area radiation processing.[5] Since the chemical reactions, such as free radical initiated addition polymerization, of interest for these commercial uses, are dose rate dependent, and invariably show optimum reaction kinetics and yield at the lower dose rates, there is little commercial application of electron machinery operating at rates much above 10^9 rads/second.

One possible exception to this generalization is in applications where reaction kinetics do not impose a limitation, such as in sterilization or in the crosslinking of polymeric materials. In these cases, high rates are tolerable and in some instances, preferred. In order to set these power levels (dose rates) in perspective with the radioisotope sources occasionally used for these applications, the rate regime typical of high level Co^{60} sources is indicated in Figure 1.

This paper is directed to the performance of practical electron guns capable of providing large area beams in the current density range from 10^{-4} to 1 ampere/cm^2, in the region between that occupied by the large area tungsten based systems, and that of the cold cathode emitters.

2. System Cathode Selection Considerations

In the evolution of large area gun development, people have traditionally looked to the established technology of the vacuum tube industry, where tungsten dispenser cathodes have been developed to provide relatively high current densities with excellent reliability in sealed systems. However a severe objection to their use (or indeed that of any low work function emitter) is their intolerance to pressure excursions, an event which is virtually unavoidable where the thin windows used for low energy applications are involved or in the demountable systems demanded by R&D work. The cost of dispenser type cathodes for large area systems becomes prohibitive, particularly in those applications where window implosions are likely. This consideration has led to the widespread use of incandescent tungsten wire emitters in many of the large area dc accelerators of intermediate power levels; while the cold cathodes for high peak power pulsed operation are also particularly attractive in this respect.

A possible alternative to the use of tungsten emitters with their very high power requirements (particularly where high current densities are sought), is a radiantly heated LaB_6 cathode[6] which will readily provide several amperes/cm^2 at 1700° K. This would be compared to a 2600° K

temperature requirement for tungsten, or 2100° K for thoriated tungsten. This material is now available in relatively large area sintered sections. Its advantages for use in demountable systems have been recognized for some time, and it has been used successfully in this laboratory in the design of space-borne[7] and high peak power industrial accelerators[8] operating at current densities of several amperes per cm^2. These bulk cathodes of square cross-section indirectly heated with a tungsten rod were required to operate in a "gassy" environment of up to 10 microns at these high current densities. In addition to its good gas tolerance, LaB_6 has also shown good recovery properties from catastrophic venting of the system.

a. Typical cw Gun Performance

A schematic of the cylindrically symmetric gun design used in the generation of extended beams in the 100-300 kV range is shown in Figure 2. These units have been manufactured with beam lengths to 1.8 meters and beam widths of up to 10 cm, using a cylindrical diode and slotted anode with a tungsten emitter to provide uniform illumination of conductively cooled transmission windows. Due to the limitations of the window structure these guns are typically operated cw at current densities of under 0.2 mA/cm^2 in the energy range of 150-250 kV. Under these conditions lifetimes of 10,000 hours or better are achieved with 15 μ titanium.

A 1.4 meter unit typical of this geometry is shown in Figure 3. This unit, rated at 200 kV x 20 kW, is 30 cm in diameter and is shown in a self-shielded configuration. The accelerator is excited by an SF_6 insulated high voltage supply and is grid controlled for precise slaving of the current output to the requirements of the application. A plot of the longitudinal beam distribution mapped from one of these units is shown in Figure 4 and demonstrates an end-end uniformity of better than $\pm$ 5%.

b. Typical Pulsed Gun Performance

Where pulsed current densities in excess of the tens of milliamps per cm^2 level are required, low work function dispenser cathodes are generally used with a longitudinal Pierce diode, or as several diodes arrayed transversely along the length of the gun. The primary advantage here is the great decrease in heater power consumption and higher emission current density of the dispenser cathode operating at $< 1700^{\circ}$ K.

An example of a self-contained, self-shielded 200 kilovolt gun for use in either the pulsed or cw modes is shown in Figure 5. This accelerator delivers a uniform beam through a 5 x 15 cm window and the window flange visible in the photograph mates with the experimental target chamber used for cavity excitation studies. The gun is energized by a gas insulated high voltage supply and is coupled to the gun via a short gas insulated transmission line and a gas:vacuum bushing. This system incorporates an auxiliary energy store (100 joules) to support peak currents of 1-2 amperes for pulse durations of up to 100 μsec. Pulse width is variable from 10 μsec to 10 milliseconds, and the pulse repetition frequency of the modulator is variable from manual single shot to 1000 ppsec.

This system is therefore capable of providing cw electron beams at energies of up to 175 keV, at current densities of ≤ 0.1 mA/cm^2, as well as delivery well controlled pulsed beams of variable width at rep rate, of up to 20 mA/cm^2. Experience with these guns has shown that peak charge fluences in the window of 200 $\mu c/cm^2$ represent a practical upper limit for good lifetime.

Some of the performance envelopes determined for this system based on window loading at one extreme, and energy variation on the other, are shown in Figure 6.

3. Beam Diagnostics

The use of low energy accelerators presents unique problems in monitoring and diagnosis of the radiation fields of interest. The dosimeters

used in determination of beam energy deposition profiles should have a thickness very much less than the range of 100 keV electrons (e.g. 14 mg/cm^2 in hydrocarbons). Their thickness will determine the resolution with which depth-dose determinations can be made so that the uniformity in depth and over the area of target irradiation can be determined. Thin, solid phase dosimeters have been used for this purpose. Good surveys of available systems have been published,[9] although relatively few of those currently in use for gamma-ray or high energy electron dosimetry are of much interest for accelerators in the range under 500 keV.

In addition to the thickness consideration, a practical dosimeter for routine use with these machines must be economical to use, easy to read out, stable against humidity and ultraviolet, and should be rate insensitive. A system which meets most of these requirements is the polyamide film dosimeter[10] which contains a hexahydroxyethyl pararosaniline cyanide dye. Good linearity in optical density change with dose is exhibited to above 10 megarads, while film thicknesses down to 25 μ (ρ = 1.1 g/cc) are available. Care must be exercised in the UV sensitivity of this film and it is typically used under 7.5 μ (2 mg/cm^2) pin-hole free aluminum foil in this laboratory. With care in calibration, these dosimeters can provide data with an accuracy of better than $\pm$ 5%.

One of the main problems encountered in the use of this dosimeter has been the slow rate of development of the film. A typical rate of development curve is shown in Figure 7 with the ordinate showing the approach of the optical density of the exposed film to its fully developed level after irradiation at 10^7 rads/second. Such a curve provides a useful guideline for film readout, but the characteristic has been found to vary with exposure level, treatment rate and film composition. One should allow at least one hour for dosimeter development if measurements of $<10\%$ error are to be realized. For most applications, this is not a serious inconvenience.

We have found this film to be particularly useful for doing high resolution studies of radiation field distributions - for example where the variation in the delivered dose over a complex target is sought. The dye uniformity and grain are adequate to permit microdensitometry to better than 10 microns resolution, and its application with a two dimensional scanning microdensitometer provides a particularly powerful radiation field mapping tool for these low energy systems.

Some typical depth-dose profile data taken with 3.5 mg/cm^2 dosimeters at a plane 3.0 cm from a 15 μ titanium window are shown in Figure 8. At these lower electron energies these accelerators do not demonstrate the peaking of the distribution expected from idealized stopping-power considerations for orthogonal incidence. The $\sim 25^{\circ}$ half angle of scatter in the window, coupled with the additional scatter in the 3 mg/cm^2 of air, provide a flattened distribution which is desirable for most practical applications of this equipment. For the beam geometry of these cylindrically symmetric diodes, an enhancement above the front surface dose is just becoming detectable at 225 kV, or at an emergent beam energy of 200 keV.

4. Regulations Controlling the Use of Self-Shielded Equipment

One of the factors inhibiting the acceptance of these energy sources in industry is the concern of the layman for any equipment producing (ionizing) radiation. Not the least of these problems has been the plethora of regulations affecting its use which existed in the sixties. The enactment of the Occupational Safety and Health Act[11] by Congress in 1970 did much to establish practical guidelines for the use of self-shielded electron machinery in industry. These standards had already been established by the National Committee for Radiation Protection[12] and by the National Bureau of Standards,[13] however they were often difficult to interpret for the safety engineer who had little, if any, background with ionizing radiation. In addition, state "regulations" were often presented so that the problems of radioisotope control were hopelessly intermingled with the

relatively simpler aspects of accelerator safety. The OSHA regulations are now generally accepted as the domestic standard for radiation safety, and a continuing effort by HEW has been under way to systematize the regulations adopted by the state radiation control agencies. Most of the state regulations are in a state of revision, are at least a decade old, and were typically last revised when the NCRP lowered the maximum permissible dose levels in 1957.

Paragraph 1910.96 of the OSHA regulation defines an "unrestricted area" as one: "...access to which is not controlled...for purposes of protection...". On the other hand, a "radiation area" is one "...in which there exists radiation at such levels that a major portion of the body could receive in any hour a dose in excess of 5 millirem, or in any 5 consecutive days, a dose in excess of 100 millirem".

The machinery described in this paper is typical of that used in a self-shielded geometry for commercial use in an unrestricted area. In order to comply with existing OSHA regulations, as well as the regulations accepted by most foreign countries, these machines are designed so that at fully rated power, their surface dose levels are well under 1 millirad/hour. Considerably higher levels are acceptable where only hand access is involved; i.e. a multiple of 15 is typically used, but this is held to a much lower value, i.e. 5 millirads/hour, for industrial equipment.

References

(1) Proc. IEEE International Pulsed Power Conference, Lubbock, Texas, Nov. 9-11, 1976; IEEE, 345 East 47th Street, N.Y., N.Y. 10017.

(2) Mesyats, G.A., "Development and Application of the Sources of Intense Electron Beams", Acad. Phys. USSR, Inst. Atm. Optics, Tomsk; Physics Publications, Novosibirsk, 1976.

(3) "Radiation Processing", Trans. First International Mtg. Rad. Proc., Puerto Rich, May 9-13, 1976; ed: J. Silverman and A.R. Van Dyken, Rad. Phys. and Chem. 9, #1-6, 1977.

(4) Frutiger, W.A. et al, "Beam Optics Design of Pulsed, Large Area Electron Accelerators in the 150-300 kV Range", J. Vac. Sci. Tech. 10, 965, 1973.

(5) Nablo, S.V. and Tripp, E.P., "Low Energy Process Applications", Rad. Phys. Chem. 9, 325, 1977.

(6) Lafferty, J.M., "Boride Cathodes", J. Appl. Phys. 22, 299, 1951.

(7) Shepherd, O. et al, "Design and Flight Test of a 30 kW Rocket-Borne Electron Accelerator", AFCRL-TR-75-0379, July 15, 1975, Air Force Cambridge Research Laboratories, Hanscom AFB, Bedford, Ma. 01731.

(8) Simcox, G.K. and Schubert, C.J., "Transformer Type Accelerators - A Compact Source of Energetic Electrons," J. Vac. Sci. Tech. 10, 968, 1973.

(9) McLaughlin, W.L., "Solid Phase Chemical Dosimeters", Technical Developments and Prospects of Sterilization by Ionizing Radiation, 219, ed: E.R.L. Gaughran and A.J. Goudie, Multiscience Publications Ltd., Montreal, 1974.

(10) Humpherys, K.C. and Kantz, A.D., "Radiachromic: A Radiation Monitoring System", Rad. Phys. Chem. 9, 737, 1977.

(11) Occupational Safety and Health Standard, Federal Register 37, #202, Part II, 21158, October 1972.

(12) Basic Radiation Protection Criteria, Recommendations of the National Committee on Radiation Protection and Measurements, NCRP Report #39, Jan. 1971.

(13) Radiological Safety in the Design and Operation of Particle Accelerators, NBS Handbook 107, Sup. of Doc., USGPO, Washington, D.C 1970.

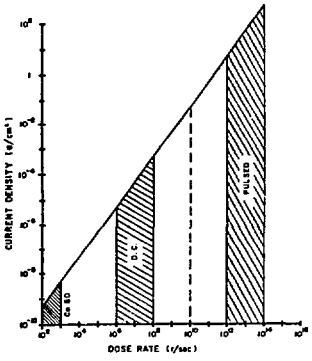

FIG. 1. DOSE RATE vs. ELECTRON CURRENT DENSITY (2 Mev)

0124

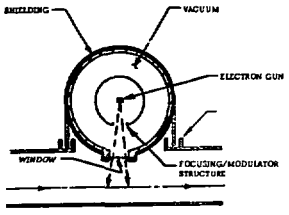

FIG. 2. ELECTROCURTAIN® ACCELERATOR SCHEMATIC

0226

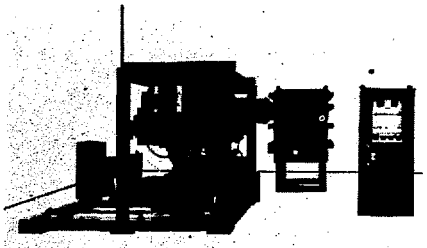

FIG. 3. 300 KV x 140 CM x 100 ma SELF-SHIELDED ELECTROCURTAIN®

0227

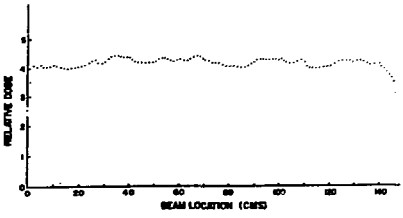

FIG. 4. LONGITUDINAL BEAM MAP (200 KV x 140 CM x 100 ma)

0228

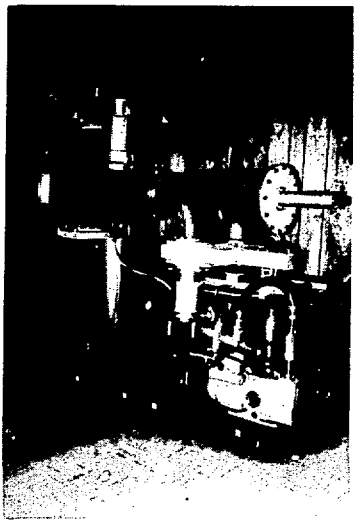

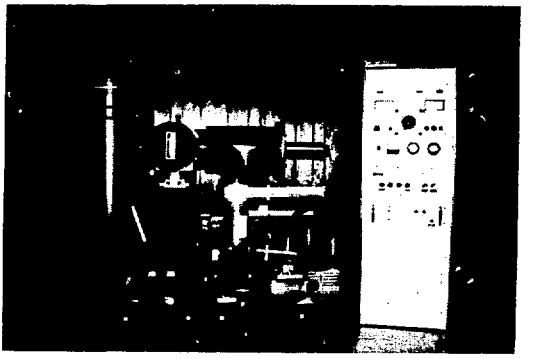

Figure 5 CB 150/15/10 Electrocurtain®
(with energy storage module).

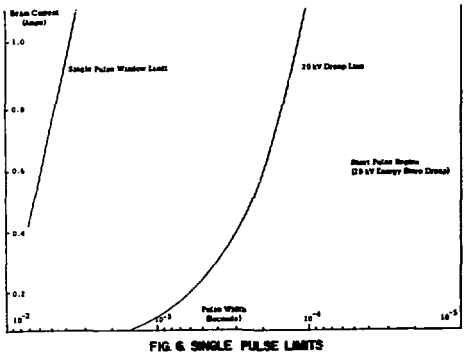

FIG. 6. SINGLE PULSE LIMITS

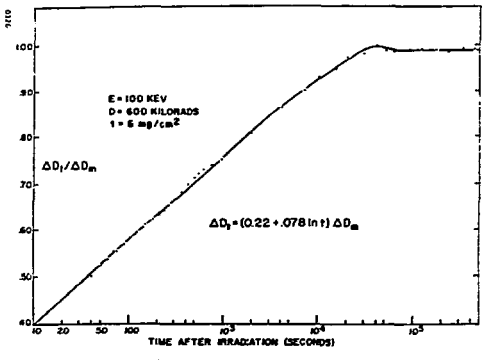

FIG. 7. TYPICAL RATE OF DEVELOPMENT OF FWT-60 FILM

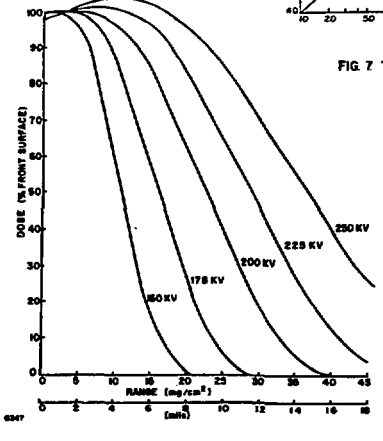

FIG. 8. EXPERIMENTAL DEPTH: DOSE PROFILES

Dup

DESIGN AND DEVELOPMENT OF A 350 kV, 100 pps ELECTRON BEAM ACCELERATOR*

G. J. Rohwein, M. T. Buttram, and K. R. Prestwich

Sandia Laboratories, Albuquerque, New Mexico 87115

ABSTRACT

A 350 kV, 300 J/pulse, 100 pulse/sec electron beam accelerator has been designed and constructed. A description of the physical features of the machine is included along with performance data from the initial operation of the system.

Introduction

Generation of electric power by inertial confinement fusion systems (ICF) will require high average power drivers. Both particle beam and gas laser drivers will require efficient, reliable, repetitive pulse power systems capable of sustained operation. Therefore system components must have extremely long lifetimes ($\sim 10^8$ shots). The components in most single shot electron beam accelerators have lifetimes of 10^5 shots or less. Developing highly efficient systems is important not only for minimizing operating costs but also to reduce energy deposition in the components that could cause heating and heat removal difficulties. Only a few repetitively operated electron beam accelerators have been developed.[1] In this paper the design and development of a

*This work was supported by the U.S. Energy Research and Development Administration, under Contract AT(29-1)-789.

30 kW average power electron beam accelerator that will be used for development of pulse power components that may be utilized in future high average power drivers for ICF systems is discussed.

General Description

An artist's sketch of the 350 kV, 30 kA, 30 ns, 100 pps accelerator is shown in Fig. 1. The system consists of a low voltage modulator section, a voltage step-up transformer, a pulse-forming line (PFL), a high-voltage switch and a load resistor or diode. Figure 2 is an electrical schematic of the system. The modulator converts DC power at 10 kV to primary pulsed power at 20 kV by resonant charging a 1.5 μF capacitor from a 14.5 μF capacitor. When the 1.5 μF capacitor is subsequently discharged through the primary of the voltage step-up transformer, the PFL is charged to 700 kV. Near the peak of the charge cycle, the output switch closes and energizes the load. At full voltage and 100 pps, the average power output of the system is 30 kW.

A dual resonance transformer was chosen for this repetitive pulser application because of the high-energy transfer efficiency.[2-5] In the present system, 94% of the energy stored in the 1.5 μF capacitor is transferred to the PFL. The 6% energy loss is dissipated in the 1.5 μF capacitor (∿ 1%), the switch (∿ 4%), and the transformer (∿ 1%).

The complete pulser system has undergone tests up to 100 pps at 15 kW average power and 30 pps at full voltage. A total of approximately 2×10^6 shots have been fired during the preliminary trials with individual runs of up to

1.5×10^5 shots. During these test runs, there have been no major component failures or heat build up problems.

Modulator

In the low voltage modulator section, the 14.5 μF first stage capacitor (C_1) resonantly charges a 1.5 μF second stage capacitor (C_2) through a diode stack, a 70 mH inductor and the first stage spark gap switch (S_1). With C_1 maintained at 11.5 kV, C_2 is charged to 21 kV for a 1.83 voltage ringing gain. The series diode stack, D_1, prevents reverse current flow between C_2 and C_1 before S_2 is fired. This allows S_1 to self extinguish when the charging current goes to zero and to be cleaned by continuous flowing air for approximately 2 ms before S_2 is fired. The charging voltage waveform at C_2 is shown in Fig. 3.

During the dual resonance discharge cycle, a 54% voltage reversal occurs across C_2. The output electrode of S_1 is clamped to ground with a diode stack, D_2, during this reversal. Without the shunt diodes, S_1 would be required to stand off twice the normal voltage or approximately 22 kV. With D_2 in the circuit, S_1 can be operated nearer to self-break ($\sim$ 70%) which assures more reliable triggering.

The switches S_1 and S_2 are shown in Figs. 4 and 5. Switch S_1 is a trigatron spark gap operated at 11 kV and 60 A. It has a tubular recessed trigger electrode insulated from the main electrode with a high strength alumina ceramic tube. By recessing the trigger electrode approximately 2 mm, it was found that erosion of the trigger electrode was virtually eliminated. The light walled trigger electrode is shielded

from the high current arc and consequently experiences very little erosion. With copper main electrodes the tip of the ceramic tube will remain intact for approximately 10^6 shots before it is necessary to renew the end by light sanding to remove resolidified metallic electrode debris.

The switch housing is purged at a rate of approximately 10 SCFM with a continuous air stream which is introduced at the periphery of the acrylic housing cavity and forms a vortex flow pattern through the switch.[6] Residual ionized gas and electrode debris are expelled from the switch through the center of both electrodes.

Switch S_2 is a 15 cm long rail gap with a tubular trigger electrode operating at 21 kV and 32 kA. It has a polycarbonate housing and a brass cover through which the hot gas and debris are expelled. Cooling air is delivered to both the main electrodes through parallel tubes and to the trigger electrode from both ends. The gap is continuously swept by air flow as indicated in Fig. 5. The jetting action from the trigger electrode air draws the air from below the main electrode uniformly up through both sides of the gap. The normal flow at full power is 30 SCFM and the operating pressure is 15 psig. The gap spacing is 4.8 mm on the high-voltage side and 3 mm on the output side which results in a mean electric field of 26 kV/cm and 35 kV/cm, respectively.

Gap S_2 is triggered with a 50 Ω coaxial discharge cable. With the cable coupled to the S_2 trigger electrode through a 2 nF capacitor and a peaking gap, the measured pulse rise time on the S_2 trigger electrode is 3 ns. This arrangement fires

switch S_2 with an average of two to three current channels. The modulator was developed and operated extensively at full power while investigating switch S_2 prior to the assembly of the complete accelerator.

Transformer and Pulse Forming Line

The charging transformer (Fig. 6) is an air core spiral strip design with a 60 cm diameter single turn primary surrounding a 44 turn copper-mylar secondary winding. The width of both windings is 10 cm. Electric field shaping rings are located on both the core and case across both margins of the transformer to minimize the field enhancement of the edges of the spiral strip. At full voltage the winding stress is 120 kV/cm which should provide a life of greater than 10^9 shots. The external case, flanges and core are fiberglass reinforced epoxy composition with an epoxy filling between the field shaping rings. The windings and the open volume inside the transformer are impregnated with an oxidation-inhibited, water-white, mineral oil to exclude the air and provide insulation around the windings and terminals. The ends of the transformer case are covered with 2.5 cm thick acrylic plates to confine the oil and support the ends of the core.

The transformer has a 1 μH primary inductance, a 1280 μH secondary inductance, and a 30 μH mutual inductance which results in a coupling coefficient of 0.84. Since the PFL is charged in the dual resonance mode, external inductances of 0.420 μH and 488 μH were added to the primary and secondary sections of the circuit, respectively, to match the frequencies and reduce the effective coupling coefficient to 0.6.

If the primary and secondary frequencies are equal, i.e., $L_1C_1 = L_2C_2$, and the effective coupling coefficient of the transformer is 0.6, the maximum charge transfer occurs at the peak of the second or reverse voltage excursion of the secondary capacitor, C_2. With perfect tuning in a lossless system, 100 percent of the energy is transferred from C_1 to C_2 in this dual resonance mode.[2-5] Figure 7 is a trace of the charging voltage on the PFL for this system. The measured transfer efficiency is 94 percent. A 21 kV charge on C_2 is required to reach 700 kV on the PFL.

The PFL is a 10 Ω oil-insulated, coaxial transmission line with inner and outer diameters of 46 and 61 cm, respectively. Its electrical length is 15 ns. It is connected to the transformer through a 60 cm long, 488 μH tuning inductor. The inductor is a helix of 12 gage insulated wire wrapped on a 30 cm acrylic tube.

High Voltage Switch

The switch between the PFL and the load is the 700 kV self-breaking, air-dielectric, spark gap shown in Fig. 8. (Air was chosen for reasons of economy.) When operating into a matched load, it conducts a peak current of 35 kA for 30 ns with a 10 ms recovery period between pulses. In 8 hours of running (about 3×10^6 shots), it must pass 3000 coulombs without degradation in performance. Optimal power flow is achieved with the switch operating as close as possible to the peak of the PFL charging waveform. However ringovers, that is pulses on which the statistical fluctuation in breakdown voltage cause the switch not to close, must be minimized to avoid excessive heat dissipation in the transformer and

second stage capacitor. The spread in breakdown voltage determines the fraction of PFL full voltage at which the switch must operate.

The switch operates at pressures up to 10 Atm with a gap length of 3 to 6 cm. Its cylindrical acrylic housing (2) has a 20 cm inner diameter and is 19 cm long. Dried and filtered air is injected from the output (larger) electrode (4) through 8 ports (5) with a rotary flow pattern which sweeps and cleans the housing.[6] Exhaust gas exits through the center of the same electrode passing through a copper cooling coil (8) located within the high voltage structure before entering nylon lines through the high field region. Both the input and output gas lines are connected to the output side of the switch to minimize the voltage standoff required. Because of a slight field enhancement, breakdown occurs over a 30 cm^2 band at the outer edge of the small electrode (1) during normal operation. Dispersion of the spark over large areas of the tungsten-copper electrode tips has reduced the electrode erosion for 2×10^6 shots to a negligible level.

The switch was operated for 2×10^5 shots at 1 to 5 pps and 1 kA peak on repetitive impulse tester with a dual resonance waveform prior to the 2×10^6 shots in the present accelerator. Data from these experiments confirmed that the electric field vs pressure curve for air is not sensitive to the first half cycle of the dual resonance waveform. The voltage breakdown distribution is observed to have a standard deviation equal to 3-5% of its mean. With ultraviolet illumination this deviation has been reduced below 1%. An arc from a needle positioned 1 cm from the smaller electrode and

resistively coupled through 25 kΩ to the larger electrode generated the UV. Figure 9 shows 30 consecutive traces (spaced manually along the time axis to display voltage stability). The total voltage pulse lasts 1.65 μsec, the positive swing 0.45 μsec. Illumination occurs shortly after the zero crossing and breakdown occurs repeatably at 450 kV, the peak of the waveform. Figure 10 displays 19 equivalent shots vertically spaced to display time jitter. The standard deviation of the breakdown time distribution is 15 ns.

Experiments conducted at repetition rates above 5 pps have used a switch without UV illumination. A 500 kV peak PFL voltage and an overmatched 30 Ω load, the current peak is 14 kA. Voltage breakdown stability was found to increase up to 30 pps for a gas flow rate of 12 SCFM. Beyond that rate stability rapidly degenerated. We assume that at low repetition rates remnant ionization from previous shots performs the function of UV preionization in stabilizing the breakdown at the expense of a constant (pulse-to-pulse) degradation in the dielectric strength of the air. At higher repetition frequencies we assume that the pulse-to-pulse delay is entering a more sharply rising portion of the dielectric strength recovery vs time curve with a consequent decrease in stability. By increasing the gas flow rate at constant pressure to 19 SCFM relatively stable breakdown has been achieved at 70 pps (Fig. 11) and operation at 100 pps is possible. Gas flow at a given pressure is currently limited by compressor capability and by the necessity to use parallel lines to S_2 and the output switch. Reconfiguration to use the cleaned and cooled

gas from the output switch in S_2 plus reduction of pressure drops in the gas feeds should allow us to reach 33 SCFM at which flow we presently believe stable 100 pps operation will be possible.

A superposition of the output for 20 shots into a 30 Ω water load at 25 pps is shown in Fig. 12. The pulse amplitude is 350 kV, the width (FWHM) is 40 ns. Pulse-to-pulse voltage jitter (full width) is not greater than 7%.

ACKNOWLEDGMENT

The authors wish to thank John Corley and Martin O'Malley for their assistance in constructing the equipment and conducting the modulator and full system experiments.

REFERENCES

1. G. J. Rohwein and M. T. Buttram, SAND 77-0174 (1977).
2. T. H. Martin, SC-RR-71 0341 (1971).
3. E. A. Abramyan, IEEE Trans. Nucl. Sci. NS 18 (1971).
4. D. Finkelstein, P. Goldberg, and J. Shuchatuwitz, Rev. Sci. Instr., 37, No. 2 (1966).
5. C. R. J. Hoffman, Rev. Sci, Instr., 46, No. 1 (1975).
6. C. Edwards, M. D. Hutchinson, J. C. Martin, and T. H. Storr, AWRE Report SSWA/JCM/755/99, unpublished (1975).

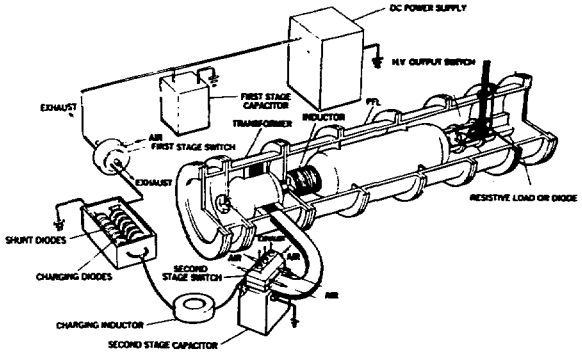

Fig. 1 - 100 pps, 350 kV Electron Beam Accelerator

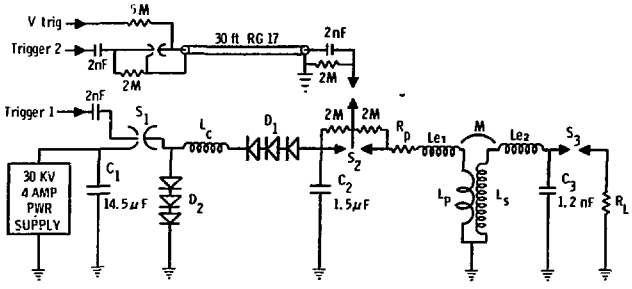

Fig. 2 - Schematic of 100 pps Accelerator

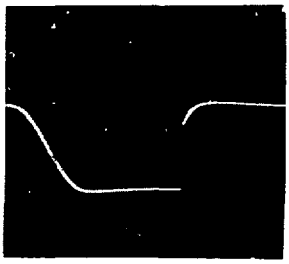

V = 11 kV/div
T = 1 ms/div

Fig. 3 - Charging Waveform on Second Stage Capacitor

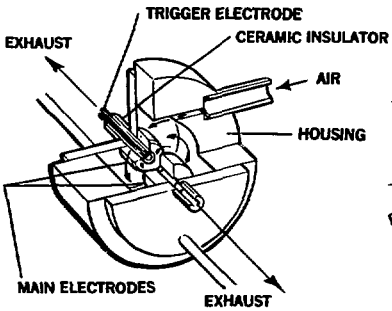

Fig. 4 - First Stage Switch

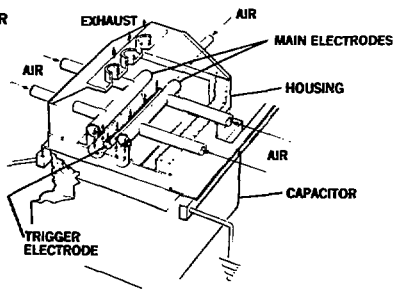

Fig. 5 - Second Stage Switch

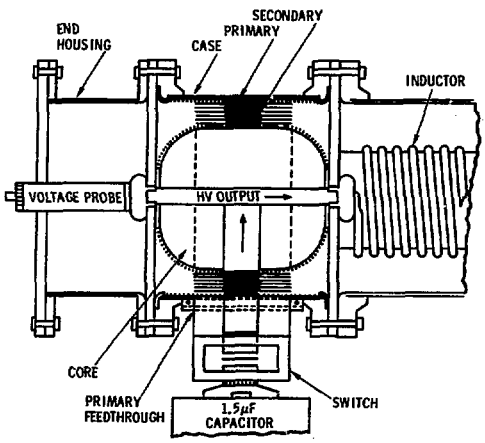

Fig. 6 - High Voltage Transformer

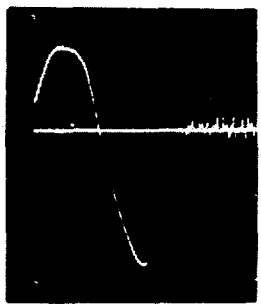

Fig. 7 - Charging Voltage Waveform on the PFL
V = 300 kV/div
T = 2 μs/div

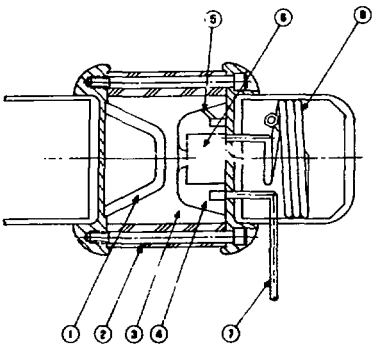

Fig. 8 - High Voltage Switch

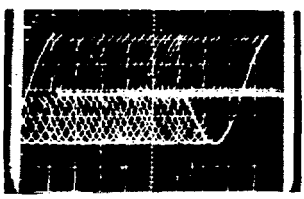

Fig. 9 - Sequence of High Voltage Switch Tests Showing Voltage Jitter
V = 190 kV/div
T = .5 μs/div

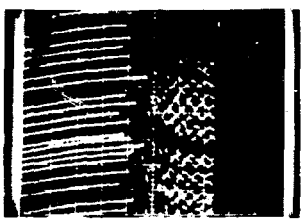

Fig. 10 - Sequence of High Voltage Switch Tests Showing Time Jitter
T = 50 ns/div

Fig. 11 - H.V. Switch Breakdown at 70 pps, V = 160 kV/div
T = 2 ms/div

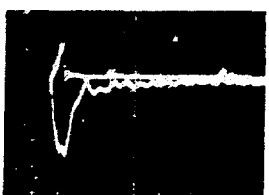

Fig. 12 - PFL Output Voltage, 20 shots Superimposed
V = 120 kV/div
T = 50 ns/div

INDUCTIVE STORAGE FOR HIGH POWER REB ACCELERATORS

Ihor M. Vitkovitsky, D. Conte, R.D. Ford and W.H. Lupton

Naval Research Laboratory, Washington, D.C. 20375

Abstract

Investigation of inductive storage technology for powering 10^{11} to 10^{12} W relativistic electron beam accelerators is presented. Circuits for effective power amplification using inertial energy storage units as current sources for generating high voltage have been analyzed. The analysis, based on using economical, high current, opening switch modules with command triggering capability, indicates that good efficiencies can be obtained. Experimental results supporting the analytical projection are summarized. The experimental results include generation of 300 kV inductive voltage at the output of 85 kJ magnetic storage coil and demonstration of inductive charging of an 8 Ohm water-dielectric pulse line to 500 kV.

I. INTRODUCTION

Applications of electron and ion beams in such areas as fusion, laser excitation and microwave production has stimulated consideration of inductive storage for powering appropriate beam sources. Increasing energy and power required by these applications make the use of inherently more compact and economical inductive storage an attractive pulsed power source for production of intense beams. Several laboratories have initiated studies related to replacing the existing methods of energy storage for particle beam sources as well as for future needs by using inductive storage. Small accelerators for production of electron beams of 50-100 nsec duration have been developed. For example, beam energy of several

kilojoules was formed in experiments by Mesyats et. al. [1], using the output of the current interrupting switch directly across the diode. D. Conte has shown that 2 kJ beams can be formed using conventional pulse forming water lines. The preliminary experiments are reported in Ref. [2]. In these experiments, the water pulse line was charged by interrupting rapidly the inductor current. Long pulse (1 μsec) electron beams were generated in experiments, by Glukhikh et. al. [3].

The major problem associated with practical use of inductive concepts in production of intense charge particle beams, requiring power output in 10^{10} to 10^{12} W range is the interruption of current. Such high power requirements suggest that switches must have fast opening times (in 0.1 to 1.0 μsec range) and be able to withstand voltages exceeding 1 MV. A number of analytical studies seeking to alleviate these constraints has appeared, including use of transformers [4] for decoupling of high voltage from switching elements, series switches [5] and use of commutating stages [6]. Experimental studies on switching techniques at the Naval Research Laboratory suggests that such switches are ready for use in inductively driven REB accelerators. Versions of high current (100 kA) explosive switch described in Ref. [7] were shown to be capable of supporting electric stresses up to 45 kV/cm when used in conjunction with an exploding wire (or foil) fuse. Other tests have shown that these switches withstand inductive voltage up to 300 kV. Fuse opening times as short as 0.25 μsec have been achieved.

The development of current sources with an output in a range from hundreds of kiloamperes to several megamperes and from hundreds of kilojoules to several megajoules, [8], [9], including designs specifically tailored to high current electron accelerators [10], is providing very compact primary energy storage when compared with capacitive systems.

Availability of these current sources which can now be effectively switched to provide necessary compression of energy (i.e., power amplification) makes it feasible to increase the accelerator output from 10 kJ range [1], [2] by at least one or two orders of magnitude.

II. GENERATION OF HIGH POWER OUTPUT

There are two major approaches for generating high power pulses suitable for production of intense particle beams. Figures 1 and 2 show schematically each of the circuits and their characteristics. Each has a distinct advantage that can be exploited to a degree dependent on the application and on the required output level.

The circuit in Fig. 1 demonstrates schematically the use of magnetic energy stored in the inductor, L_o, to charge a pulse line of capacity C. The energy transfer is accomplished by interrupting the current I_o by an opening switch represented as a variable resistor with resistance, R_o, at the time of vaporization, t_o. Auxiliary switch, S_1, can be used during the voltage build-up across the inductor to reduce the time for charging the pulse line capacity, C. This circuit was investigated experimentally with 2 kJ stored in the pulse line [27].

Analysis of the performance of inductive charging of pulse lines is summarized in Fig. 1 Normalized voltage $(V/I_o)\sqrt{C/L_o}$ is computed for fuses exploded in water using the experimental results summarized in [2]. The maximum voltage developed across the pulse line is determined by R_o and t_o. The pulse line voltage, depending on the choice of L_o and C can not exceed the product of the electric field, E, (at which value restrikes occur in the fuse) and the fuse length ℓ. This field is represented in Fig. 1 by a dashed line, $E\sqrt{t_o} = 2600\ V/ms^{1/2}$, conservatively taken in accordance with the results of reference [6]. More recent work [11] shows

that for t_o = 4 μsec the constant can be as high as 4000 V/ms$^{1/2}$. An additional limit on the choice of circuit parameters and power output arises in those cases where the pulse line charging time, t_{ch}, is constrained as in using of water dielectrics with time dependent breakdown strength [12]. Because the inductor current must increase as t_{ch} decreases, to obtain given pulse line voltage, this condition establishes the source and switch current ratings as factors which limit the accelerator output energy. Figure 1, in addition, provides the system efficiency $\eta = CV^2/L_oI_o^2$, obtained by squaring the normalized voltage.

Because the current output from compact and economical current sources, such as inertial storage systems, peaks typically in 0.1 to 1.0 sec, the opening switch in Fig. 1 must consist of more than one element. First of these elements can be a command-triggered exploding switch [7]. It has opening time of 20 μsec and must be commutated by fuses to operate at high voltage. The additional function of the fuse stage is to steepen the opening time to about 1 μsec. Since, further, the jitter in the triggering of the exploding switches is less than 1 μsec, it makes such switches suitable for synchronized charging of multiple pulse line accelerator such as that proposed in Ref. [13]. Table 1 lists circuit parameters of an inductive charging of 100 and 1000 kJ pulse lines to 1 MV, using the combination of these exploding switches with appropriate fuse commutation. Several parameter choices are provided to demonstrate their effects on the pulse line performance.

TABLE I. 100 and 1000 kJ Inductively Charged Pulse Lines*

(V = 1 MV, C = 0.2 (2.0) μF)

t_o(μs)	L_oC(μs)	L_o(μH)		I_o(kA)		η
50	10	500	(50)	26	(265)	0.57
50	5	125	(12.5)	66	(660)	0.37
50	2	20	(2)	270	(2700)	0.13
20	2	20	(2)	165	(1650)	0.37
10	2	20	(2)	130	(1300)	0.57

*The storage and pulse line parameters for 1000 kJ system (L_o, I_o and C) are given in parenthesis.

The circuit shown in Fig. 2 represents an alternate inductive technique for generating short, high power pulses. A fast opening switch assembly, consisting of three switch stages (i.e. an exploding switch with a fuse, followed by another fast fuse), replaces the pulse line used in Fig. 1, as a pulse-forming element. Studies related to staging of fuses have shown that output pulse rise time of 50 to 250 nsec [1], [11], at a megavolt level can be achieved. Thus, such an approach can be used very effectively for directly powering accelerating structures that require short pulses.

The analysis describing the power output from an inductive storage suitable for accelerator applications can be performed with sufficiently accurate results when three switch stages are represented by a single switch, as shown in Fig. 2. This is the case because almost all of the energy is dissipated in the second stage. In the case of the high voltage short pulse system, the inductance in series with the load must also be included. The time dependance of the fuse resistance and the energy to be dissipated in heating the fuse material determine the pulse shape and efficiency. The main effect of these factors is determined by

theoretical analysis giving the load current, $I_L(t)$, from which the power output and voltage across the load can be derived. During its vaporization the fuse acts as a dissipative element and its resistance goes through a range of values. The simplest model is a resistance which increases abruptly to a value R_o. The resulting efficiency of energy transport W_L/W_o is given in Fig. 2.

In designing a practical energy source for high power accelerators, the important criterion usually is the output voltage, V, for a given power requirement. Suppose, that R_L and L_L are specified, then it is evident that W_o and V are functions of L_o/L_L and R_o/R_L only. To obtain realistic relations between these quantities, so that a more accurate estimate of the performance and design parameters of the all-inductive pulser can be made, the equations for the circuit in Fig. 2 have been solved numerically using experimental data for aluminum fuses exploded in water [11]. For dimensionless presentation of these results, time, t_o (nearly equal to the fuse explosion time), is defined as the ratio of $W_v\sigma_o/j^2_o$, where W_v is the vaporization energy of 2.5×10^{10} J/m^3 and $\sigma_o = 2.4 \times 10^6$ mho/m is the conductivity at time t_o. J_o is the current density in the fuse. The normalized voltage is shown in Fig. 3 as functions of R_o/R_L (which is proportional to fuse length) and normalized time. The voltage, limited by the restrikes along the fuse, can not attain values above the straight dashed line. This limit is based on recent data [11], giving $E_{max}\, t_o = 4000$. The current and voltage waveforms obtained by selecting a fuse corresponding to the intersection of the voltage curves with the limiting field line are shown in Fig. 3. These waveforms, having fast rise time and slow decay, are characteristic of inductors driving resistive loads.

In the last year, high current, high voltage, opening switch development progressed sufficiently, so that inductive charging of pulse lines, as well as use of entirely inductive systes, can be considered practical for accelerator applications. The most important results of the experimental program are following developments. The circuit shown in Fig. 1, representing a method for charging of pulse lines, has been tested at NRL up to 500 kV, storing 2kJ in an 8 Ohm line [2]. The exploding switch testing, stressing the high voltage applications, was continued using 85kJ, 6kV capacitor bank, to drive an inductor to generate 300 kV across 90 cm long switch. The design of this switch and its performance below 100 kV is described in Ref. [7]. Other designs were tested showing that up to 47 kV/cm can be maintained across short switch sections. These results indicate that accelerator designs can become highly compact, and therefore inexpensive, as compared with present designs. Finally, fast (250 nsec) rise time, 1 MV, pulses were generated using arrays of wires exploded in water. Investigation of their characteristics shows that up to 20 kV/cm can be maintained across such wires. These arrays replaced the output stage of an inductive system shown in Fig. 2. Exploding such arrays in water [11], as well as in air [1], indicates that accelerator designs with short output pulse based on the approach shown schematically in Fig. 2 can be projected for operation at several megavolts across resistive-inductive loads.

III. REFERENCES

1. Yu. A. Kotov, N. G. Kolganov, V. S. Sedoi, B. M. Kovaltchuk, G. A. Mesyats, Proceedings of the First International Pulsed Power Conference, IEEE Cat. No. 76H1147-8 REG 5, Lubbock, Texas (1976).

2. D. Conte, R. Ford, W. H. Lupton, J. D. Shipman, Jr., P. Turchi, I. M. Vitkovitsky, Conference Record on the IEEE International Conference on Plasma Science, Cat. No. 77CH1205-4NPS, (1977).

3. V. A. Glukhikh, O. A. Gusev, M. P. Svin'in, O. P. Pechersky, A. S. Perlin, E. M. Mellikh, E. P. Pavlow, G. M. Latmanizova, V. S. Kuznetsov, M. I. Avramenko, V. B. Markov, L. A. Vikhodtsev, N. G. Beruchev, S. A. Kolyubakin, The High-Current Microsecond Electron Beam Accelerator, Preprint D-0302, NIIEFA, Leningrad, USSR, (1976).

4. L. V. Dubovoi, I. M. Roife, E. V. Seredenko, B. A. Stekolnikov, Feasibility of Microsecond Range High Current Accelerator, NIIEFA Review Report OT-5, Leningrad (1974).

5. L. Liebing, Z. Angew. Phys. 26, 345-350, (1969).

6. U. Braunsberger, J. Salge, U. Schwarz, Proc. of the Eighth Symposium on Fusion Technology, Jutphaas, Nederlands, (1974).

7. R. D. Ford, I. M. Vitkovitsky, Explosively Actuated 100 kA Opening Switch for High Voltage Applications, NRL Memorandum Report 3561, (1977).

8. W. F. Weldon, M. D. Driga, H. H. Woodson, H. G. Rylander, "Energy Storage, Compression and Switching" ed. W. H. Bostick, V. Nardi, O.S.F. Zucker, Plenum Press, New York, N. Y. (1976).

9. A. E. Robson, P. Turchi, W. Lupton, M. Ury, W. Warnick, Op. Cit. in Ref. 8.

10. V. A. Glukhikh, B. G. Kvasev, V. V. Kharitonov, V. N. Skripunov, Self-Excited Homopolar Generator Development for High Current Electron Accelerator, NIIEFA Report A-0294, Leningrad, (1976).

11. D. Conte, R. D. Ford, W. H. Lupton, I. M. Vitkovitsky, to be published in Proc. of the 7th Symposium on Engineering Problems of Fusion Research, Knoxville, Tenn., (1977).

12. A. R. Miller, Proc. of the Fifth Symposium on Engineering Problems of Fusion Research, Princeton, N. J. (1973).

13. P. A. Miller, R. I. Butler, M. Cowan, J. R. Freeman J. W. Poukey, T. P. Wright, G. Yonas, Phys. Rev. Lett., 39, 92-95, (1977).

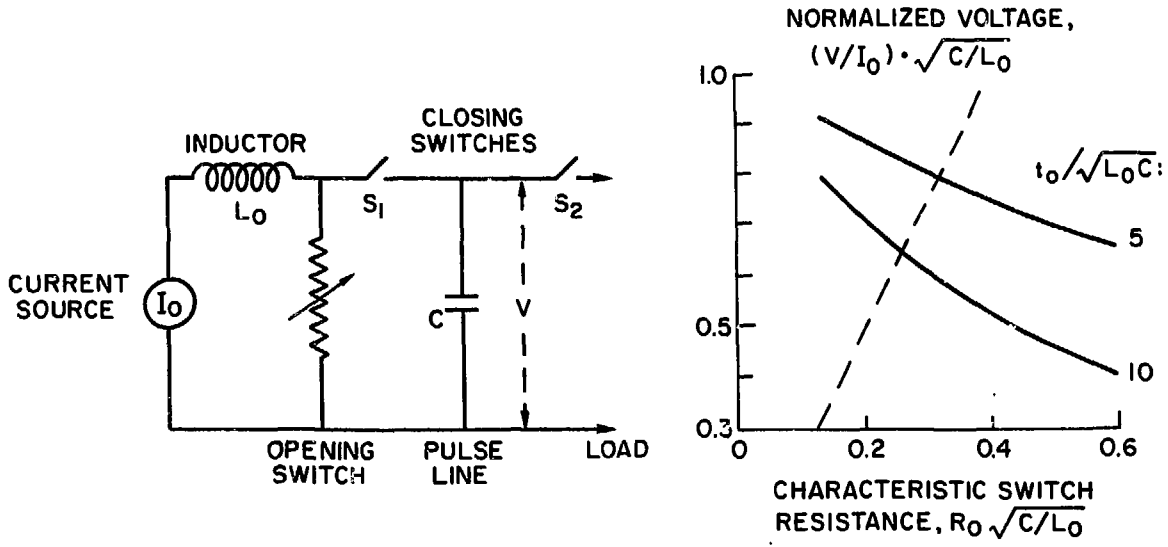

Fig. 1 INDUCTIVE STORAGE FOR PULSE LINE CHARGING

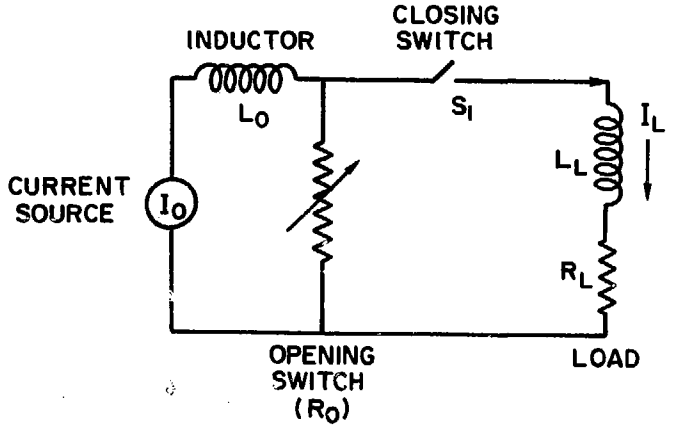

ENERGY TRANSFER EFFICIENCY:

$$\frac{W_L}{W_O} = \frac{1}{1 + R_L/R_O + L_L/L_O}$$

$$W_O = (1/2)\, L_O\, I_O^2$$

$$W_L = \int_0^\infty R_L\, I_L^2\, dt$$

Fig. 2 INDUCTIVE STORAGE FOR DRIVING INDUCTIVE/RESISTIVE LOAD

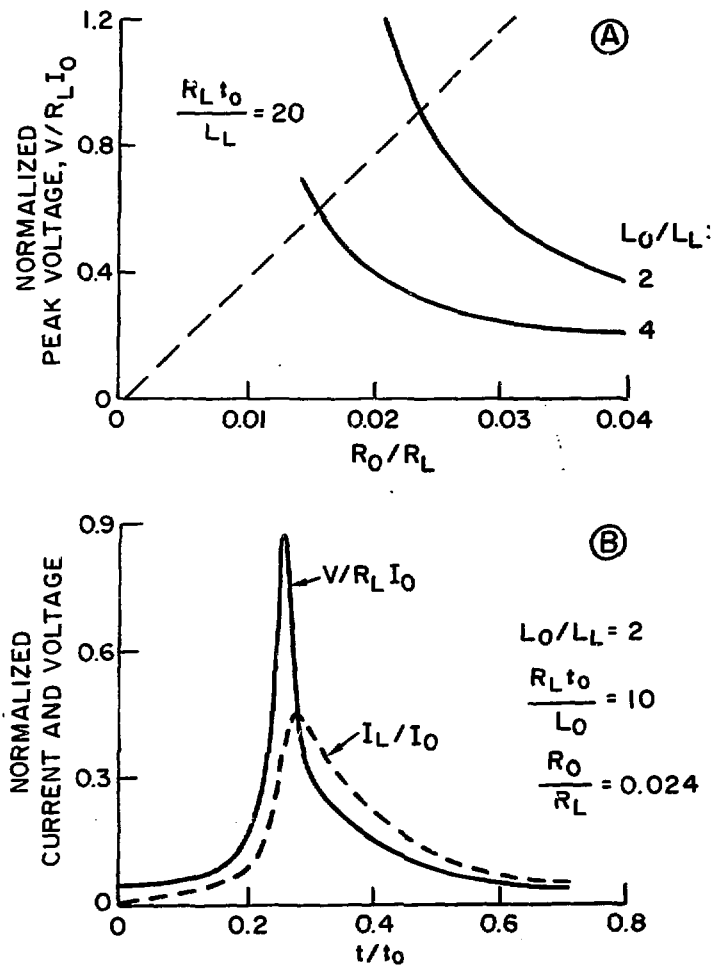

Fig. 3A PEAK VOLTAGE DEPENDENCE ON FUSE LENGTH.
B LOAD VOLTAGE AND CURRENT TIME DEPENDENCE

LASER APPLICATIONS

PROTON BEAM EXCITED LASERS

A. W. Ali

Naval Research Laboratory, Washington, D. C. 20375

The concept of proton beam pumped high pressure (> atmosphere) gas lasers will be discussed. Several new high pressure gas lasers produced by the application of relativistic electron beams can be excited by high energy proton beams as well. These lasers, excimer, charge exchange and energy exchange types, have a unique common denominator. They all depend on the number of atomic ions produced at the outset by the electron beam. Therefore, in principle, the more ionization produced, the higher will be the laser power density. MeV proton beams, traversing gaseous medium, have shorter mean free paths in comparison with electron beams of the same energy. The stopping powers of gases are much larger for protons compared to that of electrons. Therefore, protons deposit more energy per unit volume compared to electrons of the same energy, and hence create more ion pairs. Higher laser power densities will result from the application of MeV proton beams in contrast with MeV electron beams.

The kinetics of a new high pressure charge exchange laser, in a gaseous mixture of He and O_2, will be discussed. Its gain coefficient will be calculated under MeV proton beam pumping scheme indicating the possibility of a new high power laser.

exchange lasers.[13-14] The kinetics of these lasers leading to the production of the upper laser level and hence inversion, are illustrated below:

A. Excimer Laser from Xenon

$$e + Xe \rightarrow Xe^{+} + 2\,e \qquad (1)$$

$$Xe^{+} + Xe + Xe \rightarrow Xe_2^{+} + Xe \qquad (2)$$

$$Xe_2^{+} + e \rightarrow Xe^{*} + Xe \qquad (3)$$

$$Xe^{*} + Xe + Xe \rightarrow Xe_2^{*} + Xe \qquad (4)$$

B. Energy Exchange Laser in Ar - N_2 Mixture (Ar >> N_2)

$$e + Ar \rightarrow Ar^{+} + 2\,e \qquad (5)$$

$$Ar^{+} + Ar + Ar \rightarrow Ar_2^{+} + Ar \qquad (6)$$

$$Ar_2^{+} + e \rightarrow Ar^{*} + Ar \qquad (7)$$

$$Ar^{*} + N_2 \rightarrow N_2^{*} + Ar \qquad (8)$$

C. Charge Exchange Laser in He - N_2 Mixture (He >> N_2)

$$e + He \rightarrow He^{+} + 2\,e \qquad (9)$$

$$He^{+} + He + He \rightarrow He_2^{+} + He \qquad (10)$$

$$He_2^{+} + N_2 \rightarrow (N_2^{+})^{*} + He + He \qquad (11)$$

The first step in the kinetics of these lasers is the ionization produced by the passage of the e-beam. However, the proton beam will initiate that step as well. Thus, in principle the above lasers can be produced by proton beams.

The application of proton beams to the excitation of $He_2^{+} + N_2$ charge exchange laser should be routine since it is in the visible. This laser was produced by a 1 MeV electron beam with a current density of 1.3 KA/cm^2. For comparison we consider one of NRL's proton beam[16] devices. This device gives proton energies of 0.3-0.4 MeV and a current density of 0.1 KA/cm^2. In the first place the stopping power[19], L(E), (the energy absorbed) of He for proton beams with 0.3-0.4 MeV is

$\sim$ (6-4) X 10^{-15} eV-cm^2 (see Fig. 1). For 1 MeV electrons, on the other hand, the stopping power is $\sim 10^{-18}$ eV-cm^2 (see Eq. 3, Ref. 18). However, the density of ions (He^+) produced by a charged particle beam is proportional to L(E) times the current density. Therefore, for a given time, the number of ions produced by the proton beam (0.3-0.4 MeV) is at least two orders of magnitude larger than that produced by 1 MeV electron. Therefore, one expects higher laser power density using these proton beams compared to the above electron beams.

III Kinetics of $He_2^+ + 0_2$ Laser

We propose that the following near resonance charge exchange reaction

$$He_2^+ + 0_2 \rightarrow 0_2^+ (b^4 \Sigma) + 2\ He \qquad (12)$$

will result in a new laser[20] in the visible. According to the Franck-Condon principle, this reaction will populate higher vibrational levels of $b^4 \Sigma$. This state is the upper level of the first negative bands system of 0_2^+ which corresponds to $b^4 \Sigma \rightarrow a^4 \pi$ transitions in the visible[21]. Figure 2 shows the energy diagram for levels of interest.

This laser can be developed by the application of an e-beam or a proton beam incident on a high pressure mixture of He and 0_2 (He$\gg 0_2$). The passage of the charged particle beam will produce the helium atomic ions (Reaction 9) which in turn are converted into He_2^+ ions (Reaction 10) with a rate coefficient[22] 1.0 X 10^{-31} cm^6/sec. Those molecular ions then charge exchange with 0_2 with a total rate coefficient[23] of 1.0 X 10^{-9} cm^3/sec. Half of these reactions excite the upper laser level and the other half dissociatively charge exchange with 0_2. The atomic and the molecular ions recombine with the free electron through collisional radiative processes and are generally negligible[20] for times of interest. The processes that may affect the upper and the

lower laser levels are: the dissociative recombination, the quenching by O_2 and the de-excitations by the free electrons. The excited states of O_2^+ can be assumed to dissociatively recombine at the same rate as O_2^+ ground state. Quenching rate of the lower laser level by O_2 has been measured[25] and is 3×10^{-10} cm^3/sec. A similar rate can be assumed for the upper laser level. The electron de-excitation rates can be estimated using rates given by von-Regemorter[26]. Therefore, the impact of these processes on the inversion density can be estimated with increasing electron density, lower electron temperature and higher O_2 density. Other processes such as the formation of O_2^- and O_4^+ have negligible[20] effects on the inversion density. Also the amount of neutral hydrogen atoms produced via charge exchange of protons with helium is negligible[18].

Finally, a simple analysis[20] for this laser using a proton beam (0.3-0.4 MeV) with a current density of 0.1 KA/cm^2 gives a gain coefficient of ~ 0.3 cm^{-1} for two atmospheres of He mixed with 2 Torrs of O_2 and a proton pulse of 5 nsec. This indicates that a laser in the visible (6800 - 4992A°) is highly possible.

REFERENCES

1. S. E.Graybill and S. V. Nablo, Appl. Phys. Lett. 8, 18 (1966).
2. W. T. Link, IEEE Trans. Nucl. Sci. 14, 777 (1967).
3. F. M. Charbonnier, J. P. Barhous, J. L. Brewster, W. P. Dyke, and F. J. Grundhauser, IEEE, Trans. Nucl. Sci. 14, 789 (1967).
4. M. Clerc and M. Schmidt, C. R. Acad. Sci. B272, 668 (1971).
5. D. A. Leonard, Appl. Phys. Lett. 7, 4 (1965).
6. J. D. Shipman Jr., Appl. Phys. Lett. 10, 3 (1967).
7. A. W. Ali, A. C. Kolb and A. D. Anderson, Appl. Opt. 6, 2115 (1967).
8. N. G. Basov, V. A. Danilychev, and Yu. M. Popov, Soviet J. Quant. Elect. 1, 18 (1971).
9. H. A. Koehler, L. J. Ferderber, D. L. Redheaa, P. J. Ebert, Appl. Phys. Lett. 21, 198 (1972).
10. H. A. Koehler, L. J. Ferderber, D. L. Redhead, and P. J. Ebert, Phys. Rev. A9, 768 (1974) IBID A12, 968 (1975).
11. S. K. Searles and G. A. Hart, Appl. Phys. Lett. 25, 79 (1974).
12. N. G. Basov, A. N. Brunin, V. A. Danilychev, V. A. Dolgikh, O. M. Kerimov, A. N. Lobanov, S. I. Sagitov, and A. F. Suchkov, Sov. J. Quant. Elect. 5, 1218 (1975).
13. C. B. Collins and A. J. Cunningham, S. M. Curry, B. W. Johnson, and M. Stockton, Appl. Phys. Lett. 24, 477 (1974).
14. N. G. Basov, L. A. Vasilev, V. A. Danilychev, G. G. Dolgov-Savelev, V. A. Dolgikh, O. M. Kerimov, L. L. Kozorovitskii, V. K. Orlov and D. D. Khodkevich, Sov. J. Quant. Elect. 5, 869 (1975).
15. S. Humphries, J. J. Lee and R. N. Sudan, Appl. Phys. Lett. 25, 20 (1974).
16. J. Golden, C. A. Kapetanakos, S. J. Marsh and S. J. Stephanakis, Phys. Rev. Lett. 38, 1301 (1977) and references therein for other

proton beam devices and earlier work.

17. A. W. Ali, J. Golden, C. A. Kapetanakos and R. W. Waynant , "Charge Exchange Lyman α (1215A°) Laser Using Intense Pulsed Proton Beam", NRL Memo Report 3064 (1975).
18. A. W. Ali, "Proton Beam Pumping of High Pressure Gas Lasers", Naval Research Lab Memo Report 3519 (1977).
19. A. Dalgarno, Chapt. 15 in "Atomic and Molecular Processes", Bates Ed. Academic Press, New York (1962).
20. A. W. Ali, "Theory of $He_2^+ + O_2$ Charge Exchange Laser", Naval Research Lab Memo Report 3562 (1977).
21. R. W. Pearse and A. G. Gaydon, "Identification of Molecular Spectra", Wiley, New York (1963).
22. E. C. Beaty and P. L. Patterson, Phys. Rev. 137, A346 (1965).
23. F. C. Fehsenfeld, A. L. Schmeltekoph, D. B. Dunkin and E. E. Ferguson, ESSA Tech. Report ERL 135-AL3, Boulder, Colorado (1969).
24. M. Biondi, Can. J. Chem. 47, 1711 (1969).
25. E. E. Ferguson, Chapt. 18 in "Defense Nuclear Agency Reaction Rate Handbook", Bortner and Baurer, Eds. Published by DASIAC, G. E. TEMPO, Santa Barbara, CA (1972).
26. H. Von Regemorter, Astrophys. J. 136, 906 (1962).

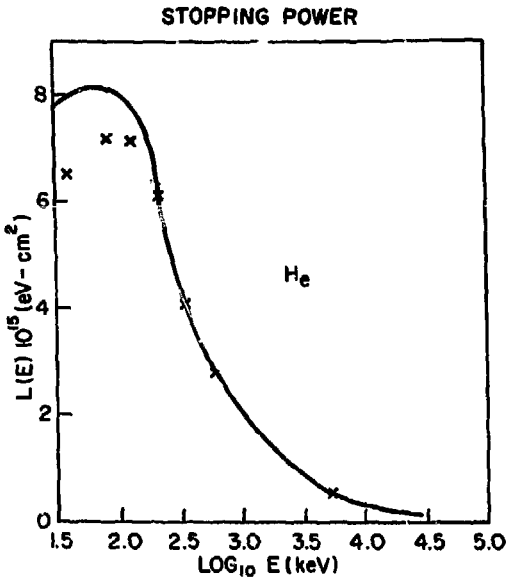

878

Fig. 1. The stopping power of He for protons as a function of proton energy. Calculated and experimental (indicated by XX) values are shown. See Ref. 19 for more detail.

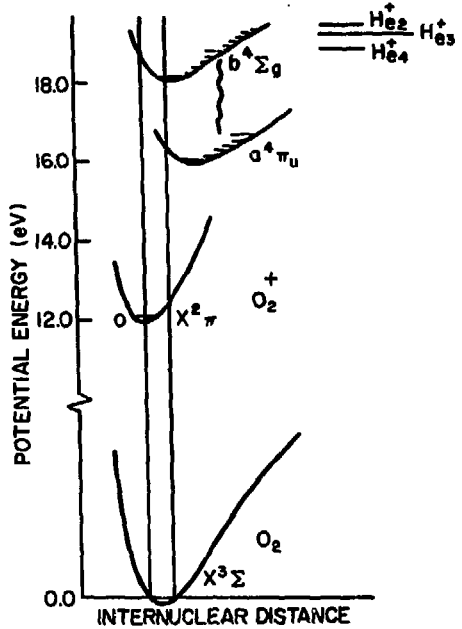

Fig. 2. The potential energy diagram of relevant O_2, O_2^+ AND POSITIONS OF He^+ are shown indicating the near resonance nature of $He^+ + O_2$ charge exchange.

RECENT ADVANCES IN COLD CATHODE TECHNOLOGY AS APPLIED TO HIGH POWER LASERS

G. K. Loda

Systems, Science and Software, Hayward, California 94540

Advances in cold cathode electron guns for laser application have continued over the last few years. Specific design and performance data will be discussed for several recently constructed systems. These include a large area (12 m^2) grid controlled gun for CO_2 lasers, high current density guns for KrF lasers, and a 100 Hz triode gun for a CO_2 laser. Preliminary results on an extension of this technology to a new two electrode cathode geometry will also be discussed. Issues to be addressed include the stability of electron emission and power supply drive requirements.

Section 1 INTRODUCTION

Development of cold cathode electron guns for laser applications has continued at Systems, Science and Software since the first International Conference on Electron Beam Research and Technology was held. Principal developments have been in the area of grid controlled triode guns and in relatively high current density large area diode guns.

Section 2 GRID CONTROLLED GUNS

Two grid controlled guns have been developed which together span a very large parameter range. One unit, Fig. 1, is a gun developed for the Los Alamos Scientific Laboratories High Energy Gas Laser Facility. The gun is a

full scale prototype of one of six guns that will be utilized in this 100 kjoule,1 nanosecond pulse laser fusion facility. A grid controlled gun was required for two reasons:

1. The largest machine tool available for generating the copper output mirrors determined a maximum diameter for the annular laser discharge. This then set a limit on the size of electron gun. Operation of a diode electron gun of this diameter would not have allowed operation at the low current densities required.

2. In order to limit the self generated magnetic field effects it is desired to make the cathode diameter as large as possible.

This large area cylindrical gun has been operated in the following parameter ranges:

1. Beam area 120,000 sq. centimeters (1.35 meter diameter by 2.8 meters long).

2. Beam current density 20 to 200 milliameters per sq. centimeter.

3. Accelerating voltage 300 to 500 KV.

4. Pulse duration 1 to 5 microseconds.

The expressions governing the impedance behavior of the triode gun are similar to those used on the cold cathode diode. In this case however space change limiting occurs in the region between the cathode and the grid. To develop the proper grid cathode voltage we have utilized a self biased grid circuit as is shown in Fig. 2. The grid is at ground potential before the application of the high voltage

pulse to the cathode to allow for a high electric field to be present on the cathode surface. This insures uniform ignition of emission sites. Once the cathode conducts current the grid approaches the cathode potential with its final potential being determined by the value of the grid current I_g, passing through the grid bias resistor R_g. The space charge equation for the cathode grid region can now be written

$$I_k = 2.3\times10^{-6} A_1 \, V_{gk}^{3/2} d^{-2} \quad \text{where } A_1 = \text{area of grid}, \; V_{gk} = \text{cathode to grid voltage}, \; d = \text{cathode grid separation} \tag{1}$$

Writing in terms of R_g we have

$$I_k = 2.3\times10^{-6} A_1 \, (V_k I_g \, R_g)^{3/2} d^{-2} \tag{2}$$

Since the grid has a known opacity we can relate I_k and I_g giving the complete space charge equation in terms of I_k, V_k, and R_g.

$$I_k = 2.3\times10^{6} A \, (V_k - c \, I_k \, R_g)^{3/2} d^{-2} \tag{3}$$

where c is the grid opacity

This transcendental equation is most easily solved numerically with the results given in Fig. 3. Actual measurements are also indicated on this figure showing agreement to within 10 to 20%. This close agreement with the very simple analysis given above has been confirmed (Ref. 1), in a second smaller cylindrical gun of the same basic design at Los Alamos.

An unexpected benefit of the triode has been in the control of the impedance collapse problem that are characteristics of cold cathode guns. Impedance collapse has been found to be a significant limitation in diode type cold cathode electron guns. The self generated cathode plasma moves toward the anode with a characteristic velocity generally determined by the cathode material. These velocities have been inferred from impedance measurements to be in the range of 0.5 cm/μs to 5 cm/μs. This is accomplished by fitting the space-charge equation

$$I = k_1 \frac{V^{3/2}}{(d-vt)^2}$$

where v is the plasma velocity, to the impedance time history of the diode.

For the self-biased triode the situation is quite different since the grid circuit stabilizes the gun impedance by always referencing the cathode current to the voltage drop across the grid resistance.

We can solve equation (3) for $I(d_1)$ and since $d = (X_1' vt)$ we can solve for J(t). Fig. 4 illustrates I(t) for the following conditions:

X_1 = 20 cm

v = 1 cm / μs

V_k = 500 kV

R_G = 168 ohms

For a 10 μsec pulse the analysis shows an increase of less than 10% in the output current density for a factor of two change in the effective anode-cathode separation. The same relative closure in a diode gun would have resulted in a current increase by a factor of four.

At the time t = 20 μs the cathode surface should impinge on the grid structure causing the loss of grid control. The gun should then operate as a diode with the grid resistance R_G acting only as a parallel load on the power supply.

One of the principle areas of investigation in the development of this prototype was to determine the effect of the magnetic field generated by the flow of current along the cathode surface on the trajectories of electrons within the triode.

We have not attempted a self-consistent treatment of this problem but have instead performed a very simple analysis of the problem to provide a background for viewing the experimental data.

If the following assumptions are made the analysis of this problem become quite easy:

1. B_θ is a constant in the z and r direction.
2. Significant deflection occurs only in the cathode-grid region.
3. E_r is constant.

Thus the problem reduces to solving the trajectory equations for a particle in a crosed magnetic-electric field. The equaticns of motion are given by

$$r = \left(\frac{m}{e}\right) \frac{E_r}{B_\theta^2} \left[1-\cos\left(\frac{e}{M}B_\theta \; t\right)\right] \tag{5}$$

$$z = \left(\frac{m}{e}\right) \frac{E_r}{B_\theta^2} \left[\left(\frac{e}{m}\right)B_\theta t-\sin\left(\frac{e}{m} B_\theta \; t\right)\right] \tag{6}$$

Deflection of the beam edge will then be given by simultaneously solving for z when $r = x_1$.

B_θ is the magnetic field generated by the current flowing along the cathode surface or

$$B_\theta = \frac{\mu_0}{2\pi} \frac{I}{\rho} \tag{7}$$

where ρ is mean radius between the cathode and grid.

Since the gun is space-charge limited we can write E_r in terms of current density. Thus

$$I = J_1 A_1 = k' \frac{V^{3/2}}{d^2} = k' \frac{E^{3/2}}{d^{1/2}}$$

or

$$E_r = \left[\frac{d^{1/2}}{k'}\right]^{3/2} I^{2/3} \tag{8}$$

substituting (2-13) and (2-14) into equation (2-11) and (2-12) we have the following

$$r = a_3 I^{-4/3} \left[1-\cos\left(a_4 It\right)\right] \tag{9}$$

$$z = a_3 I^{-4/3} \left[a_4 It-\sin\left(a_4 It\right)\right] \tag{10}$$

where

$$a_3 = \left(\frac{m}{e}\right)\left[\frac{10^4 d^{1/2}}{(2.3\cdot 10^{-6})(A_1)}\right]^{2/3}\left[\frac{\mu_0}{2\pi\rho}\right]^{-2}$$

$$a_4 = \left(\frac{e}{m}\right) \frac{\mu_0}{2\pi\rho}$$

For the cylindrical gun the following constants are appropriate.

$X_1 = 0.2$ m

$\rho = 0.375$ m

$A_1 = 4.2\ m^2$

A_1 is taken as one-half of the total grid area since two feedthroughs are utilized. The current I refers to the current flowing through one feedthrough only.

The results of this analysis are shown in Fig. 5. It is apparent that significant distortion of the beam edge can be expected for the higher current density condition.

The experimental points in Fig. 5 show that we have correctly predicted the trend of the behavior with this rough analysis but that significant departures exist at the higher currents. This is most likely a result of additional beam bending in a grid anode region. While operating the gun at very high beam densities and with current feeding the gun from one end only, we were in fact able to observe cutoff of the beam for at least the first 1 to 1-1/2 meters of the cathode length.

A smaller scale version of the cylindrical device was built with a beam area of 10 by 100 sq. centimeters. The design was similar to the cylindrical device with the exception of additional focus electrodes added to compensate for the lack of symmetry in the now planer beam device. The device shown in Fig. 6 was operated at repetition rates up to 100 pps. using a thyratron switched line type driver.

The parameter range investigated was:

Accelerating voltage	200 kV
Current density	25 to 100 mA/cm^2
Beam area	10 by 100 cm^2
Repetition rate	1 to 100 pps
Pulse duration	10 microseconds
Run time	10 seconds (typical)
Line driver power	20 kW average
Beam power	5 kW average
Beam uniformity	± 10%

The impedance control behavior of the triode circuit discussed earlier is clearly shown in Fig. 7. The cathode grid spacing for this gun was only 15 centimeters as compared to an assumed plasma motion of almost 10 centimeters yet the current has remained constant throughout the pulse.

Section 3 HIGH CURRENT DENSITY LARGE AREA DIODE GUNS

Recent advances in rare gas halogen lasers has prompted the need for large area high current density electron guns in order to scale these lasers to higher output powers. One of the devices had the following performance specifications: current densities from 5 to 20 A/cm^2 for pulse durations from 2 to 0.5 μs; beam size of 20 x 100 cm^2 with current density uniform within ± 15 percent accelerating voltages from 250 to 400 kV; and beam current risetime less than 50 ns.

All of the above specifications were individually within the state-of-the-art. However, in combination, these specifications defined a new system; significant

effort was required to design a reliable system to satisfy the combined requirements.

Two areas of particular concern were beam uniformity and the e-beam window.

At the high electric fields required for the high current operation, beam nonuniformity resulting from non-uniform generation of the cathode plasma was not expected to be of concern and indeed it was not. However, at these high currents, the self magnetic field of the beam will pinch the sides of the beam inward. Analytic calculations (Ref. 2) were performed to estimate the magnitude of this effect; then by carefully adjusting the cathode surface during testing, we were able to significantly reduce the magnetic effect by counter balancing it with a divergent electric field.

Even after adjusting the fields properly, a significant fraction of the electrons strike the foil support at a non-normal angle of incidence. State-of-the-art window supports for high pressure systems (5 atm operating pressure) call for closely spaced transverse ribs with large ratio of depth (in the beam direction) to spacing. These structures are, of course, opaque to the non-normal electrons. A new composite window design was devised (Fig. 8) that allows for transmission of most of the non-normal electrons thus increasing the beam current through-put and the beam uniformity.

REFERENCES

1. W. T. Leland, Private Communication

2. L. G. Schlitt and L. P. Bradley, International Topical Conference on Electron Beam Research and Technology, Nov. 1975.

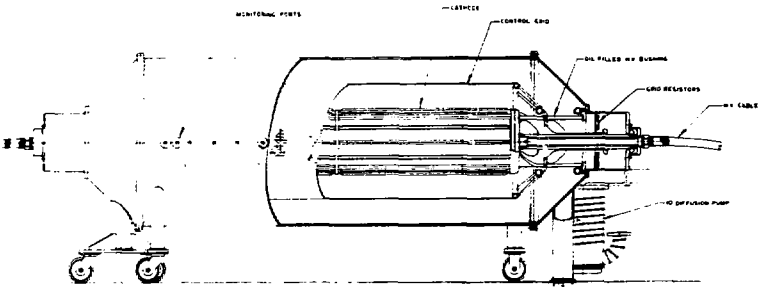

Fig. 1 Model 35280-12 Cylindrical Electron Gun

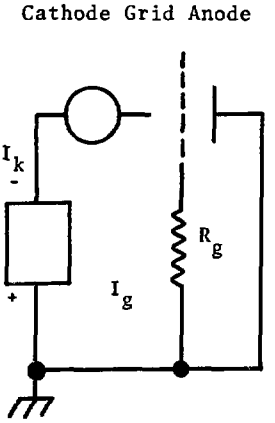

Fig. 2 Grid Bias Circuit

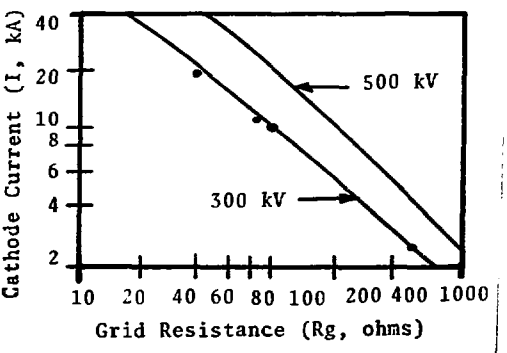

Fig. 3 Cathode Current as a Function of Grid Resistance

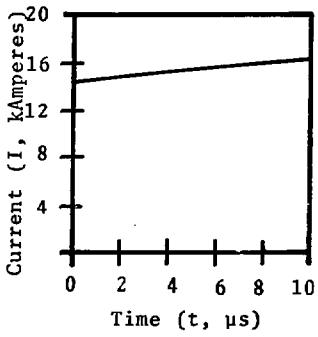

Fig. 4 Current vs Time

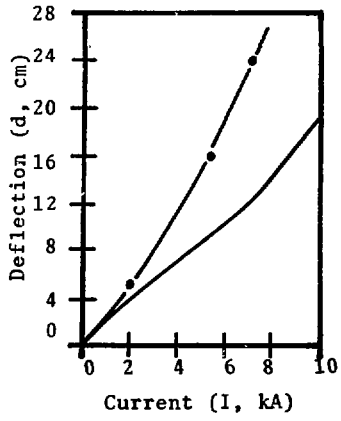

Fig. 5 Beam Edge Deflection as a Function of Cathode Current Single Feed - 50% Amplitude Points

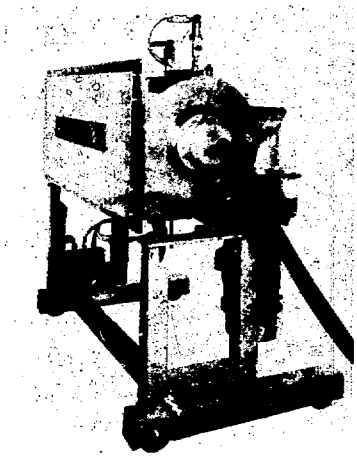

Fig. 6 Model 10100RP100 10 pps, 10 μs Cold Cathode Gun

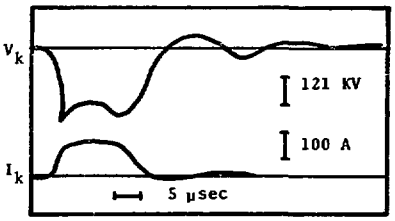

Fig. 7 Diagnostic Traces
25 ma/cm^2, 100 pps

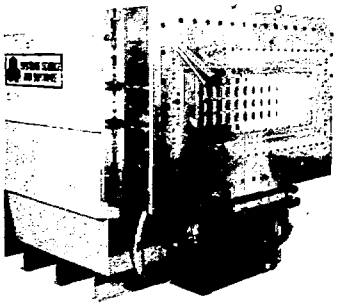

Fig. 8 Model 20100
Electron Gun

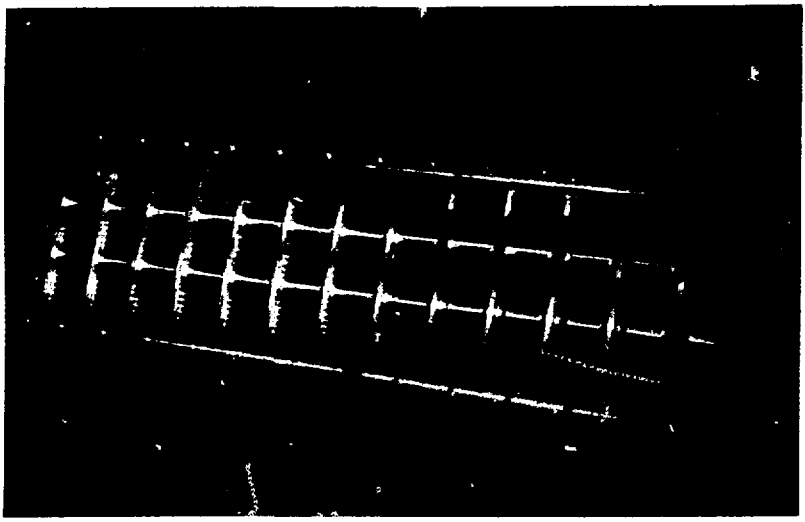

Fig. 9 Model 20100 Composite Window Structure

E-BEAMS FOR LASER EXCITATION*

J. J. Ramirez, K. R. Prestwich, R. S. Clark,
and M. T. Buttram

Sandia Laboratories, Albuquerque, New Mexico 87115

ABSTRACT

The operating characteristics of a 1 MV, 200 kA, 20 ns radial electron beam diode are presented together with beam transport and deposition measurements in various gases. Initial results on the emission characteristics and stability of 1-10 A/cm^2, 1 μsec diodes are described.

Introduction

Various gas laser schemes require electron beams with widely different pulse durations, current densities, and geometries. High power (1 MV, 130-260 A/cm^2, 20 ns) radially converging beams could be highly effective for pumping high gain lasers. Spatially and temporally uniform, low current density (1-40 A/cm^2), microsecond pulse duration electron beams are needed for direct excitation of photolytic U-V sources. In this paper we report on investigations of both cases are discussed.

HIGH POWER RADIAL DIODE

Use of high power radially converging electron beams for laser excitation were investigated on the REBLE accelerator facility.[1] An artists drawing of the REBLE diode is

*This work was supported by the U.S. Energy Research and Development Administration, under Contract AT(29-1)-789.

shown in Fig. 1. The 1 MV, 200 kA, 20 ns radial e-beam is generated at the annular cathode and converges through the thin-foil cylindrical anode. Typical diode waveforms are shown in Fig. 2.

Diode Operation

Studies of various cathode materials and geometries revealed that cathodes made of thin annular metal foils exhibited the shortest turn-on time, gave more uniform current emission, and had better shot to shot reproducibility than any other cathode types investigated. It was found that the current density pattern on the anode surface could be manipulated easily by making suitable changes in the number of blades, the separation between the blades, and the anode-cathode gap spacing. By making such changes, the current density uniformity at the anode could be maintained $\pm$ 10 percent along the circumference of the anode and to $\pm$ 15 percent along the length of the anode. The current densities at the anode were 100-250 A/cm^2.

The impedance of a single annular cathode blade can be expressed as

$$Z(1\text{-blade}) = K\,(x^2/AV^{\frac{1}{2}}) \qquad (1)$$

where x is the A-K gap spacing in cm, A is the area in cm^2 covered by the beam at the anode surface, and V is the diode voltage in MV.[2] The constant K was determined to be 675 from data such as that shown in Fig. 3. The height (h) of the beam at the anode was experimentally determined to be within 10 percent of twice the A-K gap. These values for K and h give a proper description of the impedance for a cathode

consisting of two blades, if the area covered by these two blades is twice the area covered by one blade. This was found to be true for both 20 and 10 cm diameter anodes. When substantial overlap exists between the emission patterns of the individual blades, the impedance of N-blades is greater than the impedance of 1 blade divided by N.

Beam Transport

The total beam energy exiting from the anode foil into the gas chamber was measured using a 60-element calorimeter system. The calorimeter was placed inside the evacuated (1 torr) gas chamber with the elements located within 0.3 cm of the anode foil. The total beam energy measured with the calorimeter was 1.2 $\pm$ .2 kJ out of 1.7 $\pm$ .2 kJ total diode beam energy. The average electron energy obtained from the I-V waveforms was 0.46 MV. At this energy, simple dE/dx considerations indicate that 70 percent of the incident electron energy would be transmitted through the .005 cm thick ss anode, in good agreement with the measurements.

A 2.3 cm diameter, 30 cm long Faraday cup (F.C.) was placed along the axis of the gas chamber. It collected electrons with energies greater than 150 keV. The chamber was pressurized with 100-2000 torr SF_6, xenon, krypton, argon, or nitrogen and time correlated measurements made of the F.C. current and total diode current. These measurements show that space charge fields do not cause appreciable delay in the arrival of the beam pulse at the chamber axis indicating the beam propagated readily through the various gases at these pressures. The ratio of the peak F.C. current to peak

diode current was found to be linearly dependent on the gas pressure. At 100 torr this ratio was less than 1 percent for all gases. Scattering of the beam at the anode foil causes the beam inside the anode to approximate an isotropic source and most of the radial convergence characteristic is lost. One-dimensional Monte Carlo calculations show that the outgoing distribution for a normally incident beam onto the anode foil approximates a Gaussian with a FWHM of $\sim 85°$.

Energy Deposition

Measurements were made of the spatially resolved beam energy deposition throughout the gas volume and compared to Monte Carlo electron-photon transport code calculations. The energy deposition was determined in two ways: by passive radiochromic dosimetry techniques, and by measuring the VUV light emitted by the xenon eximer ($\sim$ 1720 Å).

For the passive dosimetry measurements, 1.2 cm wide strips of radiochromic film running the length of the gas chamber were placed at a given radial position. The film was sandwiched between strips of black paper to prevent exposure to light. By scanning the film after exposure, a spatially-resolved measure of the dose in J/gm delivered to the film was obtained. Measurements were conducted at various pressures of xenon, krypton, argon, nitrogen, and SF_6 gas. For each gas and pressure, measurements were made with the film placed at a radius of 1.4, 5.6, or 9.7 cm. Typical results of these measurements and histogram plots of the corresponding Monte Carlo calculations are shown in Fig. 4. The total beam energy incident on the anode was used to convert the

code calculations to J/gm. The Z = 0 position corresponds to the midplane of the incident cylindrical beam. The agreement between calculations and measurements were good for all gases and pressures investigated except for SF_6 at pressures above 600 torr.[3] The total energy deposited in the gas as obtained from these calculations is also in good agreement with measurements made of the rise in the gas pressure after irradiation by the beam.

To get another reading of the radial profile of the energy deposition in the gas, an experiment was performed to measure the light emitted by the xenon eximer ($\sim$ 1720 Å). A schematic of the experimental configuration is shown in Fig. 5. Three different collimated photodiode arms were used so that the measurements at the different radial positions were made on the same e-beam shot. By integrating over the full temporal extent of the xenon radiation, the energy radiated per cm^2 along a direction parallel to the axis of the gas chamber was determined.[4] Results of these measurements are shown in Fig. 6 for various gas pressures. The estimated total error in the absolute value of these measured energies is $\pm$ 10 percent. To within the experimental error the measured radial profile of the emitted light is uniform at a pressure of 1600 torr. We estimate that at this pressure 20 percent of the total energy deposited in the gas results in Xe^* radiation at $\approx$ 1720 Å.

The experiments conducted on REBLE strongly suggest that high power radial electron beams can indeed be used to efficiently excite gas laser systems. Except for SF_6 gas at high

pressures, electron-photon transport codes can be relied on, to predict the energy deposition profiles to better than 20 percent. The case of the SF_6 anomaly may be due to its strong electronegative character. This anomaly with SF_6 has also been observed in the transverse excitation geometry.[5]

LOW CURRENT DENSITY DIODES

A program is underway to study electron emission in diodes that produce ∿ 300 kV, 10 A/cm^2, 1 microsecond e-beams using the LEGS and LPN accelerators whose equivalent circuits and output waveforms are shown in Figs. 7 and 8. Output parameters are listed in Table 1.

Emission Suppression

Laser applications require beam current densities of 1-10 A/cm^2 at the anode; therefore, spurious electron emission should be kept 1 or 2 orders of magnitude below this level. Several investigators have studied methods to suppress electron emission in vacuum gaps for d-c[6] and short pulse[7] (few tens of ns) applications; however, data for 1 μs pulse duration has not been reported. Bare metal and dielectric coated cathodes were tested using the test set-up of Fig. 9. The electric field on the 0.95 cm radius of the cathode is enhanced over the mean values quoted below by 1.4. Breakdown occurred in this enhanced region except as noted. All cathodes tested were aluminum with a 32 machine finish. The surface was polished with 600 grit sandpaper and diamond polish (15-1 micron paste). If coatings were used, they were applied to this substrate.

Table 2 is a tabulation of anode-cathode spacing,

electric field, and time to vacuum breakdown for the cathodes tested. When breakdown occurred, the current rise preceded the breakdown time by a few hundred nanoseconds. Referring to Table 2, Cases 1 and 2 are the same cathode with the electric field increased until breakdown occurred in the plane region. Case 3 is a fresh cathode with a closer spacing. The breakdown field for seven shots is less than the previous cases. The point of arc was random across the plane and radius of the cathode. The cathode of Case 3 was re-polished and re-spaced for Cases 4 and 5 in which a series of six consecutive shots were fired. Case 4 is the first shot of the series and did not emit at 70 kV/cm; however, five succeeding shots (Case 5) did emit off the radius at the same fields. The results of coating this cathode with silicone oil is seen in Cases 6 and 7. An acrylic clear lacquer was used to coat the cathodes of Cases 8, 9, and 10. The acrylic coating was 60 microns thick. The spacing was changed between Case 8 and 9 in order to obtain higher field strengths. Case 10 is the same cathode as Case 9 after it had experienced vacuum breakdown. These investigations indicate dielectric coatings can be beneficial in suppressing pre-breakdown current and improving vacuum breakdown strength significantly.

Emission Enhancement and Stability

A cathode of 10.2 cm diameter graphite felt, a material of densely packed graphite fibers with the fiber ends positioned in a random direction, was subjected to electric fields of 20-45 kV/cm. At 20 kV/cm, the cathode plasma

formed at discreet locations as shown in the open shutter photograph of Fig. 10. The current began to rise within a few tens of nanoseconds of the voltage rise. With 45 kV/cm electric fields, the same cathode plasma patterns were evident. These higher field shots had a shorter current turn-on-time and higher current amplitude. Radiochromic film measurements at the anode indicated current density variations of 50 percent for the low field case. For the same electric field but larger gap spacing, the uniformity of the anode current density should be improved.
proved.

Any cathode which emits from isolated sites will apparently be unstable to local current oscillations of the type shown in Fig. 11. The upper trace is the LPN voltage waveform, the lower is the local current density along the diode axis. The cathode is a 2 cm long needle mounted at the center of the cathode assembly of Fig. 9. For a 3 cm A-K gap and a 220 kV pulse, bursts lasting less than 50 ns are observed during which the current density exceeds five times the background. This instability in diodes with needle cathodes has been studied extensively[8] and it has been shown empirically that the time at which the instability occurs when averaged over many events is inversely proportional to $j^{0.42}$ for current densities $10^2 \leq j \leq 10^4$ A/cm^2. Figure 13 presents data for j down to 2.5 A/cm^2 taken on LPN with A-K gaps between 1 and 6 cm and voltages near 200 kV. Each point is an average of 5 to 10 shots. The error bars are calculated from the rms scatter of the data divided by the square

root of the number of events. Clearly for $j > 20$ A/cm^2 the current density at which instability occurs is subject to large fluctuation whereas the time is well defined. Below 10 A/cm^2 this situation is reversed.

For a needle cathode the local current density instability can always be seen in the total current as well. For cathodes consisting of a blade, carbon felt, or a hemisphere of radius comparable to the A-K gap the current density generally exhibits the instability although the total current frequently does not. Figure 12 shows an event for which the needle has been replaced by a 50 μm thick stainless steel foil blade. The increase in current density on axis relative to the ambient is reduced compared to the needle case and the time to instability is increased, on the average. The open circle point of Fig. 13 which is taken from blade cathode data illustrates the fact that current instability from a blade occurs later in time and at a higher current density than does the instability from a needle.

REFERENCES

1. J. J. Ramirez and K. R. Prestwich, Proc. of Int'l. Pulsed Power Conf., Lubbock, TX, IE-3 (1976).
2. T. H. Martin, L. P. Bradley, Bul. Phys. Soc. 16, 1229 (1971).
3. J. J. Ramirez and J. A. Halbleib, Presentation at APS Plasma Division Meeting, Atlanta, GA, (1977).
4. A. W. Johnson and J. J. Ramirez, Presentation at APS Plasma Division Meeting, Atlanta, GA, (1977).
5. R. A. Gerber and E. L. Patterson, Bul. Am. Phys. Soc. 21, 1147 (1976).

6. L. Jedynak, Proc. of First Symp. on the Insulation of High Voltages in Vacuum, p. 147 (1964).

7. G. B. Frazier, P.I. Report PIFR-784 (1975).

8. D. I. Proskurovskii, et al., Sov. Phys, Tech. Phys, 20 1342 (1974).

Table 1
LEGS and LPN Accelerator
Output Parameters

Pulser	Output Voltage	Pulse Width	Line Width	Impedance	Cathode Area
LEGS	4e7 kV	30 ns	1 m	4 Ω	1.1e3 cm²
LPN	360 kV	200 ns*	1.1 m	1 Ω	1.1e3 cm²

*With ... Pulse ... pulse: 1.4 / 27 ns)

Table 2
Vacuum Breakdown of Bare Metal and Dielectric Coated Cathodes

Case	Cathode Type	A-K Spacing (cm)	Electric Field (kV/cm)	Breakdown Time (usec)
1	Bare Metal	2.5	115	Full Pulse
2	Bare Metal	2.5	127	1.1
3	Bare Metal	1.27	100	0.4-1.0
4	Re-Polished Metal	1.9	70	Full Pulse
5	Re-Polished Metal	1.9	70-82	0.8
6	Silicone Oil	1.9	114	Full Pulse
7	Silicone Oil	1.9	133	0.75
8	Acrylic	1.9	165	Full Pulse
9	Acrylic	1.27	228	1.1
10	Acrylic	1.27	228	0.58

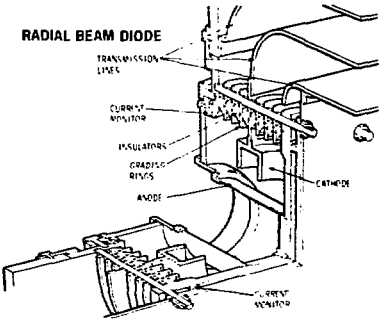

Fig. 1 - REBLE Diode

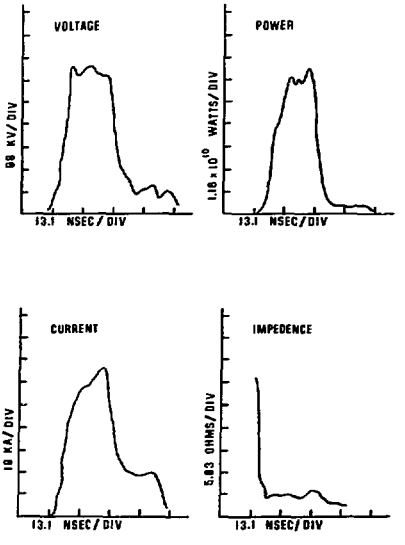

Fig. 2 - Diode Waveforms

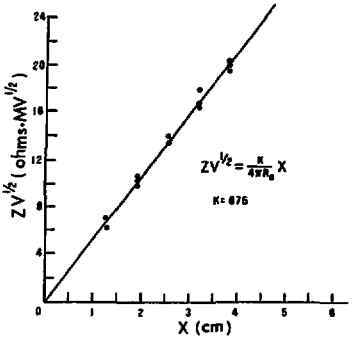

Fig. 3 - Impedance of a single annular blade cathode of radius R_o + X

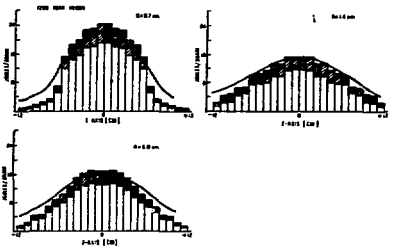

Fig. 4 - Measured and calculated dose delivered to radiochromic film

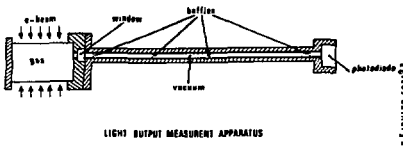

Fig. 5 - Experimental configuration for light output measurements

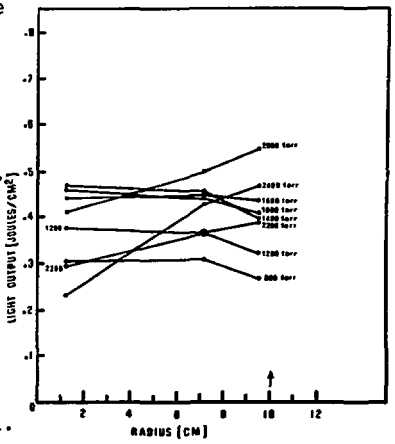

Fig. 6 - Light emitted by xenon eximer at various pressures. The arrow indicates the position of the anode foil.

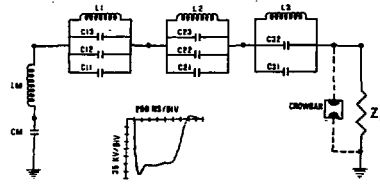

Fig. 7 - Equivalent circuit and output waveform of LEGS Accelerator

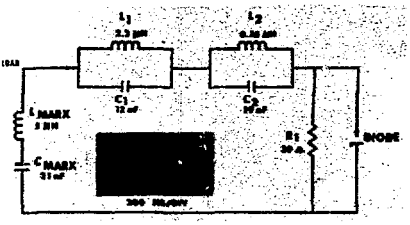

Fig. 8 - Equivalent circuit and output waveform of LPN Accelerator

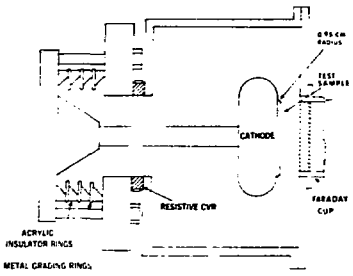

Fig. 9 - LPN Diode Configuration

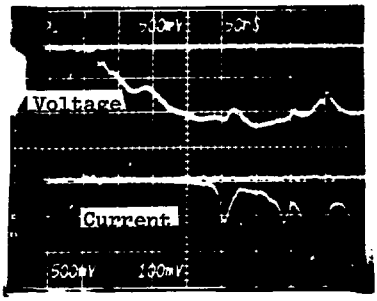

Fig. 11 - Diode Waveforms Needle Cathode

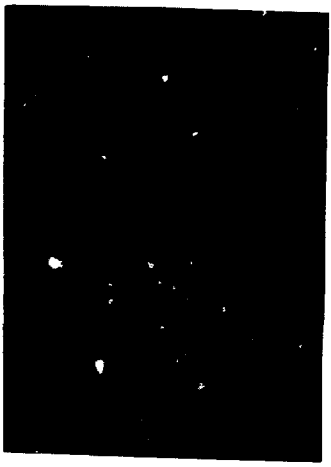

Fig. 10 - Electron Emission from a Graphite Felt Cathode (Metallic Mirror Anode)

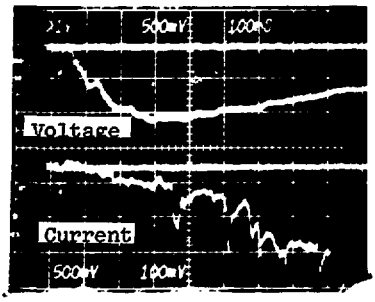

Fig. 12 - Diode Waveforms Blade Cathode

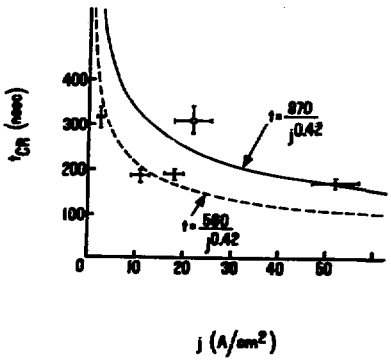

Fig. 13 - Time to Instability vs. Anode Current Density

CONFERENCE DIRECTORY

E. A. Abramyan
Electrophysics Division
Institute of High Temperatures
Korovinskoye Chossee
Moscow 127412 USSR

J. Adamski
Boeing Radiation Effects Laboratory
P.O. Box 3999
Seattle, Washington 98124

A. W. Ali
Code 7709
Naval Research Laboratory
Washington, D.C. 20375

C. Armstrong
P.O. Box 5342
North Carolina State University
Raleigh, NC 27607

P. L. Auer
Mechanical and Aerospace Eng.
224 Upson Hall
Cornell University
Ithaca, NY 14853

R. T. Avery
Lawrence Berkeley Laboratory
Building 46-189
Berkeley, CA 94720

J.-P. Babuel-Peyrissac
Comm. à l'Energie Atomique
Centre d'Etudes de LIMEIL
BP 27, Villeneuve
94190 Saint Georges, FRANCE

D. P. Bacon
Dartmouth College
Hanover, NH 03755

V. L. Bailey
Physics International Company
2700 Merced St.
San Leandro, CA 94577

R. O. Bangerter
Lawrence Livermore Laboratory
P.O. Box 808, L-545
Livermore, CA 94550

G. W. Barr
Sandia Laboratories
Albuquerque, NM 87115

E. H. Beckner
Organization 5200
Sandia Laboratories
Albuquerque, NM 87115

W. Beezhold
Sandia Laboratories
Albuquerque, NM 87115

J. Benford
Physics International Company
2700 Merced St.
San Leandro, CA 94577

W. Bennett
Department of Physics
North Carolina State University
Box 5342
Raleigh, NC 27607

R. Bleach
Naval Research Laboratory
Washington, D.C. 20375

S. P. Bougaev
Institute of High Current Electronics
Academicheski, Avenue 2
Tomsk, USSR

J. R. Boyce
Ward Laboratory
Cornell University
Ithaca, NY 14853

L. Bradley
Lawrence Livermore Laboratory
P.O. Box 808
Livermore, CA 94550

H. Brandt
Harry Diamond Laboratories
2800 Powder Mill Road
Adelphi, MD 20783

R. J. Briggs
Lawrence Livermore Laboratory
P.O. Box 808, L-306
Livermore, CA 94550

CONFERENCE DIRECTORY (continued)

A. Bromborsky
Harry Diamond Laboratories
2800 Powder Mill Road
Adelphi, MD 20783

Dr. M. Buttram
Division 5246
Sandia Laboratories
Albuquerque, NM 87115

J.-M. Buzzi
Ecole Polytechnique Lab.
P.M.I.
91128 Palaiseau, FRANCE

J. Cabé
Comm. à l'Energie Atomique
BP 14
21120 Is-sur-Tille, FRANCE

P. Caldwell
Dept. of Army, Harry Diamond
Laboratories, AMXDO-RBH
2800 Powder Mill Road
Adelphi, MD 20783

M. Caponi
TRW
Redondo Beach, CA 90278

N. Carron
Mission Research Corporation
735 State Street
P.O. Box 719
Santa Barbara, CA 93102

F. W. Chambers
Lawrence Livermore Laboratory
P.O. Box 808, L-306
Livermore, CA 94550

J. Chang
Sandia Laboratories
Albuquerque, NM 87115

J. C. Clark
Lawrence Livermore Laboratory
P.O. Box 808
Livermore, CA 94550

M. Clark
Air Force Weapons Laboratory
Kirtland Air Force Base,
New Mexico 87117

R. Clark
Division 5245
Sandia Laboratories
Albuquerque, NM 87115

M. J. Clauser
Division 5241
Sandia Laboratories
Albuquerque, NM 87115

T. Coffey
Naval Research Laboratory
Plasma Physics Division
Bldg. 101, Rm. 123
Washington, D. C. 20375

W. C. Condit
Lawrence Livermore Laboratory
P.O. Box 808
Livermore, CA 94550

D. L. Cook
Sandia Laboratories
Albuquerque, NM 87115

G. Cooperstein
Naval Research Laboratory
Code 7720
Washington, D. C. 20375

R. L. Copeland
Boeing Radiation Effects Lab.
P.O. Box 3999
Seattle, Washington 98124

J. Creedon
Physics International Company
2700 Merced Street
San Leandro, CA 94577

W. Crewson
Pulsar Associates, Inc.
7911 Hershel Ave., Suite 400
La Jolla, CA 92037

G. Dahlbacka
Physics International Company
2700 Merced St.
San Leandro, CA 94577

A. Dangor
Imperial College
Prince Consort Road
London SW, ENGLAND

F. Delobeau
Comm à l'Energie Atomique
BP 63
92120 Montrouge, FRANCE

B. Demidov
Kurchatov Institute of Atomic Energy
123182 Moscow, USSR

M. S. DiCapua
Physics International Company
2700 Merced St.
San Leandro, CA 94577

W. Doggett
Physics Department
North Carolina State Univ.
Raleigh, NC 27607

H. Dogliani
Air Force Weapons Laboratory
Kirtland Air Force Base,
New Mexico 87117

H. J. Doucet
Lab. P.M.I.
Ecole Polytechnique
Palteau de Palaiseau
91120 Palaiseau, FRANCE

W. F. Dove
DCTR/ERDA
Washington, D.C. 20545

K. Dreyer
Air Force Weapons Laboratory
Kirtland Air Force Base,
New Mexico 87117

A. T. Drobot
5432 Lighthouse Lane
Burke, VA 22015

B. Duborgel
C.E.A.
BP 27 Villeneuve
94190 St. Georges, FRANCE

A. Faltens
Lawrence Berkeley Laboratory
University of California
Berkeley, CA 94720

T. J. Fessenden
Lawrence Livermore Laboratory
P.O. Box 808, L-305
Livermore, CA 94550

R. Fiorito
Naval Surface Weapons Center
White Oak Laboratory
Silver Springs, MD 20910

A. Fisher
University of California
Department of Physics
Irvine, CA 92664

H. H. Fleischmann
Applied and Engineering Physics
205 Clark Hall
Cornell University
Ithaca, NY 14853

G. Frazier
Physics International Company
2700 Merced Street
San Leandro, CA 94577

J. R. Freeman
Division 5241
Sandia Laboratories
Albuquerque, NM 87115

M. Friedman
Naval Research Laboratory
Division of Plasma Physics
Code 7700
Washington, D.C. 20375

T. Genoni
Air Force Weapons Laboratory
Kirtland Air Force Base,
New Mexico 87117

R. Genuario
Physics International Company
2700 Merced St.
San Leandro, CA 94577

M. Gerver
Laboratory of Plasma Studies
Upson Hall
Cornell University
Ithaca, NY 14853

P. Gilad
Weizmann Institute of Science
Rehovot, ISRAEL

B. Godfrey
Los Alamos Scientific Laboratory
P.O. Box 1663, T-6 MS 531
Los Alamos, NM 87545

T. Godlove
Electron Beam App. Branch
Naval Research Laboratory
Code 7740
Washington, D.C. 20375

J. Golden
Naval Research Laboratory
Division of Plasma Physics
Code 7700, Bldg. 101, Rm. 113C
Washington, D.C. 20375

E. Goldman
Physics International Company
2700 Merced Street
San Leandro, CA 94577

S. H. Goldstein
Dept. of Astronomy and Physics
University of Maryland
College Park, MD 20742

V. L. Granatstein
Naval Research Laboratory
Division of Plasma Physics
Code 7700
Washington, D.C. 20375

E. H. A. Granneman
FOM-Institute for Atomic and
Molecular Physics
Kruislaan 407
Amsterdam-WGM THE NETHERLANDS

M. Greenspan
Laboratory of Plasma Studies
Upson Hall
Cornell University
Ithaca, NY 14853

H. Greim
Naval Surface Weapons Center
White Oak Laboratory
Silver Springs, MD 20910

J. Guillory
University of Maryland
Dept. of Physics and Astronomy
College Park, MD 20742

W. P. Gula
Los Alamos Scientific Laboratory
Group T-6, MS 531
Los Alamos, NM 87545

R. L. Gullickson
Air Force Office of Scientific
Research
AFOSR/NP
Bolling Air Force Base,
Washington, D.C. 20332

D. A. Hammer
Laboratory of Plasma Studies
Upson Hall
Cornell University
Ithaca, NY 14853

J. Hansman
MIT
77 Massachusetts Ave.
Cambridge, MA 02139

CONFERENCE DIRECTORY (continued)

N. Harris
Ion Physics Corporation
P.O. Box 416
South Bedford St.
Burlington, MA 01803

J. L. Harrison
Maxwell Laboratories
9244 Balboa Ave.
San Diego, CA 92123

D. Hasti
Austin Research Associates
600 W. 28th St.
Austin TX 78705

R. Hoeberling
Air Force Weapons Laboratory
Kirtland Air Force Base,
New Mexico 87117

I. Hofmann
Lawrence Berkeley Laboratory
University of California
Berkeley, CA 94720

P. Hsu
3333 Handley Avenue
Idaho Falls, ID 83401

C. Huddleston
Naval Surface Weapons Laboratory
White Oak Laboratory
Silver Springs, MD 20910

D. Hudgings
ERA Laboratory
Dept. of Electrical Engineering
University of Maryland
College Park, MD 20742

S. Humphries, Jr.
Sandia Laboratories
Division 5244
Albuquerque, NM 87115

P. Hunter
Naval Surface Weapons Center
White Oak Laboratory
Silver Springs, MD 20910

G. Huttlin
Harry Diamond Laboratories
2800 Powder Mill Drive
Adelphi, MD 20783

H. Ishizuka
Lawrence Livermore Laboratory
University of California
Livermore, CA 94550

D. Johnson
Sandia Laboratories
Division 5245
Albuquerque, NM 87115

M. Johnson
Division of Magnetic Fusion Energy
U.S. ERDA
Washington, D.C. 20545

D. L. Judd
Lawrence Berkeley Laboratory
University of California
Berkeley, CA 94720

C. A. Kapetanakos
Naval Research Laboratory
Code 7760
Washington, D. C. 20375

S. Kassel
The Rand Corporation
2100 M. Street, N.W.
Washington, D. C. 20037

A. Kehs
Harry Diamond Laboratories
2800 Powder Mill Road
Adelphi, MD 20783

H. Kim
Dept. of Physics & Astronomy
University of Maryland
College Park, MD 20742

N. M. King
Rutherford Laboratory, SRC
Chilton, near Didcot
Oxon, OX 11 OQX, ENGLAND

A. Klein
Systems, Science & Software
P.O. Box 4803
Hayward, CA 94540

R. Kligman
Naval Surface Weapons Center
White Oak Laboratory
Silver Springs, MD 20910

A. A. Kolomensky
Lebedev Physical Institute
Academy of Sciences
Leninsky Prospect, 53
Moscow 11733, USSR

R. Kulkarni
University of Maryland
College Park, MD 20742

B. Kulke
Lawrence Livermore Laboratory
P.O. Box 808
Livermore, CA 94549

B. Kusse
Laboratory of Plasma Studies
Upson Hall
Cornell University
Ithaca, NY 14853

G. Kuswa
Sandia Laboratories
Albuquerque, NM 87115

M. Lampe
Naval Research Laboratory
Washington, D.C. 20375

E. Lauer
Lawrence Livermore Laboratory
Box 808
Livermore, CA 94550

E. P. Lee
Lawrence Livermore Laboratory
P.O. Box 808
Livermore, CA 94550

R. Lee
Naval Research Laboratory
Code 7750
Washington, D.C. 20375

R. L. Liboff
Electrical Engineering
214 Phillips Hall
Cornell University
Ithaca, NY 14853

L. Libelo, Jr.
Naval Surface Weapons Center
White Oak Laboratory
Silver Springs, MD 20910

B. Lippmann
Physics International Company
2700 Merced Street
San Leandro, CA 94577

T. Lockner
Naval Research Laboratory
Code 7740
Washington, D.C. 20375

G. K. Loda
Systems, Science & Software
P.O. Box 4803
Hayward, CA 94540

O. Lopez
Physics International Company
2700 Merced Street
San Leandro, CA 94577

R. V. Lovelace
225 Clark Hall
Cornell University
Ithaca, NY 14853

L. C. Madsen
Los Alamos Scientific Laboratory
Group TD-2
Los Alamos, NM 87545

R. Mahaffey
Naval Research Laboratory
Plasma Physics Division
Code 7760
Washington, D.C. 20375

J. C. Martin
AWRE SSWA H36
Aldermaston, Berkshire
ENGLAND

R. L. Martin
Argonne National Laboratory
9700 South Cass Avenue
Argonne, IL 60439

T. H. Martin
Division 5245
Sandia Laboratories
Albuquerque, NM 87115

A. Maschke
Brookhaven National Laboratories
Associated Universities, Inc.
Upton, L.I., NY 11973

D. H. McDaniel
Division 5245
Sandia Laboratories
Albuquerque, NM 87115

J. H. McNally
Los Alamos Scientific Laboratory
Los Alamos, NM 87545

D. Meeker
Lawrence Livermore Laboratory
P.O. Box 808
Livermore, CA 94550

R. A. Meger
ERA Laboratory - EE
University of Maryland
College Park, MD 20742

G. H. Miley
214 Engineering Laboratory
University of Illinois
Urbana, IL 61801

P. Miller
Division 5242
Sandia Laboratories
Albuquerque, NM 87115

R. B. Miller
Sandia Laboratories
Albuquerque, NM 87115

R. Missert
4455 Genessee St.
Buffalo, NY 14221

A. Mohri
Institute of Plasma Physics
Nagoya University
Nagoya, JAPAN

G. E. Moore
Analytic Services, Inc.
5613 Leesburg Pike
Falls Church, VA 22041

E. Morse
Engineering Laboratory
University of Illinois
Urbana, IL 61801

D. Mosher
Naval Research Laboratory
Division of Plasma Physics
Code 7700
Washington, D.C. 20375

T. Mukutmoni
11201 Balcones Woods Cove
Austin, TX 78759

S. V. Nablo
Energy Sciences, Inc.
Burlington Rd.
Bedford, MA 01730

E. Nardi
Weizmann Institute of Science
Dept. of Nuclear Physics
Rehovot, ISRAEL

J. A. Nation
Dept. of Electrical Engineering
Phillips Hall
Cornell University
Ithaca, NY 14853

K. Neilson
Physics International Company
2700 Merced Street
San Leandro, CA 94577

K. Nishihara
Inst. of Laser Engineering
Osaka University
Yamada-Kami, Suita
Osaka 565, JAPAN

C. Olson
Division 5241
Sandia Laboratories
Albuquerque, NM 87115

E. Ott
Dept. of Electrical Engineering
Phillips Hall
Cornell University
Ithaca, NY 14853

A. Palevsky
Massachusetts Institute of Technology
77 Massachusetts Ave.
Cambridge, MA 02139

V. Papadichev
P.N. Lebedev Institute of the Academy of Sciences
Leninsky Prospect 53
Moscow 11733, USSR

R. K. Parker
Naval Research Laboratory
Code 7740
Washington, D.C. 20375

J. Pasour
Naval Research Laboratory
Code 7740
Washington, D.C. 20375

E. Peleg
Laboratory of Plasma Studies
Cornell University, Upson Hall
Ithaca, NY 14853

A. Penfold
Telic Corporation
1631 Colorado Ave.
Santa Monica, CA 90291

G. Peters
Naval Surface Weapons Center
White Oak Laboratory
Silver Springs, MD 20910

D. A. Phelps
Maxwell Laboratories, Inc.
9244 Balboa Ave.
San Diego, CA 92123

K. Prestwich
Sandia Laboratories
Division 5246, Box 5800
Albuquerque, NM 87115

T. Prevender
Sandia Laboratories
Albuquerque, NM 87115

D. S. Prono
Lawrence Livermore Laboratory
P.O. Box 808, L-306
Livermore, CA 94550

S. D. Putnam
Physics International Company
2700 Merced Street
San Leandro, CA 94577

J. J. Ramirez
Division 5245
Sandia Laboratories
Albuquerque, NM 87115

A. Ramrus
Maxwell Laboratories, Inc.
9244 Balboa Ave.
San Diego, CA 92123

M. Read
Naval Research Laboratory
Code 7740
Washington, D.C. 20375

M. Reed
B.D.M. Corporation
Albuquerque, NM 87115

M. P. Reiser
University of Maryland
Department of Physics and Astronomy
College Park, MD 20742

W. W. Rienstra
Austin Research Associates
600 W. 28th St.
Austin, TX 78705

T. Roberts
Ballistic Missile Defense Systems
P.O. Box 1500
Huntsville, Alabama 35807

G. J. Rohwein
Division 5245
Sandia Laboratories
Albuquerque, NM 87115

N. Rostoker
Department of Physics
University of California
Irvine, CA 92717

H. L. Sahlin
Lawrence Livermore Laboratory
P.O. Box 808
Livermore, CA 94550

D. Samaras
Air Force Office of Scientific Research
Bolling Air Force Base
Washington, D.C. 20332

F. Sandel
236 H. Mudd Bldg.
Columbia University
New York, NY 10027

J. Sari
Calspan Corporation
P.O. Box 235
Buffalo, NY 14221

D. Schallhorn
Harry Diamond Laboratories
2800 Powder Mill Rd.
Adelphi, MD 20783

S. P. Schlesinger
Harvey Mudd School of Elec. Eng.
Columbia University
New York, NY 10027

L. Schlitt
Lawrence Livermore Laboratory
Livermore, CA 94550

M. Seidl
Stevens Institute of Technology
Department of Physics
Castle Point
Hoboken, NJ 07030

J. Sethian
Naval Research Laboratory
Code 7700
Washington, D.C. 20375

R. A. Shanny
RAS Scientific
7033 Via Estrada
La Jolla, CA 92037

A. Sharma
Laboratory of Plasma Studies
Cornell University
Upson Hall
Ithaca, NY 14853

R. Shefer
Massachusetts Institute of Technology
77 Massachusetts Ave.
Cambridge, MA 02139

M. Shellans
AFSC/Dept. of the Air Force
P.O. Box 92960 Worldway Postal
Los Angeles, CA 90009

S. Shope
Division 5242
Sandia Laboratories
Albuquerque, NM 87115

J. Siambis
Naval Research Laboratory
Code 7740
Washington, D.C. 20375

V. P. Smirnov
Kurchatov Institute of Atomic Energy
123182 D-182
Moscow, USSR

I. D. Smith
Physics International Company
2700 Merced St.
San Leandro, CA 94577

P. W. Spence
Physics International Company
2700 Merced St.
San Leandro, CA 94577

P. Sprangle
Naval Research Laboratory
Code 7700, Bldg 101, Rm. 113C
Washington, D. C. 20375

C. H. Stallings
Physics International Company
2700 Merced St.
San Leandro, CA 94577

S. Stephanakis
Naval Research Laboratory
Code 7700 Bldg. 71HT Rm. 116
Washington, D.C. 20375

A. G. Stewart
Harry Diamond Laboratories
2800 Powder Mill Rd.
Adelphi, MD 20783

D. C. Straw
Air Force Weapons Laboratory
Kirtland Air Force Base,
New Mexico 87117

C. D. Striffler
Dept. of Elec. Eng.
University of Maryland
College Park, MD 20742

R. N. Sudan, Director
Laboratory of Plasma Studies
Upson Hall
Cornell University
Ithaca, NY 14853

D. F. Sutter
Division of High Energy and Nuclear Physics
Mail Stop J309
Department of Energy
Washington, D.C. 20545

Director, Ballistic Res. Lab
U.S. Army ARRADCOM
Attn: DRDAR-BLD
Dr. Judith Temperly
Aberdeen Proving Gr., MD 21005

L. E. Thode
Los Alamos Scientific Laboratory
T-6 MS 531
Los Alamos, NM 87545

J. R. Thompson
Austin Research Associates
600 W. 28th St.
Austin TX 78705

A. Toepfer
Division 5242
Sandia Laboratories
Albuquerque, NM 87115

A. Trivelpiece
Maxwell Laboratories, Inc.
9244 Balboa Ave.
San Diego, CA 92123

P. Turchi
Naval Research Laboratory
Code 7700
Washington, D.C. 20375

M. Tuszewski
909 Mitchell St.
Cornell University
Ithaca, NY 14853

CONFERENCE DIRECTORY (continued)

J. T. Verdeyen
Dept. of Elec. Eng.
University of Illinois
607 E. Healy St.
Champaign, IL 61820

I. M. Vitkovitsky
Naval Research Laboratory
Division of Plasma Physics
Code 7700
Washington, D.C. 20375

T. S. Wang
University of Maryland
College Park, MD 20742

J.-M. Wersinger
Electrical Engineering
Phillips Hall
Cornell University
Ithaca, NY 14853

C. B. Wharton
Electrical Engineering
215 Phillips Hall
Cornell University
Ithaca, NY 14853

M. M. Widner
Division 5241
Sandia Laboratories
Albuquerque, NM 87115

E. Wilkinson
Ballistic Missile Defense Center
P.O. Box 1500
Huntsville, Alabama 35807

T. P. Wright
Division 5241
Sandia Laboratories
Albuquerque, NM 87115

H. Uhm
University of Maryland
College Park, MD 20742

S. V. Yadavalli
868 Thronwood Drive
Palo Alto, CA 94303

G. Yonas
Division 5241
Sandia Laboratories
Albuquerque, NM 87115

S. Yu
Lawrence Livermore Laboratory
P.O. Box 808
Livermore, CA 94550

Z. Zinamon
Weizmann Inst. of Science
P.O. Box 26
Rehovot, ISRAEL

O. S. Zucker
Lawrence Livermore Laboratory
P.O. Box 808
Livermore, CA 94550